INFORMATION TO USERS

This manuscript has been reproduced from the microfilm master. UMI films the text directly from the original or copy submitted. Thus, some thesis and dissertation copies are in typewriter face, while others may be from any type of computer printer.

The quality of this reproduction is dependent upon the quality of the copy submitted. Broken or indistinct print, colored or poor quality illustrations and photographs, print bleedthrough, substandard margins, and improper alignment can adversely affect reproduction.

In the unlikely event that the author did not send UMI a complete manuscript and there are missing pages, these will be noted. Also, if unauthorized copyright material had to be removed, a note will indicate the deletion.

Oversize materials (e.g., maps, drawings, charts) are reproduced by sectioning the original, beginning at the upper left-hand corner and continuing from left to right in equal sections with small overlaps.

Photographs included in the original manuscript have been reproduced xerographically in this copy. Higher quality 6" x 9" black and white photographic prints are available for any photographs or illustrations appearing in this copy for an additional charge. Contact UMI directly to order.

Bell & Howell Information and Learning
300 North Zeeb Road, Ann Arbor, MI 48106-1346 USA

UMI®
800-521-0600

LAND SURFACE PROCESS AND RADIOBRIGHTNESS MODELING OF THE GREAT PLAINS

by

Jasmeet Judge

A dissertation submitted in partial fulfillment
of the requirements for the degree of
Doctor of Philosophy
(Electrical Engineering and Atmospheric, Oceanic and Space Sciences)
in The University of Michigan
1999

Doctoral Committee:
Professor Anthony W. England, Chair
Professor Linda M. Abriola
Dr. Thomas J. Jackson, U.S. Department of Agriculture
Professor William R. Kuhn

To my parents, Avtar Singh and Ravinder Kaur,

and my husband, Jimmy

ACKNOWLEDGEMENTS

This dissertation is a result of the hard work and support of many people. I was fortunate to be advised and mentored by Professor Tony England, my dissertation committee chair. I have had one of the best graduate school experiences that any student can ever have. I benefited greatly from his "Tailored Mentoring and Research Style" (TMRS), tailored to each of his students' interests, strengths, and weaknesses. I admire his intellect, dedication, sincerity, and focus in teaching and mentoring.

I was privileged to have a dissertation committee matching my interdisciplinary interests. All the committee members, Professor Linda Abriola, Dr. Tom Jackson, and Professor Bill Kuhn, actively participated in the design and scope of the thesis project, and its expression in the dissertation. I thank them for their helpful suggestions and advice that made the thesis more meaningful and complete.

As with any field experiment, many people helped to make REBEX-4 and REBEX-5 successful. I thank Dr. Barry Goodison, Dr. Anne Walker, Mr. John Metcalfe, and Mr. David McNichol at the Atmospheric Environment Service, Canada, for participating in REBEX-4 and monitoring the bare soil site. From our Microwave Geophysics Group (UM-MGG), Mark Fischman was practically indispensable during the REBEX-4 experiment with his hardware expertise. I also thank the staff at the

USGS EROS Data Center for their hospitality during the experiment. Particularly, Rod Beck and his crew provided technical and ground support, and Dave Meyer willingly acted as the contact person for monitoring the field set-up. Thanks are also due to members of the UM-MGG who participated in REBEX-5. David Boprie was the key person responsible for refurbishing the radiometer system after REBEX-4, and setting it up in the field during REBEX-5.

Over the past seven years, I have worked with several faculty, staff, and students in three departments, Radiation Laboratory (EECS); Atmospheric, Oceanic and Space Sciences; and Environmental and Water Resources Engineering. I thank them all for their help and friendship. I have also developed many professional and personal relationships, particularly in the EECS department. I am indebted to the EECS-DCO staff for their prompt and efficient technical support, and to Leland Pierce for his availability and assistance. I am grateful to Richard Austin, Kathleen Bergen, Mayukh Bhattacharya, Sunil Bindiganavale, Mark Casciato, Roger DeRoo, Mark Fischman, Lee Glascoe, Lee Harle, Rashaunda Henderson, Nigel Hinds, Brian Hornbuckle, John Kendra, Stephane Legault, Ellen Lettvin, Adib Nashashibi, and Paul Siqueira for many technical and personal conversations, their friendship and support that help ease this arduous process. I thank Professor Avery Demond for her helpful suggestions and insights into soil physics.

For the past year, I have been commuting from Bloomington, Indiana. I thank many friends who offered their dwellings and put me up during my frequent visits to Ann Arbor: Carol and Jim Aldrich; Pam and Brian Beddor; Kathleen Bergen; Charlie and Mary Kaye Brown; Tony and Kathi England; Patsy and Ralph Gensley; Peggy

Goetz; Lee Harle and Randy Beckner; Nigel and Katie Hinds; Vijay and Kamini Nagpal; Sharon and David Ryder; and Jayshri Sabarinathan. They helped me keep my focus and momentum needed to complete my dissertation.

I thank Professor Fawwaz Ulaby for his financial support during the first year of my graduate school. I gratefully acknowledge Professor Tony England for supporting me for six years through his grants from the NASA Land Surface Hydrology Program. I also thank the Sloan Foundation for their fellowship which partly supported the REBEX-4 experiment.

I thank my parents for their love, encouragement, and tremendous sacrifices. No words can ever describe my gratitude for all they have done. Finally, my heart-felt thanks to my beloved husband, Jimmy, for his continuous support and encouragement throughout graduate school. It is his unconditional and abiding love that gives me the inspiration and strength I need to face everyday challenges.

TABLE OF CONTENTS

LIST OF TABLES

LIST OF FIGURES

LIST OF APPENDICES

CHAPTER 1

Introduction

The state and the amount of water stored in soil, snow, and vegetation which is available to the atmosphere through evapo-transpiration, are the most important factors governing energy and moisture fluxes at the land surface. These land surface fluxes, in turn, significantly influence local, regional, and global weather and climate. A better knowledge of the temporal and spatial distributions of stored water would allow more reliable forecasts of weather and near-term climate, agricultural productivity, floods, and drought. Land Surface Process (LSP) models simulate the fluxes at the land-air interface and estimate stored water. They are forced by weather and downwelling radiance provided by Atmospheric Models (AMs) within the General Circulation Models (GCMs). The GCMs are used for weather and near-term climate prediction and for studies of the sensitivity of the land-ocean-atmosphere system to various global climate change scenarios [195]. LSP models are also used within 3-D hydrology models for regional water cycle studies.

However well the land surface processes are simulated, current estimates of stored

water will diverge from reality without the periodic incorporation of relevant measurements, e.g., remotely sensed data such as microwave radiobrightness which can be related to surface soil moisture [63, 74, 38]. Satellite remote sensing offers the possibility of wide spatial and frequent temporal coverage of surface soil moisture that is linked to stored water through the LSP models. Satellite sensing is particularly advantageous at microwave frequencies because it is independent of sun-light and clouds, and at least at lower frequencies, of rain as well. Our Microwave Geophysics Group at the University of Michigan (UM-MGG) has developed a combined LSP and microwave emission or radiobrightness (LSP/R) model that predicts microwave brightnesses based upon the current estimates of moisture and temperature profiles when forced by weather [126, 124, 125, 123, 122, 73, 71, 111]. These brightnesses can be compared with observed radiobrightnesses and the differences used to correct errors in the estimate of stored water.

This dissertation describes research conducted to calibrate our high-fidelity, biophysically -based LSP/R model for selected sites in the Great Plains with ground-based field measurements; and to link ground-observed brightnesses to satellite-observed brightnesses. We chose to investigate the Great Plains region because it is relatively homogeneous on the scale of satellite microwave radiometers (~30-60 km), it consists of short vegetation such as crops and grasslands with relatively low biomass (~4 kg/m^2), and it occupies about 25% of the land area in North America [69] playing a significant role in continental weather and climate. Globally, crops and grasslands occupy about 35% of the land area [69] and have a significant impact upon global weather and climate.

This chapter offers an overview of existing LSP models and the processes they simulate, and a summary of some basic concepts in microwave remote sensing, particularly in microwave radiometry.

1.1 Historical Development of LSP Models

LSP models have commonly been used with the AMs. They receive downwelling radiation (shortwave and longwave), precipitation, wind speed, air temperature and relative humidity from the AMs, and pass energy, moisture, and momentum fluxes to the AMs [195]. Until the mid 1980's, these flux calculations were based upon very simple parameterizations involving albedo, moisture availability, and surface roughness [195]. The sensitivity of GCMs to these parameters have been studied extensively. Charney et al. [30, 31] investigated the GCM-sensitivity to land surface albedo by imposing desertification on a number of regions, and showed that large increases in albedo can function as a positive biophysical feedback. Walker et al. [208] and Shukla et al. [189] have demonstrated that soil moisture changes may have large feedback effects on continental climates. For example, Shukla et al. considered perfectly wet and completely dry soils and showed that dry regions were much warmer than the wet ones and that rainfall in dry soil regions was much reduced. Sud et al. [194] investigated sensitivity to surface roughness and concluded that changes in surface roughness can alter the distribution of convective precipitation through an influence upon water vapor transport. Idso et al. [94] studied the sensitivity of bare-soil albedo to changes in soil moisture. Each of these studies demonstrates a

significant coupling between the climatic behavior of the atmosphere and land-surface processes. Figure 1.1 illustrates some of the feedback mechanisms that can occur with large-scale changes in surface characteristics.

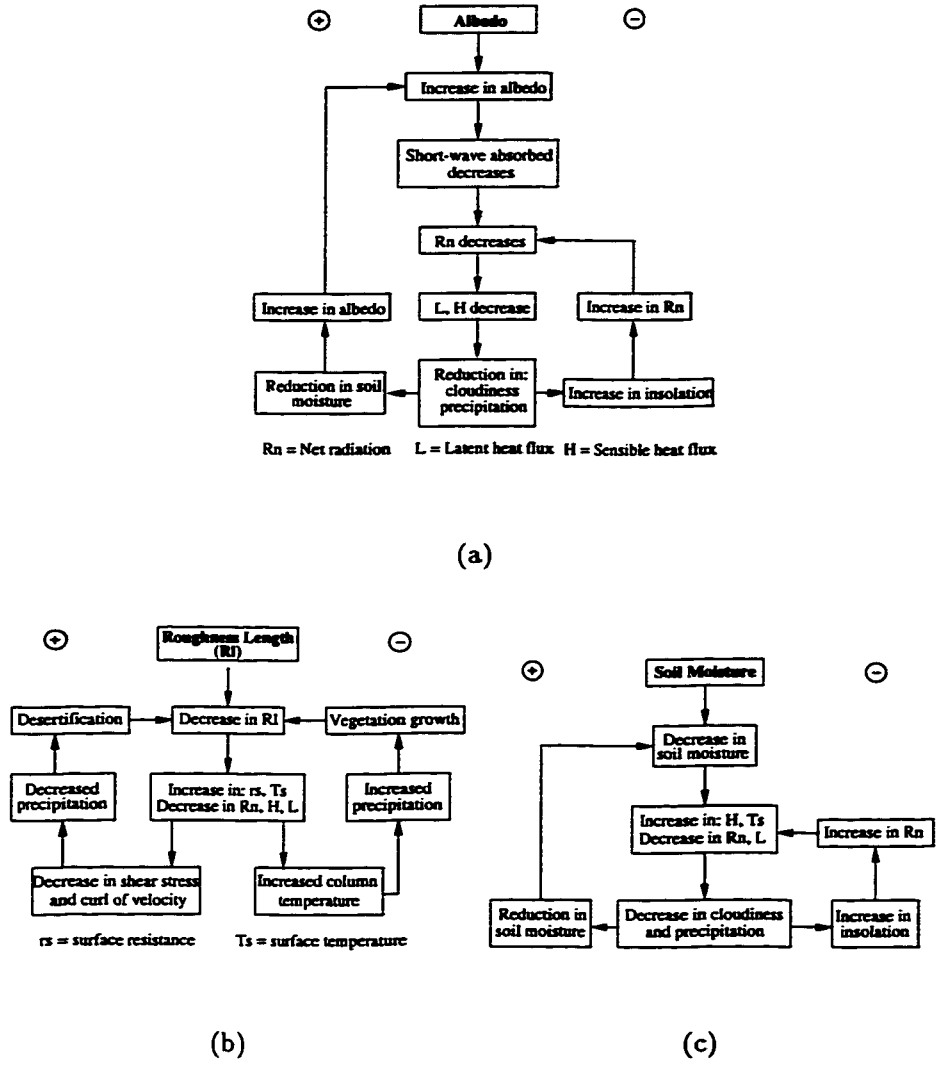

Figure 1.1: Possible consequences of large scale changes in three key surface parameters:(a) albedo (b) roughness length (c) soil moisture. The left hand side of each figure shows a positive feedback loop and the right hand side shows a negative feedback loop [195].

Dickinson et al. and Sellers et al. recognized the need for improved representations

of land-atmosphere interactions and developed new LSP models, viz., the Biosphere-Atmosphere Transfer Scheme (BATS) [48, 47] and the Simple Biosphere (SiB) [186], respectively. These models use more sophisticated and biophysically-based parameterizations for thermal and hydrologic properties of a broad range of soil and land cover types. Some parameterizations, such as moisture and heat transport in soil, remained over-simplified to avoid adding significant computational burdens to the GCMs. Many LSP models have been developed after BATS and SiB, that differ in the processes involved and in the characteristics of the parameterizations [19]. Some of the newer LSP models are outlined in Table 1.1. In 1992, the "Project for Intercomparison of Land Surface Parameterization Schemes" (PILPS) was launched to assess the performance of 23 LSP models [86, 35]. Early results from PILPS show a large variability among models in monthly averaged radiative temperatures and in latent and sensible heat fluxes. Large differences in monthly runoff suggest that these variations are related to hydrologic parameterizations [85, 133]. The importance of better hydrologic parameterizations was further demonstrated by Bonan [19] when he compared two recently developed LSP models, the Land Surface Transfer (LSX) and the Land Surface Model (LSM). These models, which primarily differ in their implementation of soil hydrology, predict significantly different latent and sensible heat fluxes [18, 20].

Over the past three years, a few high-fidelity LSP models have been developed. Although the stored water estimates have improved with such models, the estimates remain very sensitive to initial soil moisture [10, 11, 12, 33, 32, 207, 9, 217, 75, 113]. Retrospective studies with numerical weather prediction models have demonstrated

the importance of initializing LSP models with realistic soil moisture, especially so

Name	Reference
Bucket Scheme	Manabe (1969) [130]
Coupled Atmosphere-Plant-Soil model (CAPS)	Mahrt & Pan (1984) [129]
Simple Biosphere Model (SiB)	Sellers et al. (1986) [186]
Biosphere-Atmosphere Transfer Scheme (BATS)	Dickinson et al. (1986, 1992) [48, 49, 47]
UKMO	Warrilow et al. (1986)
Column model for storms (PLACE)	Wetzel & Chang (1988) [216]
Bare Essentials of Surface Transfer (BEST)	Pitman et al.(1991) [167]
GISS	Abramopoulos et al. (1988)[1] Hartke et al. (1997) [81]
Interaction Soil-Biosphere-Atmosphere (ISBA)	Noilhan & Planton (1989) [155]
SIBJMA	Sato et al. (1989) [176]
Land-Ecosystem-Atmosphere Feedback (LEAF)	Avissar & Pielke (1989) [6] Lee et al. (1992) [120]
MIT	Entekhabi & Eagleson (1989) [62]
NMC-MRF	Pan (1990) [160]
Canadian Land Surface Scheme (CLASS)	Verseghy (1991) [205, 206]
ECMWF	Blondin (1991) [17]
Agrometeorological model (AGROMET)	Moore et al. (1991) [142]
Simple SiB (SSiB)	Xue et al. (1991) [219]
CSIRO	Kowalczyk et al. (1991) [115]
Schematization des Echanges Hydriques à l'Interface entre la Biosphere et l'Atmposphere (SECHIBA)	Docoudré et al. (1993) [40]
Land surface exchange (LSX)	Pollard & Thompson (1992)
Penn State Univ. Biosphere Atmp. Model Scheme (PSUABMS)	
Hamburg/Max Planck	-
NMC/Mesoscale	-
Princeton University-1 (PU-1)	-
Variable Infiltration Capacity (VIC)	Wood et al. (1992) [218] Liang et al. (1996)[121]
Mosaic-SiB	Koster & Suarez (1992) [114]
RSTOM	Milly (1992) [137]
SPONSOR	Shmakin (1994) [188]
TOPLATS	Famiglietti & Wood (1995) [65]
BIOME	Running, S.
UGAMP	Gedney, N.
Land Surface Model (LSM)	Bonan (1996) [21, 22]
Land Surface Process/Radiobrightness Model (LSP/R)	Liou et al. (1996) [123]
IAGL Land Surface Model	Ridder (1997) [174]
Soil-canopy-atmosphere model	Lakshmi (1997) [118]
Microwave Soil Water Energy & Transpiration (MICRO-SWEAT)	Burke (1997) [25, 26]

Table 1.1: A list of some of the major existing LSP schemes [86, 85].

during extremes of weather like floods or drought. Atlas [3] showed that the 1988

drought in the Midwestern U.S. could be modeled accurately only when the model was driven by realistic initial soil moisture. Betljaars et al. [9] and Paegle et al. [158] demonstrated that the predictions of 1993 U.S. flooding in the Upper Midwest were significantly improved when initial soil moisture values were realistic. Even today, obtaining initial soil moisture is a problem. One promising possibility is to assimilate remotely-sensed soil moisture into the LSP models to improve initial moisture estimates [63, 92, 74, 38]. The initial results have been encouraging.

1.2 Processes Simulated in the LSP Models

In this section, I introduce some basic concepts, and associated equations and models used by to simulate moisture and energy transport in soil and vegetation. Figure 1.2 illustrates these processes. The net radiation (shortwave and longwave) from the atmosphere to the surface is [195]:

$$R_n = R_s^{\downarrow}(1-a) + R_l^{\downarrow} - e\sigma T_s^4 - F_{sh} - F_{lh} - F_g - F_p \tag{1.1}$$

where, $R_s^{\downarrow}$ is the insolation (W/m^2), a is the surface albedo, $R_l^{\downarrow}$ represents downwelling longwave radiation (W/m^2), $e\sigma T_s^4$ gives the upwelling longwave radiation (W/m^2), e is the surface infrared emissivity, σ is the Stefan-Boltzmann constant ($Wm^{-2}K^{-4}$), T_s is the temperature of the surface (K), F_{sh} is the sensible heat flux due to conduction to air (W/m^2), F_{lh} is the latent heat flux due to the energy released to the air by evaporation (W/m^2), F_g represents the heat flux into the ground (W/m^2), and F_p is the energy used for photosynthesis (W/m^2).

The average magnitude of F_g is typically about 10% of R_n, and F_p amounts to

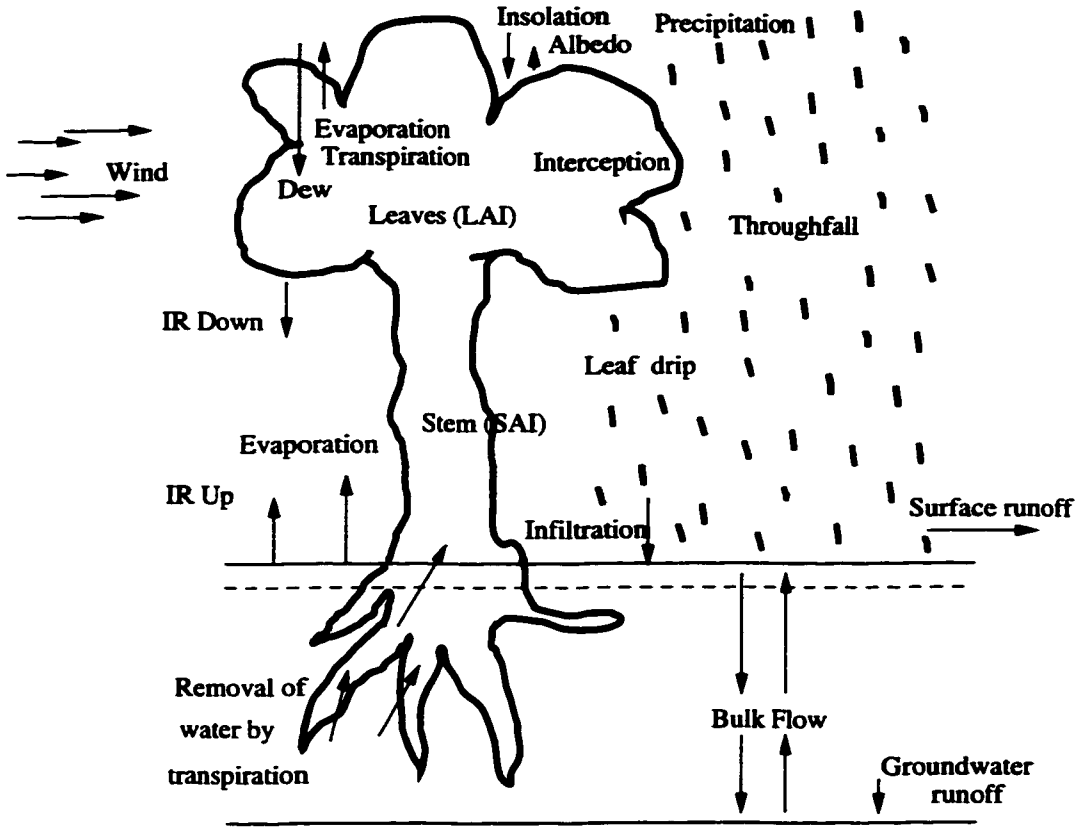

Figure 1.2: Schematic of processes involved in surface physics parameterization (adapted from [162, 48]).

less than 1% of the absorbed insolation [195]. The bulk of R_n is due to contributions from sensible and latent heat fluxes. Sensible heat flux (F_{sh}) is written:

$$F_{sh} = \left(\frac{T_s - T_r}{r_a}\right) \rho_a c_p \tag{1.2}$$

where, T_r is the air temperature (K) at reference height, z_r; r_a is the aerodynamic resistance to sensible heat transport, water vapor transport, or momentum transfer (s/m), ρ_a is the density of air (kg/m^3), and c_p is the specific heat of air (J.kg^{-1}.K^{-1}). The latent heat flux (F_{lh}) can be estimated [162]:

$$F_{lh} = L_v.E = L_v.\rho_a \left(\frac{q(z_r) - q(0)}{r_a}\right).f \tag{1.3}$$

where, L_v is the latent heat of evaporation (J/kg), E is the rate of evaporation to the atmosphere (kg/m^2.s), f is the evaporation efficiency, $q(z_r)$ is the specific humidity of air at reference height, and $q(0)$ is the specific humidity of air at the surface. Aerodynamic resistance, (r_a), is approximated:

$$r_a = \frac{1}{u_r}\left[\frac{1}{k} ln\left(\frac{z_r}{z_0}\right)\right]^2 \tag{1.4}$$

where, u_r is the wind speed at reference height, z_r; k is the von Karman's constant, usually taken as 0.4, and z_0 is the surface roughness length (m).

There are three commonly used parameterization schemes for moisture and heat transport in soil: Manabe's bucket model, the force restore method, and diffusion theory. The bucket model is the simplest of the moisture transport models ([24],[130]). In this parameterization, soil is modeled as a "bucket" with a field capacity of 15 cm. During precipitation, the bucket fills with the water that exceeds evaporation. The overflow becomes the runoff. When soil is near saturation, evaporation takes place at its potential rate, but when moisture levels are below a critical value in unsaturated soils, the evaporation rate is diminished by the ratio of the current soil moisture to the critical value. This model provides reasonable bounds rather than realistic values for evaporation rate because it ignores two processes which influence evapo-transpiration, viz., canopy resistance and diffusion in soil. The model is useful for GCMs that use diurnally averaged solar heating, but it is inappropriate for LSP models such as SiB or BATS that use a diurnal cycle of solar radiation [45, 46, 186].

The second parameterization scheme, called the force-restore method, was developed independently by Bhumralkar [13] and Blackadar [14], and later used by

Deardorff [43, 44]. This method models un-coupled heat and moisture transport in a two-layer soil whose surface layer is a few millimeters thick and whose bulk layer is 0.5 meters thick. Above the soil, a vegetation canopy interacts with the soil surface and the atmosphere. This parameterization is called the "force-restore method" because the heat fluxes at the ground (the forcing term) are modified by the bulk soil layer's temperature (the restoring term) to estimate the net heat flux at the surface [44]. Hunt compared the predictions of the bucket model with those of the force-restore technique for bare-soil with a diurnal mean sun and showed that the force-restore model has a more realistic fast initial response to drying conditions followed by a slow release of deeper water [93]. Modified versions of the force-restore technique are used in several LSP models such as BATS, SiB, LSM, and LSX.

The third parameterization scheme is the diffusion theory developed by Philip and de Vries [41, 163]. This theory models coupled heat and moisture transport in soil and describes this non-isothermal moisture flow, in liquid and vapor phases, with diffusion-type partial differential equations. Details of this theory will be discussed in Chapter 2. Some scientists have improved upon this theory, e.g., Milly and Eagleson [138] and Milly [136] developed a matric-head formulation to incorporate hysteresis and soil inhomogeneities based upon the water-content formulation of the diffusion model. Bach [7] used Milly's formulation to study the moisture transport in Otero sandy loam soil and concluded that the diffusion theory simulates non-isothermal moisture transport in soil adequately.

1.3 Remote Sensing Approach to Soil Moisture Estimation

As mentioned earlier, remotely-sensed data is being incorporated into LSP models to improve soil moisture estimates [94, 180]. Three remote-sensing approaches that rely on water's extreme thermal and dielectric properties, can be used to estimate surface soil moisture (moisture in the upper 5 cm of soil). These are, the thermal infrared (TIR) approach, which involves measuring the diurnal range of surface temperature or the canopy-air temperature differential [95, 171, 83, 84]; the active microwave approach, which involves measuring the backscatter coefficients of the surface [197, 15, 132]; and the passive microwave or the microwave radiometry approach, which involves measuring the microwave emission (brightness temperatures) of the surface [182, 154, 101, 178]. Microwave sensing is more suitable for observations during cloudy and rainy days than TIR sensing. TIR and active microwave techniques are highly sensitive to roughness and vegetation cover. While it may be possible to calibrate these techniques to each unique terrain and the maturity of its vegetation canopy, the effort would be enormous on a global scale. Microwave radiometry at 1.4 GHz has proven most successful for sensing soil moisture because its dominant sensitivity is to the dielectric contrast at the land-atmosphere interface, and this contrast is determined primarily by the moisture content of the upper 5 cm of soil [180]. Furthermore, successful soil moisture estimation has been demonstrated through as much as 6 kg/m^2 [102, 99, 181]. Though microwave radiometry offers lower spatial resolution (~30-60 km), its resolution is still comparable to the grid-cell size in climate

and hydrologic models (~10-30 km).

Microwave radiometry has been a focus of research since the 1960's. Poe et. al first reported observed correlations between microwave emission from soils and their moisture content [169]. Since then, various field experiments with ground- and aircraft-based radiometers have made it possible to relate soil and vegetation parameters to microwave emission at various frequencies, polarizations, and incidence angles [159, 131, 98]. Newton and McCllelan [153] and Njoku and Kong [154] conducted experiments over vegetated and bare sandy controlled fields, respectively. England and Johnson [57, 104, 157] used L-band radiometry to map the spatial pattern of surface soil moisture as an indication of underlying faults. Schmugge et. al. [180, 183, 177], Eagleman and Lin [53], Burke et. al. [27], Jackson [103], Wang et. al. [211, 213] were also involved in some of the early soil moisture field studies conducted at various frequencies and polarizations. Schmugge [177, 179], Wang et al. [212], and Mo et al. [139, 140] studied the multifrequency effects of soil texture and roughness on its microwave emissions. Reutov and Shutko [173] did experimental work to retrieve surface moisture from multispectral observations of bare soil.

Early theoretical studies on brightness temperatures and emission from structured media were conducted in by Peake [161] and Stogryn [192]. England [55, 56, 61] studied thermal microwave emission from scattering layers and found that scattering decreases emission from soils. Njoku and Kong [154] developed a theory for passive microwave remote sensing of surface soil moisture and temperature profiles. Jackson et al. [101] and Schmugge et al. [182] described various theoretical and experimental techniques using microwave remote sensing for soil moisture estimation.

Camillo et al. developed one of the first LSP models to be used with remotely sensed brightness temperatures [28, 29]. Their "Soil and Atmosphere Boundary Layer" model considered thermal and hydraulic transport in soil as a coupled process and took into account the feedback mechanisms between energy and moisture balances. The model also discretized the soil into nodes, where distances between the nodes increased with depth allowing it to capture temporal variations in soil moisture in the upper few centimeters. Liou et al. followed a similar modeling strategy with a more complex and physically realistic soil hydrology in their LSP/R model [123]. Recently, Lakshmi et al. [118] and Burke et al. [26] have also developed LSP models that are linked with satellite brightnesses.

1.3.1 Microwave Emission from Land Surface

Terrain brightnesses primarily depend on the water column density of vegetation cover [202, 199, 204, 198, 203, 209, 100, 154, 101] and vertical distribution of moisture and temperature in the upper 5 cm of soil [180]. When the vegetation is less dense, the radiometric responses also depend on soil texture [177, 52, 212] and surface roughness [34, 196, 139]. The frequencies of interest for soil moisture studies have been the Nimbus-7 Scanning Multichannel Microwave Radiometer (SMMR) frequencies of 6, 10.7, 18.0 and 37 GHz; the Defense Meteorological Satellite Program (DMSP) Special Sensor Microwave/Imager (SSM/I) frequencies of 19.35, 37.0 GHz, and 85.5 GHz; the L-band frequency of 1.4 GHz; the S-band frequency of 2.65 GHz; and the C-band frequency of 5.0 GHz. The lower frequencies are preferred because of their higher

sensitivity to soil moisture, with L-band being the most sensitive [182, 103, 184]. In the microwave region of interest, we can apply Rayleigh-Jean's approximation (1.5b) to the Planck's law (1.5a), and surface emission becomes proportional to the product of physical temperature and emissivity (equations 1.5a - 1.5d) [200].

$$B_f = \frac{2hf^3}{c^2}\left(\frac{1}{e^{\frac{hf}{kT}}-1}\right) \tag{1.5a}$$

$$\frac{hf}{kT} \ll 1 \tag{1.5b}$$

$$B_f = \frac{2f^2kT}{c^2} \tag{1.5c}$$

$$e = \frac{B}{B_{bb}} = \frac{T_B}{T} \tag{1.5d}$$

where, B_f is the blackbody spectral density ($\mathrm{Wm^{-2}sr^{-1}Hz^{-1}}$), h is the Planck's constant (Jsec), f is the frequency (Hz), c is the speed of light in the medium (m/sec), k is the Boltzmann's constant (J/K), B_{bb} is the brightness ($\mathrm{W/m^2.sr}$) of a blackbody, T is the physical temperature of the blackbody (K), e is the emissivity, B is the brightness of a material ($\mathrm{W/m^2.sr}$), and T_B is the brightness temperature of the material (K). The brightness temperature observed by a radiometer at a height, h, above the ground (bare-soil) contains components from several different sources [200]:

$$T_B = \tau(h)[rT_{sky} + (1-r)T_{surf}] + T_{atm} \tag{1.6}$$

where, $\tau(h)$ is the atmosphere transmission, r is reflectivity of the surface ($= 1 - e$), T_{sky} is the downwelling sky brightness (K), T_{surf} is the effective surface temperature (K), and T_{atm} is the upwelling emission from the atmosphere between the surface and the radiometer. If we use lower frequencies, we can ignore the atmospheric effects

and [58]:

$$T_B = e.T_{surf} \tag{1.7}$$

The emissivity of a surface is sensitive to its moisture content because of the large contrast between the dielectric properties of free water and those of the dry medium. For example, the relative permittivity of water at 1 GHz is nearly 80, while that of dry soils is approximately 4. As the moisture content of soil increases, the dielectric constant of the soil-water mixture also increases, so that the emissivity of the soil changes from approximately 0.95 for dry soils to 0.6 or less for wet soils [178]. The dielectric properties of typical soils at microwave frequencies have been studied by Hoekstra and Delaney [88], Hallikainen et al. [80], Dobson et al. [52], and England et al. [60], to name a few. Dobson et al. [52] estimated the dielectric constant for moist soils with an empirical refractive model [201] which considered soil as a mixture of solids, air, bound-water, and free-water. The reflectivity (r) of a smooth soil surface with a homogeneous moisture distribution can be calculated using the Fresnel equations of electromagnetic theory (1.8) [200].

$$r = \begin{cases} \left|\frac{\eta_a cos\theta_a - \eta_g cos\theta_g}{\eta_a cos\theta_a + \eta_g cos\theta_g}\right|^2 & \text{horizontal polarization} \\ \left|\frac{\eta_g cos\theta_a - \eta_a cos\theta_g}{\eta_g cos\theta_a + \eta_a cos\theta_g}\right|^2 & \text{vertical polarization} \end{cases} \tag{1.8}$$

where, η_a is the intrinsic impedance for air, η_g is the intrinsic impedance for ground, θ_a is the incidence angle, and θ_g is the transmission angle in soil.

The dielectric properties of vegetation are more difficult to estimate than soil because the sizes of the dielectric constituents of vegetation, such as leaves and stalks, are comparable to or larger than the wavelengths used [201]. If lower frequencies ($\leq$20

GHz) are used, we can develop approximate models to estimate effective relative permittivity of the vegetation canopy [202]. The dielectric properties of different vegetation have been experimentally studied by Nelson [146, 147, 148, 149], Nelson and Stetson [150], Kraszewski [116], Ferrazzoli et al. [66], and Ulaby et al. [201, 202, 199, 204, 198, 203, 54]. The dual-dispersion model developed by Ulaby et al. [198] remains the most widely used model to estimate the effective relative permittivity of a vegetation canopy. It models the dielectric constant of vegetation as an additive mixture of three components: a free-water component, a bulk vegetation-bound water component, and a nondispersive residual component [198].

1.4 Dissertation Objectives

This dissertation represents an important step toward assimilating remotely sensed microwave radiometric data to improve soil moisture estimates. It focuses on the "forward" modeling of terrain brightnesses using our community LSP/R model, and comparing the ground-based brightness observations with the satellite brightnesses. It investigates the following questions:

1. Is the implementation of numerical methods in the LSP/R model qualitatively and quantitatively accurate?
2. How well does the model estimate soil thermal and hydraulic transport and terrain brightnesses during summertime, when the land surface processes are dominant, in the mid-latitude regions for relatively homogeneous terrains?

3. Is the model "easily" extendible to the regions with different soil and terrain types?
4. How well do the brightnesses observed from the satellite correlate with those observed at the ground, and how well do the experimental sites during REBEX-4 and REBEX-5 represent the regions within their respective SSM/I pixels?
5. Can the remotely-sensed SSM/I brightnesses be potentially assimilated to improve soil moisture estimates by the LSP/R models?

1.5 Dissertation Format

In this dissertation, chapter 2 contains a description of our community LSP/R model and my modifications to it; and a discussion of results from the tests conducted to ensure the accurate implementation of numerical methods used in the model. Chapter 3 contains the observations made during our fourth and fifth Radiobrightness Energy Balance Experiments (REBEX-4 and REBEX-5). Data from these experiments were used to calibrate the modified LSP/R model for bare soil, brome grass, and winter-wheat stubble. I compare my model estimates with our field observations in chapter 4, and ground-based brightness observations with resampled satellite brightnesses in chapter 5. Chapter 6 is a summary of my results and original contributions, and my recommendations for future research.

CHAPTER 2

The LSP/R Model

This chapter gives a brief summary of our community Land Surface Process/Radiobrightness (LSP/R) model, a description of modifications made to it, and a discussion of results from three tests conducted to ensure the accuracy of the numerical simulation.

2.1 The Community LSP/R Model

Our community LSP/R model for moist prairie soils, representative of the northern Great Plains, was developed by Liou et al. to simulate the effects of coupled moisture and heat transport on the temperature and moisture of soil and vegetation, as well as on the brightness of terrain [124, 126]. This biophysically-based model has two modules: a 1-d Hydrology [124], or more appropriately, 1-d Thermal and Hydrology (1-dTH) module, and a Radiobrightness (R) module. The 1-dTH module simulates surface processes when forced by weather, and estimates temperature and moisture profiles in soil and canopy. The R module estimates apparent terrain brightnesses based upon the profiles from the 1-dTH module. A thorough description of the LSP/R

model can be found in recently published papers by Liou et al. [122, 124, 126]. This section gives a summary of the two modules in the community model. A schematic diagram of how the two modules are connected is given in Figure 2.1.

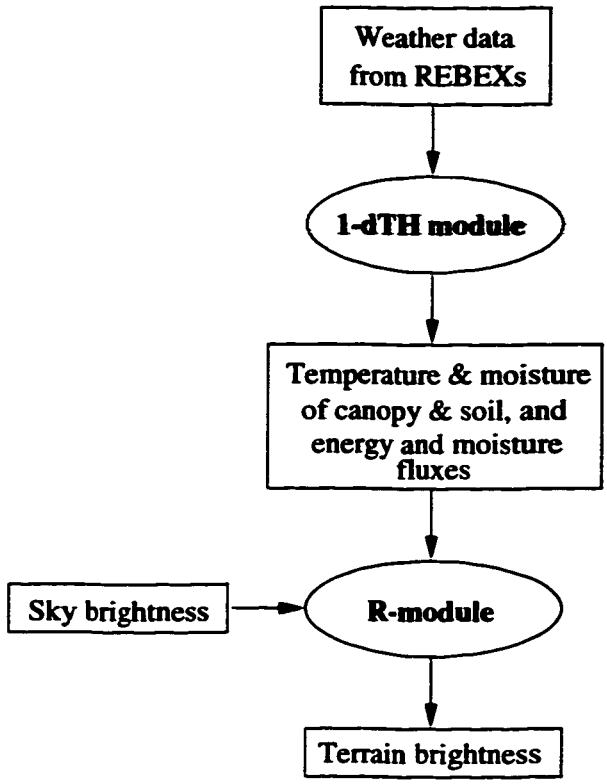

Figure 2.1: A flow diagram of interactions between 1-dTH and R module in the LSP/R model.

2.1.1 The 1-d Thermal and Hydrology (1-dTH) Module

2.1.1.1 Biophysics and Governing Equations

The 1-dTH module consists of bi-layered vegetation over a homogeneous soil with uniform constitutive properties. Figure 2.2 shows the surface processes simulated in the module. The vegetation cover, which includes a canopy and a thatch layer, can

vary from 0%, for bare soil to 100% for vegetated soil. Figure 2.3 gives a pictorial representation of a partially-vegetated field that may be represented in the module. In the figure, the vegetation and the soil cover are 0.5. The module ignores soil-air interactions in the vegetated soil as the vegetation cover is assumed to be a 100% in those areas [compare Figures 2.3 and 2.8].

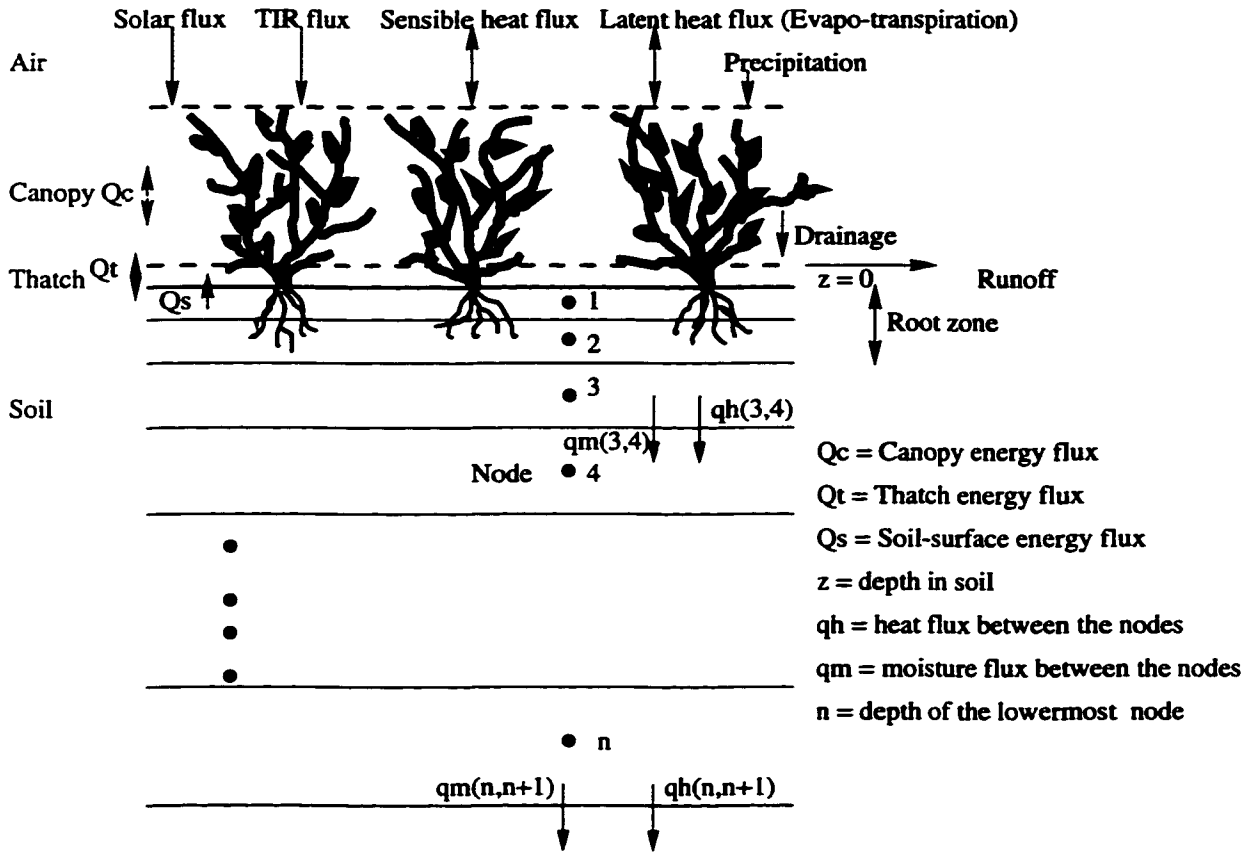

Figure 2.2: Land surface processes simulated in the 1-dTH module (adapted from [126]).

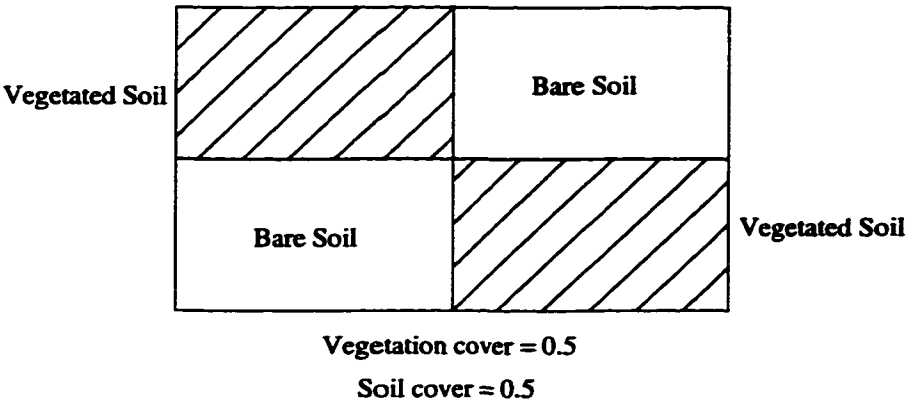

Figure 2.3: A pictorial representation of a partially vegetated surface simulated by the 1-dTH module.

The module uses the following mass and energy conservation equations to simulate coupled thermal and moisture transport in canopy, thatch and soil.

Canopy

Canopy is a photosynthetically active vegetation layer in the 1-dTH module. Energy fluxes in this layer are primarily driven by insolation and canopy thermal infrared (TIR) emission, while moisture fluxes are driven by evaporation and transpiration. The energy and moisture transport equations for the canopy are:

$$\frac{\partial X_{mc}}{\partial t} = \rho_l(P_c - D_c - E_c) \tag{2.1a}$$

$$\frac{\partial X_{hc}}{\partial t} = -(H_c + L_c - R_{nc}) \tag{2.1b}$$

where,

- X_{mc} and X_{hc} are the total moisture and heat contents per unit area stored in the canopy, respectively, (kg/m^2 & J/m^2),
- ρ_l is the density of liquid water (kg/m^3),
- P_c, D_c and E_c are the rates of precipitation, water drainage and evaporation (m/s),

• H_c is the sensible heat flux between the atmosphere and the canopy(W/m^2),

• L_c is the latent heat flux between the atmosphere and the canopy due to evaporation from the wet fraction and transpiration from the dry fraction of the canopy (W/m^2) and,

• R_{nc} is the net radiation (longwave and shortwave) absorbed by the canopy (W/m^2)

$$R_{nc} = veg[(1-\tau_c)(1-A_c)Q_{s,d} + Q_{l,d} + e_t\sigma T_t^4 - 2e_c\sigma T_c^4] \quad (2.2)$$

where,

– veg is the fraction of vegetation cover (e.g. $= 0.5$ in Figure 2.3),

– $\tau_c = Exp[-\kappa_c * LAI]$ is the transmissivity of shortwave radiation for the canopy as described by the non-scattering Beer's law of radiative transfer. $\kappa_c = 0.4/cos(Z)$ is the extinction coefficient [206] and LAI is the Leaf Area Index of the canopy,

– A_c is the albedo of the canopy,

– $Q_{s,d}$ and $Q_{l,d}$ are the downwelling shortwave and longwave radiation, respectively (W/m^2),

– e_c and e_t are the thermal infra-red emissivities of the canopy and thatch, respectively,

– σ is the Stefan-Boltzmann constant (W/m^2) and,

– T_c and T_t are the canopy and thatch temperatures, respectively, (K).

Thatch

Thatch is a thermally insulating, non-photosynthetic layer in the module that is used to simulate energy absorption by organic matter above the soil. It does not hold any moisture and has no influence on the moisture exchanges between the canopy

and the soil. This layer is more prominent in regions that are undisturbed and has a significant impact on energy interactions between the canopy and the soil. The energy balance equation for the thatch is:

$$\frac{\partial X_{ht}}{\partial t} = R_{nt} \tag{2.3}$$

where,

- X_{ht} is the total heat content per unit thatch area (J/m^2) and,
- R_{nt} is the net radiation (longwave and shortwave) absorbed by the thatch layer (kg/m^3), and is given by

$$R_{nt} = veg[\tau_c(1-A_c)(1-A_t)(1-\tau_t)Q_{s,d} + e_c\sigma T_c^4 + e_s\sigma T_s^4 - 2e_t\sigma T_t^4] \tag{2.4}$$

where,

  - veg, τ_c, $Q_{s,d}$, e_c, e_t, σ, T_t, and T_c are as defined for equation 2.2,
  - A_t is the albedo of the thatch,
  - e_s is the emissivity of the soil and,
  - T_s is the temperature of the soil surface (K).

Soil

The soil is homogeneous with uniform constitutive properties. It is discretized into 60 nodes[1]. Because the nodes closer to soil surface are more influenced by weather changes than the deeper nodes, the distances between the nodes increase with depth. The upper few nodes form a root-zone where transpiration in the roots is simulated. The constitutive properties of soil, such as moisture and thermal diffusivities, tortuos-

[1]The term "layers" refers to soil zones with different constitutive properties. A homogeneous soil has only one layer. The term "nodes" refers to discretizations of the layer(s) in the numerical simulation.

ity, thermal conductivity, and water retention, are estimated from empirical models, detailed descriptions of which are given in [124, 42, 112, 117, 175]. The moisture and energy balance equations for the soil are,

$$\frac{\partial X_m}{\partial t} = -\nabla \cdot \vec{q}_m \tag{2.5a}$$

$$\frac{\partial X_h}{\partial t} = -\nabla \cdot \vec{q}_h \tag{2.5b}$$

where,

- X_m and X_h are the total moisture and heat contents per unit volume, respectively (kg/m^3 & J/m^3) and,
- $\vec{q}_m$ and $\vec{q}_m$ are the moisture and heat flux densities, respectively ($kg/m^2.s$ & $J/m^2.s$).

X_m, X_h, $\vec{q}_h$ and $\vec{q}_m$ are given by the diffusion type equations from Philip and deVries [41, 166, 124].

$$X_m = \rho_l(\theta_l + \theta_v) \tag{2.6a}$$

$$X_h = C_m(T - T_0) + L_0\rho_l\theta_v + \rho_l \int_0^{\theta_l} W d\theta \tag{2.6b}$$

$$\vec{q}_m = -\rho_l(D_T\nabla T + D_\theta \nabla\theta + K\hat{k}) \tag{2.6c}$$

$$\vec{q}_h = -\lambda\nabla T + L_0\vec{q}_v + (c_p q_v + c_l q_l)(T - T_0) \tag{2.6d}$$

where,

- $C_m = C_d + c_l\rho_l\theta_l + c_p\rho_l\theta_v$,
- ρ_l is the density of liquid water (kg/m^3),
- $\theta = \theta_l + \theta_v$ is the volumetric moisture (liquid and vapor) content (m^3/m^3),
- θ_l is the volumetric liquid fraction (m^3/m^3),
- θ_v is the volumetric vapor content (m^3 of precipitable water/m^3),

- C_m and C_d are the volumetric heat capacities of moist and dry soil, respectively $(J/m^3.K)$,
- c_p is the specific heat of water vapor at constant pressure $(J/kg.K)$,
- c_l is the specific heat of liquid water $(J/kg.K)$,
- T is the absolute temperature (K),
- L_0 is the latent heat of vaporization at the reference temperature, T_0 (J/kg),
- W is the differential heat of wetting,
- D_T and D_θ are the thermal and isothermal moisture (liquid and vapor) diffusivities, respectively $(m^2/K.s)$,
- K is the unsaturated hydraulic conductivity (m/s),
- λ is the thermal conductivity of soil $(J/m.K.s)$ and,
- $\vec{q}_v$ and $\vec{q}_l$ are the vector vapor flux densities, respectively $(kg/m^2.s$ & $J/m^2.s)$.

Boundary Conditions

At the upper boundary, i.e., at the interface between soil and vegetation, moisture and energy fluxes are primarily driven by net precipitation and radiation reaching the soil surface as follows:

$$q_m(0,1) = \rho_l(D_c - E_s - E_{tr} - Runoff) \quad (2.7a)$$

$$q_h(0,1) = R_{ns} - H_s - L_s \quad (2.7b)$$

where,

- $q_m(0,1)$ and $q_h(0,1)$ are the moisture and heat fluxes at the interface between nodes 0 (vegetation) and 1 (soil surface), respectively,
- ρ_l is the density of liquid water (kg/m^3),

- H_s and L_s are the sensible and latent heat fluxes from the soil, respectively (W/m^2),
- D_c is the rate of drainage (= total precipitation -interception by the canopy) from the canopy (m/s),
- E_s is the rate of evaporation from the soil (m/s),
- E_{tr} is rate of transpiration from the soil (root zone)(m/s) and,
- R_{ns} is the net radiation (longwave and shortwave) absorbed by the soil (W/m^2),

$$\begin{aligned} R_{ns} &= veg[e_t\sigma T_t^4 + \tau_c\tau_t(1-A_c)(1-A_t)(1-A_s)Q_{s,d}] \\ &\quad +(1-veg)[(1-A_s)Q_{s,d} + Q_{l,d}] - e_s\sigma T_s^4 \end{aligned} \tag{2.8}$$

where, A_s is the albedo of soil and all other symbols have been defined in the corresponding net radiation equations for canopy (2.2) and thatch (2.4).

At the lower boundary (n, see Figure 2.2), the module assumes that the energy (q_h) and moisture (q_m) fluxes are the same as those for the layer above ($n-1$),

$$q_m(n, n+1) = q_m(n-1, n) \qquad q_h(n, n+1) = q_h(n-1, n) \tag{2.9}$$

2.1.1.2 Module Algorithm and Implementation

A flow diagram of the algorithm of computations in the 1-dTH module is given in Figure 2.4. To begin, the soil and the vegetation properties are initialized and the initial energy and moisture fluxes are calculated. For the next time step, we force the module with weather [see Chapter 4], and apply a two-dimensional Newton Raphson technique in conjunction with a finite difference method to balance energy and moisture fluxes at the soil surface. This boundary-flux matching process is repeated until a specified convergence criterion is satisfied, as shown in Figure 2.6. The new

fluxes are used to estimate the new surface temperature and moisture. Once the surface temperature and moisture are estimated, the difference method is employed to calculate the new fluxes, temperature, and moisture at each node in the soil.

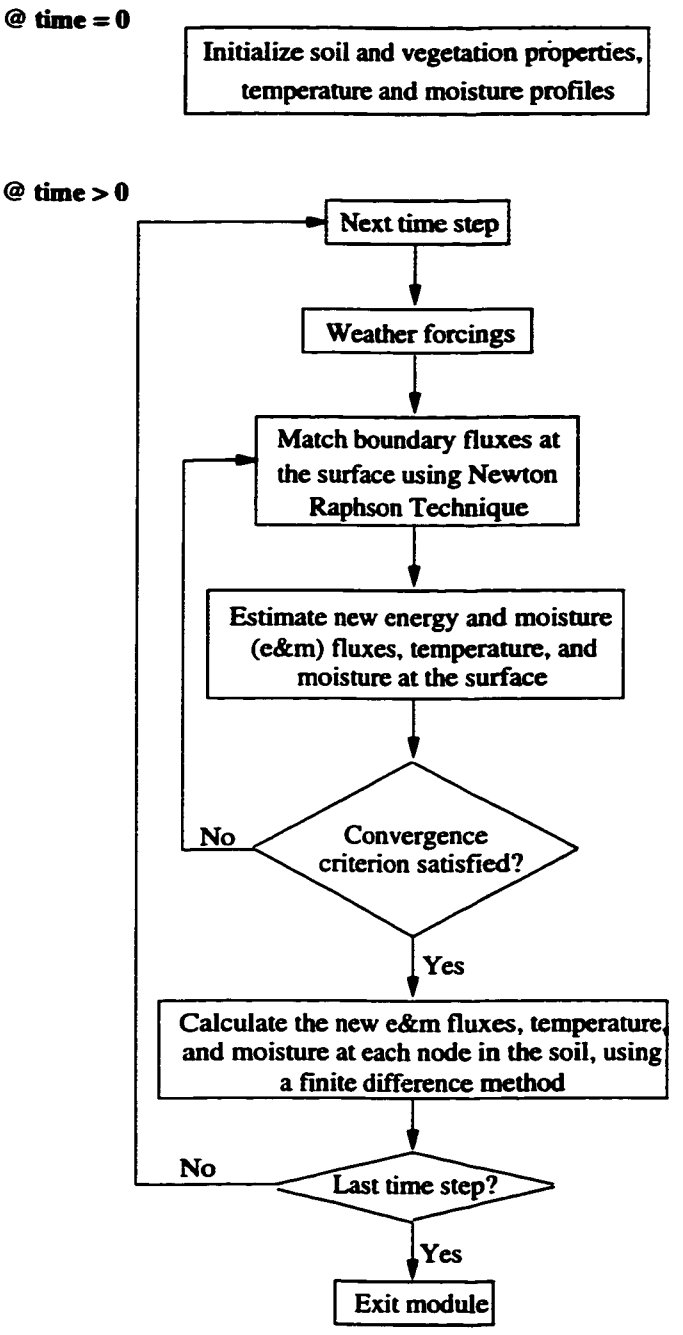

Figure 2.4: A flow diagram of 1-dTH module algorithm.

In the 1-dTH module, an explicit finite difference method [28, 126] is employed to

solve the non-linear, coupled moisture (2.5a) and energy (2.5b) conservation equations for soil. When we combine the equations 2.5a through 2.6b, we get two equations of the form:

$$M\frac{\partial\theta_l}{\partial t} + E\frac{\partial T}{\partial t} = X \qquad N\frac{\partial\theta_l}{\partial t} + F\frac{\partial T}{\partial t} = Y \tag{2.10}$$

$$X = -\frac{1}{\rho_l}\frac{\partial q_m}{\partial z} \qquad Y = -\frac{\partial q_h}{\partial z}$$

where, M, N, E and F are defined from equations 2.5a through 2.6b, and are functions of the soil properties (see equations A.16, A.17, A.18, and A.19 in Appendix A). $\frac{\partial\theta_l}{\partial t}$ and $\frac{\partial T}{\partial t}$ are the changes in water content and temperature with time. Solving the above equations for $\frac{\partial\theta_l}{\partial t}$ and $\frac{\partial T}{\partial t}$, results in:

$$\frac{\partial\theta_l}{\partial t} = \frac{FX - EY}{MF - EN} \qquad \frac{\partial T}{\partial t} = \frac{MY - NX}{MF - EN} \tag{2.11}$$

Figure 2.5 gives a schematic representation of the finite difference method as implemented in the module.

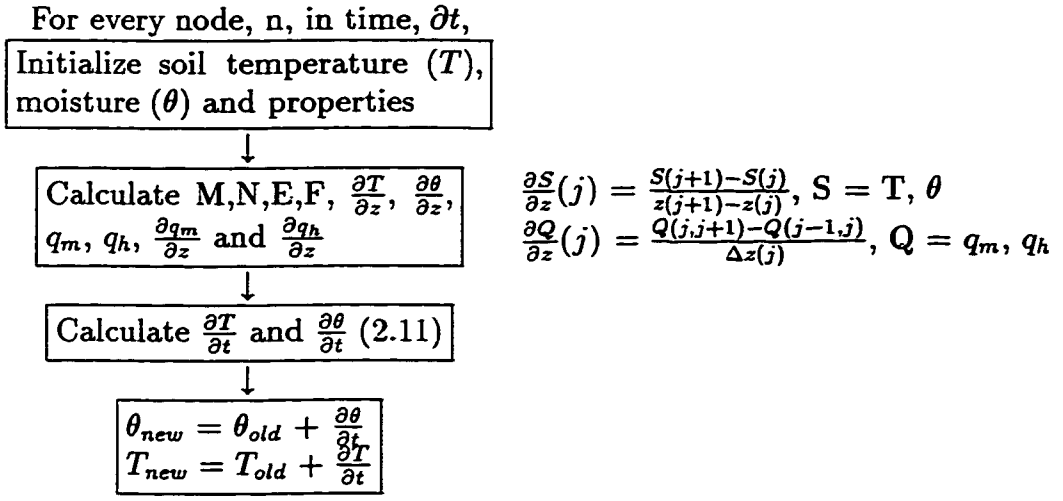

where q_m and q_h are the moisture and energy fluxes, respectively,

Figure 2.5: A schematic representation of the finite difference method used in the 1-dTH module.

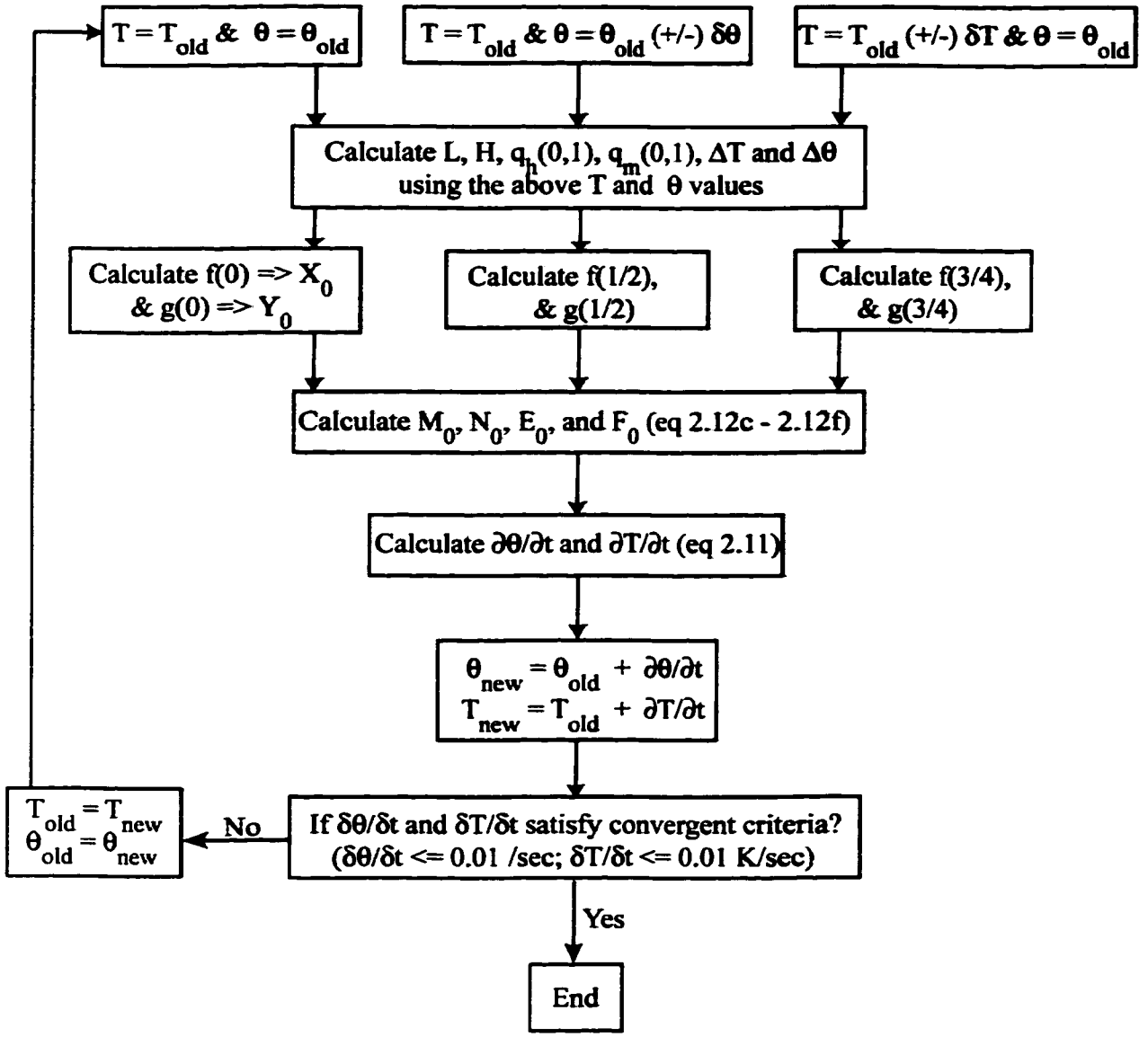

Figure 2.6: A flow diagram showing how the boundary fluxes are matched using a combination of Newton-Raphson technique and the finite difference method in the 1-dTH module.

where,

$$f = M_1 \Delta\theta + E_1 \Delta T \qquad g = N_1 \Delta\theta + F_1 \Delta T \tag{2.12}$$

$$M_0 = \frac{f(2) - f(1)}{2\delta\theta} \qquad E_0 = \frac{f(4) - f(3)}{2\delta\theta} \tag{2.13}$$

$$N_0 = \frac{g(2) - g(1)}{2\delta T} \qquad F_0 = \frac{g(4) - g(3)}{2\delta T} \tag{2.14}$$

$$\Delta\theta = \theta - \theta_1 \qquad \delta\theta = 1\text{x}10^{-10}$$

$$\Delta T = T - T_1 \qquad \delta T = 1\text{x}10^{-10}$$

$$\text{L} = \text{Latent heat flux} \qquad \text{H} = \text{Sensible heat flux}$$

- θ is the volumetric moisture content (m^3/m^3),
- T is the temperature (K) and,
- Subscripts 0 and 1 refer to the parameter values for the current and the last time steps, respectively.

2.1.2 The Radiobrightness (R) Module

The R module estimates the non-scattering emission from a canopy-cloud layer over a semi-infinite, homogeneous, and smooth-surfaced soil. The net brightness of the terrain is [126]:

$$T_b = T_{bs} + T_{bc,d} + T_{bc,u} + T_{bsky} \tag{2.15}$$

where,

- T_{bs} is the emission from soil at the top of the canopy after being attenuated through the canopy (K),
- $T_{bc,d}$ is the downwelling emission from the canopy reflected by the soil and attenuated through the canopy (K),
- $T_{bc,u}$ is the upwelling emission from the canopy (K) and,

• T_{bsky} is the downwelling sky emission reflected by the soil and attenuated through the canopy (K).

Figure 2.7 shows the different brightness components of the R module [126].

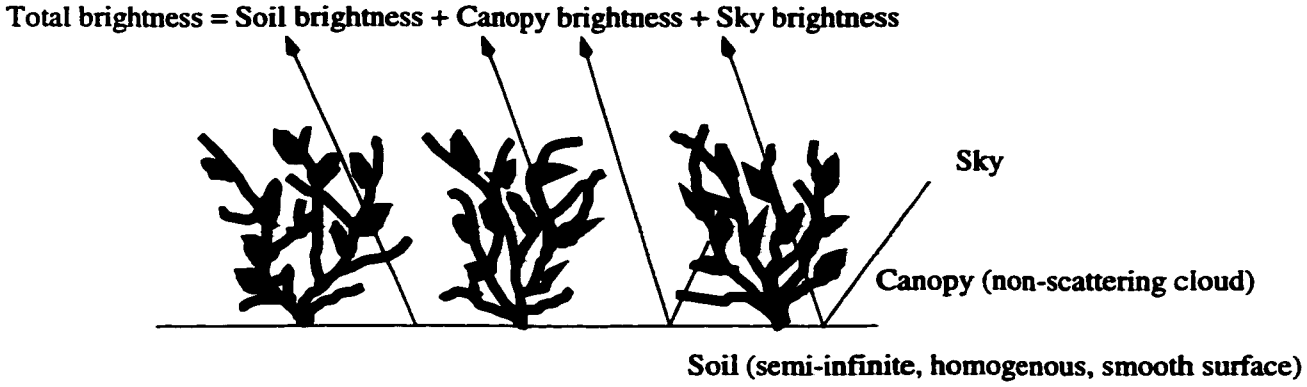

Figure 2.7: Brightness components in the R module

The relative permittivity and reflectivity of soil is estimated from a four-component mixture model by Dobson et al. [52] and Fresnel equations, respectively. The relative permittivity of the canopy is estimated from the dual-dispersion model by Ulaby and El-Rayes [198]. The attenuation through the canopy depends on its optical depth (τ), which is modeled empirically as [126].

$$\tau = \frac{n_c.k.B.\mathrm{Exp}\left[\frac{h_c}{0.1149} - 1\right]}{\rho_w} \tag{2.16}$$

where,

• n_c is the refractive index of the canopy,

• k is the wave number,

• ρ_w is the density of water (kg/m^3),

• B is the canopy wet biomass (kg/m^2) and,

• h_c is the canopy canopy height (m).

2.2 Model Modifications

This section describes my modifications to the community model. Some of these were minor, yet important, e.g., correcting sign errors or logical errors in the formulae used to solve certain quantities. These modifications are discussed in Appendix A. Only the major structural changes to the model are presented here.

2.2.1 The 1-dTH Module

I implemented five major modifications to the community 1-dTH module. The first was to include soil-air interactions in the vegetated area. These interactions were ignored in the community module, as mentioned earlier, in section 2.1.1.1. I found this modification particularly necessary for sparsely vegetated areas, e.g. wheat-stubble, where much of the soil is exposed. The energy and moisture fluxes between soil and air in such areas are a function of Leaf Area Index (LAI). Figure 2.8 shows the modified representation of a partially vegetated scene (compare with Figure 2.3). This modification affects the amount of longwave and shortwave radiation absorbed by canopy (R_{nc}), thatch (R_{nt}), and soil (R_{ns}) as follows.

$$R_{nc} = veg[(1-\tau_c)(1-A_c)Q_{s,d} + vfrac\,(Q_{l,d} + e_c e_t \sigma T_t^4 - 2e_c\sigma T_c^4)] \quad (2.17)$$

$$R_{nt} = veg[\tau_c(1-A_c)(1-A_t)(1-\tau_t)Q_{s,d} + vfrac\; e_c\sigma T_c^4 + sfrac\; Q_{l,d} + e_s\sigma T_s^4 - 2e_t\sigma T_t^4] \quad (2.18)$$

$$R_{ns} = veg[e_t\sigma T_t^4 + \tau_c\tau_t(1-A_c)(1-A_t)(1-A_s)Q_{s,d}] + (1-veg)$$
$$[(1-A_s)Q_{s,d} + Q_{l,d}] - e_s\sigma T_s^4 \quad (2.19)$$

where, all the variables are as defined for equations 2.2 through 2.8, and $vfrac$ and $sfrac$ are vegetation and soil fractions within the vegetated area. $sfrac$ is estimated from [206] as:

$$sfrac = \text{Exp}[-0.8 * LAI] \qquad vfrac = 1 - sfrac \quad (2.20)$$

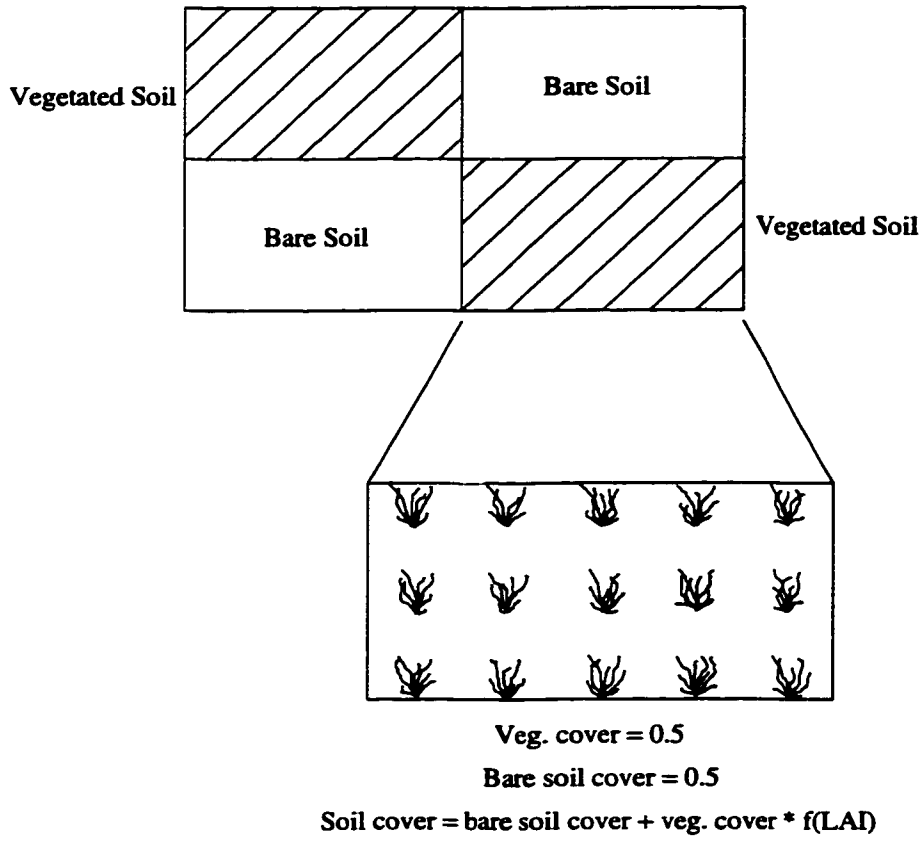

Figure 2.8: Pictorial representation of the vegetated surface simulated by the modified LSP/R model.

The second modification was to include layers of distinct physical, thermal and hydraulic properties in the soil. In the community module, the soil was a homogeneous

medium with uniform constitutive properties. This assumption was not realistic because constitutive properties vary with depth in soil. In this modification, the layers are discretized into nodes of varying thicknesses, with each layer exhibiting uniform constitutive properties throughout its thickness. The number of nodes per layer depends upon the results from convergence tests [see Chapter 4, section 4.1.1.4].

The third modification was to generalize the parameters required for estimating soil water retention. The 1-dTH module uses a two-parameter junction model by Rossi and Nimmo [175]. This junction model used an air entry pressure (Ψ_0) and a pore size index (λ_p), reported by Rossi and Nimmo for a set of example soils. It was necessary to relate these to soil texture, so that the model could be extended to different soils. For the modified version, I used empirical formulations that depend only on soil texture [170], i.e.,

$$\begin{aligned}\lambda_p &= \exp[-0.784 + 0.018S - 1.062\theta_a - 5\text{x}10^{-5}S^2 - 3\text{x}10^{-3}C^2 + \\ &\quad 1.111{\theta_a}^2 - 0.031S\theta_a + 3\text{x}10^{-4}S^2{\theta_a}^2 - 6\text{x}10^{-3}C^2{\theta_a}^2 - \\ &\quad 2\text{x}10^{-6}S^2C + 8\text{x}10^{-3}C^2\theta_a - 7\text{x}10^{-3}{\theta_a}^2C] \qquad (2.21)\\ \Psi_0 &= 0.01\exp[5.34 + 0.185C - 2.484\theta - .002C^2 - 0.044S\theta_a - \\ &\quad 0.167C\theta_a + 1\text{x}10^{-3}S^2{\theta_a}^2 - 0.009C^2{\theta_a}^2 - 1\text{x}10^{-5}S^2C + \\ &\quad 9\text{x}10^{-3}C^2\theta_a - 7\text{x}10^{-4}S^2\theta_a + 1\text{x}10^{-6}SC^2 + 0.5{\theta_a}^2C] \qquad (2.22)\end{aligned}$$

where, S, C and θ_a are the fractions of sand, clay and air in the soil.

The fourth modification was to include an infiltration model for soil during precipitation events. The community model was only calibrated during drydown periods and did not account for changes in infiltration with time, or with soil properties [122].

The maximum infiltration rate (IR), defined as the volume of water per unit area of soil that is allowed into the soil per second (m/sec), depends on soil hydraulic and physical properties, soil temperature, vegetation cover, and surface characteristics like slope and roughness [76]. The IR was estimated using a quasi-analytic solution to Richard's equation for vertical infiltration in a homogeneous soil with a constant initial moisture profile [164, 163, 165, 79] (equation 2.23). The quasi-analytic solution could be used because it is applied only to estimate IR at the surface and the soil properties of the surface node are homogeneous. The transport of moisture in the deeper nodes is governed by the conservation equations 2.5a and 2.5b.

$$i(t) = A + \frac{S}{2} t^{-\frac{1}{2}} \tag{2.23}$$

where,

$$A = \delta K_{sat}$$

$$S = 2K_{sat}\Psi_f(\theta_s - \theta)$$

where, δ is an empirical parameter set to 0.66 [164], K_{sat} is the saturated hydraulic conductivity, θ_s is the saturated moisture content, θ is the moisture content before precipitation, Ψ_f is the matric head of the wetting front estimated as the air entry pressure Ψ_0 [172].

The infiltration model included in the 1-dTH module is physically simplistic in that it does not include the affect of ponded water on infiltration rate (IR) when precipitation rate (PR)is high. When the PR is less than the estimated IR, the model uses PR for moisture flux estimation at the surface, otherwise it uses IR. Any excess rain during high PR is treated as runoff.

The fifth modification was to alter the lower boundary conditions, from conditions on energy and moisture fluxes to conditions on temperature and moisture content. Because fluxes appear as derivatives in the energy and moisture conservation equations (2.5a and 2.5b), they are harder to implement and their physical consequences are harder to understand. In the modified module, I set the temperature (T) and moisture (θ) of the last node to be the same as those for the node above, i.e,

$$\theta_m(n) = \theta_m(n-1) \qquad T(n) = T(n-1) \tag{2.24}$$

The boundary condition for moisture is realistic because the soil is modeled to a depth of 5 m, which corresponds to saturated zones in the Great Plains region and the moisture movement is primarily horizontal. The boundary condition for temperature is not physically realistic and warrants some discussion. The numerical method used in the model, i.e., the forward explicit finite difference method, does not lend itself to be forced at the lower boundary. I could assign a passive[2] condition at the lower boundary without compromising the model estimates, if the time required for a temperature change at the upper boundary to reach the lower boundary exceeded the duration of the simulation. A temperature change at the surface reaches the lower boundary at 5 m in approximately 73 days, based upon an analytical analysis similar to the one described in Section 2.3.3. A temperature rise of 20 K was introduced at the surface of a 5 m soil column whose initial temperature and volumetric moisture were 293.15 K and 20%, respectively. The moisture was held at the equilibrium value and the lower boundary was closed to moisture or heat flow. Figure 2.9 shows the

[2]It is a passive condition, because a constant temperature implies zero thermal flux.

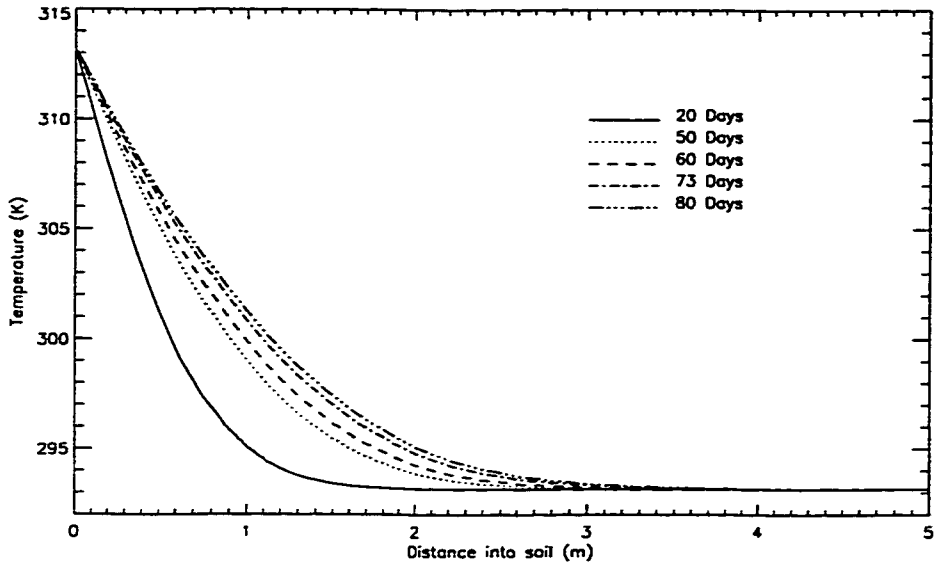

(a)

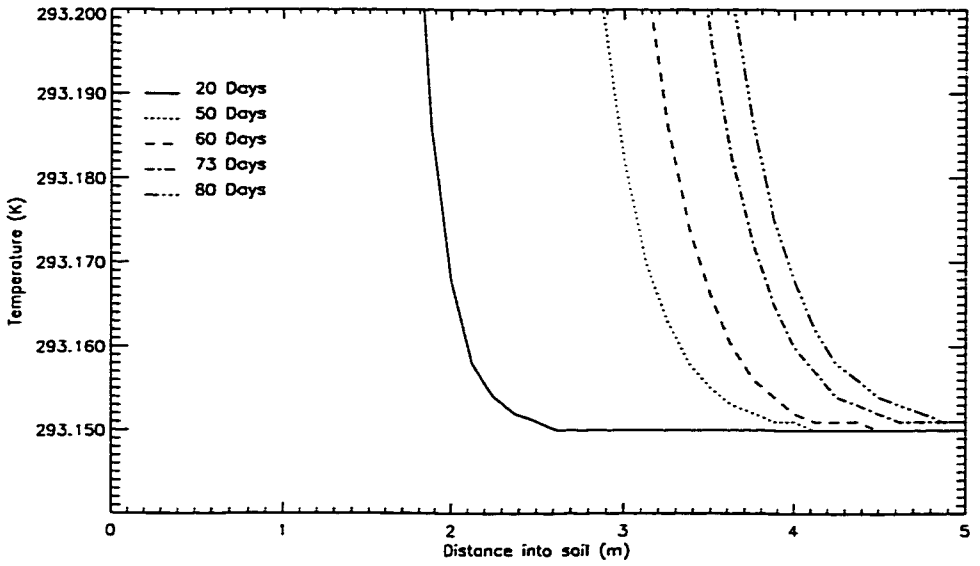

(b)

Figure 2.9: Results from an analytic solution to calculate the time necessary for a thermal pulse at the surface to reach the lower boundary at the depth of 5 m. (a) Temperature profiles in soil as functions of time (b) The temperature profiles zoomed-in to show the pulse at the surface reaching 5m on the 73rd day.

temperature profile in the soil after 20, 50, 60, 73, and 80 days. There was a .001 K rise in temperature at the depth of 5 m after day 73. My model simulations are only for 20-30 days (see Chapter 4). If the simulations were inter-seasonal or annual, then the lower boundary should be forced with climatic temperatures.

2.2.2 The R-Module

I made two major modifications to the R module. The first, was to generalize the formulation for canopy optical thickness (τ). In the community module, the optical thickness was modeled empirically (2.16), where the functional dependence of biomass vs. canopy height was obtained from a field experiment [39]. This modification was necessary to extend the module for different canopy biomass distributions. The modified formulation of τ is [See Appendix A for derivation]:

$$\tau = -\frac{2kn_cB}{\rho_c} \tag{2.25}$$

where,

- ρ_c is the density of wet vegetated material (kg/m^3),
- n_c is the complex refractive index of the canopy,
- B is the wet biomass of the canopy(kg/m^2), and
- k is the wave number.

The second modification was to account for roughness in the soil surface. In the community module, the soil had an idealized, specular surface, which is an incorrect assumption for most real surfaces. I found this modification was necessary for bare-soil surfaces that were ploughed and disked. Details of this modification are

presented in section 4.1.2.2, where existing bare-soil rough surface emission models are investigated.

2.3 Model Testing

Because the 1-dTH module is more complex than the R-module, only the former was extensively tested. This section describes the three tests conducted to ensure that the numerical simulation in the 1-dTH module is implemented correctly, both qualitatively and quantitatively. This testing was critical because such tests were never conducted during the development of the community module. The first test checked errors in mass and energy balance in the module. The second, a qualitative test, confirmed that the physics of moisture and energy flow is correctly simulated for a homogeneous soil when a symmetric initial temperature profile is used. The third, a quantitative test, compared the numerical solution with an analytic solution to a simpler transport problem. All the three tests were conducted for bare soil cases (vegetation cover = 0), as the vegetation layer is treated as a separate layer in the module from a numerical standpoint. This section describes these tests in detail and discusses their results.

2.3.1 Mass and Energy Balance

The 1-dTH module was tested for the conservation of mass (moisture) and energy. After all the mass and energy fluxes at the boundary, and changes in the fluxes at all the nodes in the soil, have been calculated, the following mass and energy balance

should hold for the soil as a whole. For each time increment,

$$q_m(0,1) - q_m(n,n+1) = \sum_{i=1}^{n} \partial(X_m)_i \Delta z_i \tag{2.26a}$$

$$q_h(0,1) - q_h(n,n+1) = \sum_{i=1}^{n} \partial(X_h)_i \Delta z_i \tag{2.26b}$$

where,

- $q_m(0,1)$ and $q_h(0,1)$ are the net moisture (kg/m^2) and heat fluxes (J/m^2) into the soil surface at the interface between nodes 0 and 1, respectively,
- $q_m(n,n+1)$ and $q_h(n,n+1)$ are the net moisture and heat fluxes out of the lower boundary i.e. at the interface between nodes n and $n+1$, respectively,
- $\partial(X_m)_i$ and $\partial(X_h)_i$ are the changes in moisture (kg/m^3) and heat content (J/m^3) per unit volume in the ith node, respectively,
- n is depth of the bottom node (m),
- Δz_i is thickness of the ith node (m).

Differences between the left and the right hand sides of equations 2.26a and 2.26b represent the instantaneous errors in moisture balance (err_{mb}), and in energy balance (err_{eb}), respectively. The cumulative relative errors (CREs) for mass, err_{rm}, and for energy, err_{re}, were calculated with respect to the maximum of moisture and energy fluxes at the upper and the lower boundaries as shown in equations 2.27a and 2.27b, respectively. After a time interval, t_f,

$$err_{rm} = \frac{\sum_{t=1}^{t_f} (err_{mb})_t}{\sum_{t=1}^{t_f} max\left[|q_m(0,1)|, |q_m(n,n+1)|\right]} \tag{2.27a}$$

$$err_{re} = \frac{\sum_{t=1}^{t_f}(err_{eb})_t}{\sum_{t=1}^{t_f} max\left[|q_h(0,1)|, |q_h(n,n+1)|\right]} \quad (2.27b)$$

The CREs were used to evaluate the accuracy of a numerical solution. Figures 2.10 and 2.11 show these errors for a 12-day bare-soil model simulation during summertime, from Julian day 193 (June 11) through day 205 (June 23) in 1996. Weather forcings to run the model were obtained from our fourth Radiobrightness Energy Balance Experiment (REBEX-4) ([106], Chapter 3, Appendix B). These forcings included incoming radiant fluxes, air temperature, relative humidity, wind, and precipitation. The initial and boundary conditions for the simulation are discussed in section 4.1.1.2. The time-step for the simulation was 3 sec. The soil was modeled up to 5 m, and discretized into 60 nodes with 9 nodes in the upper 5.5 cm. Soil constitutive properties were constant with depth as given in Table 2.1, and are discussed in section 4.1.1.3.

Properties	**Values**
Texture	3.9% sand, 65.1% silt, 31.0% clay
Porosity	0.46
Sat. Hydr. Cond.	4.74×10^{-7} m/sec
Field Capacity	0.294 % by volume

Table 2.1: Soil constitutive properties used for model simulation to evaluate errors in mass and energy balance.

Figures 2.10 and 2.11 show the CREs and the magnitude of the terms in mass and energy balance, respectively. The CREs were negligible throughout the simulation period (Figures 2.10(a) and 2.11(a)) relative to the magnitude of incoming or outgoing heat/moisture fluxes. While the CREs are small, they say nothing about the

magnitude of the absolute errors themselves. Figures 2.10(b-e) and 2.11(b-e) show the magnitude of the instantaneous errors and of each term in the balance equations 2.26a and 2.26b. Figures 2.10(b) and 2.11(b) show instantaneous errors in mass and energy, respectively. The magnitudes of these errors are very small, with the maximum error in moisture balance of $\sim 5\text{x}10^{-7}\ kg/m^2$ and in energy balance of $\sim 2\ J/m^2$. Figure 2.10(c) shows the net moisture flux entering the upper boundary, with precipitation on Julian days 194, 196, 198, and 203. Figure 2.11(c) shows the net incoming energy flux at the upper boundary which is primarily driven by insolation. Throughout the simulation period, energy fluxes vary slowly with time during the night and during clear days (Julian day 197 and 200), but change rapidly during partly cloudy days. Figures 2.10(d) and 2.11(d) show moisture and energy fluxes at the lower boundary. These fluxes exhibit small dynamic ranges of $\sim 2\text{x}10^{-4}\ kg/m^2$ for moisture, and ~ 2 J/m^2 for energy. Figures 2.10(e) and 2.11(e) show the total changes in the bulk soil moisture and heat content, respectively. These changes follow the more dynamic and stronger fluxes of the upper boundary.

2.3.2 Moisture and Energy Flow in a Homogeneous Soil

The 1-dTH module run with a symmetric initial temperature profile [Figure 2.12(a)], a constant initial moisture profile (0.3 m^3/m^3), and zero heat and moisture fluxes at the upper and lower boundaries confirmed the proper implementation of coupled moisture and energy propagation in a homogeneous soil profile. The soil was modeled up to 1 m and discretized into 20 equally spaced nodes with uniform

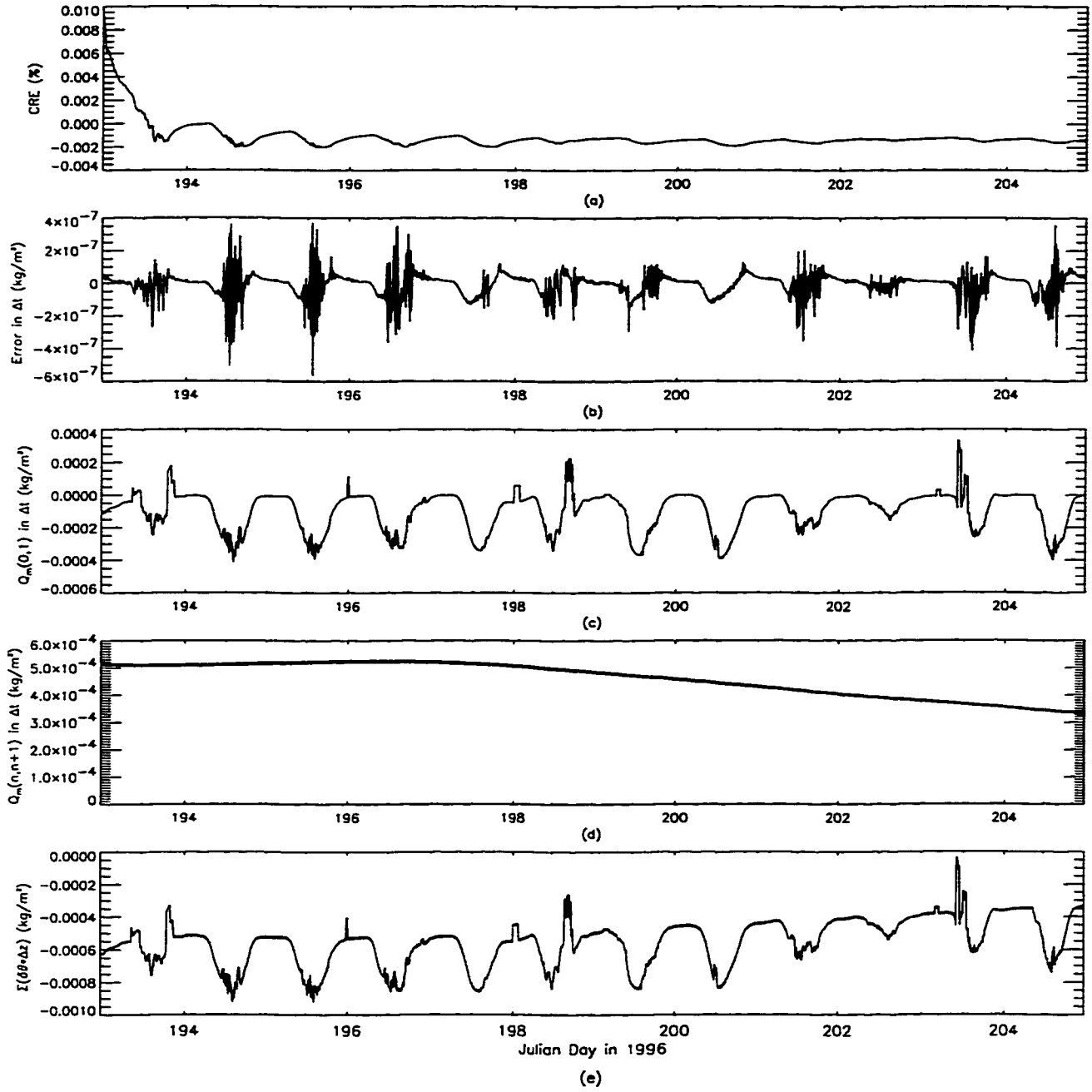

Figure 2.10: Error in mass balance. (a) Cumulative relative error as given by equation 2.27a (b) Instantaneous error during each time step Δt (c) Moisture flux incident on the upper boundary during each time step (d) Moisture flux out of the lower boundary during each time step, and (e) Total change in moisture content in the bulk soil.

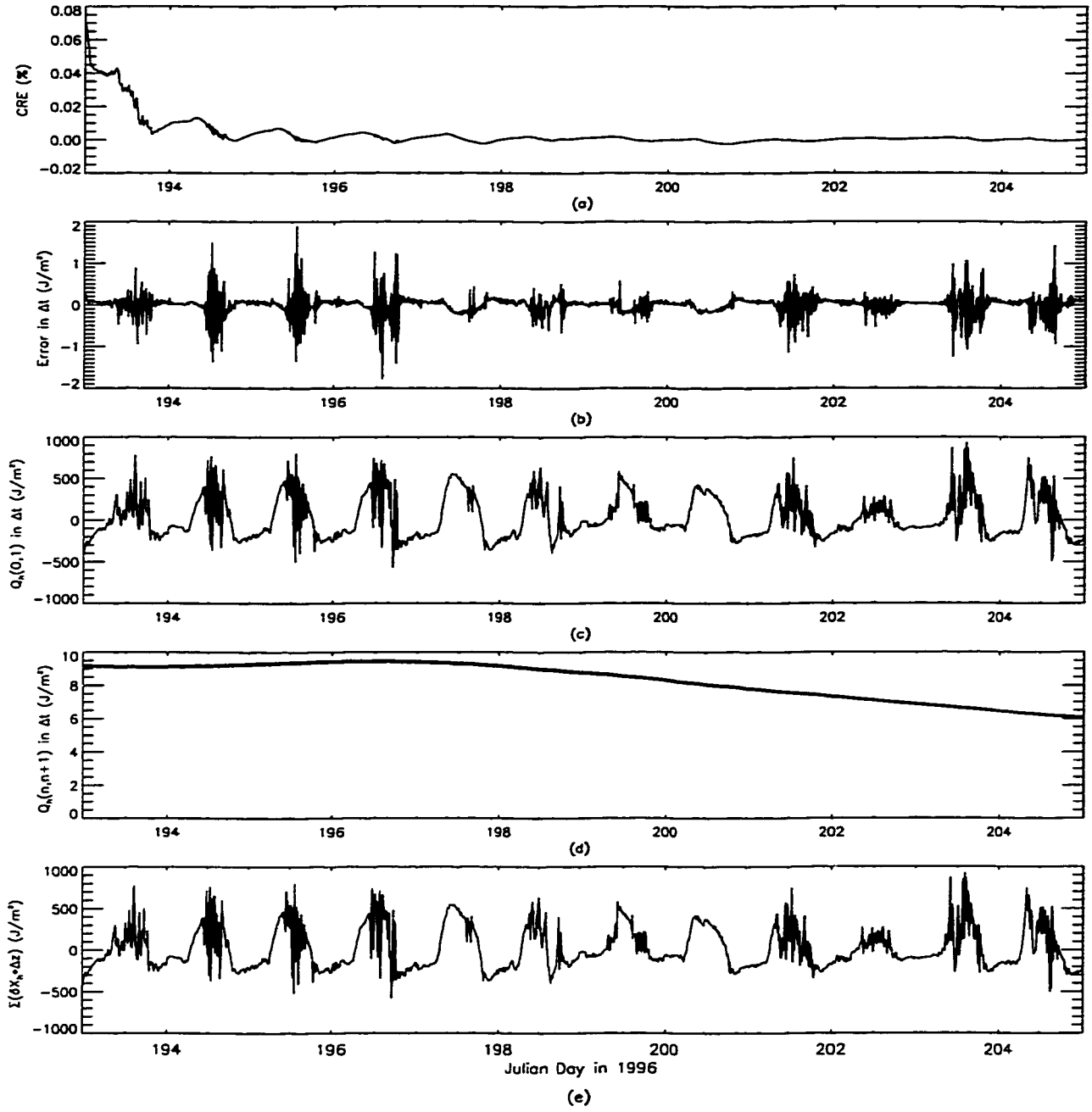

Figure 2.11: Error in energy balance. (a) Cumulative relative error as given by equation 2.27b (b) Instantaneous error during each time step Δt (c) Energy flux incident on the upper boundary during each time step (d) Energy flux out of the lower boundary during each time step, and (e) Total change in the heat content in the bulk soil.

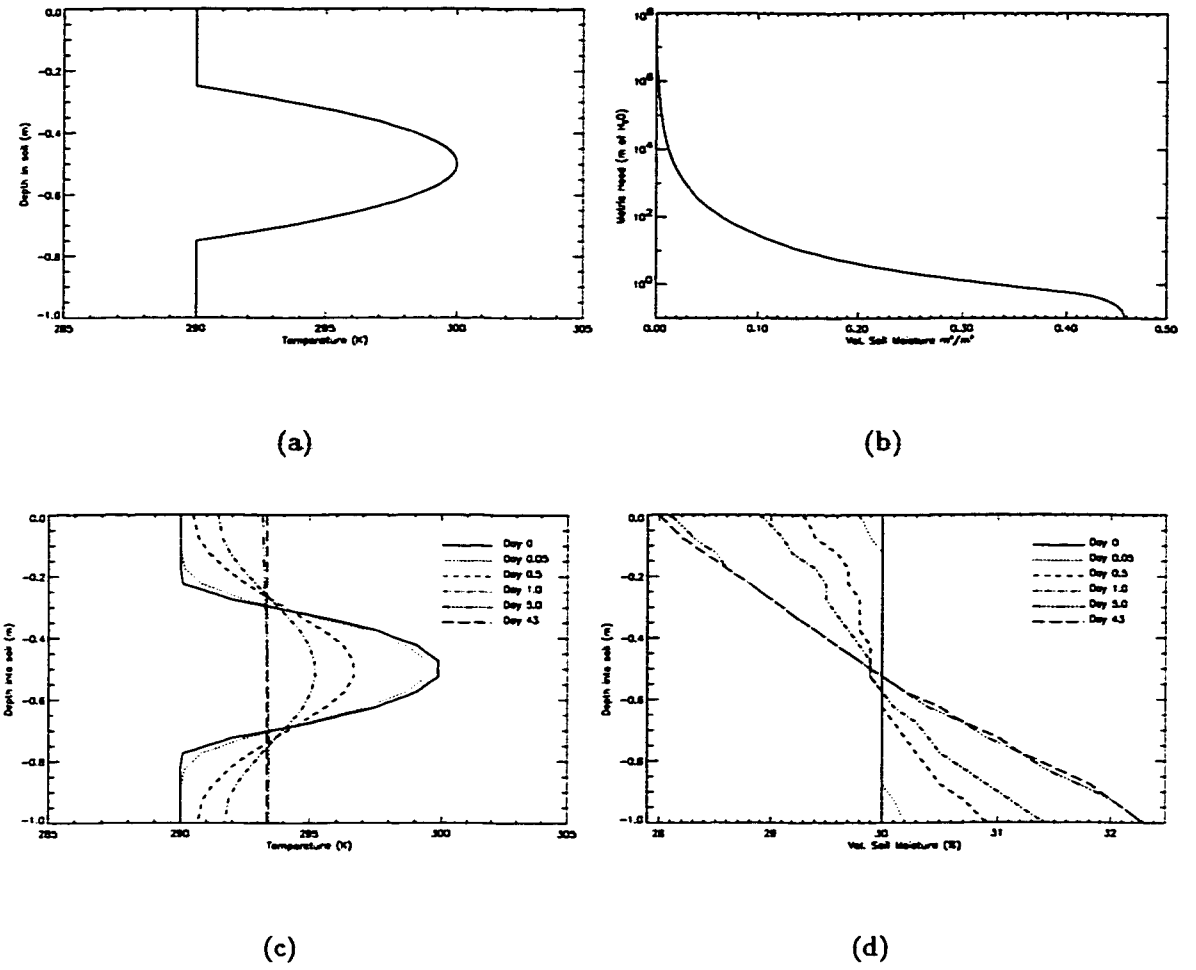

Figure 2.12: Propagation of moisture and heat: (a) Initial temperature profile. (b) Soil retention curve from the two-parameter junction model of Rossi and Nimmo [175] at soil temperature 295 K. (c) Temperature profiles and (d) Moisture profiles during the 43-day model run.

constitutive properties (see Table 2.1).

Figures 2.12(c) and 2.12(d) show the temperature and moisture profiles for selected times during a 43-day model simulation. Heat flowed down the temperature gradient as expected, and the soil came to an equilibrium temperature after approximately 6 days [Figure 2.12(c)]. The moisture not only followed the negative of the

temperature gradient, but it also followed gravity. Because the capillary retention curve is linear about the moisture value of 0.3 m^3/m^3 [Figure 2.12(b)], the moisture profile at equilibrium is linear with depth [see Figure 2.12(d)].

2.3.3 The 1-dTH Numerical Solution vs. an Analytic Solution for a Simple Transport Problem

I verified quantitative correctness by comparing the finite difference solution with an analytic solution for a simpler problem chosen to simulate the dynamics of vapor-dominated systems with strong coupling between moisture and heat transport [136]. In this problem, a very dry soil column at some equilibrium temperature (T) and vapor density (ρ_v) is subjected to a sudden increase in vapor density (ρ_{v0}) at the upper boundary, while the temperature at the boundary is held constant at its original value (T). The lower boundary is closed to heat and moisture flow. Vapor diffuses into the column, condenses, and releases heat. This results in a temporary rise in the temperature of the medium, though it eventually returns to the value at the boundary as heat diffuses back out of the column [136].

I used an analytic solution for this problem as outlined by Crank [36]. Equations 2.28a and 2.28b can be linearized in the form 2.28c and 2.28d.

$$D\frac{\partial^2 \rho_v}{\partial z^2} - \frac{\partial}{\partial t}(\rho_v - \lambda_c T) = 0 \qquad (2.28a)$$

$$\mathbb{D}\frac{\partial^2 T}{\partial z^2} - \frac{\partial}{\partial t}(T - \nu_c \rho_v) = 0 \qquad (2.28b)$$

$$\Delta\rho_v = \rho_{v0} F_1 + f(F_1, F_2, \rho_{v0}, T_0) \qquad (2.28c)$$

$$\Delta T = T_0 F_2 + f(F_1, F_2, \rho_{v0}, T_0) \qquad (2.28d)$$

where D, $\mathbb{D}$, λ_c and ν_c are constants that depend on soil properties (see [36]),

• ρ_{v0} and T_0 are the initial changes in vapor density (kg/m^3) and temperature (K) forced at the upper boundary, respectively. ($T_0 = 0$ for our problem) and,

• $\Delta\rho_v$ and ΔT are the changes in vapor density and temperature profiles as functions of time.

The first terms on the right hand sides of the equations 2.28c and 2.28d represent the solution if the diffusion of vapor density and temperature were de-coupled. The soil would come to an equilibrium with $\Delta\rho_v = \rho_{v0}$ and $\Delta T = T_0$, as functions F_1 and F_2 increased from $0 \rightarrow 1$ when time increased from $0 \rightarrow \infty$. The second terms represent the solution from coupling between the two diffusion processes.

The forms of F_1 and F_2 depend on the shape of the medium. The soil can be as a plane sheet of thickness, n, and F_1 and F_2 become

$$F_1 = \sum_{i=0}^{\infty}(-1)^i \text{erfc}\frac{(2i+1)z-n}{2\sqrt{Dt}} + \sum_{i=0}^{\infty}(-1)^i \text{erfc}\frac{(2i+1)z+n}{2\sqrt{Dt}} \quad (2.29a)$$

$$F_2 = \sum_{i=0}^{\infty}(-1)^i \text{erfc}\frac{(2i+1)z-n}{2\sqrt{\mathbb{D}t}} + \sum_{i=0}^{\infty}(-1)^i \text{erfc}\frac{(2i+1)z+n}{2\sqrt{\mathbb{D}t}} \quad (2.29b)$$

where,

• $\text{erfc}\, x = 1 - \frac{2}{\pi^{1/2}}\int_0^x \exp(-\eta^2)\text{d}\eta$,

• z is the depth in soil (m) and,

• t is the time (sec).

The change in temperature, ΔT, vapor density, $\Delta\rho_v$, and moisture, ΔV_f, as functions of depth and time are given by [36] as follows:

$$\Delta T = T_0 F_2 - \frac{(1-\mu_2{}^2\mathbb{D})T_0 - \nu_c\rho_{v0}}{\mathbb{D}(\mu_1{}^2 - \mu_2{}^2)}(F_2 - F_1) \quad (2.30a)$$

$$\Delta\rho_v = \rho_{v0}F_1 - \frac{(1-\mu_1{}^2 D)\rho_{v0} - \lambda_c T_0}{D(\mu_1{}^2 - \mu_2{}^2)}(F_2 - F_1) \quad (2.30b)$$

$$\Delta V_f = \sigma_c \Delta \rho_v - \omega_c \Delta T \tag{2.30c}$$

where,

$$\mu_1{}^2 = \frac{1}{D} + \frac{\lambda_c \nu_c}{\mathbb{D} - D} \qquad \mu_2{}^2 = \frac{1}{\mathbb{D}} - \frac{\lambda_c \nu_c}{\mathbb{D} - D}$$
$$\sigma_c = \frac{\partial V_f}{\partial \rho_v} \qquad \omega_c = \frac{\partial V_f}{\partial T}$$

The equations 2.5a and 2.5b can be linearized to match the form of equations 2.28a and 2.28b if we assume negligible transport of sensible heat by water vapor and negligible liquid flow, as follows [136],

$$\theta_a \frac{\partial \rho_v}{\partial t} + (\rho_l - \rho_v) \frac{\partial \theta_m}{\partial t} = \frac{\partial}{\partial z}\left[D_m \frac{\partial \rho_v}{\partial z} \right] \tag{2.31a}$$

$$C_m \frac{\partial T}{\partial t} - \rho_l (L + W) \frac{\partial \theta_m}{\partial t} = \frac{\partial}{\partial z}\left[\left(\lambda - D_m \frac{\partial \rho_v}{\partial T}\bigg|_{\Psi} \right) \frac{\partial T}{\partial z} \right] \tag{2.31b}$$

where,

$$L = L_0 + (c_p - c_l)(T - T0)$$

- θ_a, ρ_v, ρ_l, λ, C_m, c_l, c_p, L_0, T, T_0 and W have been defined for equations 2.6a - 2.6d,
- θ_m is the volumetric moisture content (m^3/m^3),
- D_m is an effective molecular diffusivity (m^2/sec) and,
- Ψ is the matric head (m).

To compare the analytic solution for the above described problem with its numerical solution, I chose Yolo light clay because it has been extensively studied and its properties are well documented [163, 82, 136]. These properties are tabulated in Table 2.2 and the soil water retention curve is given by equations 2.33a and 2.33b. The soil column was 0.1 m thick with initial and boundary conditions given in equations 2.32a

through 2.32f. Because the analytic solution is based upon constant soil properties, thermal capacity, latent heat of vaporization, humidity, and thermal conductivity were kept constant in the numerical simulation to achieve a better comparison. The changes in moisture and vapor density with matric potential were also held constant.

Properties/Parameters	**Values**
Porosity	0.495
Thermal Cond.	0.165 $J/m.K.sec$
Thermal Cap.	1.673663x10^6 $J/m^3.K$
Latent heat of vap.(L)	2.45616x10^6 J/kg
σ_c	0.274 m^3/kg
ω_c	0 K^{-1}
D	3.63x10^{-8} m^2/sec
$\mathbb{D}$	9.89x10^{-8} m^2/sec
λ_c	0 $kg/m^3.K$
ν_c	395.286 $K.m^3/kg$

Table 2.2: Soil properties for Yolo light clay and other parameters used to calculate the analytic solution. The same soil properties were also used by the numerical model.

$$\rho_v = \rho_v^* \qquad t = 0 \qquad 0 \leqslant z \leqslant 0.1 \tag{2.32a}$$

$$T = T^* \qquad t = 0 \qquad 0 \leqslant z \leqslant 0.1 \tag{2.32b}$$

$$\rho_v = \rho_v^* + \rho_{v0} \qquad t \geqslant 0 \qquad z = 0 \tag{2.32c}$$

$$T = T^* \qquad t > 0 \qquad z = 0 \tag{2.32d}$$

$$q_m = 0 \qquad t \geqslant 0 \qquad z = 0.1m \tag{2.32e}$$

$$q_h = 0 \qquad t \geqslant 0 \qquad z = 0.1m \tag{2.32f}$$

where,

- $\rho_v^* = 4.03\text{x}10^{-3} kg/m^3$,

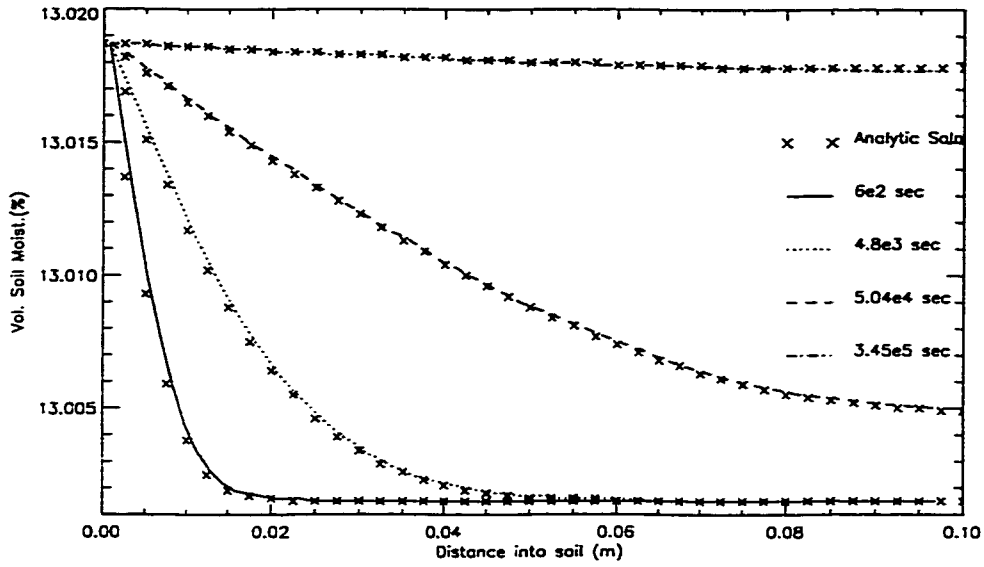

(a)

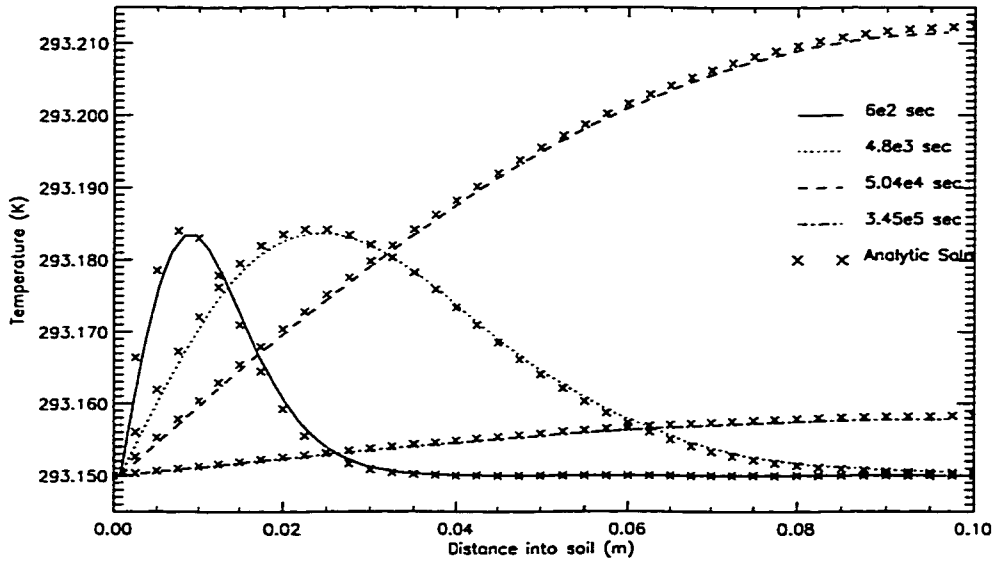

(b)

Figure 2.13: Comparison of analytic and numerical solution. (a) Volumetric soil moisture profiles. (b) Temperature profiles in soil as functions of time.

- $T^* = 293.15K$ and,
- $\rho_{v0} = 0.63\text{x}10^{-3} kg/m^3$.

$$\theta_m = 0.371\left[1 + \left(\frac{log(\Psi)}{2.26}\right)^4\right]^{-1} + 0.124 \qquad \Psi < 0.01m \qquad (2.33a)$$

$$\theta_m = 0.495 \qquad \Psi \geqslant 0.01m \qquad (2.33b)$$

Figures 2.13(a) and 2.13(b) compare the numerical and the analytic solutions for moisture and temperature profiles as time progresses from 10 minutes to 4 days. The temperature rose as the increased vapor density penetrated into the lower layers and condensed. The system reached equilibrium after ~5 days. The numerical solution follows the analytic solution with a maximum difference of ~2.2 mK for temperature and ~0.0006 % for moisture over the comparison period.

2.4 Summary

- There were five major modifications to the 1-dTH module of our community LSP/R model. They were: 1) the inclusion of soil-air interactions in vegetated areas, 2) the inclusion of layers of distinct soil constitutive properties, 3) the generalization of the parameters required to estimate soil water retention, 4) inclusion of an infiltration model during precipitation, and 5) the implementation of more physically realistic lower boundary conditions.
- There were two major modifications to the R-module of our community LSP/R model. They were: 1) generalizing the expression for canopy

optical thickness and 2) including soil surface roughness.

- The modified 1-dTH module was shown to conserve mass and energy, with the maximum errors being $\sim$ 5x10^{-7} kg/m^2 and $\sim$ 2 J/m^2, respectively, for a 12-day simulation period.

- The 1-dTH module simulated heat and moisture transport in a homogeneous soil with constant initial temperature and moisture profiles, to verify the numerical implementation qualitatively. The modeled energy propagated down the temperature gradient, and the moisture followed the negative of the temperature gradient and also followed gravity. The equilibrium profile for the soil moisture matched the slope of the soil-water retention curve.

- The numerical solution was compared to an analytic solution for moisture and energy transport in a vapor-dominated homogeneous soil to confirm the quantitative accuracy of the numerical methods used in the 1-dTH module. The solutions compared well, with the maximum differences of $\sim$2.2 mK for temperature and $\sim$6x10^{-4} % for volumetric soil moisture.

CHAPTER 3

The Field Experiments REBEX-4 & REBEX-5

Beginning in 1992, our Microwave Geophysics Group (UM-MGG) has been conducting field campaigns, known as the Radiobrightness Energy Balance Experiments (REBEXs), to observe terrain brightnesses, thermal and hydraulic conditions in soil and vegetation, and co-located micro-meteorological (micro-met) parameters. There have been two major goals for these experiments; first, to calibrate the LSP/R model for different terrain and weather conditions with the field observations, and second, to correlate ground-based brightnesses with satellite observations to study the effects of intervening atmosphere and larger spatial aggregations on remotely-sensed brightnesses. The first experiment, REBEX-1, was conducted in a temperate grassland during fall and winter to study the surface processes and emission from a snow-covered terrain [72, 71]. The third experiment, REBEX-3, was conducted in the arctic tundra for one year to study the processes in a permafrost terrain [110, 111]. REBEX-0 [109] and REBEX-2 were shake-down experiments conducted in the nearby University of Michigan Matthaei Botanical Gardens (UM-MBG), to test the field-equipment before

it was deployed in remote locations for extended periods.

In this chapter, I present the motivation for conducting the fourth and the fifth experiments, viz., REBEX-4 and REBEX-5; the experimental setup and observations made during these two REBEXs; and the processing and analysis of the data collected.

3.1 REBEX-4

The earlier REBEXs were conducted during periods when surface fluxes were not very strong and the studies focussed primarily on freeze/thaw cycles. To ensure the realistic simulation of land surface processes, it is important to calibrate the LSP/R model for periods when these processes are dominant and strongly coupled. Our fourth field experiment, REBEX-4, took place during the spring and summer of 1996, in a temperate, sub-humid region. It was a joint experiment in collaboration with the Climate Processes and Earth Observation Division, Climate Research Branch (CCRD) of Atmospheric Environment Service (AES), Canada, at the US Geological Survey's (USGS) Earth Resources Observation System (EROS) Data Center, about 30 km north-east of Sioux Falls, South Dakota [see Figure 3.1]. The field site was chosen close to the REBEX-1 site (within 50 m) to obtain a dataset spanning the four seasons for the same location. This section contains a description of the site and terrain, experimental setup, and measurements made during REBEX-4.

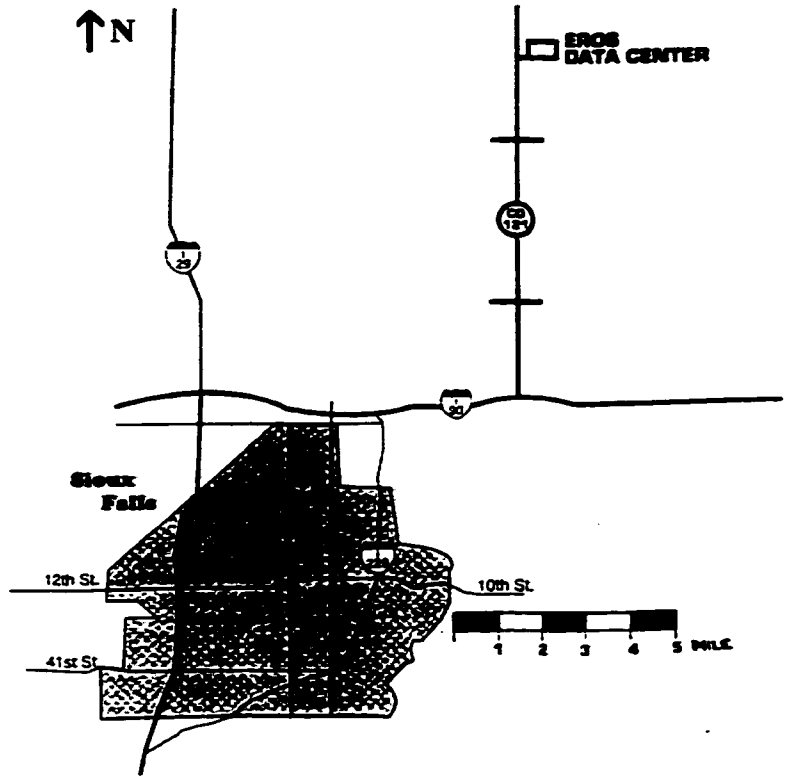

Figure 3.1: Sioux Falls and vicinity showing location of the EROS Data Center.

3.1.1 Site and Terrain Description

Two terrain types were monitored during REBEX-4, bare-soil and brome-grass. CCRD monitored the bare-soil site. The site was prepared by removing the existing vegetation, tilling, and disking to create a somewhat smooth surface. A weak herbicide was sprayed to ensure no new vegetation grew during the course of the experiment. The site was checked periodically and any new weeds were removed. UM-MGG monitored a brome-grass site which had been undisturbed for several years. Both sites were located ~200 m south-east of the EROS Data Center (EDC) building with a deep drainage ditch between the building and the sites. The sites were rela-

tively flat open areas with gentle slopes toward the west (the ditch) and the south. The bare-soil site was approximately 25 m west of the grass-site. Figures 3.2 and 3.3 show the two sites near the EDC building.

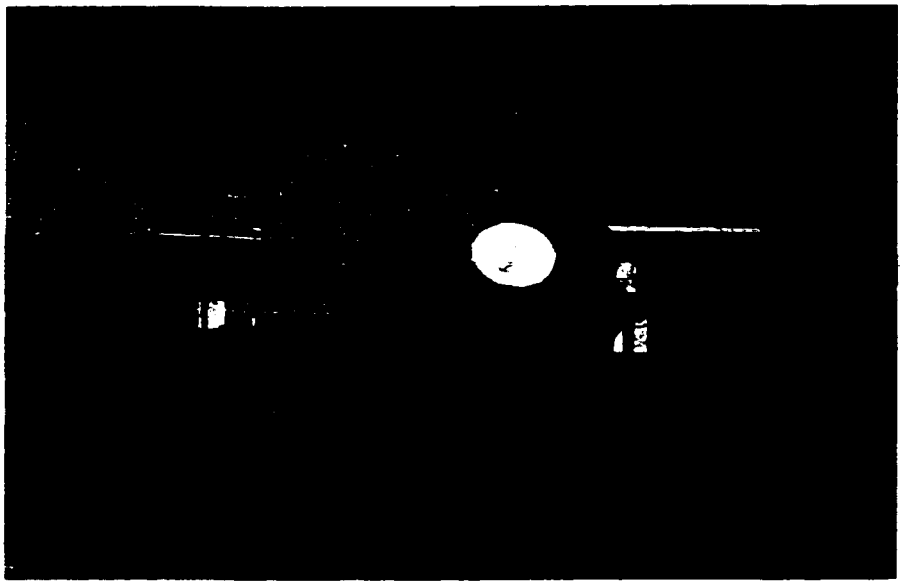

Figure 3.2: Bare-soil site during REBEX-4.

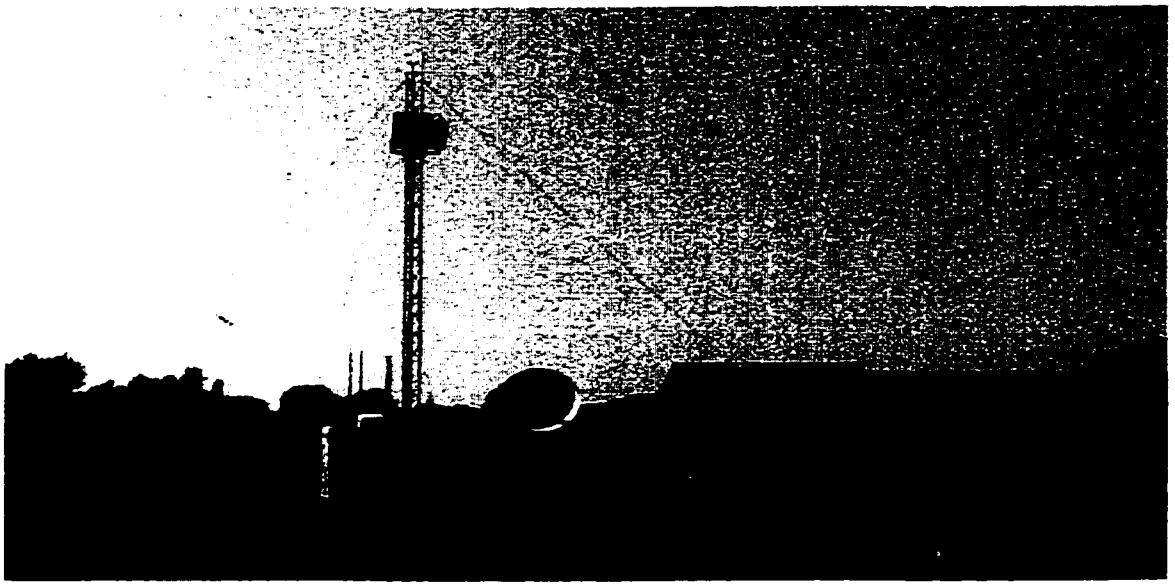

Figure 3.3: Brome-grass site during REBEX-4.

3.1.2 Experimental Setup

The CCRD and the UM-MGG sensors communicated with two on-site computers situated in a small trailer [see Figure 3.4]. The trailer had power, telephone, and data lines provided by the EDC. In this section, I describe the installation and layout of the sensors at both the sites.

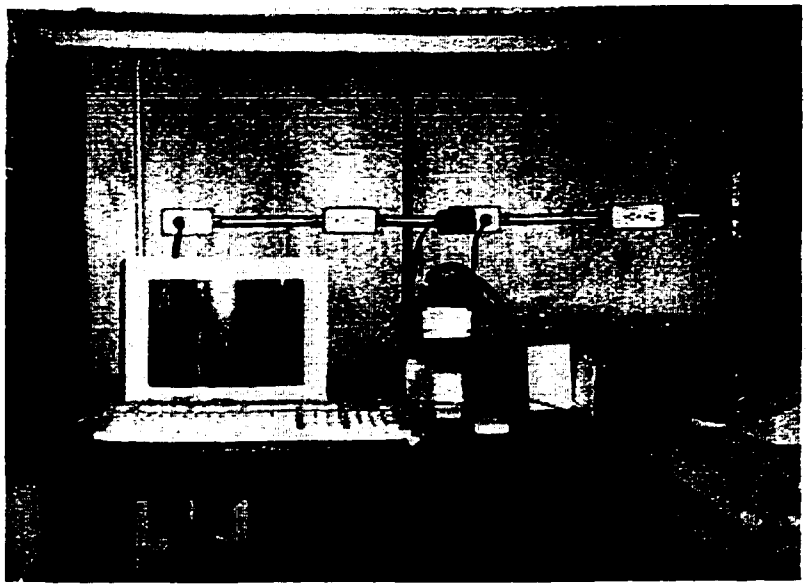

Figure 3.4: An inside view of the trailer.

3.1.2.1 Bare-Soil Site

The bare-soil patch was approximately 289 m^2. Figure 3.5 shows a sketch of the instrument layout at the site. CCRD's Hand-Held Radiometers (HHRs) at the SSM/I frequencies of 19.35, 37.0, and 85.5 GHz, a thermal infrared (TIR) radiometer, and a video camera were mounted on a 2 m pole toward the north edge of the patch to achieve the SSM/I incidence angle of 53°. Figure 3.6 shows a close-up of the pole-mounted instruments. The HHRs were manufactured by MPB Technologies, and each was a total power radiometer with single frequency and polarization. To

change polarities, the radiometers were rotated through 90° by an antenna rotator used in combination with a manual elevation and azimuth positioner. Table 3.1 gives specifications for the HHR.

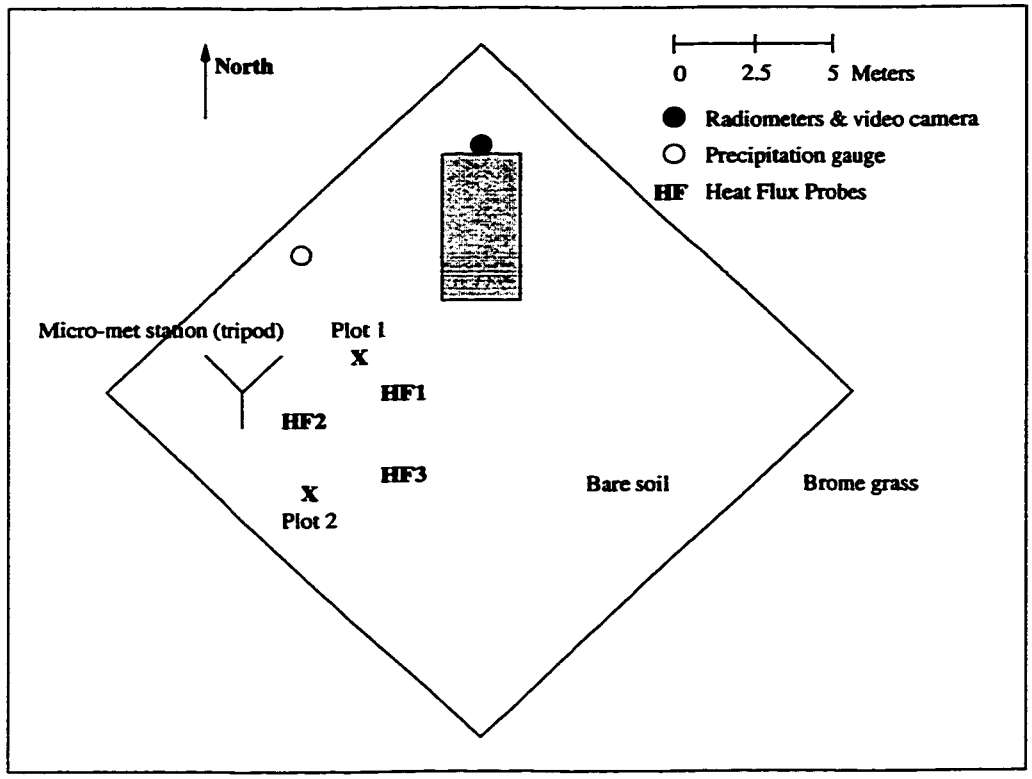

Figure 3.5: A sketch of sensor layout at the bare-soil site.

Frequency (GHz)	19.35	37.0	85.5
Beamwidth (°)	29	8	3.3
IF bandwidth (MHz)	600	600	600
Integration time (sec)	0.07	0.07	0.07
ΔT (K)	1.0	1.0	1.0
FOV (at 2m, 53°) (cm)	90 x 150	25 x 40	10 x 15
Power (V)	12	12	12

Table 3.1: CCRD's Hand-Held Radiometer specifications.

Prior to field deployment, the microwave radiometers were calibrated in the CCRD laboratory using a three point calibration, performed at room temperature (about 295 K), in a cold chamber at 235 K, and with liquid nitrogen (LN_2) at 77 K. For calibration

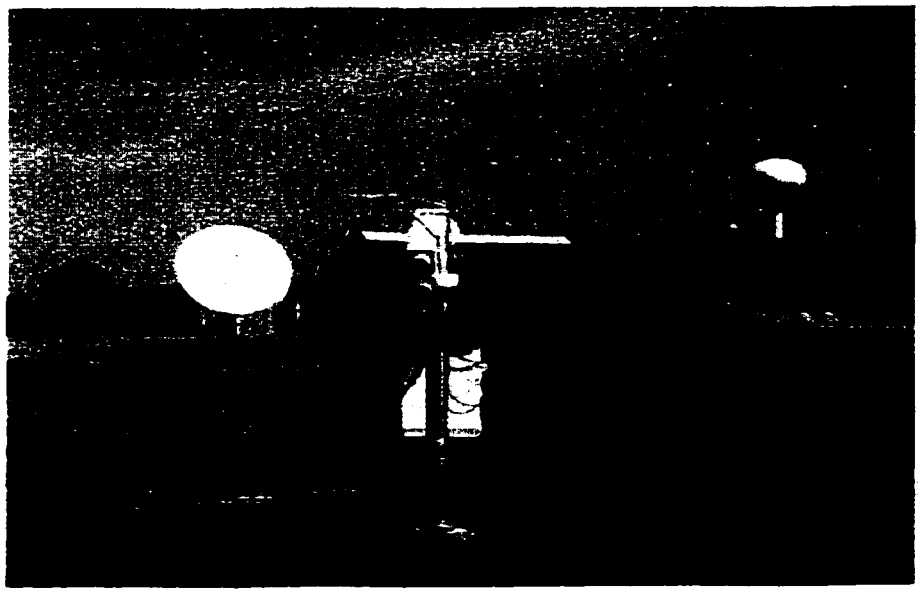

Figure 3.6: A close up of the CCRD radiometers and the video camera mounted on the 2-m pole.

with LN_2, CCRD used a modified cryogenic target, developed by Solheim [190]. The calibration setup consisted of a blackbody absorber (e.g. Eccosorb) with a convoluted surface, placed in a polystyrene foam container with its convolutions facing down. The absorber was immersed in LN_2 (~20 liters) and the radiometer looked up through the bottom of the foam container at the target (LN_2). CCRD fabricated an aluminum enclosure with angular braces at the top [see Figure 3.7(a)]. The radiometer fitted inside the enclosure and the foam container was supported by the braces [see Figure 3.7(b)]. An aluminum plate was placed above the foam container to shield the target. Initial testing with the setup indicated that the target temperature was about 20 K higher than the expected 77 K. There was condensation and ice at the bottom of the container and heavy frost accumulation on its sides. To reduce condensation, the space between the enclosure and the radiometer was filled with a slow and continuous

flow of dry nitrogen during calibration. This resulted in stable target temperature of near 77 K for about 20-30 minutes. In the field, the radiometers performed a self-calibration before every observation (10 minutes) using two plates at different physical temperatures. One plate was at ambient temperature and the other plate was maintained at a slightly higher temperature (~330 K, depending on the ambient temperature).

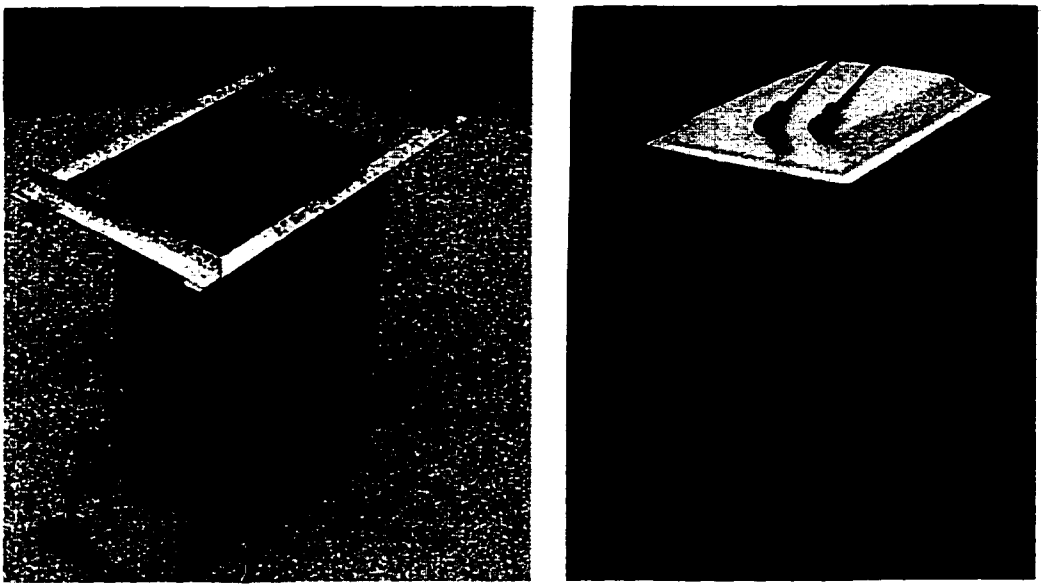

(a) (b)

Figure 3.7: Calibration with liquid nitrogen. (a) A close up of the enclosure. (b) Calibration set-up with a foam container on the braces and a radiometer inside the enclosure.

The radiometers, the camera, and the positioner were all controlled by a Campbell Scientific datalogger (CR10), also mounted on the pole [see Figure 3.8]. The observations recorded by the CR10 logger were downloaded to a long-term storage module (CS SM716).

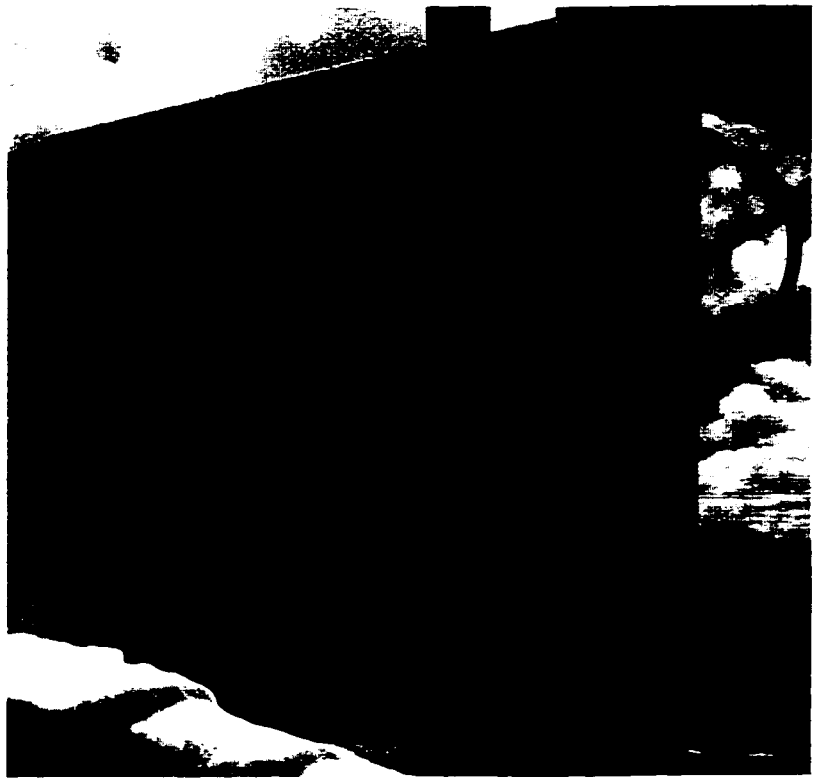

Figure 3.8: A close up of the Campbell Scientific datalogger (CR10).

A tripod with micro-met instruments at different heights, was situated at the west end of the patch, about 8 m from the radiometers [see Figure 3.5]. The instruments included an air temperature and relative humidity probe, two anemometers, two pyranometers (to measure upwelling and downwelling shortwave radiation), and a net radiometer (to measure the net incoming radiation). Figure 3.9 shows a close up of the sensors mounted on the tripod. A tipping bucket precipitation gauge, three soil heat flux probes, and six soil temperature and moisture probes were also installed at the site. The rain-gauge was situated between the radiometers and the tripod [see Figure 3.5]. The soil temperature and moisture probes were installed in two plots about 5 m apart at the depths of 2, 5, and 8 cm. Table 3.2 gives a description of the micro-met sensors. The sensors were controlled by a Campbell Scientific datalogger

(CR21X) and the observations were downloaded to the CS SM716 storage module.

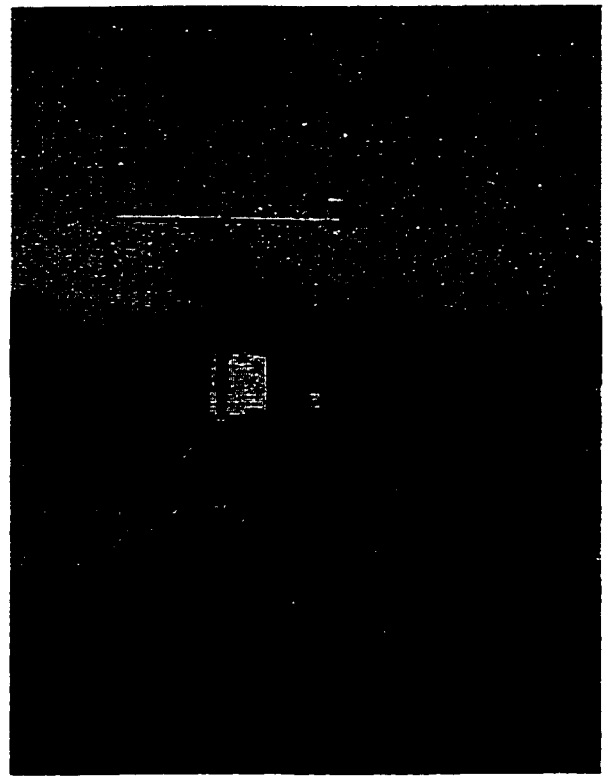

Figure 3.9: A close up of the CCRD micro-met sensors on the tripod.

Parameter	Sensor Type	Height ↓ / Depth ↑
Air temperature (°C)	Vaisala HMP35CF	↑ 1.5 m
Relative humidity (%)	Vaisala HMP36CF	↑ 1.5 m
Wind speed (m/sec)	RM Young wind sentry	↑ 1.45 & 3.6 m
Precipitation (mm)	Lambrecht tipping bucket	↑ 0.5 m
Soil temperature (°C)	CS 107BAM	↓ 2, 5, 8 cm
Soil moisture (% by volume)	CS 615	↓ 2, 5, 8 cm
Net radiation (W/m^2)	Middleton Pyrradiometer CN1-R	↑ 0.65 cm
Downwelling solar hemispherical flux (W/m^2)	Kipp and Zonen CM 11	↑ 3.5 m
Upwelling solar hemispherical flux (W/m^2)	Kipp and Zonen CM 11	↑ 3.3 m
TIR temperature (°C)	Everest 4000.4 GL	↑ 2.0 m
Soil heat flux (W/m^2)	Middleton CN3	↓ 2.0 cm
Video camera	Panasonic B/W CCTV Model WV-BP314	↑ 2.0 m

Table 3.2: Micrometeorological sensors at the bare-soil site.

An on-site computer (Dell 486P) controlled the experiment cycle through an application program using Campbell Scientific's PC208E communication software. The dataloggers (CR10 and CR21X) communicated with the computer via a Campbell Scientific MD9 multidrop interface and the PC208E. Symantec Softwares' Norton

pcANYWHERE (version 2.0) was used to connect to the computer remotely and download data to a computer at CCRD everyday. The experiment control software could also be edited using pcANYWHERE, when necessary. A more detailed report of the equipment installation and set up is given in [78, 77].

3.1.2.2 Brome-Grass Site

I monitored the brome-grass site using UM-MGG's second generation Tower Mounted Radiometer System (TMRS2) and a Micro-Meteorological Station (MMS) which were designed and built by Kim and England [110, 111][see Figure 3.3]. Details of the hardware and software of TMRS2 and MMS are given in [110, 111] and will only be summarized here. The general layout of the sensors installed at the grass site is given in Figure 3.10.

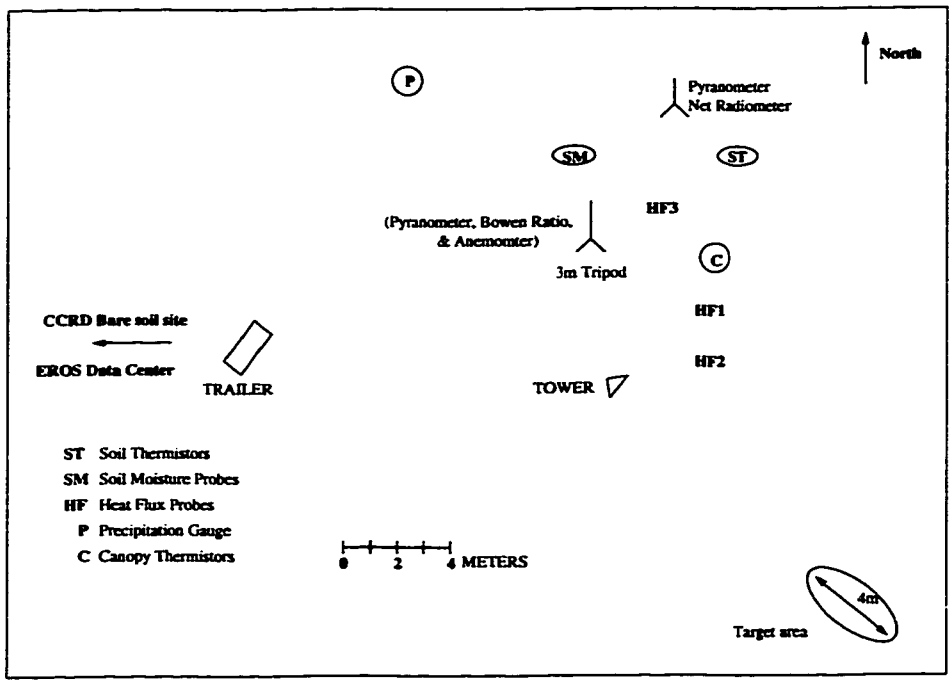

Figure 3.10: Layout of the sensors at the grass site.

The TMRS2 setup consisted of three microwave radiometers, a thermal infrared (TIR) radiometer, a video camera, and an anemometer mounted on a 10 m tower. Three insulated boxes contained the microwave radiometers, and an uninsulated box contained both the TIR radiometer and the camera. All the four boxes were situated in a metal housing that rested on a Hazer at the SSM/I angle of 53°. The Hazer could move up and down the tower with a cable fed through a pulley and a winch. Two of the microwave radiometers were dual polarized at 19.35 and 37.0 GHz, while one was single H-polarized at 85.5 GHz. Figures 3.11 and 3.12 show the TMRS2 set up and a close-up of the tower-sensors, respectively. The radiometer specifications are given in Table 3.3.

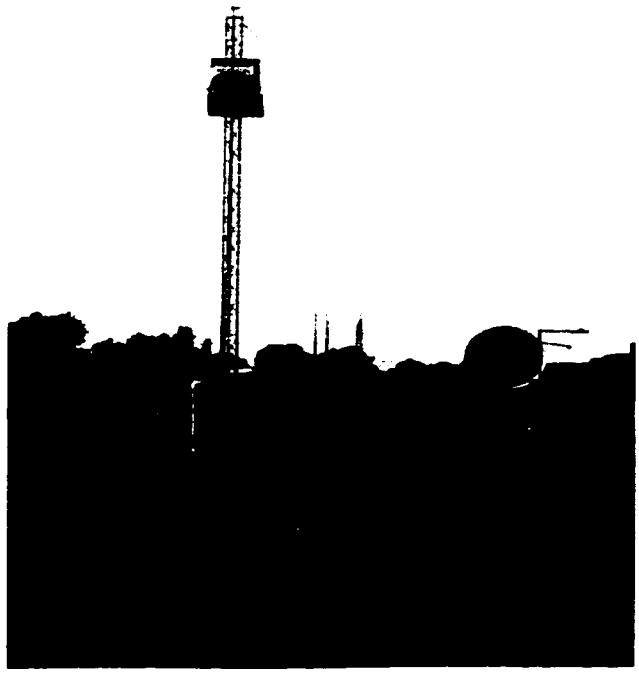

Figure 3.11: A close up of the tower during REBEX-4.

Figure 3.12: A close up of the radiometers and the video camera situated in the housing.

Frequency (GHz)	19.35	37.0	85.5
Polarization	V,H	V,H	H
3dB Beamwidth (°)	10	10	10
IF bandwidth (MHz)	10-250	100-1000	100-1500
Integration time (sec)	1	1	1
ΔT (K)	0.05	0.04	0.07

Table 3.3: TMRS2 Radiometer specifications [111].

For the given location, the best orientation for the tower-sensors (housing) was facing south-east. There were a line of trees about 50 m south, a relatively undulating ground toward the north, and CCRD's bare-soil site ~25 m west. The target area for the radiometers was 4m x 2m about 12 m from the tower. A circular patch of approximately 25 m diameter was sectioned off using reflector markers, with the target-area centered in the patch. The tower-sensors were controlled by a Control and Data Management System (CDMS) inside a small trailer via a fiber-optic link.

The MMS consisted of two tripods (3 m and 1.25 m), a precipitation gauge with a wind-screen [see Figure 3.13], three soil heat flux probes, twelve soil temperature probes, six canopy air temperature probes, six soil moisture probes, and a 10 m anemometer. The 3 m tripod included an air temperature and relative humidity probe (at 2 m), an anemometer (at 2 m), a pyranometer (at 3 m, for downwelling solar radiation), and a Bowen Ratio (BR) system. The 1.25 m tripod included a pyranometer (for upwelling shortwave radiation) and a net radiometer. Figure 3.14 shows the arrangement of the MMS sensors on the two tripods, and Table 3.4 gives the sensor descriptions.

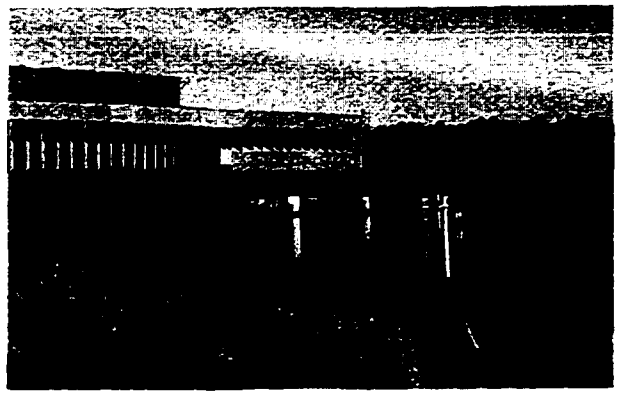

Figure 3.13: A close up of the precipitation gauge with a wind screen.

The CDMS controlled and multiplexed between all the sensors (TMRS2 and MMS). It consisted of an on-site computer (Macintosh II) and a control circuit that linked the sensors to the computer. The control circuit communicated with the computer via National Instruments' NB-MIO-16, NB-DIO-24, and NB-TIO-10 boards. An application program written in Hypercard controlled the experiment cycle, data collection, and data storage. The on-site computer could be reached remotely via Timbuktu software to download data and make changes to the control software.

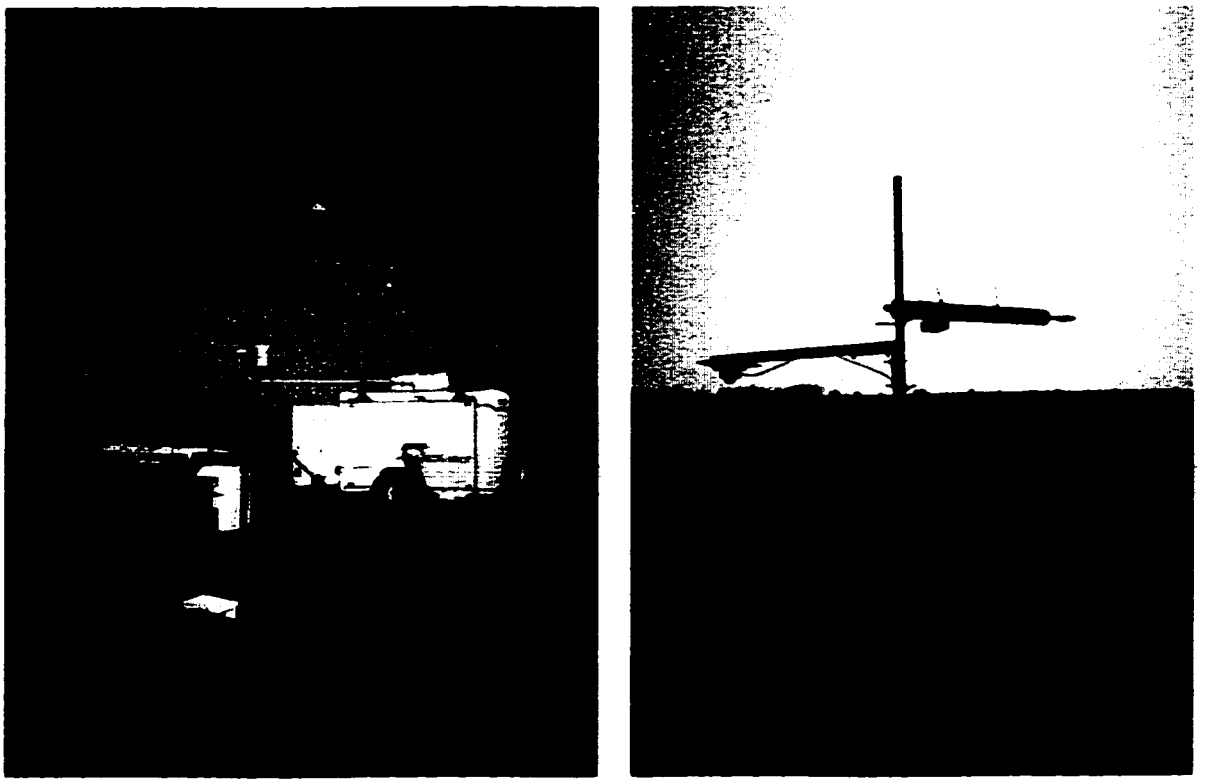

(a) (b)

Figure 3.14: Micrometeorological setup at the grass site (a) A close up of the 3 m tripod (b) A close up of the 1.25 m tripod with a net radiometer and an upwelling pyranometer.

Parameter	Sensor Type	Height ↓ / Depth ↑
Air temperature (°C) Relative humidity (%)	Vaisala HMP-35AC	↑ 2 m
Wind velocity (m/sec, °)	Davis Instruments 7911	↑ 2 m
Wind speed (m/sec)	Met-One 014A	↑ 10 m
Precipitation (mm)	Texas Electronics 525	↑ 0.6 m
Soil temperature (°C)	CS 107B	↓ 2, 4, 8, 16, 32, 64 cm
Soil moisture (% by volume)	Tektronix & CS	↓ 2, 4, 8, 16, 32 cm
Net radiation (W/m^2)	REBS Q-6.2	↑ 1 m
Downwelling solar hemispherical flux (W/m^2)	Eppley Pyranometer 848	↑ 3 m
Upwelling solar hemispherical flux (W/m^2)	Eppley Pyranometer 848	↑ 1 m
TIR temperature (°C)	Everest 4000 ALCS	↑ 10 m
Soil heat flux (W/m^2)	Thornwaite 610	↓ 2.0 m
Video Images	CCTV Corp. GBC-CCD-375 (B/W)	↑ 10 m

Table 3.4: Micrometeorological sensors at the grass site.

3.1.2.3 Field System Modifications

The equipment needed to be repaired and refurbished after the year-long REBEX-3 experiment. Some of the MMS sensors required recalibration. The two pyranometers, the net radiometer, the 10-m anemometer, the soil heat flux sensors, the TIR radiometer, and the air temperature and humidity probe were sent for factory recalibration. The Bowen Ratio system suffered from a factory-generated design flaw during REBEX-3 [111] and was upgraded. The thermistors for soil temperature measurements were recalibrated by inserting them in ice-water bath at 0°C. Six new thermistors were added to the MMS to measure air temperature profile in the grass canopy.

The microwave radiometers were calibrated once, before the system was transported to the EDC. In the field, the radiometers were calibrated seven times [106]. Each calibration consisted of a hot load (a microwave absorber at ambient temperature) and a cold load (a microwave absorber immersed in LN_2) measurement. Because the radiometers were not calibrated for every observation, it was important to maintain them at the temperatures at which they were calibrated, with excellent temperature control. Heaters with software-controlled duty cycles maintained the reference temperatures within 0.01 K.

During REBEX-3, TMRS2 had problems with the housing-door positioning system. For a normal measurement cycle, the door opened at two angles (e.g. 43° and 56° for REBEX-4) to record the reflected sky brightnesses before it opened fully to observe the terrain brightnesses. A potentiometer capable of finite number of turns was

used to determine the door position (angle). The potentiometer shaft was attached to a door-motor with plastic gears. To make sure that the door was completely opened or closed, the motor was run for a few seconds longer than needed. This put undue force on the shaft and rotated it beyond its maximum number of turns, which led to mechanical damage of the potentiometer during REBEX-3. Fischman [67, 68] developed a new door positioning mechanism for REBEX-4, using a rotary optical encoder. The optical encoder allows infinite turns and is more precise than the potentiometer. Because the encoder is digital, it is less susceptible to noise.

As mentioned earlier, the previous REBEXs were conducted under milder temperatures than could be expected during REBEX-4. Some hardware modifications were necessary so that the radiometers could be exposed to summer temperatures of up to 38 °C. A new, more compact video camera was installed, and power to the camera and the TIR radiometer was obtained from AC solid state relays, eliminating two previously used AC adapters and thus reducing heat dissipation. Eight heat sinks from AAVID Thermal Technologies were installed on top of the housing to increase thermal dissipation. The heat sinks were staggered to maximize the air flow through the sinks [50] [see Figure 3.15(a)]. However, during the experiment (REBEX-4), the heat sinks were not enough to keep the housing from overheating. Another layer of radiation shield and a thermal transfer structure was added to increase air flow [see Figure 3.15(b)].

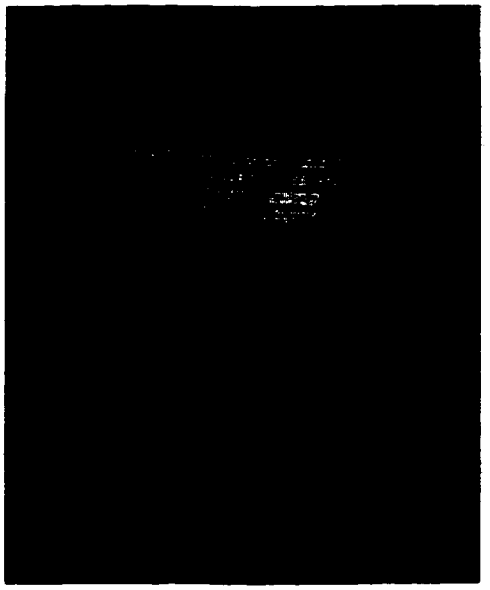

(a)

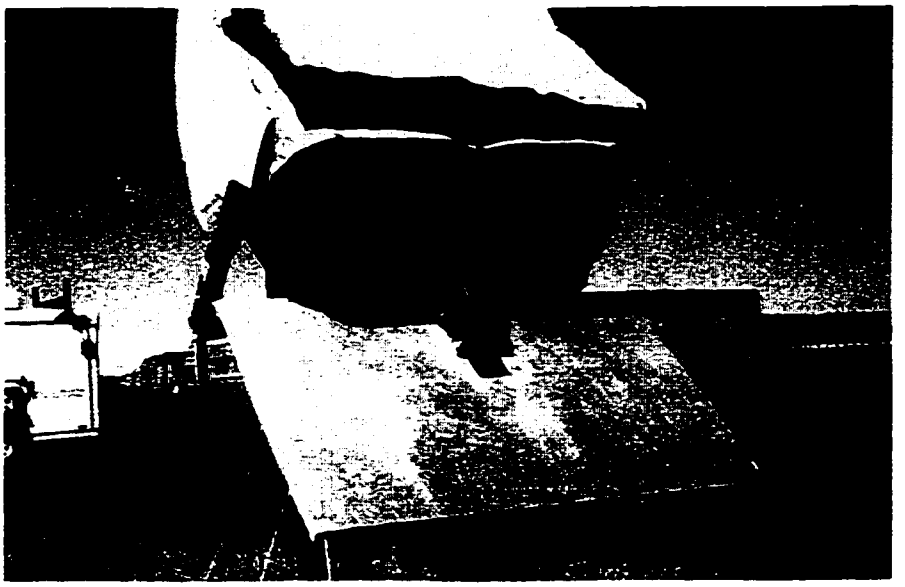

(b)

Figure 3.15: Housing modifications for increased air flow. (a) A close up of heatsinks on top of the housing. (b) A close up of an addition thermal transfer structure added on top of the heatsinks.

A few software modifications were required to get the system ready for REBEX-4. I altered the control software to include the new calibration factors for the MMS sensors and to correct the formulae that converted output voltages from the soil heat flux probes and the net radiometer to their respective physical quantities. A door-control and positioning program was added to link the new optical encoder. A calibration curve of door position vs. the duration of the actuator motor-run was generated and used to control the door positioning during the experiment. Although one might argue that the resulting calibration curve may not have been accurate as the motor movement may be altered with temperature changes, but on monitoring the door position during my site-visits, I found door angle values given by the curve to be within 2-3°, which was acceptable for our purposes. Software changes were also made to modify data format and content in the output files. The complete field system was tested at the UM-MBG for one week before it was transported to the EDC.

3.1.3 Observations: Data Collection and Problems

3.1.3.1 Bare Soil

The sensors were installed on Julian day (JD[1]) 190 - 191. The first set of complete observations was recorded on JD 193 (July 11) and the last set was recorded on JD 270 (September 26). Overall, the micro-met setup worked well and we have continuous weather and radiance data for 78 days. The microwave radiometers suffered some

[1]Julian day for REBEX-4 refers to Julian day in 1996.

hardware problems during the course of the experiment. In this section, I describe the observations and the associated equipment problems at the bare soil-site.

Microwave Emission

Terrain brightnesses were measured every 10 minutes, at the SSM/I frequencies of 19.35, 37.0, and 85.5 GHz. The radiometers were rotated every 30 minutes to switch polarization resulting in three brightness measurements at one polarization, followed by three measurements at the other polarization. The 37 GHz radiometer was shut down after JD 195 due to a shutter solenoid failure. It had to be shipped to the manufacturer, but could not be repaired in time to be used during REBEX-4. The 85 GHz radiometer suffered from the same problem on JD 222 and was also inoperable for the rest of the experiment. The 19 GHz radiometer incurred a defective reference load temperature sensor on JD 226 and was also shut down. For the bare-soil site, we have microwave brightnesses at 19 GHz for 36 days, at 85 GHz for 31 days, and at 37 GHz for only 3 days. The observations at 19 GHz are shown in Figure B.5 in Appendix B.

Micro-meteorological parameters

All the weather and radiance measurements at the bare-soil site were made every 10 minutes. These measurements included downwelling and upwelling solar radiation, net incoming radiation (longwave plus shortwave), wind speed at 1.45 m and 3.6 m, air temperature and relative humidity at 1.5 m, and precipitation. The dataset contained no missing data and all the sensors were fully functional throughout of the experiment (JD 193-270). During my site-visits, I observed dew on the domes of the pyranometers and the net-radiometer. The little dust that accumulated on

the domes required cleaning only once during the experiment. Small insects had also become stuck in the water-flow channel of the precipitation gauge. Although I cleaned the channel often, the accuracy of the gauge is still questionable. The micro-met observations are presented in Figures B.1 - B.3 in Appendix B.

Soil: Thermal and Hydraulic conditions

Soil moisture and temperatures were measured at depths of 2, 5, and 8 cm every 30 minutes [see Figure B.4 and B.5 in Appendix B]. CCRD used two sets (viz., plot-1 and plot-2) of three sensors each, for these measurements. Two of the temperature sensors in plot-2, at 2 and 8 cm, gave intermittent erroneous data (see section 3.1.4). The 2 cm soil moisture probe in plot-1 had some technical problems so that the observations from this probe may not be reliable. Surface temperature was measured using the TIR radiometer every 10 minutes. The sensor was turned off from JD 236 to 257 because the microwave radiometers were inoperable during this time, and the TIR radiometer was controlled by the same software as the other radiometers. Three observations for soil heat flux were recorded at a depth of 2 cm at random locations within the bare-soil patch [see Figure B.5 in Appendix B].

Soil-core samples were collected for moisture and bulk density measurements on JD 191 (June 9) and 269 (September 25). An Oakfield Apparatus Co. soil sampler (inner diameter = 2.03 cm, length = 10 cm) was used for the moisture samples and a Soil Moisture Equipment Corp. model 200-A soil core sampler (inner diameter = 5.372 cm, length = 6 cm) was used for the bulk density samples. Six core samples were taken for soil moisture measurements on both days. Three samples were taken for bulk density measurements on JD 191 (Table 3.5), and two were taken on JD 269

(Table 3.6).

Sample	Volume cm^3	Wet wt gm	Dry wt gm	Vol. soil moisture (%)	Bulk Density gm/cc
1	32.36	50.3	43.9	19.77	
2	64.73	117.6	99.4	28.12	
3	64.73	110.2	93.0	26.57	
4	64.73	129.8	106.7	35.69	
5	64.73	125.2	102.3	35.38	
6	64.73	115.5	99.3	25.03	
1bd	136	204.1	172.4	23.31	1.20
2bd	136	189.4	155.0	25.29	1.33
3bd	136	202.0	161.2	30.0	1.25

Table 3.5: Soil moisture and bulk density measurements made on Julian day 191. "bd" refers to the cores used for the bulk density measurements.

Sample	Volume cm^3	Wet wt gm	Dry wt gm	Vol. soil moisture (%)	Bulk Density gm/cc
1	64.73	108.8	85.3	36.60	
2	64.73	114.6	88.8	39.86	
3	64.73	136.8	109.4	42.33	
4	64.73	130.8	103.2	42.64	
5	64.73	120.1	93.7	40.78	
6	64.73	128.3	100.1	43.56	
1bd	136	177.7	127.8	36.69	1.20
2bd	136	217.5	160.9	41.62	1.46

Table 3.6: Soil moisture and bulk density measurements made on Julian day 269. "bd" refers to the cores used for the bulk density measurements.

Video Images

Black and white video images were collected on JD 198, 199, 201, 204, 206, 207, 211, 214, 218, 220, 225, 228, 232, 234, 236, 239, 242, 247, 250, 257, 264, and 270. These images were saved in JPEG format. Figure 3.16 shows an example image taken

on JD 207 (July 25). The camera's fixed iris and varying light conditions at the site rendered some images harder to interpret.

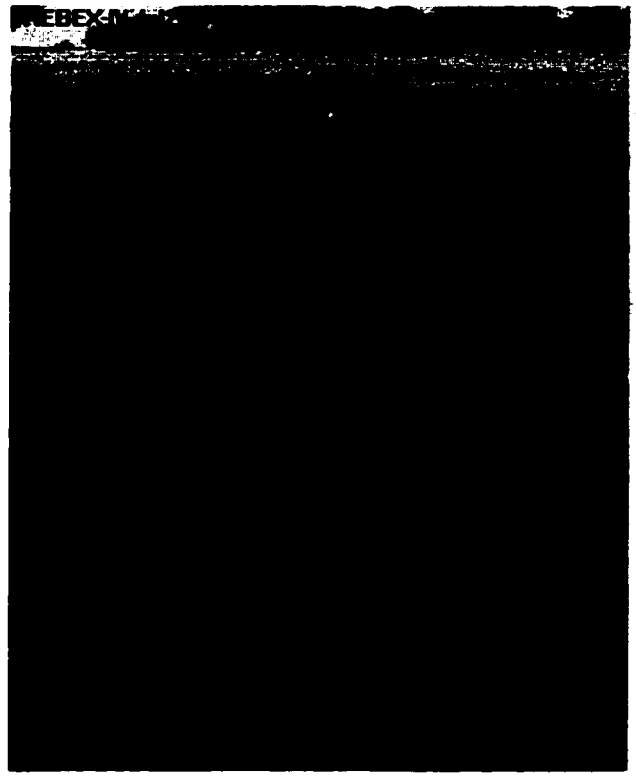

Figure 3.16: A B/W video image of the bare-soil site, taken on July 25 (JD 207).

3.1.3.2 Brome Grass

The field system was installed on JD 151 - 153. After initial problems with the hardware, the first observations were recorded on JD 156 (June 4), and the last were recorded on JD 268 (September 24). Throughout the experiment, we had intermittent hardware problems with the microwave radiometers. Because the field system was not modular, i.e., the micro-met system could not be operated while the radiometers were being repaired in the field, there are several gaps in the weather and radiance

data. This section contains a detailed description of the observations made at the grass-site and the problems encountered during data collection.

Microwave Emission

We observed terrain and reflected sky brightnesses at 19.35 (V- and H-pol), 37.0 (V- and H-pol), and 85.5 (H-pol) GHz every 30 minutes. The terrain brightnesses were observed at the SSM/I incidence angle of 53°, while the sky brightnesses were observed at the zenith angles of 43° (sky1) and 56° (sky2). The 19 GHz radiometer suffered from intermittent hardware problems during the experiment. Most of the problems were caused by the necessarily high internal temperatures. To maintain good temperature control, the internal temperature of the TMRS2 radiometers must be set higher than the maximum ambient temperature. Because the 19 GHz radiometer had the largest antenna and was most affected by the ambient temperature, the internal temperature was sometimes set as high as 329 K. The 37 and 85 GHz radiometers were set as high as 327 K and 325 K, respectively. Similar problems caused by over-heating were encountered during REBEX-5 (see Section 3.2). Given these problems during REBEX-4 and REBEX-5, the UM-MGG is developing radiometers for future experiments with thermo-electric coolers so that the internal radiometer temperatures can be set either lower or higher than the ambient temperatures, as needed [67].

On JD 194, the mixer in the 19 GHz radiometer failed, most likely because of the prolonged exposure to high temperatures. The mixer was replaced and the radiometer was operational again on JD 195. On JD 185, the -15V solid state relay in the 37 GHz radiometer failed and was replaced on JD 195. The physical temperature of

the 85 GHz antenna was no longer recorded after JD 167 when a thermistor failed. Because brightnesses at 85 GHz were not a primary focus of my study, repairing it was given a low priority. A few other radiometer problems (short data gaps) resulted from flaky electrical connections, blown out fuses, and damaged ICs. The microwave observations recorded at the grass-site are shown in Figure B.14 in Appendix B.

There were two problems with the housing door during REBEX-4. The door failed to open during an experimental cycle on JD 162 when capacitor failed in the door motor. The capacitor was replaced, and the door became operational again on JD 166. On JD 220, a threaded shaft that affixed the door to an actuator worked itself loose from the actuator so that the door was always fully open. The shaft was re-inserted in the actuator and secured with a locking nut and the door was again operational on JD 221.

Micro-meteorological parameters

The MMS at the brome grass site worked without major problems for the duration of the experiment. Every 30 minutes, the system recorded air temperature, relative humidity, and wind velocity (speed and direction) at 2 m, wind speed at 10 m, upwelling and downwelling solar radiation, net incoming radiation, Bowen Ratio (two thermocouples and air intake channels installed 1 m apart), and precipitation. Data were lost primarily during times when the radiometers were being repaired. A capacitor failed on the 10 m anemometer on JD 198. It was repaired, and the anemometer became operational on JD 238. As with the CCRD instruments, I observed dew, but no significant dust on the domes of the pyranometers and the net radiometer [see Figure 3.17]. They were cleaned only once during the experiment. Wasps nested

under one of the cup-shaped arms of the precipitation gauge. Although the nest was repeatedly removed and the area sprayed with a wasp-killer, the precipitation data may be unreliable. The micro-met observations appear in Figures B.6 - B.13 in Appendix B.

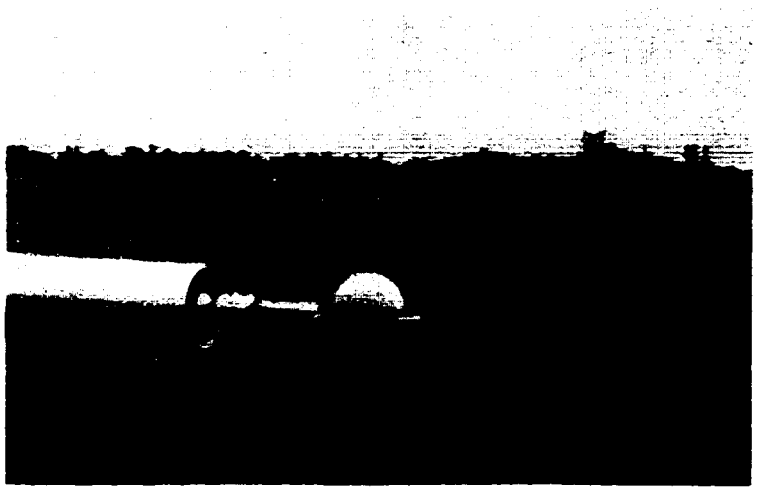

Figure 3.17: A close up of the net radiometer dome to show dew on the upper hemisphere.

Canopy: Thermal and Hydraulic conditions

The air temperature in the canopy was measured at 2, 4, 10, 32, 64, and 90 cm above the soil surface every 30 minutes. The thermistor at 2 cm was situated in the thatch layer. Six diurnal experiments were conducted to measure canopy biomass. Each experiment involved weighing wet biomass of the canopy cut from a 900 cm^2 plot, every 2-3 hours for a 24 hour-period during a precipitation-free day. Whenever there was water on the canopy due to condensation, it was included in the wet biomass measurement. The samples were dried at 70°F for 24 hours in a laboratory and weighed again. Figure 3.18 shows the results from the canopy diurnal experiments.

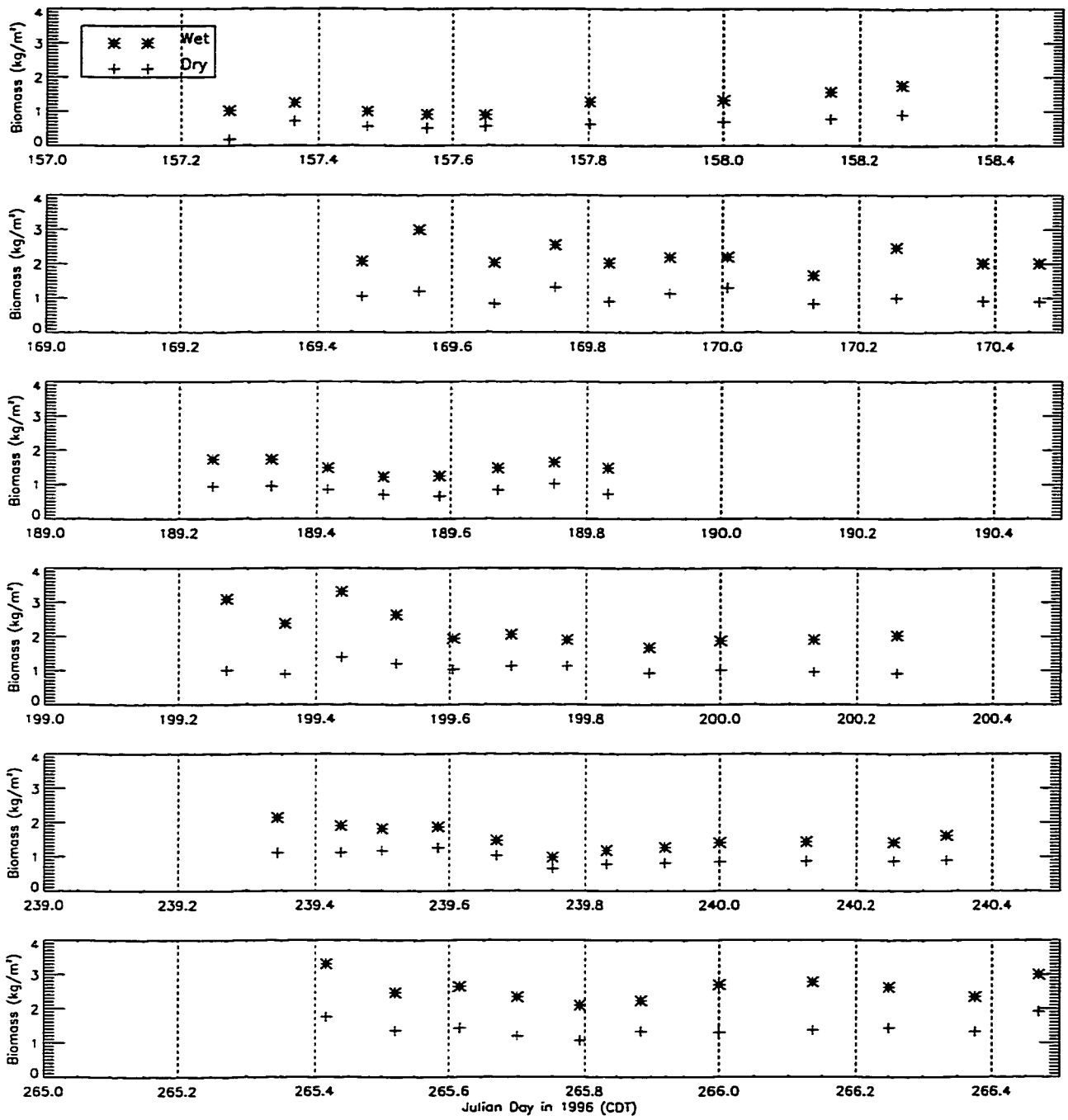

Figure 3.18: Wet and dry canopy biomass from six diurnal experiments during REBEX-4.

More detailed results are given in [106]. The experiment on JD 189 was cut short due to rain after 1900 hr. Two additional experiments were conducted to measure the

vertical distribution of the canopy biomass. The canopy was cut in 2 cm increments from a 0.372 m^2 plot and the samples were weighed. They were then dried and weighed again to measure the dry canopy biomass for each 2 cm increment. Figure 3.19 shows the results from the two experiments.

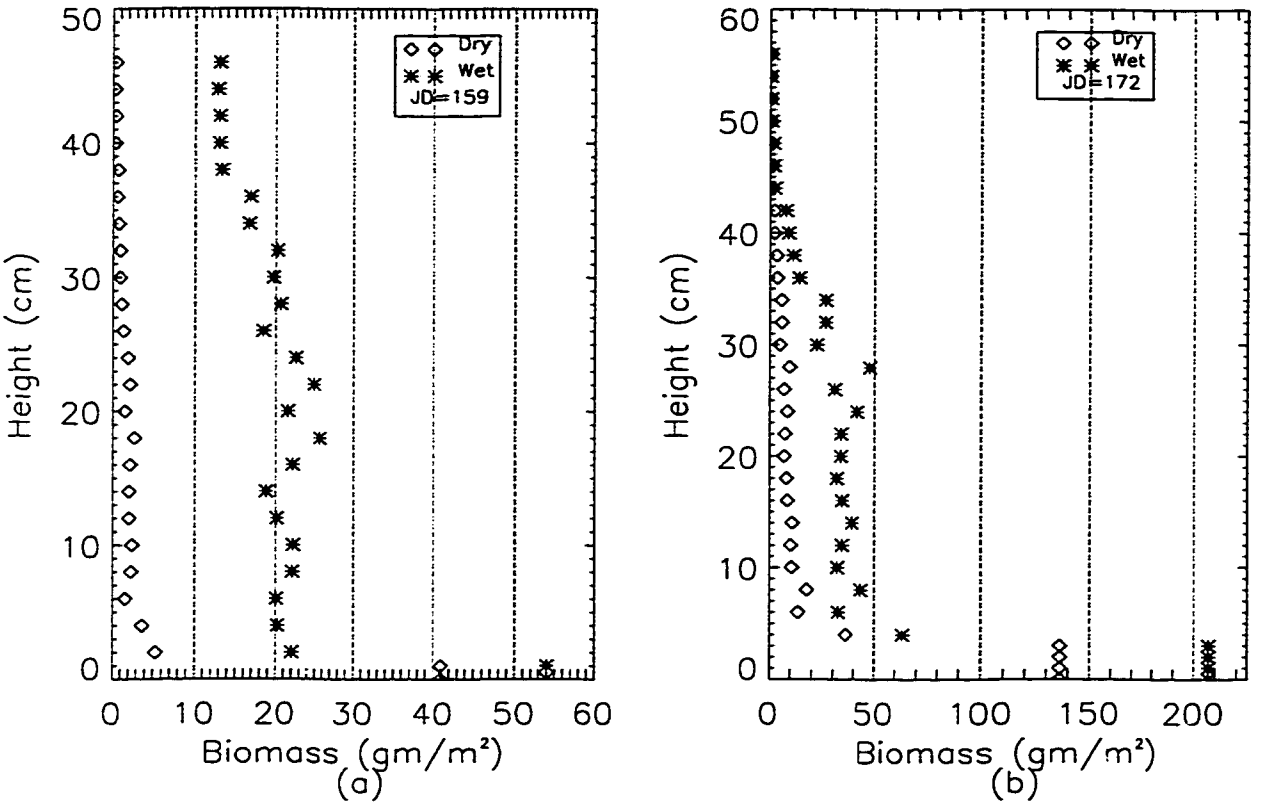

Figure 3.19: Vertical distribution of wet and dry canopy biomass from two experiments during REBEX-4 (a) JD 159 (b) JD 172.

Soil: Thermal and Hydraulic conditions

Soil temperature was measured at the depths of 2, 4, 8, 16, 32, and 64 cm in two plots every 30 minutes. Soil heat flux was measured at a depth of 2 cm every half hour at three locations within 2 m of each other. Soil moisture was measured at 2, 4, 8, 16 and 32 cm. The moisture measurements, however, were unreliable and

could not be used for model calibration. There were three problems with the moisture measurements:

1. The Tektronix cable tester [Figure 3.20] used to collect data from the Time Domain Reflectometry (TDR) probes had problems communicating with the on-site computer.
2. Calibration of the TDR probes proved to be unreliable.
3. Some of the recorded data were ambiguous.

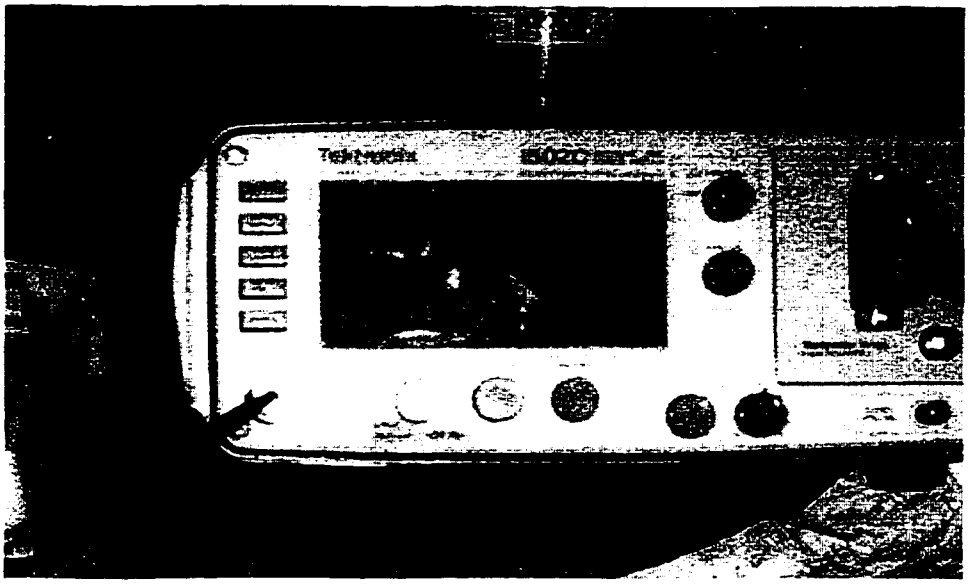

Figure 3.20: A close up of the TDR display showing the "features" corresponding to the beginning and the end of the probe.

Data from five diurnal experiments conducted to measure soil moisture were used for model initialization and calibration. Each experiment consisted of driving a cylindrical coring tool, with 7.4 cm inner diameter, into the soil to a depth of 24 cm and extracting soil samples every 2-3 hours for a 24-hour period during a precipitation-free day. Figure 3.21 shows typical thicknesses of the soil samples. The samples were

weighed either in the field or in the laboratory to get the mass of moist soil. They were baked at 100°C in the laboratory for 24 hours, and the soil samples were weighed again. Figure 3.22 shows the volumetric soil moisture in the upper 5-6 cm during the five experiments. Detailed results from the experiment are given in [106].

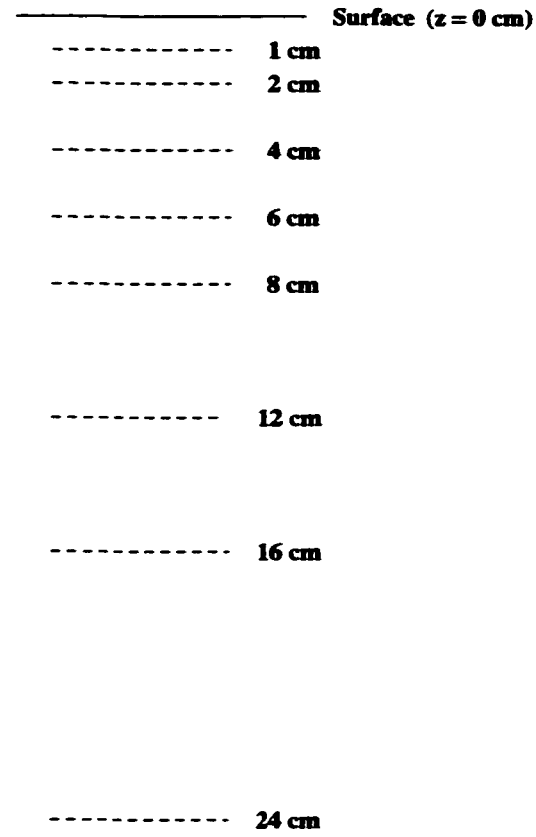

Figure 3.21: Thicknesses of soil samples during the diurnal experiments.

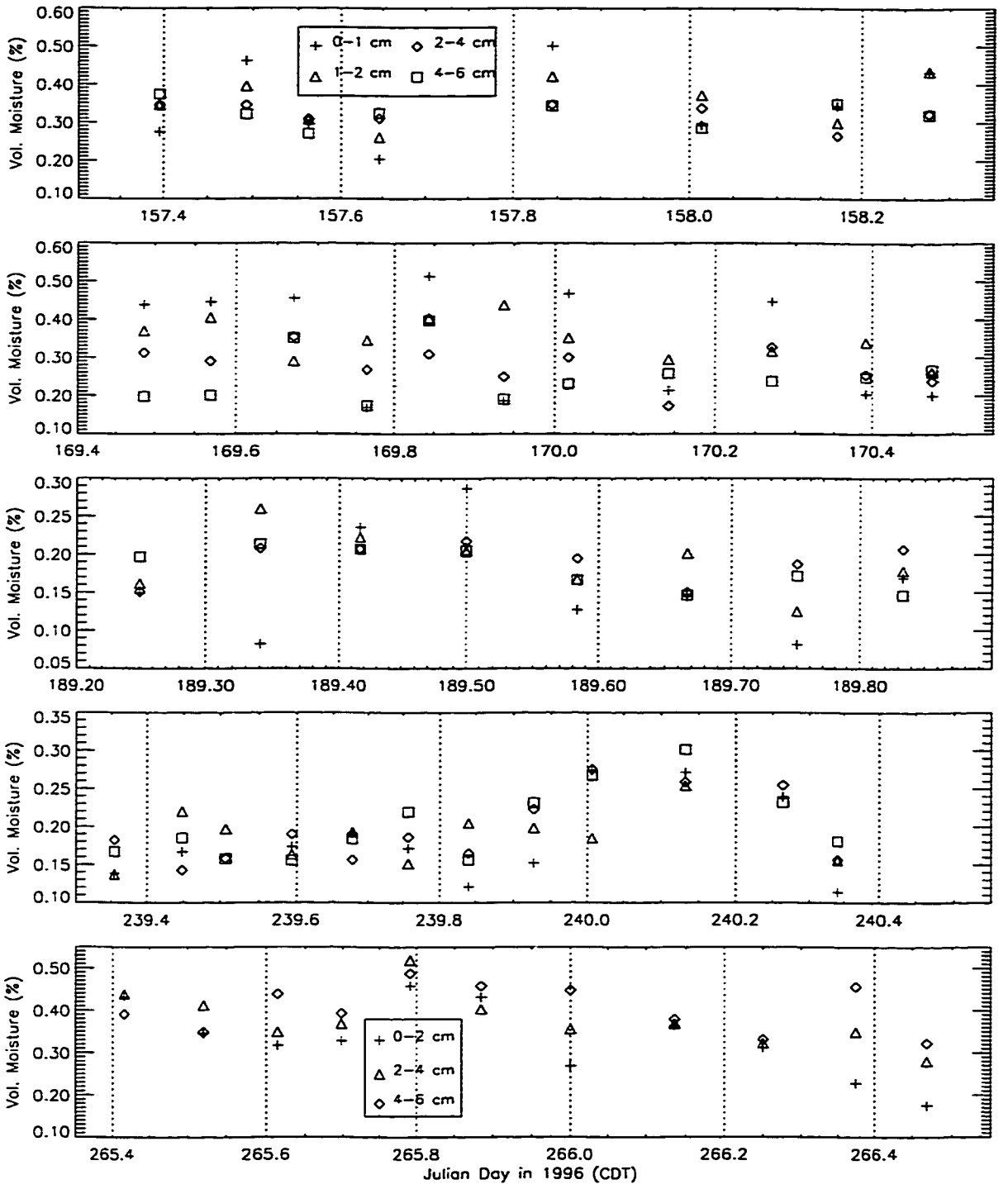

Figure 3.22: Volumetric soil moisture for the upper 6 cm at the grass site measured during REBEX-4.

Video Images

Black and white video images were recorded every day at 1600 hrs CDT. Figure 3.23 is an example of such images.

Figure 3.23: A B/W video image of the grass target area taken on August 21 (JD 234).

A detailed report of the sensor installation, observations, and problems in data collections during REBEX-4 are given in [106].

3.1.4 Data Processing and Analysis

This section contains a discussion on data processing required prior to their being used to force the LSP/R model (as inputs) and to calibrate the with model (as outputs). For the bare-soil observations, data from five sensors were suspect. The recorded maximum wind speeds at 1.45 m and 3.6 m during the entire experiment were less than 2.3 m/sec. Local weather records show wind speeds as high as 8-10

m/sec [128], and the average wind speeds from the anemometer on the MMS at the grass site were nearly 3 m/sec. There may have been a software scaling error, but CCRD could not confirm or correct the error. I used wind observations from the 10 m anemometer at the grass-site, with gaps in the data filled with extrapolated values using a logarithmic wind relationship [187] of the observations at 6.9 m from the Local Climatological Data (LCD) published by National Climatic Data Center (NCDC) for Sioux Falls, SD. The LCD observations were recorded every 3 hours and the 10-m observations were recorded every half hour. Because the LSP/R model expects data at 10 minute intervals, the wind data were linearly interpolated to 10 minute intervals. I estimated the rainfall at the sites from combined precipitation and relative humidity data from the two data sets, and from the LCD in Sioux Falls.

Two bare-soil temperature thermistors in plot-2 recorded suspect data or failed. The thermistor at 2 cm might have become uncovered, because its recorded diurnal amplitudes were higher than the 2 cm thermistor in plot-1 and matched more closely with the TIR observations for skin-temperature. The thermistor at 8 cm failed on JD 212. The soil temperature predictions by the LSP/R model were compared with the observations in plot-1.

For the grass-site, minimal processing was required because the weather and down-welling radiance inputs for the model were obtained from the observations at the bare-soil site.

3.2 REBEX-5

Our research group (UM-MGG) had a unique opportunity to participate in an interdisciplinary investigation, the Southern Great Plains Hydrology Experiment - 1997 (SGP'97), during the summer of 1997. It was conducted from June 18 (JD[2] 169) through July 17 (JD 198), and covered 11,000 km^2 of Oklahoma. One of its major objectives was to estimate soil moisture and temperature using remote sensing at different spatial scales [98]. Investigators from several institutions around the world collaborated to measure and map soil and vegetation properties; to monitor radiant fluxes and soil temperature and moisture profiles; and to record weather. Microwave brightness and radar observations were made from ground, aircraft and satellites. The UM-MGG conducted REBEX-5[3] as a contribution to the SGP'97 at Department of Energy's Atmospheric Radiation Measurement - Cloud and Radiation Testbed (ARM-CART) Central Facility (CF) near Lamont, OK [107].

3.2.1 Site and Terrain Description

Two terrain types were monitored at the REBEX-5 [Figure 3.24] site; senescent winter wheat (from JD 170-176.67) and, after harvest, wheat-stubble (from JD 177-198). The wheat field (CF-02) was ~100 m south-west of the main building of the CF. The site was relatively flat with the wheat growing in rows that were 30 cm apart. An ARM-CART 60 ft tower with sensors for wind velocity, temperature, and relative humidity at different heights was located 75 m south-west of the REBEX-

[2]Julian day for REBEX-5 refers to Julian day in 1997.
[3]REBEX-5 was a team effort and credit is due to all who participated.

5 site. Investigators from NASA Goddard Space Flight Center (NASA-GSFC) and Global Hydrology and Climate Center (GHCC) monitored a grass (CF-01) and a wheat site (CF-02) 50 m south-east of our site.

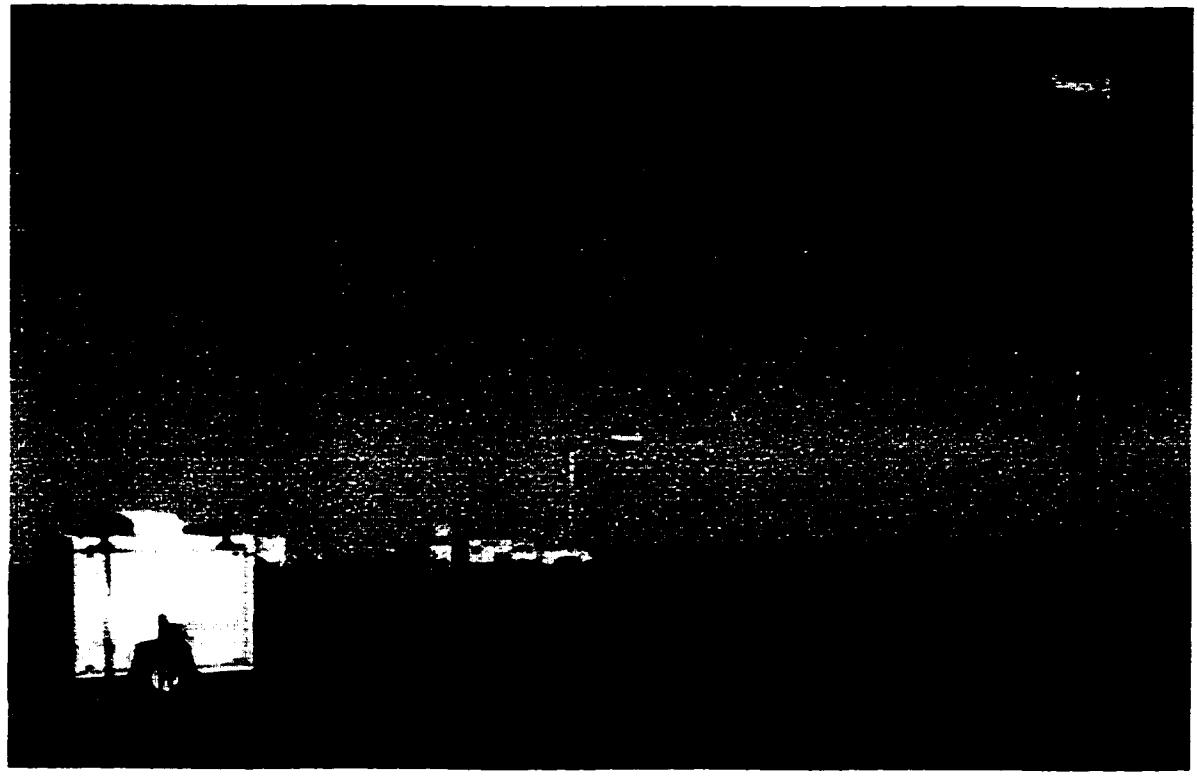

Figure 3.24: Experimental setup during REBEX-5 in Oklahoma. A truck-mounted radiometer system from NASA-GSFC/USDA can be seen in the background.

3.2.2 Experimental Setup and Observations

REBEX-5 was a much simpler experiment than REBEX-4 because only the TMRS2 was used to monitor the wheat site. The MMS was being re-designed and could not be used for REBEX-5. The micro-met data needed for the model calibration was obtained from the ARM-CART and the GHCC sensors (see Chapter 4). The TMRS2

system was identical to the one used in REBEX-4 with no major hardware modifications and only minor software changes. The harnesses and connectors in the housing were refurbished, and the 10 m anemometer was connected directly to the CDMS in the trailer (during REBEX-4, the anemometer was connected to the 3 m tripod). The control software was changed to include the anemometer modification. Power and a telephone line were provided by the CF.

The TMRS2 tower faced the north-east and observed a 4m x 2m area. We observed microwave brightnesses at the three SSM/I frequencies and TIR temperatures of terrain and sky, and 10-m wind speeds every 30 minutes [see Appendix B]. Video images were recorded once per day.

The microwave radiometers were calibrated using the hot and cold load measurements (as in REBEX-4) three times during the experiment. The set temperatures had to be as high as 332 K for the 19 and 37 GHz radiometers to maintain good temperature control. Toward the end of the experiment (JD 193), the 19 GHz radiometer began malfunctioning and was turned off on JD 196. After REBEX-5, the failure was traced to a loose electrical connection. The TIR radiometer gave intermittent values of 0 K for the skin temperatures. These anomalies occurred between early and late afternoons only and are thought to be associated with high afternoon temperatures. The 0 K values were filled in with the observations from the ARM-CART TIR sensor. Gaps in 10 m wind speed data were also filled using data from the ARM-CART anemometer.

The UM-MGG also measured canopy biomass during four diurnal experiments: two with senescent winter-wheat and two with wheat-stubble. These experiments

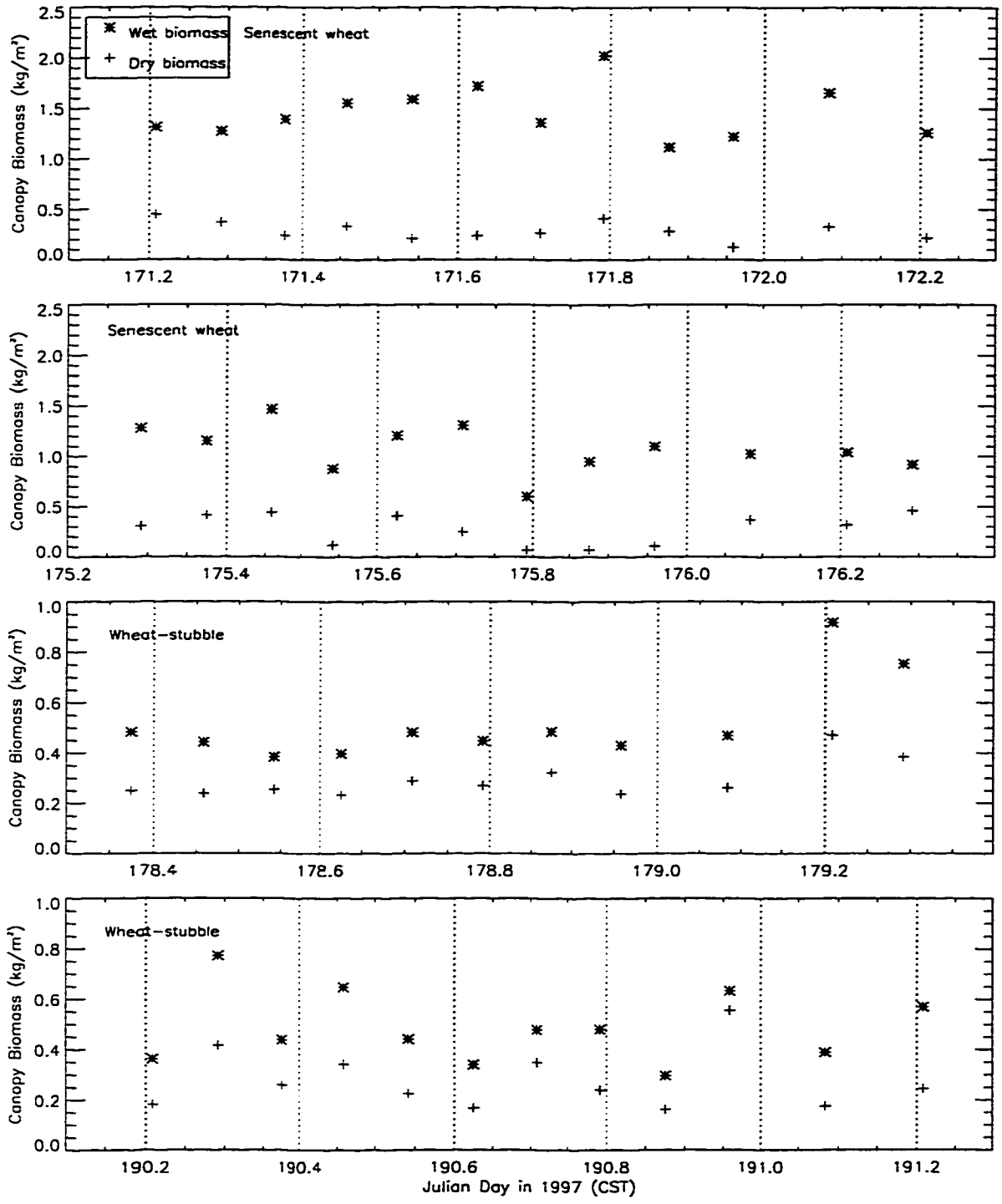

Figure 3.25: Wet and dry canopy biomass from four diurnal experiments during REBEX-5.

were conducted in the same manner as the canopy diurnals during REBEX-4 (see

section 3.1). Figure 3.25 shows the wet and dry canopy biomass measurements during the four experiments. Detailed observations during the diurnal experiments are given in [107].

3.3 Summary

- REBEX-4 was conducted in collaboration with CCRD, AES, Canada on the grounds of EROS Data Center, near Sioux Falls, SD, from June through September in 1996. Co-located and continuous microwave brightnesses and micrometeorological observations were made at a bare soil and a brome grass site. Soil thermal and hydraulic conditions were also monitored at both sites.
- REBEX-5 was conducted as the University of Michigan's contribution to SGP'97. During REBEX-5, we observed continuous microwave brightnesses of senescent winter wheat, and after harvest, winter wheat-stubble, from mid-June through mid-July in 1997 at the ARM-CART Central Facility near Lamont, OK.

CHAPTER 4

LSP/R Model Calibration

In this chapter, I describe the calibration of the modified LSP/R model [see Chapter 2] for three terrain types, viz., bare soil, brome grass, and winter wheat-stubble. I also discuss the results from the comparison of model estimates with the field observations during REBEX-4 and REBEX-5, described in Chapter 3. The chapter contains details of only the model parameters that were specific to each terrain. The parameters and physical constants that were the same for all three terrains are summarized in Appendix C.

4.1 Bare Soil

4.1.1 The 1-dTH Module

This section provides details of the 1-dTH module calibration for bare soil, including discussions on constrained and un-constrained parameters used in the model simulation.

4.1.1.1 Simulation Period and Input Variables

I ran the 1-dTH module for 24 days, from Julian Day (JD) 194 (July 12) through 218 (August 5) in 1996. The module was forced with downwelling solar and longwave radiation, wind speed at 10 m, air temperature and relative humidity at 2 m, and precipitation. Figures 4.1 and 4.2 show these forcings for the simulation period as observed during REBEX-4. The downwelling longwave radiation ($R_l^{\downarrow}$) was not measured during REBEX-4, but was estimated from the observed downwelling ($R_s^{\downarrow}$) and upwelling ($R_s^{\uparrow}$) solar radiation, net incoming radiation ($R_n^{\downarrow}$), and soil thermal infrared temperature (T_{IR}) as,

$$R_l^{\downarrow} = R_n^{\downarrow} - (R_s^{\downarrow} - R_s^{\uparrow}) + e_t \sigma T_{IR}^4 \tag{4.1}$$

where, e_t is the infrared emissivity of the soil surface, and σ is the Stefan-Boltzmann constant. Figure 4.3 shows the estimated $R_l^{\downarrow}$.

4.1.1.2 Initial and Boundary Conditions

The initial conditions for the upper 8 cm of soil moisture and temperatures were obtained from the REBEX-4 observations. The temperature profile for the deeper layers was estimated from an annual model [125]. The moisture profile for the saturated layers below the water-table, at 2 m [16], was equal to porosity. The profile was linearly interpolated for the soil nodes between 8 cm and 2 m, but their values were altered during calibration to provide a best fit between the model estimates and the field observations. Figure 4.4 shows the initial temperature and the moisture profiles. The surface boundary condition was from the energy balance among short and long-

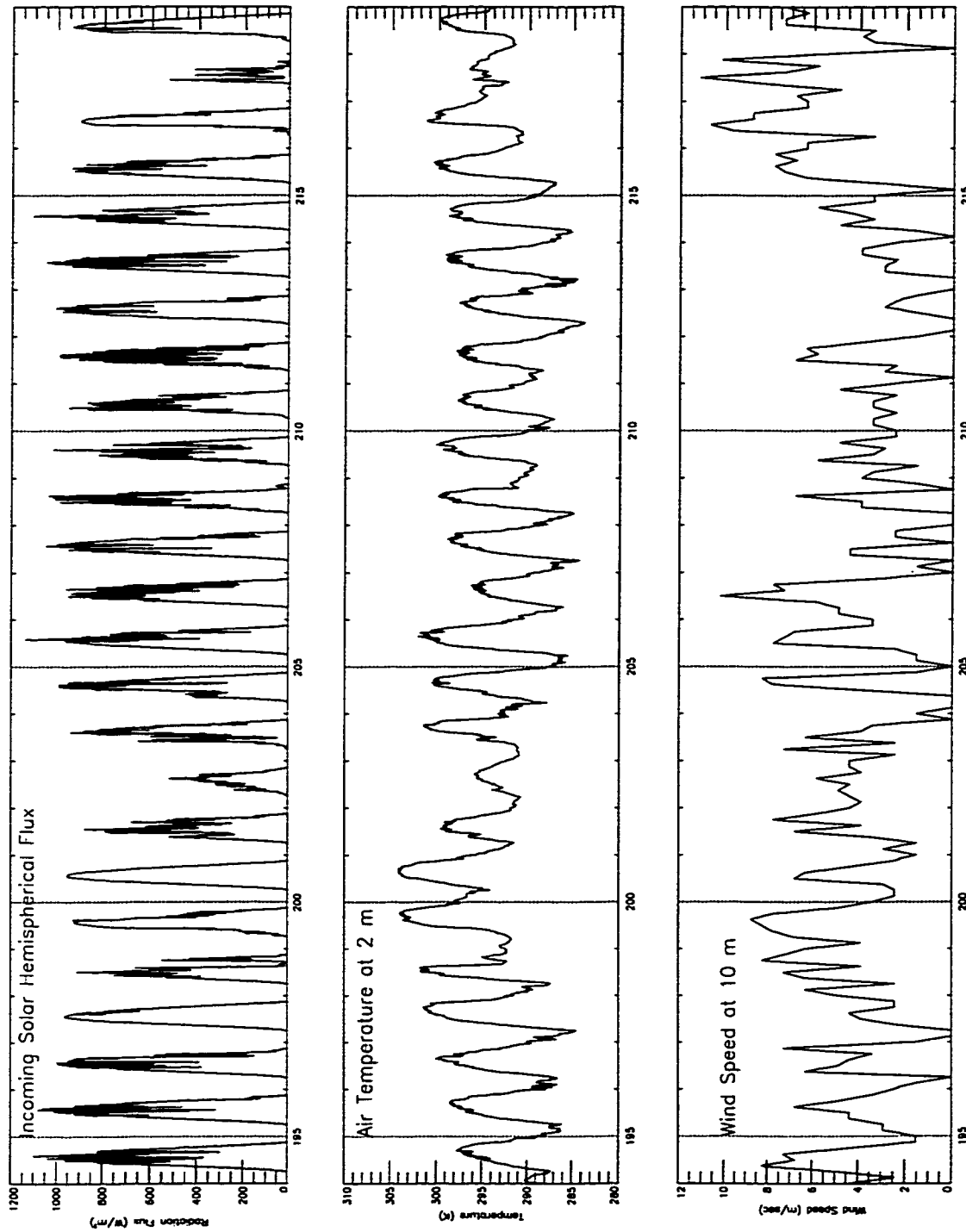

Figure 4.1: Weather forcings from REBEX-4 for the bare soil simulation: Downwelling solar radiation, air temperature, and wind speed.

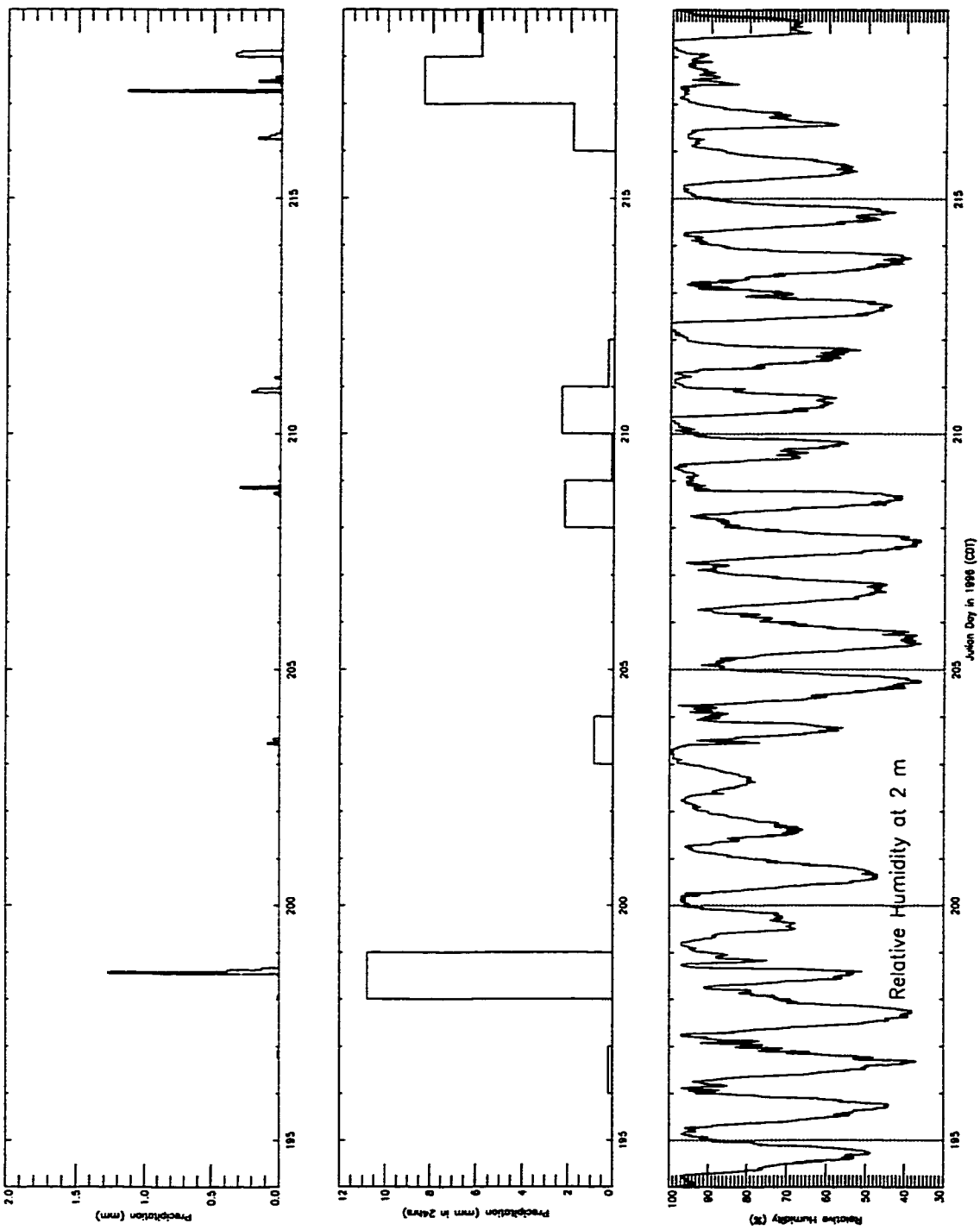

Figure 4.2: Weather forcings from REBEX-4 for the bare soil model simulation: Precipitation and relative humidity.

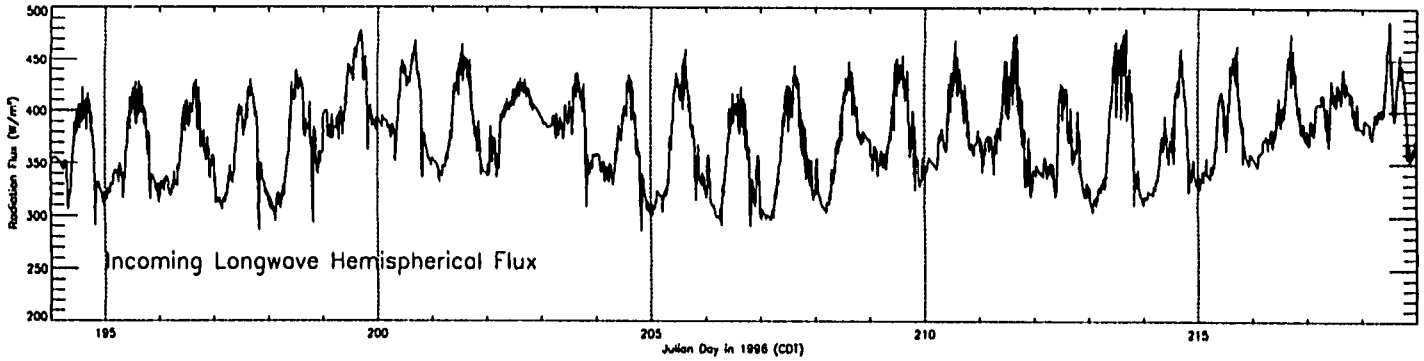

Figure 4.3: Downwelling longwave radiation estimated from equation (4.1) in the bare soil model.

wave radiation, and sensible and latent heat exchanges as described in section 2.1.1.1. At the lowermost boundary (node), the temperature and the moisture was the same as for the node above [see section 2.2.1].

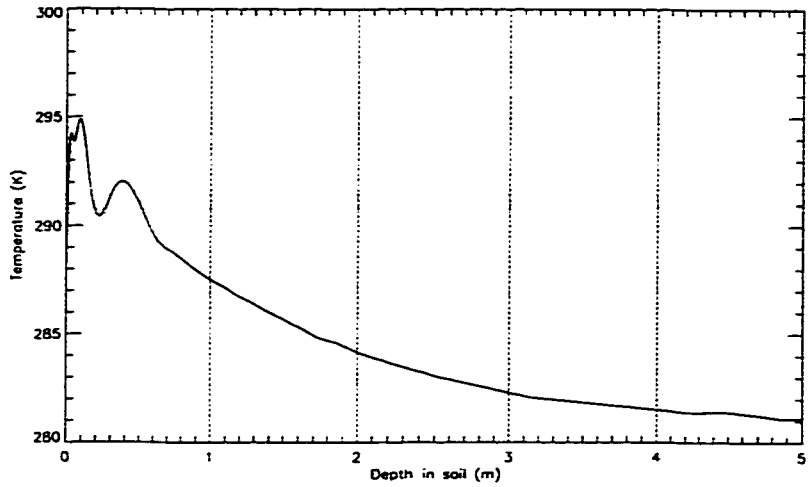

(a)

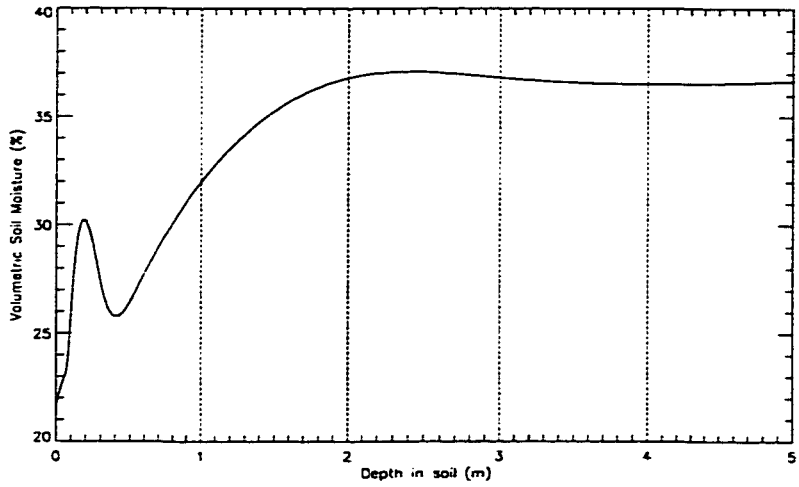

(b)

Figure 4.4: Initial conditions for bare soil simulation: (a) Soil temperature and (b) Moisture profile.

4.1.1.3 Soil Properties

Physical Properties

The soil at the REBEX-4 site was a Silty Clay Loam. Estimates of silt, clay, and sand fractions, wilting point, and field capacity were obtained from a soil survey report [151]. Estimated range of porosities, 46-49%, were from the bulk density calculations discussed in Chapter 3. The roughness length of the soil, i.e., the height above the surface where the wind speed vanishes, was estimated from [187]. The physical properties for the upper 5 cm are tabulated in Table 4.1. Linear interpolation was used to assign these properties to each node in the module.

Properties	Values
Silt fraction (%)	65.1
Clay fraction (%)	31.0
Sand fraction (%)	3.9
Field capacity (m^3/m^3)	0.294
Wilting point (m^3/m^3)	0.145
Porosity (%)	48.0
Roughness length (m)	0.02-0.09

Table 4.1: Soil physical properties in the upper 5 cm at the REBEX-4 site.

Thermal Properties

Thermal conductivity, as a function of soil constituents, particle shape, and moisture, was from an empirical model by deVries [42, 122, 71]. The model was unchanged in the modified module. For simplicity, the shape of the soil particles were assumed to be spherical. During the module simulation, the thermal conductivity of soil varied between 0.58 and 0.65 W/m.K. Various thermal properties of the soil constituents

are summarized in Appendix C.

Hydraulic Properties

Soil hydraulic conductivity is a function of saturated hydraulic conductivity and matric head [143, 175]. The saturated hydraulic conductivity depends on physical properties of the soil and can vary over orders of magnitude [87, 76, 151]. For the REBEX-4 site, Nestrud et al. [151] estimated a range of 1.76×10^{-5} to 5.64×10^{-6} m/sec and I measured a value of 2×10^{-7} m/sec using a laboratory tension apparatus [106] on a soil sample taken from the site. The saturated conductivity was the only unconstrained constitutive property in the bare soil model, and its value for each node was varied within the allowed range to calibrate the module. The assigned values were 2×10^{-7} m/sec in the top 1 cm of soil and 5×10^{-7} m/sec in the next 4 cm.

I used the relationship between matric head and soil water content given by the two-parameter junction model by Rossi and Nimmo [175]. The equations, described in detail by Liou et al. [122], were unchanged in my version of the model, except for the estimates of air entry pressure and pore size index, discussed in section 2.2. Figure 4.5 shows matric head and hydraulic conductivity as functions of water content in the top 5 cm of the soil.

Radiation Properties

Two parameters in the module describe the radiation properties of the soil,viz., thermal infrared (TIR) emissivity and shortwave albedo. A typical range for TIR emissivities of bare soils is 0.94-0.98 [162]. I chose 0.96. The albedos of most agricultural soils vary between 0.2 and 0.4 [2], but are functions of solar angle; cloud cover; soil physical properties such as color and roughness [187], and soil moisture [96]. The

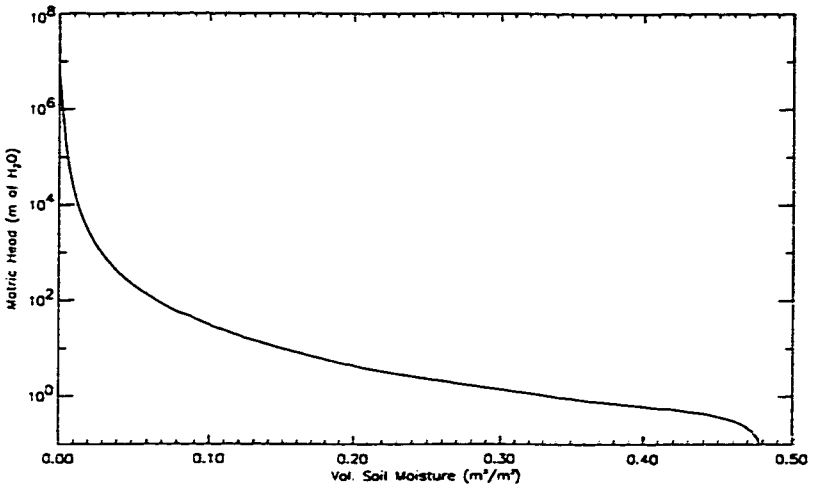

(a)

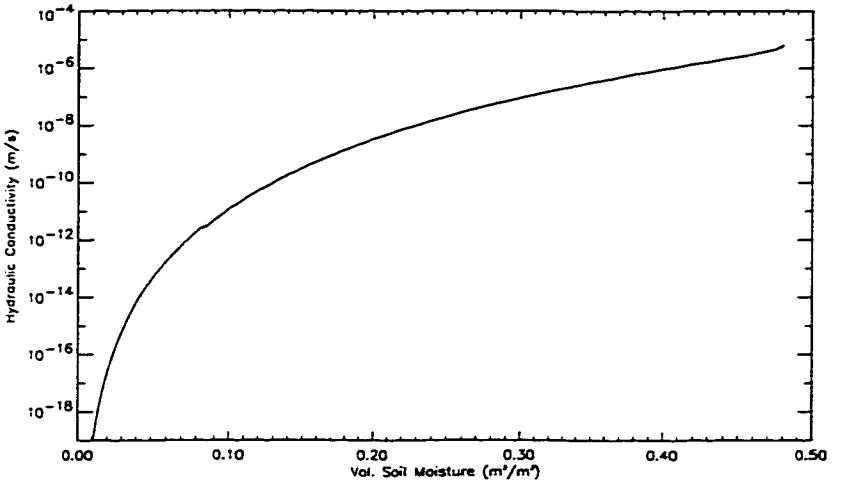

(b)

Figure 4.5: Hydraulic properties of soil. (a) Matric head and (b) Hydraulic conductivity as functions of soil moisture.

soil albedo was constant at 0.3 in the community model [124]. I used a variable albedo obtained by fitting observed values of $R_s^{\uparrow}/R_s^{\downarrow}$ to cubic polynomials for clear

and cloudy days as functions of the solar angle [see Figure 4.6]. The results were,

$$\begin{aligned} alb_{cldy} &= 0.33 - 0.5862\ cosZ + 0.75\ cos^2Z - 0.325\ cos^3Z \\ alb_{clr} &= 0.49 - 1.7\ cosZ + 2.9\ cos^2Z - 1.58\ cos^3Z \end{aligned} \tag{4.2}$$

where, alb_{cldy} and alb_{clr} are cloudy and clear day albedos, respectively, and Z is the solar zenith angle.

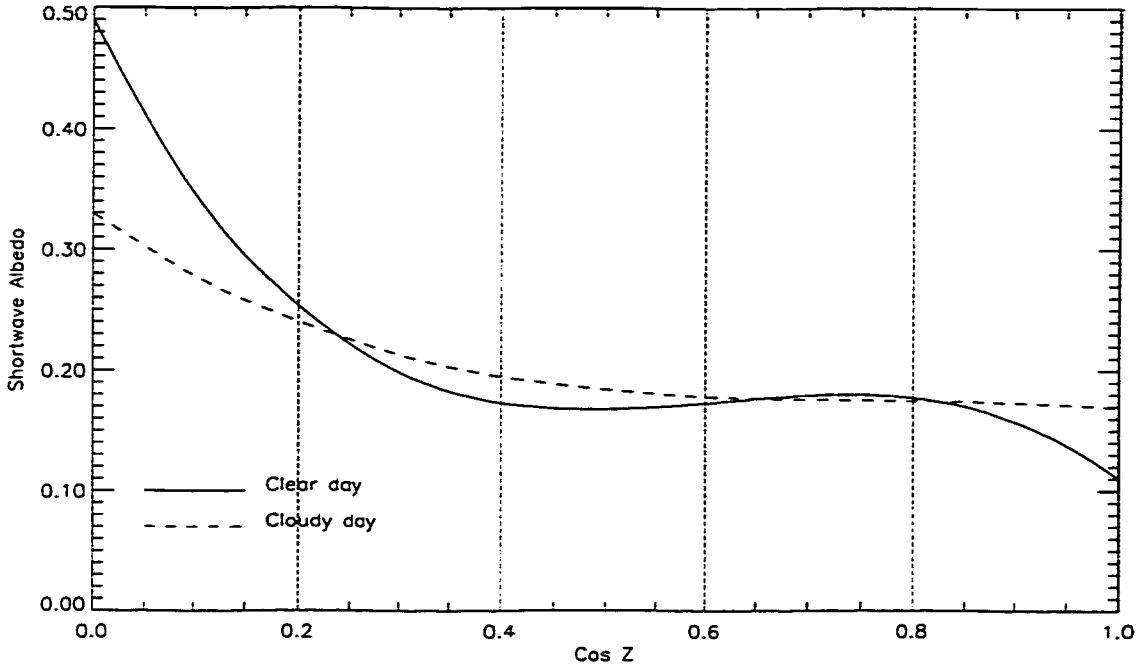

Figure 4.6: Solar albedo for the bare soil during REBEX-4.

4.1.1.4 Solution Convergence

The 1-dTH module was run using different spatial and temporal resolutions to test for convergence. Figures 4.7 and 4.8 show the results of the convergence tests as observed in soil temperatures and moisture at the depth of 5 cm. As expected, the soil temperature and moisture estimates converged as the time interval between each module update, or the time steps, decreased. Similar convergence was achieved as

the inter-nodal distances were decreased. In general, the time-steps and inter-nodal distances at which the solution converges depend upon the soil properties and the strength of forcings at the upper boundary. Figure 4.7(a-b) show the temperatures and the moisture for a five-day simulation, from JD 193 (July 11) through 198 (July 16) in 1996, as the time-steps decreased from 4.6 to 1.5 seconds. The soil was discretized into 61 nodes with 8 nodes in the top 5 cm during the simulation. Model estimated profiles after 5 days achieved convergence when the time-step was decreased to 3 seconds. A further decrease in the time-step to 2 or 1.5 seconds produced changes in the moisture and temperature estimates of $\leqslant 0.04\%$ and $\leqslant 0.05$ K, respectively.

Figures 4.8(a-b) show the soil temperature at 5 cm and the total moisture in the upper 5 cm for a 3 second time step, as the total number of nodes increased from 40 to 70, or from 3 to 13 in the upper 5 cm. As the number of nodes in the top 5 cm increased from 3 to 8, the temperature and moisture estimates oscillated within $\sim$0.05 K and 0.2 mm/m^2, respectively. The oscillations decreased by half, as the number of nodes increased from 8 to 13. For all the model simulations in this dissertation, the time step was 3 seconds and the soil was discretized into 61 nodes with 8 nodes in the upper 5 cm.

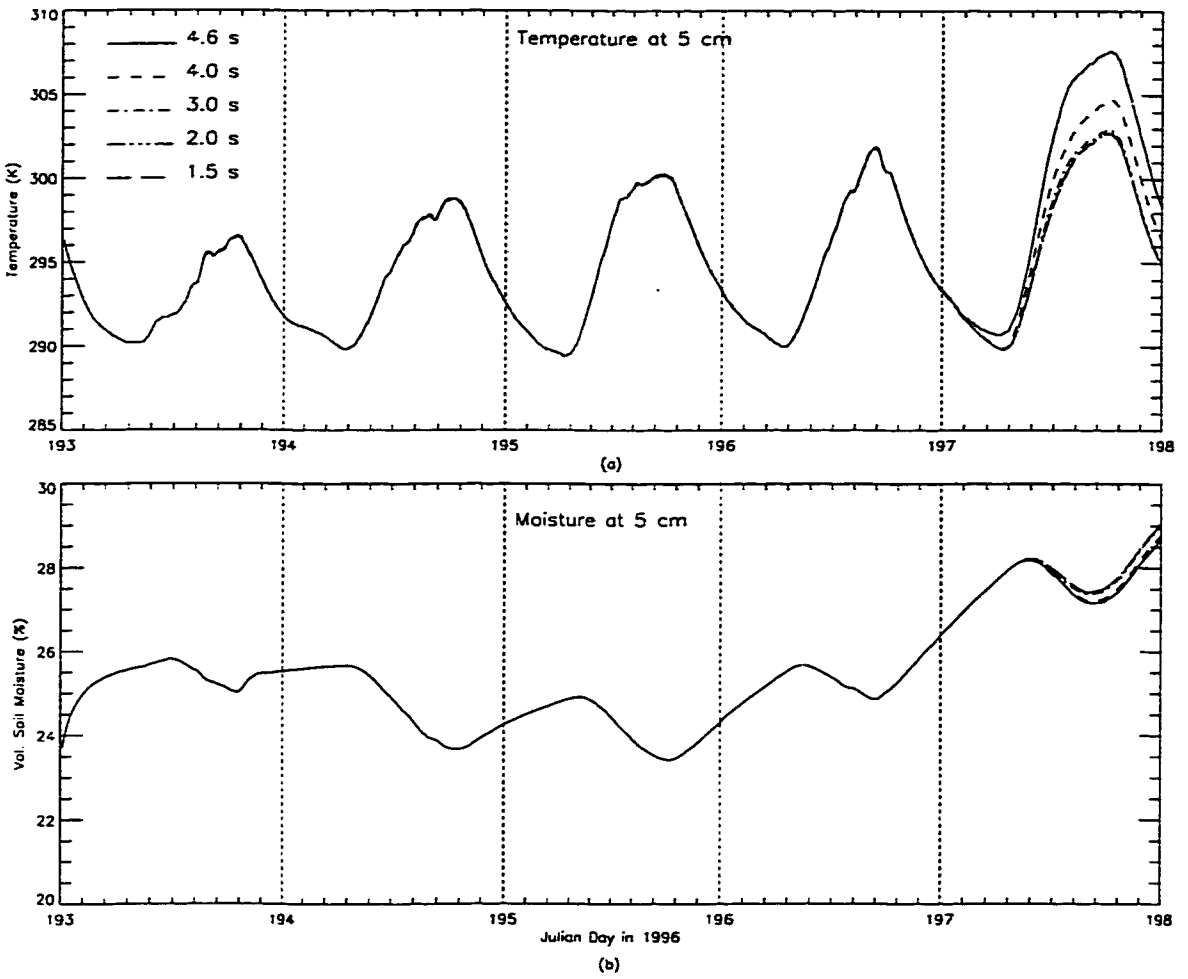

Figure 4.7: Temporal convergence: (a) Soil temperature and (b) Moisture at depth of 5 cm.

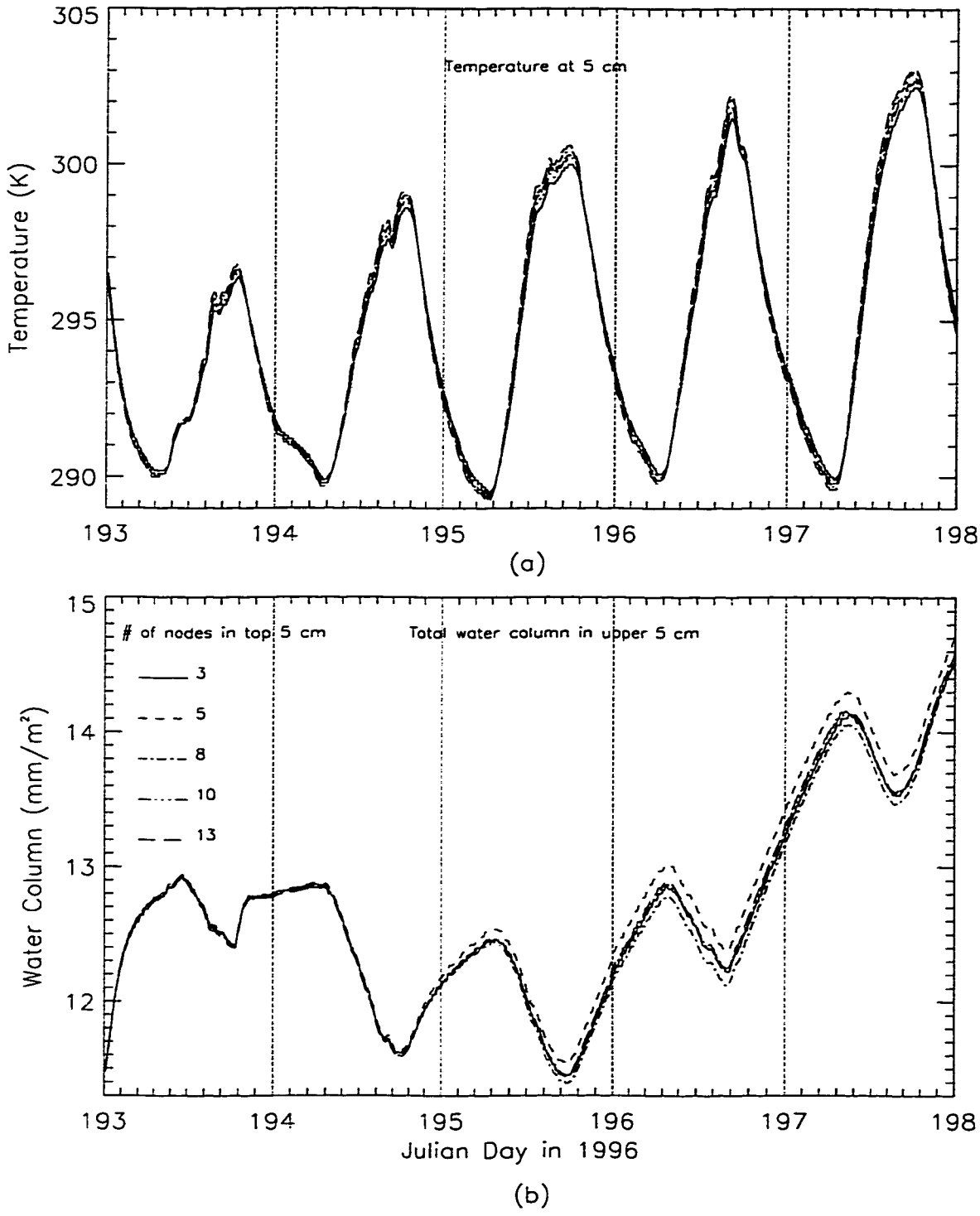

Figure 4.8: Spatial convergence: (a) Soil temperature at 5 cm and (b) Total water column in the upper 5 cm.

4.1.1.5 Comparison with Field Observations: Results and Discussion

In this section, I compare the 1-dTH module estimates[1] of soil temperatures, moisture, and heat fluxes with the REBEX-4 data. Figures 4.9(a-d) show comparisons of modeled and measured soil temperatures at the surface, and at depths of 2, 5, and 8 cm, respectively. The modeled surface temperature actually represents the temperature over the upper 2 mm of soil, but is compared with the observed skin temperature (TIR). Overall, the 1-dTH module captures the diurnal variations in the soil temperatures at 2, 5, and 8 cm as indicated by low mean differences between the estimated and the observed temperatures and their standard deviations [Table 4.2]. The module under-estimates the surface temperatures during the day by ~10 K, but estimates realistic temperatures during the night. We expected a difference of 2-3 K between the skin temperature and the 2 mm layer temperature, but a 10 K difference combined with the slightly higher amplitude module temperatures at 2 cm suggests that the modeled thermal conductivities of the soil surface may be too low. Modeled conductivities include only a conduction process and not an inter-particulate radiative transport process. Radiative transport could be significant in the under-dense artificially created bare soil surface of REBEX-4. Including the radiative transport would increase the thermal conductivity in such soils. For lower layers, below 2 cm, modeled temperatures match with the observations well. Modeled heat fluxes also match the observed fluxes at 2 cm [Figure 4.10].

[1]The model "estimates" refer to the calibrated results.

Depths	Mean	Standard Deviation
Surface (1 mm vs. TIR)	-1.77 K	6.81 K
2 cm	-0.99 K	3.87 K
5 cm	-0.89 K	2.84 K
8 cm	-0.82 K	2.28 K
Heat Flux (2 cm)	-7.29 (W/m^2)	38.19 (W/m^2)

Table 4.2: Mean differences and their standard deviations for the soil temperatures and heat fluxes. (Difference = Estimated-Observed).

In Figures 4.9(b-d) and 4.10, the module estimates for temperatures and heat fluxes on JD 207 are uncharacteristically high. This was most likely due to particularly low wind speeds on that day. In general, as the wind speed decreases, the roughness length increases [162]. In the module, the roughness length varies between 0.02 and 0.09 m, depending on wind speed. More sensitivity studies are required to see the affect of different roughness lengths and wind speed on model output, and to make simulations more realistic during low wind periods.

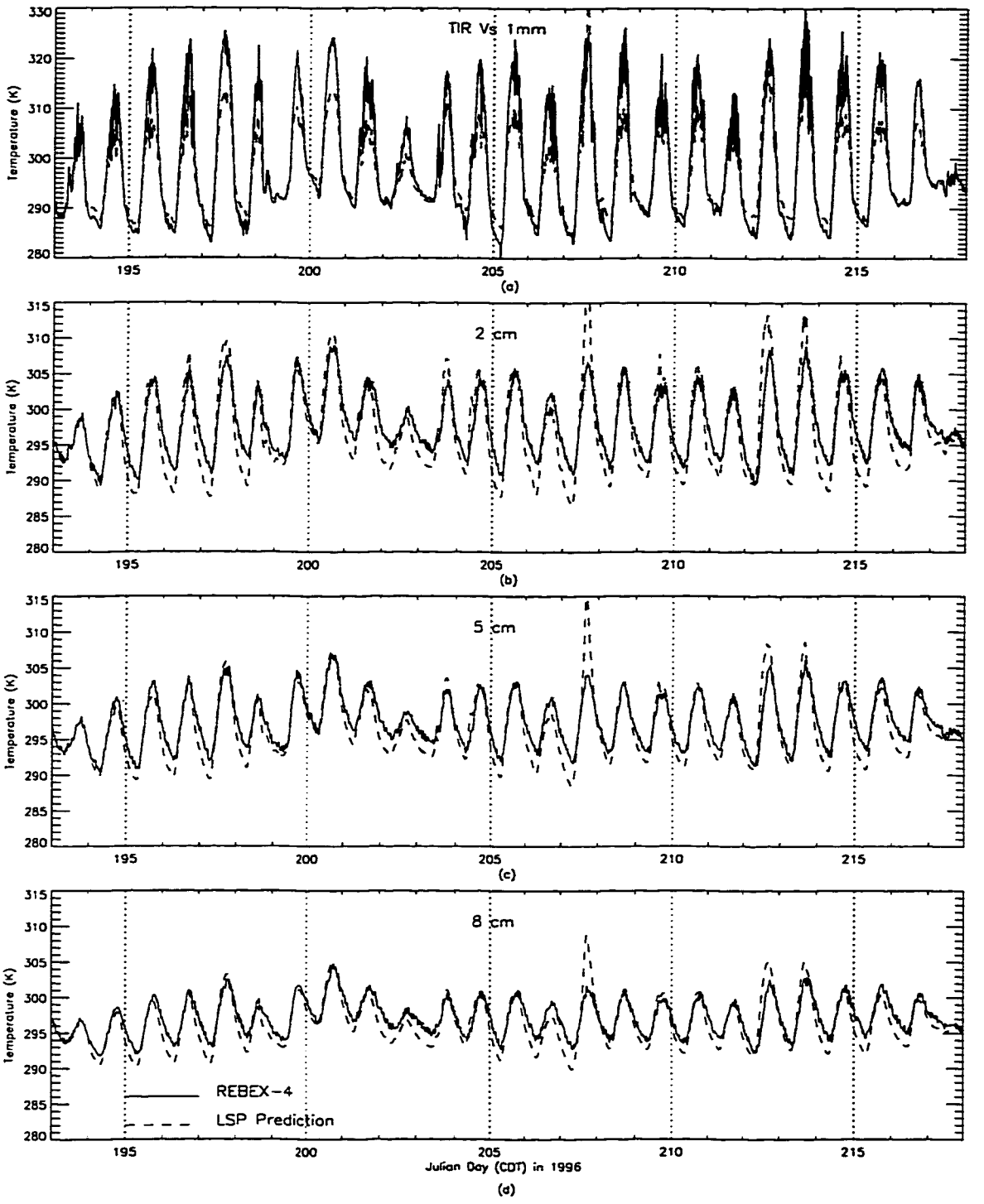

Figure 4.9: A comparison of the estimated and the observed soil temperatures for the bare soil at (a) Surface (b) 2 cm (c) 5 cm, and (d) 8 cm.

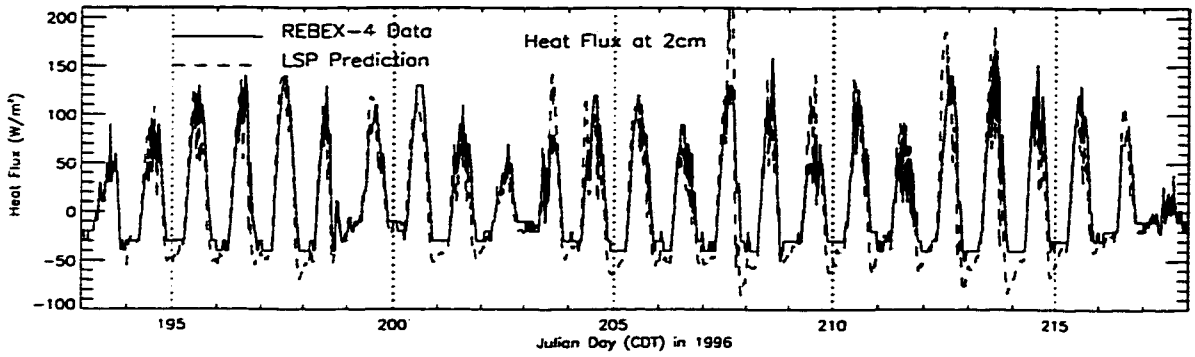

Figure 4.10: A comparison of the estimated and the observed heat fluxes into the ground at 2 cm.

Figure 4.11(a-c) compares the estimated and the observed soil moisture at depths of 2, 5, and 8 cm, respectively. The module estimates realistic mean moisture values at the observed depths as given in Table 4.3. The deviations of 1.5% by volume for the 2 cm depth, are acceptable and fall within the range of experimental errors using the TDR probes [134]. The estimated and the observed moisture at 2 cm are approximately 180° out of phase. The phases of the observed values seem to track the thermal variations in the soil. The period of the TDR probe-signal is sensitive to the changes in soil temperature [37], which could explain the phase differences and also the stronger diurnal variations observed at the lower layers.

Depths	Mean (% by vol.)	Standard Deviation (% by vol.)
2 cm	-0.86	1.50
5 cm	-0.05	0.82
8 cm	-0.65	0.86

Table 4.3: Mean differences and their standard deviations for the volumetric soil moisture. (Differences = Estimated - Observed)

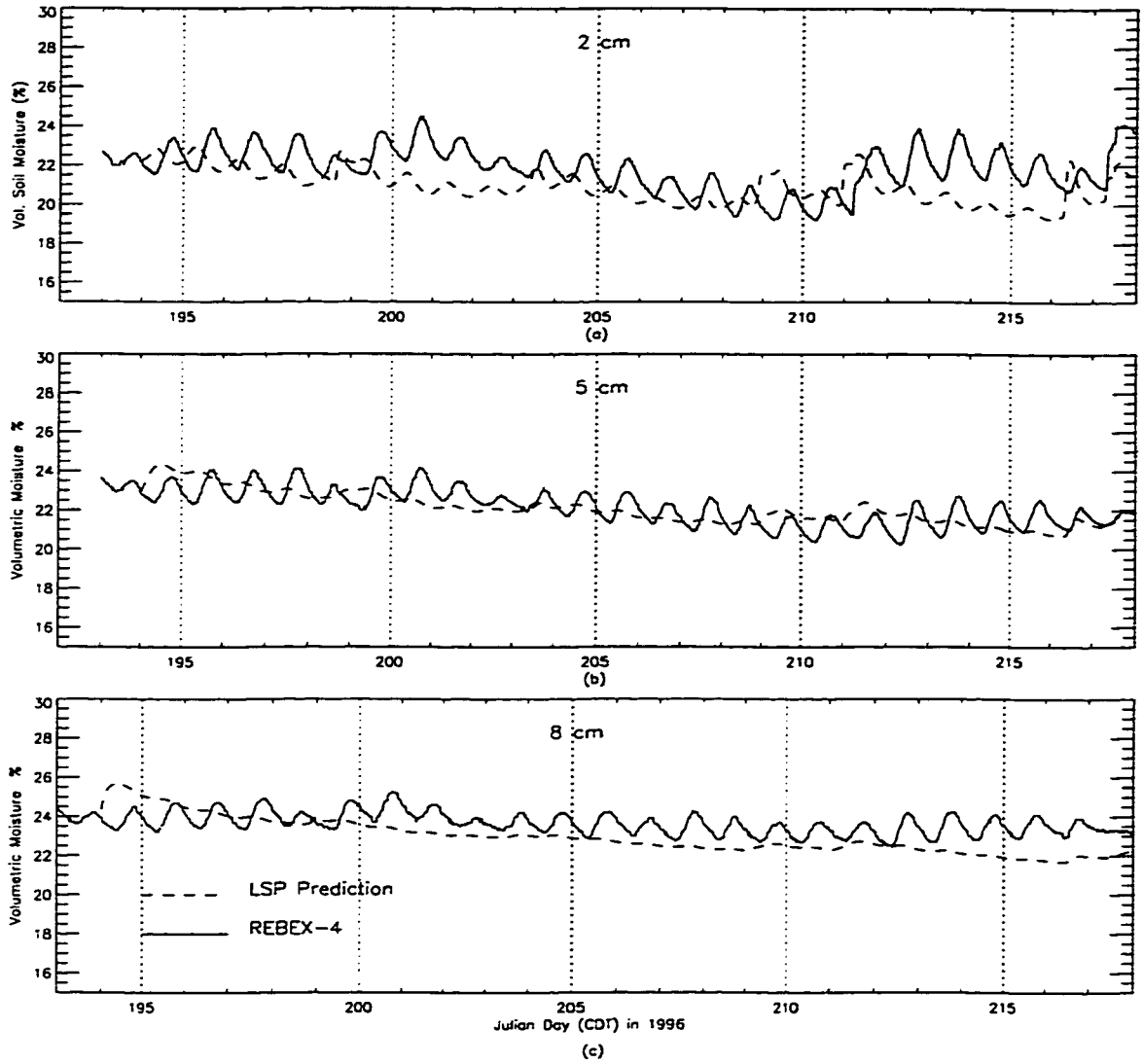

Figure 4.11: A comparison of the estimated and the observed soil moisture at (a) 2 cm (b) 5 cm and (c) 8 cm.

4.1.2 The R-Module

This section contains a description of the R-module calibration for bare soil and compares the results with the REBEX-4 field observations. The comparison was based only on the 19 GHz observations because lower frequencies are desirable for soil moisture applications [section 1.3.1].

4.1.2.1 Input Variables and Soil Properties

The R-module was run for the same 25 day period as the 1-dTH module (JD 193-218). It was forced with the temperature gradients, surface temperature, and moisture estimates from the 1-dTH module[2], as well as downwelling sky brightnesses. The sky brightnesses observed during REBEX-4 could not be used because of calibration problems at colder temperatures [111]. From our earlier studies, the sky brightnesses at 19 GHz were found to vary between 20-60 K, as estimated from the expressions given by Ulaby [200] using temperature and density profiles from rawinsonde data at Huron, South Dakota, about 200 km from the REBEX-4 site [71, 105]. The module brightnesses were 20 K for clear and 50 K for cloudy days.

The physical properties of soil were the same as the soil in the 1-dTH module [Table 4.1]. The dielectric constant for the dry soil solids was 4.0 [201]. The soil was specular, incoherent, multi-layer emitter with dielectric properties from Dobson et al.'s four-component mixing model [see section 1.3.1].

4.1.2.2 Comparison with Field Observations: Results and Discussion

Figure 4.12(a) shows the estimated and the observed V-pol soil brightnesses at 19 GHz. The module captures the diurnal variations in the brightnesses as suggested by low mean differences between the estimated and the observed brightnesses (Table 4.4). The estimates are brighter by ~10 K than the observed data during the day, but match fairly well during the night. This over-estimation could be explained by

[2]The R-module was not tested with the observed data, prior to calibration, due to lack of surface soil moisture observations.

the lower surface temperature estimates in the 1-dTH module. The lower estimated temperatures result in less negative temperature gradients[3] and higher brightnesses than those observed.

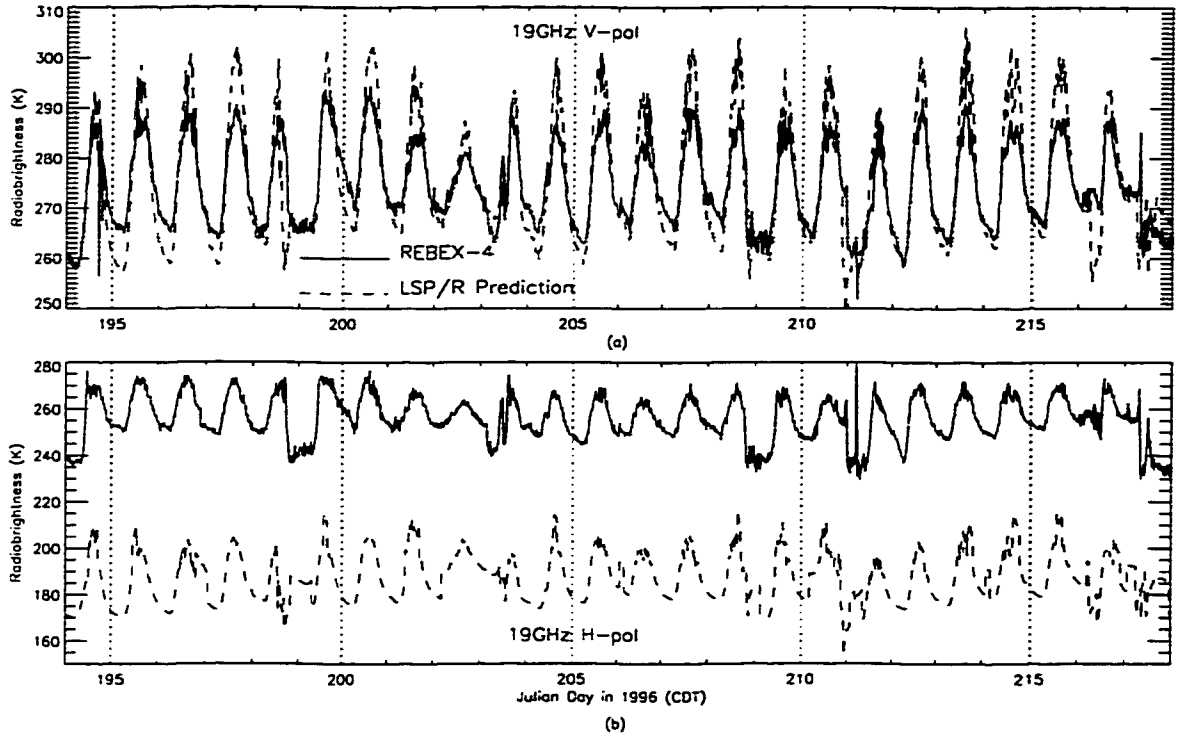

Figure 4.12: A comparison of the estimated and the observed brightnesses at 19 GHz using a smooth surface approximation for bare soil.

Figure 4.12(b) compares the estimated and the observed 19 GHz H-pol brightnesses. Although, the diurnal variations in the brightness are captured well, the module under-estimates mean brightnesses that are offset by ~70 K. V-pol estimates do not exhibit a similar discrepancy because the H-pol brightnesses are more sensitive to the soil moisture and surface features such as, roughness at the incidence angle close to Brewster angle. As mentioned earlier, in Chapter 3, the bare soil site

[3]Temperature gradient is defined positive toward the surface.

was artificially created by removing the vegetation and ploughing the ground. Although it was somewhat smoothed by disking, the surface was still rough with loose soil aggregates. Schmugge et al. [185] found similar large differences (~30 K) between the airborne observations at 1.4 GHz and the calculated brightnesses using the smooth-surface approximation. They attributed the differences to surface roughness. Later, Choudhury et al. [34] demonstrated that roughness effects could account for such large differences with their simplistic semi-empirical reflectivity model. The effects of soil roughness on microwave brightness is not well understood, particularly at the SSM/I frequencies, and only semi-empirical models exist. In the next section, I present a qualitative discussion on roughness effects and some of the often used models. The aim of the discussion is not to calibrate the R-module using these rough surface models, or to evaluate these models quantitatively, but to demonstrate surface roughness as a significant factor toward more realistic H-pol brightness estimates at the bare soil site, through the use of the models.

Polarization	Mean difference K	Standard Deviation K
V	0.5	5.82
H	-69.69	7.69

Table 4.4: Means differences and their standard deviations for the 19 GHz brightnesses using smooth surface approximation for bare soil. (Difference = Estimated-Observed).

Surface Roughness

The effects of soil roughness on microwave emission have been studied mostly for lower frequencies, viz., 1.4-10 GHz [180, 185, 34, 212, 141, 196], where the soil

moisture retrieval is most promising. In general, the roughness increases surface emissivity and brightness, with a larger increase for wetter soils [152, 34]. The most commonly used semi-empirical model at 1.4 GHz, developed by Wang and Choudhury [210], includes only coherent reflectivity. The Fresnel reflectivity is modified using two empirical parameters, roughness height h, and polarization mixing ratio Q. Both the parameters are obtained from measured data and are not physically realistic. The expression used to calculate reflectivity at polarization p is,

$$r_p(\theta) \;=\; [Q\; r_{0q}(\theta) + (1-Q)\; r_{0p}(\theta)]\; exp(-h\; G(\theta)) \qquad (4.3)$$

where, r_{0p} and r_{0q} are the Fresnel reflectivities at polarizations p and q, and G is a function of incidence angle ($= cos^2\theta$). Wang et al. modified the above expression using field data at 1.4, 5, and 10.7 GHz and found that the $cos^2\theta$ dependence for G was not realistic and used G=1 for their study [212]. Although, both h and Q increased with frequency, the dependence of Q was strong, while that of h was not. The values for h and Q varied between 0-0.6 and 0-0.3, respectively [212]. For 19 GHz, h=0.8 and Q=0.2 produced the best fit between the observed and the estimated soil brightnesses at H-pol during REBEX-4 [Figure 4.13]. The V-pol brightnesses remain largely unaffected with <5 K increase in diurnal amplitude.

Mo and Schmugge [141] improved upon the Wang and Choudhury's reflectivity model by integrating the bistatic scattering coefficient over the upper hemisphere with the incoherent scattering term included. Instead of polarization mixing ratios, they used the following semi-empirical function to estimate reflectivity r_p,

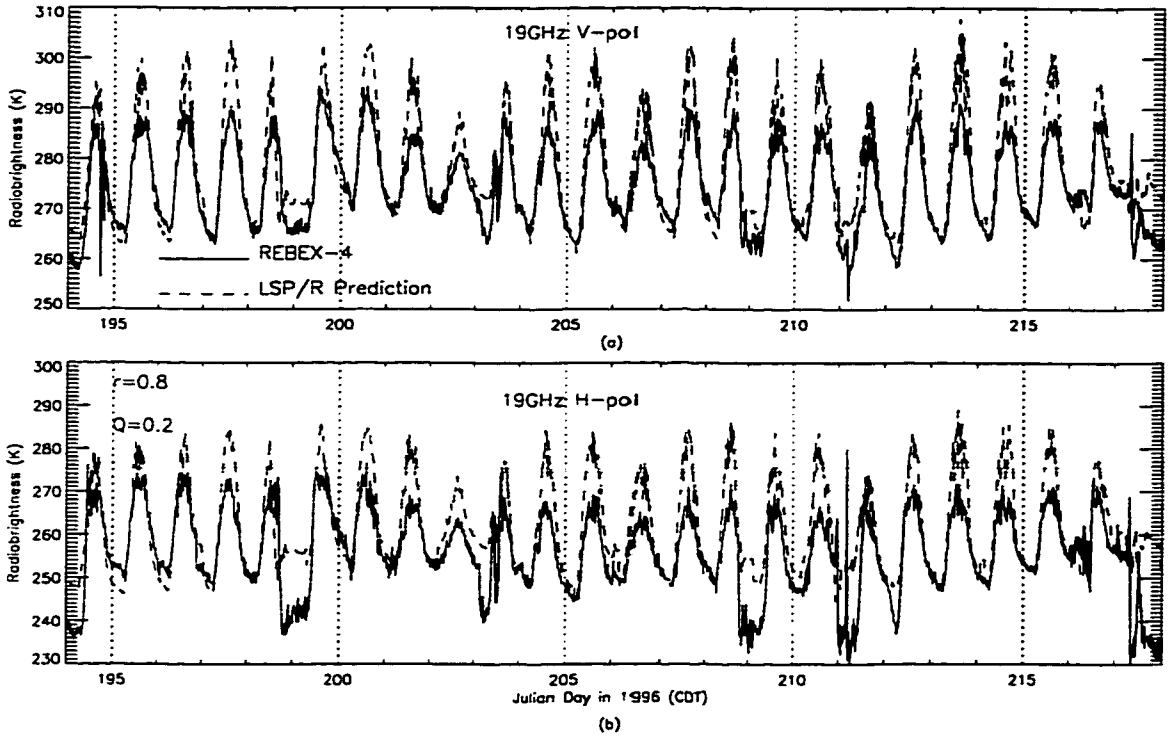

Figure 4.13: A comparison of the estimated and the observed 19 GHz brightnesses of bare soil using Wang and Choudhury's reflectivity model.

$$r_p(\theta) \;=\; r_{0p}(\theta)\; exp(-G)$$

where, r_{0p} is the Fresnel reflectivity at polarization p, $G = -ln[S(\theta)f(ks, kl, \theta)]$, $S(\theta)$ is the shadowing function, and f is a function of wave number k, standard deviation s, and the autocorrelation length of surface height l.

Recently, Wegmüller and Mätzler [214] used a similar theoretical strategy and extended the semi-empirical model to a wider frequency range of 1-100 GHz. They used about 1000 ground-based microwave measurements at incidence angles between 20° and 70° and achieved the following function to estimate rough bare soil reflectivities

[214],

$$r_h(m_v, ks, \theta) = r_{0h}\, exp\{-(ks)^{\sqrt{0.1cos\theta}}\} \tag{4.4}$$

$$r_v(m_v, ks, \theta) = r_h\, (cos\theta)^{0.655} \qquad \theta \leqslant 60° \tag{4.5}$$

$$r_v(m_v, ks, \theta) = r_h\, [0.635 - 0.0014(\theta - 60°)] \qquad 60° \leqslant \theta \leqslant 70° \tag{4.6}$$

Figure 4.14 shows the R-module brightness estimates using their semi-empirical model with ks=1. The H-pol brightnesses showed significant improvement when either of the rough surface models were used.

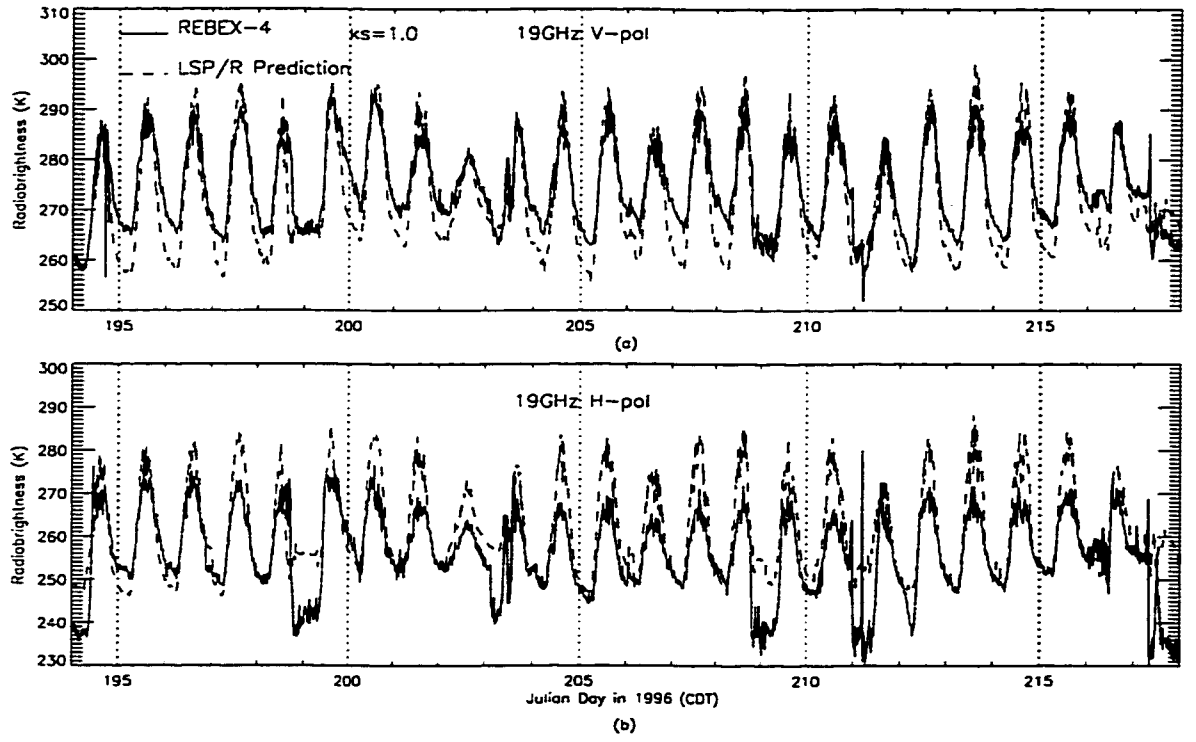

Figure 4.14: A comparison of the estimated and the observed 19 GHz brightnesses of bare soil using Wegmüller and Mätzler's semi-empirical model.

One of the major drawbacks of the existing semi-empirical models is the assumption of a normally-distributed, Gaussian surface. Most naturally occurring surfaces

are scaling surfaces, i.e., their power spectral density function is linear on a log-log plot, and cannot be described by a single correlation length or roughness height [4, 5]. The roughness phenomena or spectrum affecting brightnesses vary with different frequencies and one or two empirical parameters cannot be used over a wide range of frequencies [97]. A new model which is more physically realistic should be developed to further understand the effects of roughness on the microwave emission.

4.2 Brome Grass

4.2.1 The 1-dTH Module

In this section, I describe the calibration of the 1-dTH module for brome grass and compare the results with the field observations.

4.2.1.1 Simulation Period and Input Variables

The 1-dTH module simulated the land surface processes for 22 days from JD 196 (July 14) through 218 (August 5) in 1996. The module was forced with the same weather and downwelling radiance data as was used to force the 1-dTH module for the bare soil [Figures 4.1 through 4.3].

4.2.1.2 Initial and Boundary Conditions

The initial conditions for the canopy, thatch, and upper 64 cm of soil temperatures were obtained from REBEX-4. The temperatures for deeper layers were estimated from an annual model [123]. Initial canopy moisture and soil moisture for the upper

24 cm were obtained from a diurnal experiment conducted closest to the beginning of the simulation period, on JD 189 (July 7) [see section 3.1.3.2]. The moisture profile for the deeper layers was obtained using a similar strategy as in the bare soil model. Figures 4.15(a-b) show the initial temperature and moisture profiles used for the simulation. The upper and lower boundary conditions were the same as those in the bare soil module.

4.2.1.3 Canopy and Soil Properties

During the simulation period, the brome grass canopy was fully mature with an average height of 70 cm. In general, the Leaf Area Index (LAI) for mature grass canopies ranges between 2-4 [126]. After running the module with several LAI values, LAI=3.5 provided the best fit between the module estimates and the observations. Because the REBEX-4 grass site had been undisturbed for several years, the thatch was approximately 2-3 cm thick and accounted for ~25-30% of the canopy weight [see section 3.1.3.2]. Table 4.5 gives the canopy properties included in the module. The albedo of the canopy was estimated by curve-fitting the observed values for a clear and a cloudy day as done in the bare soil module (equation 4.7). Figure 4.16 shows the canopy albedo curves used in the module.

Properties	Values
LAI	3.5 [unconstrained parameter]
Root depth (cm)	25 [106]
Height(hc) (cm)	70 [106]
IR Emissivity	0.95 [195]
Roughness Length	0.2*hc [206]
Displacement height	0.65*hc [206]

Table 4.5: Canopy properties at the REBEX-4 grass site.

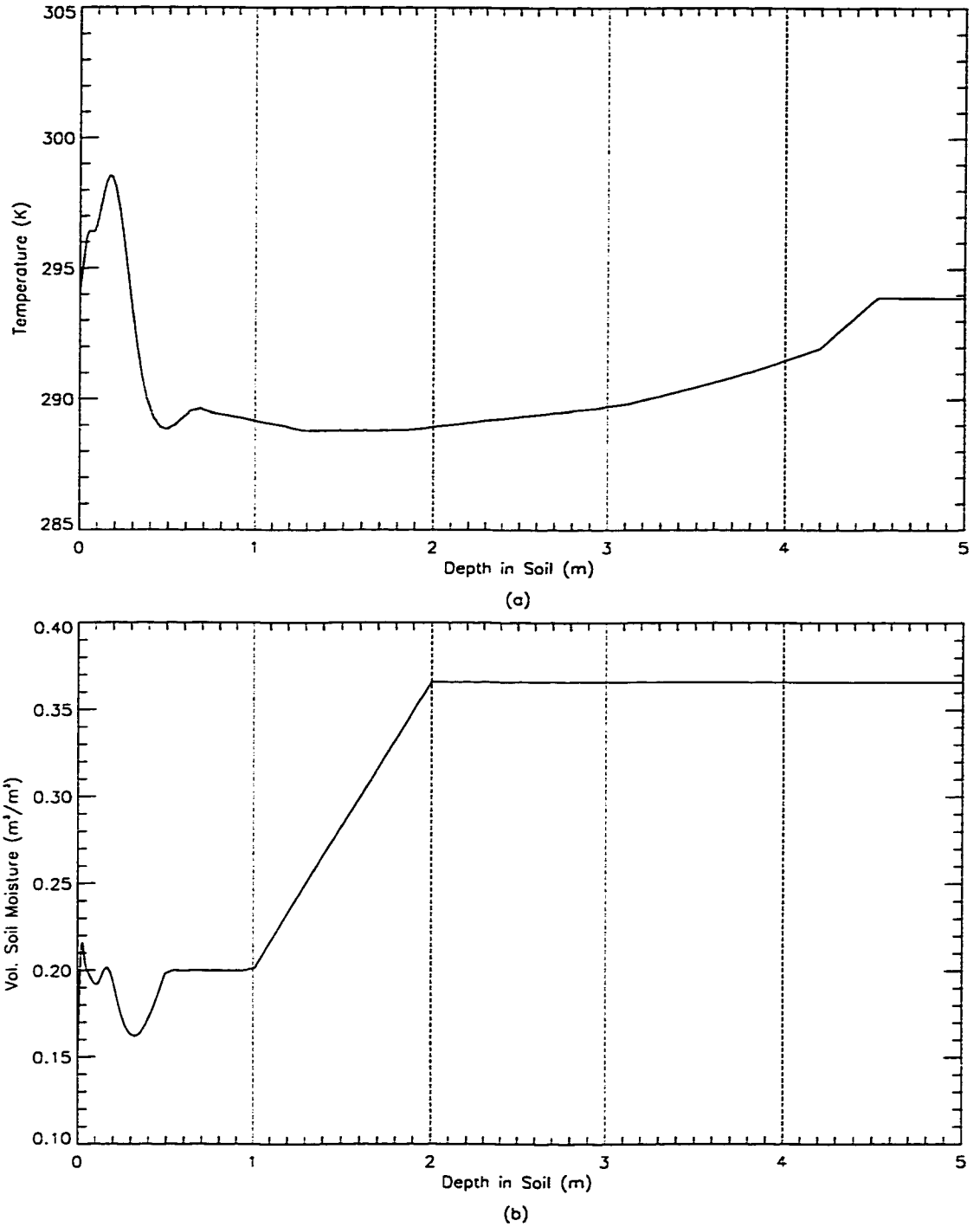

Figure 4.15: Initial conditions: (a)Temperature and (b) Moisture profile.

$$\begin{aligned} \text{for} \qquad & 0.15 \leqslant cosZ \leqslant 0.9, \\ alb_{cldy} &= 1.35 - 4.83\ cosZ + 6.82\ cos^2Z - 3.25\ cos^3Z \\ alb_{clr} &= 1.08 - 4.33\ cosZ + 6.97\ cos^2Z - 3.68\ cos^3Z \end{aligned} \tag{4.7}$$

where, alb_{cldy} and alb_{clr} are the albedos during cloudy and clear days, respectively, and Z is the solar zenith angle.

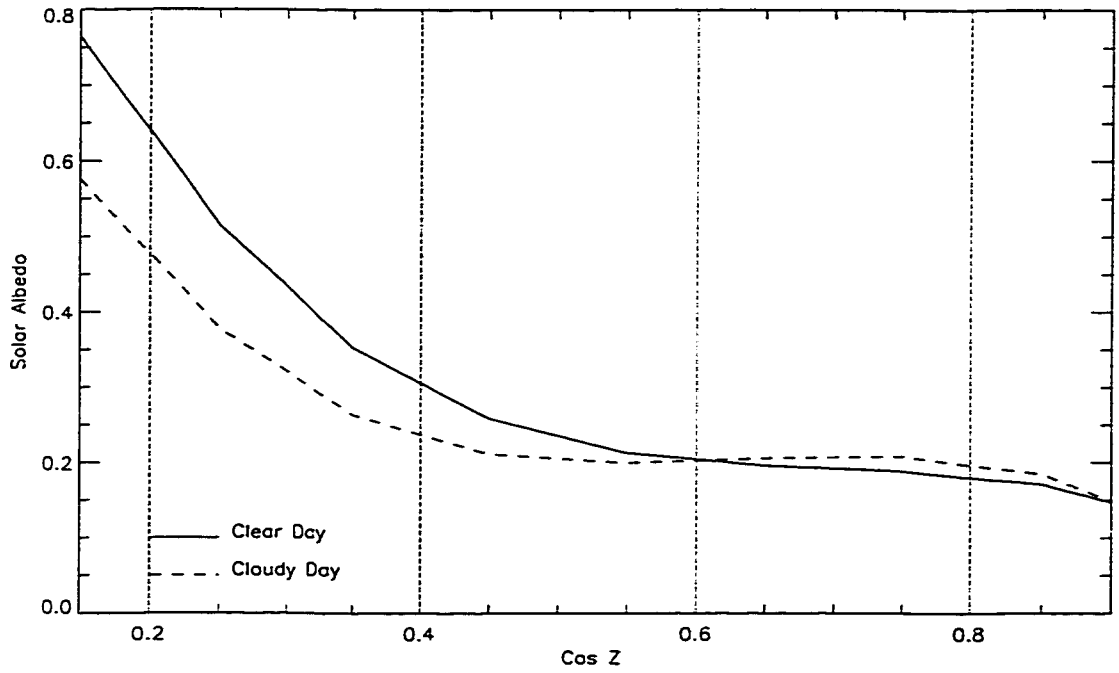

Figure 4.16: Solar albedo for brome grass during REBEX-4.

The soil at the grass site was the same as the bare soil site, except for the presence of organic material in the top 5 cm. The albedo of the soil was constant at 0.33. Table 4.6 gives the soil constituent fractions and porosities for the upper 5 cm.

Properties	Values	
	0-1 cm	1-5 cm
Silt fraction (%)	60	25
Clay fraction (%)	30	2.5
Sand fraction (%)	1	1
Organic matter (%)	8	71.5
Porosity (%)	60	50

Table 4.6: Soil properties (unconstrained parameters) in the upper 5 cm at the REBEX-4 grass site.

4.2.1.4 Comparison with Field Observations: Results and Discussion

Figures 4.17 and 4.18 compare the observed and the estimated temperatures of canopy, thatch, and soil at the depths of 2, 4, 8, 32, and 64 cm. The module canopy and thatch temperatures match the observed temperatures well, as indicated by the low mean differences in Table 4.7. Although the module estimates realistic diurnal variations in soil temperatures for the upper 16 cm, it under-estimates mean temperatures and amplitudes of the variations by ~5 K. The module may be over-estimating thermal inertia in soil due to high thermal conductivity and/or soil density. In the module, the lower layers (between 5 and 16 cm) of the soil did not have any organic matter, which would increase the thermal conductivity estimates. The under-estimated temperatures and amplitudes could also be an indication of unrealistic initial moisture profiles, because the soil moisture estimates could not be evaluated during the calibration due to sensor problems [see section 3.1.3.2] as well. The heat fluxes into the ground at 2 cm match the observed values well [Figure 4.19], which implies that the energy exchanges between thatch, canopy, and soil are being realis-

tically modeled, and that the correct amount of thermal energy is being transported into the soil. The temperature at the deeper layers of 32 and 64 cm compare well with the observed temperatures. Table 4.7 gives the mean differences and their standard deviations between the estimated and the observed temperatures and heat fluxes.

Depths	Mean	Standard Deviation
Canopy	0.30 K	2.80 K
Thatch	0.69 K	2.93 K
2 cm	-2.52 K	2.07 K
4 cm	-2.61 K	1.58 K
8 cm	-2.30 K	1.20 K
16 cm	-2.20 K	1.21 K
32 cm	-1.01 K	0.32 K
64 cm	1.00 K	0.26 K
Heat Flux (2 cm)	-2.36 (W/m^2)	27.32 (W/m^2)

Table 4.7: Mean differences and their standard deviations between the estimated and the observed temperatures and heat fluxes (Difference = Estimated-Observed).

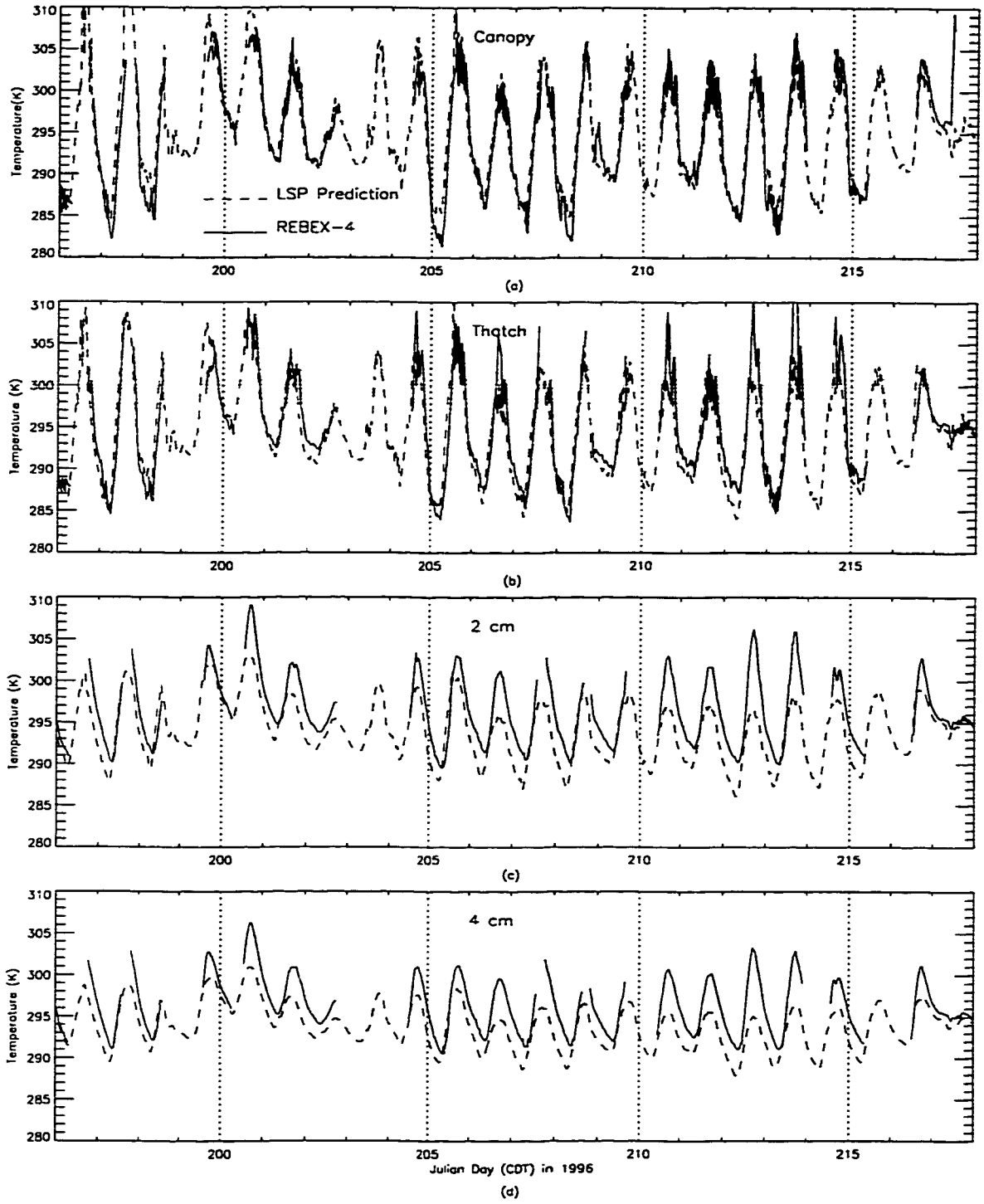

Figure 4.17: A comparison of the estimated and the observed temperatures at the grass site. (a) Canopy (b) Thatch, and Soil at (c) 2 cm (d) 4 cm.

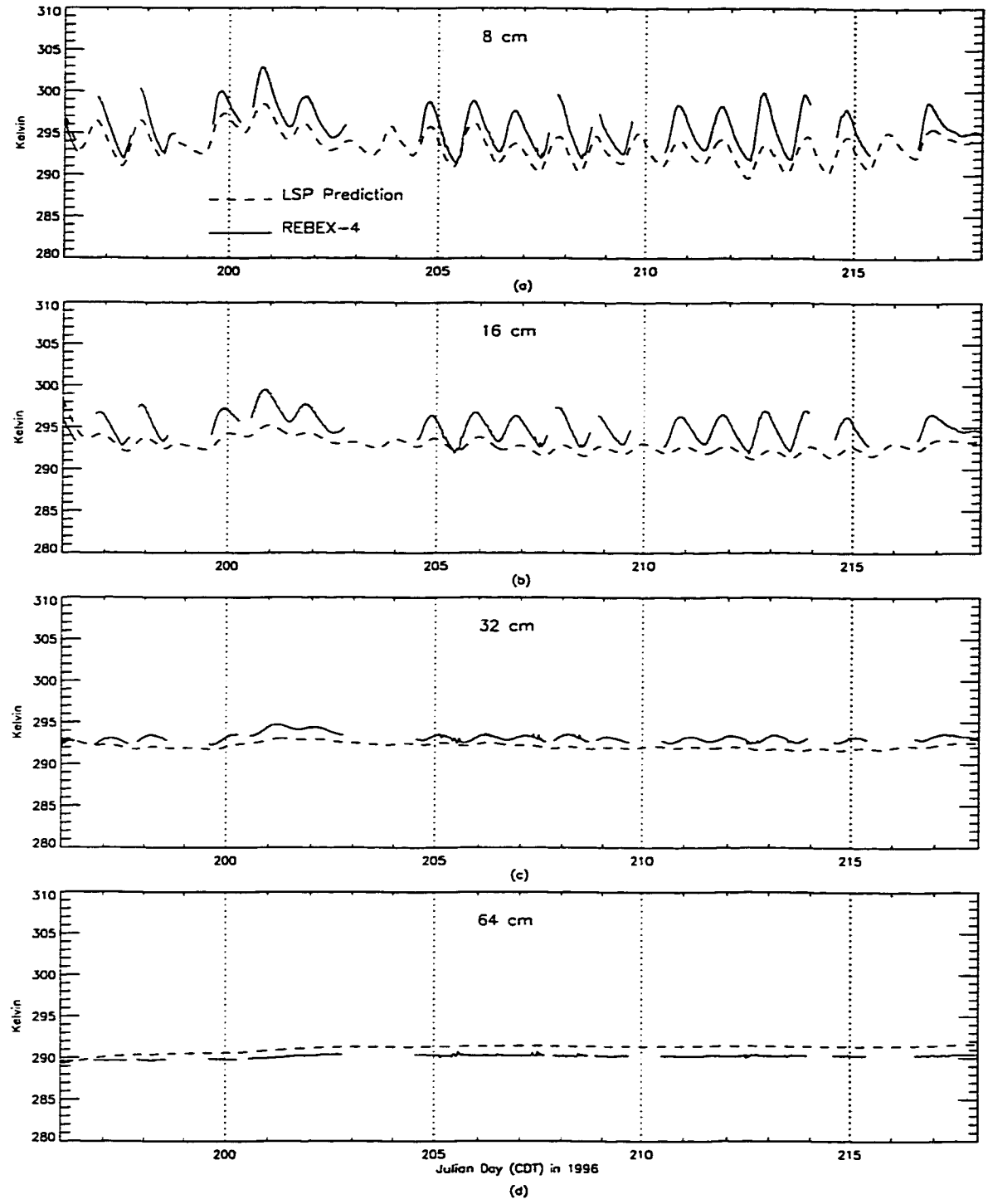

Figure 4.18: A comparison of the estimated and the observed soil temperatures at the grass site. (a) 8 cm (b) 16 cm (c) 32 cm and (d) 64 cm.

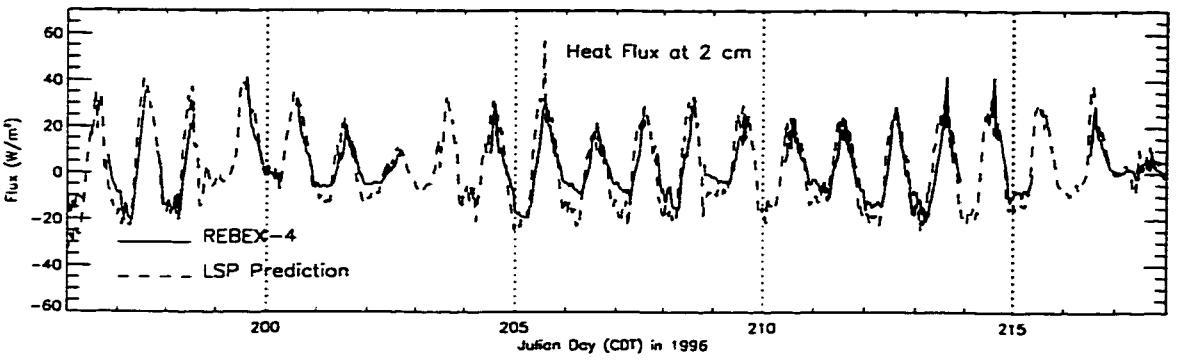

Figure 4.19: A comparison of the estimated and the observed heat fluxes into the ground at 2 cm for the grass site.

4.2.2 The R-Module

In this section, I describe the R-module calibration for brome grass and compare the model estimates of 19 GHz terrain brightnesses with the field observations.

4.2.2.1 Input Variables and Terrain Properties

The R-module was run for the same 22 day simulation period as the 1-dTH module, and was forced with the estimates of temperature gradients, temperatures, and moisture for the canopy and surface from the 1-dTH module. The sky brightnesses were the same as in the bare soil R-module.

The physical properties of the canopy and soil were the same as the 1-dTH module [Tables 4.6 and 4.5]. The dielectric properties of the canopy were estimated from a dual-dispersion model by Ulaby and El-Rayes as mentioned in section 2.1.2 and described in [122, 198]. The dielectric permittivity of the soil was from the mixing model used in the bare soil module.

4.2.2.2 Comparison with Field Observations: Results and Discussion

Figures 4.20(a-b) show the V and H-pol estimated and observed terrain brightnesses at 19 GHz. The estimated H-pol brightnesses match the observed brightnesses well, whereas the mean V-pol brightnesses are over-estimated by ~7 K [Table 4.8]. Approximately, 98% of the total emission at 19 GHz is from the canopy during the REBEX-4, when the canopy biomasses were up to 3 kg/m^2 and the optical thicknesses were ~2.7. The realistic estimates of the H-pol brightnesses reflect the accurate canopy moisture and temperature estimates by the 1-dTH module. The R-module estimates canopy emission independent of polarization, unlike the estimates for soil and reflected canopy and sky brightnesses. The soil surface contribution to the total emission is more at V-pol than H-pol in the presence of a significant canopy cover. Because the modeled soil surface is specular, the observed V-pol rough surface emissivities are lower than the modeled V-pol emissivities near the Brewster angle. This would account for the over-predictions of V-pol brightnesses by the model. Low brightnesses are observed on rainy days: JD 208, 209, 211, and 212 [Figure 4.20].

Polarization	Mean difference K	Standard Deviation K
V	6.36	4.38
H	0.89	4.44

Table 4.8: Means differences and their standard deviations between the estimated and the observed terrain brightnesses at 19 GHz for the grass site. (Difference = Estimated-Observed).

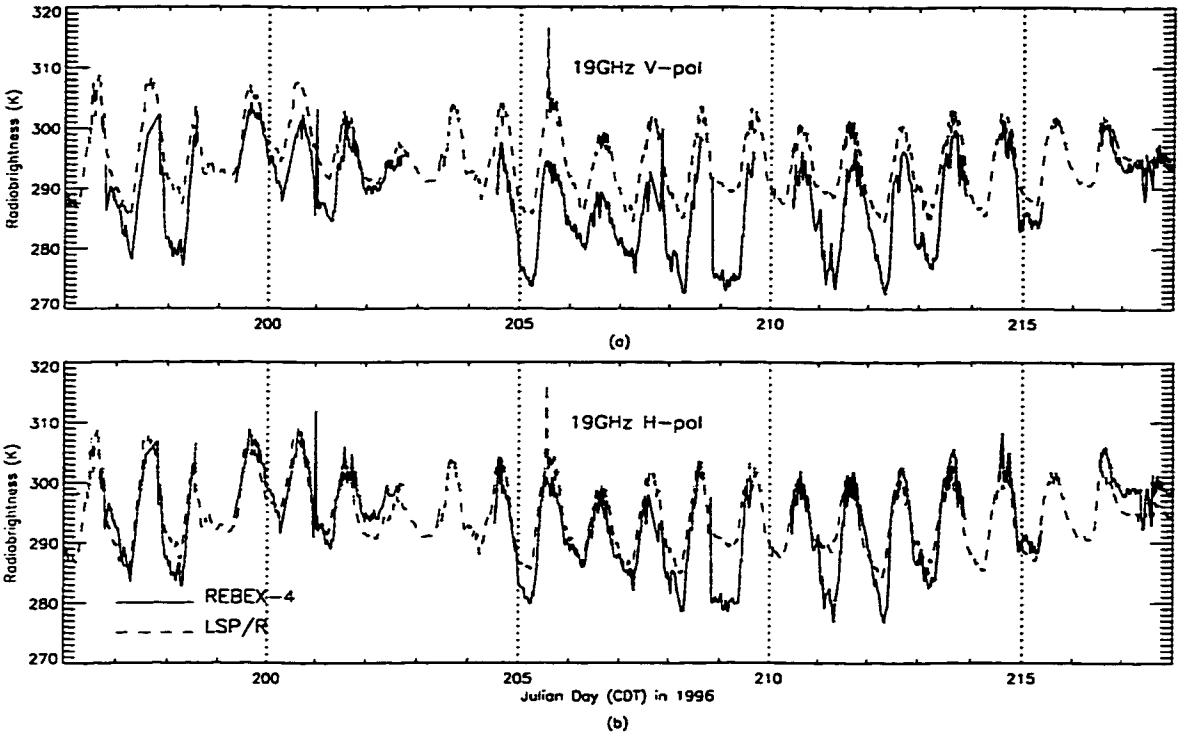

Figure 4.20: A comparison of the estimated and the observed terrain brightnesses at 19 GHz for the grass site.

4.3 Winter Wheat-Stubble

4.3.1 The 1-dTH Module

This section describes the calibration of the 1-dTH module for wheat stubble and compares the module estimates with the field observations [108].

4.3.1.1 Simulation Period and Input Variables

The wheat module was run for 16 days from JD 182 (July 1) through 198 (July 16) in 1997. Boundary forcings at the surface, viz., downwelling solar and long-

wave radiation, air temperature and relative humidity at 2 m, wind speed at 10 m, precipitation, and vapor pressure were obtained from observations during SGP'97 [98, 37, 119]. Figures 4.21 and 4.22 show the input forcings during the simulation period.

4.3.1.2 Initial and Boundary Conditions

Initial canopy moisture was the mean of the measured moisture from the two diurnal experiments during REBEX-5 [see 3.2.2]. The initial conditions for canopy temperature, and for soil moisture and temperature profiles for the upper 60 cm, were obtained from the SGP'97 measurements [191, 37, 119]. The temperature profile for the deeper layers was estimated from an annual model [123], while the moisture profiles were my best estimates using a similar strategy as in the bare soil module. Figure 4.23 shows the initial temperature and moisture profiles used for the simulation. The upper and the lower boundary conditions were the same as for the bare soil and the brome grass module, and are described in section 2.1.1.1.

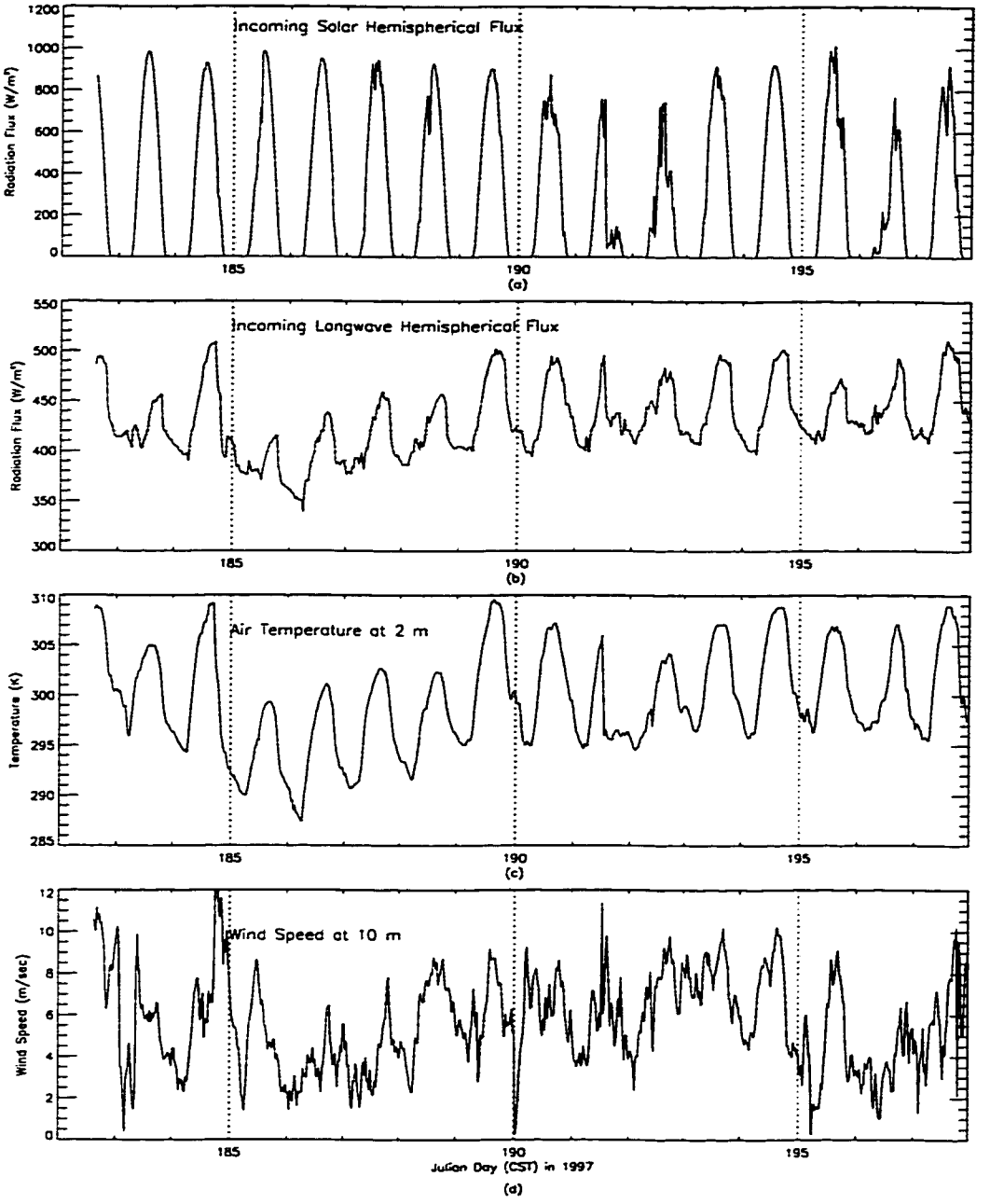

Figure 4.21: Weather forcings from SGP'97 for the wheat stubble simulation: (a) Downwelling solar radiation (b) Downwelling longwave radiation (c) Air temperature, and (d) Wind speed.

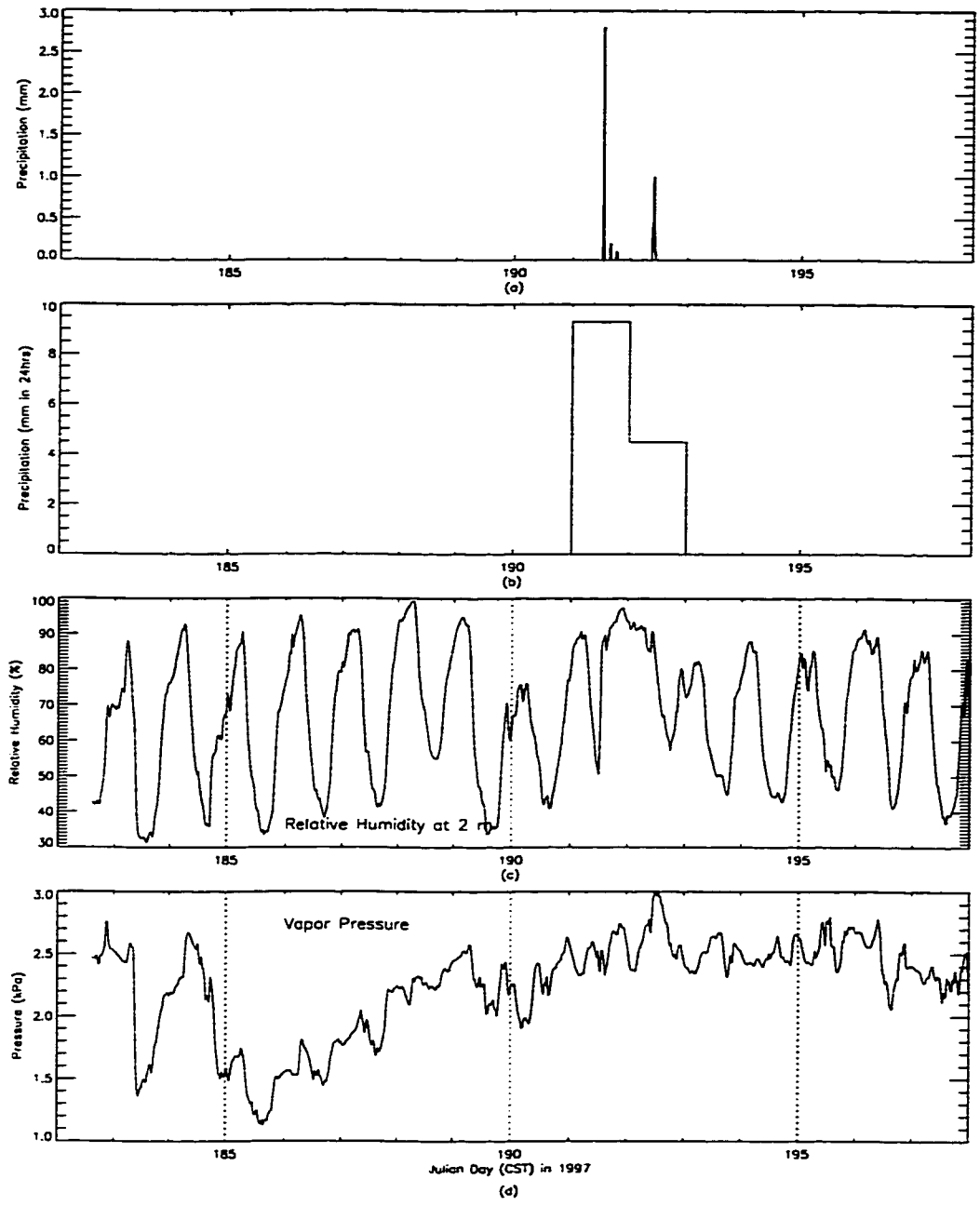

Figure 4.22: Weather forcings from SGP'97 for the wheat stubble simulation: (a) Precipitation (b) Cumulative precipitation (c) Relative humidity, and (d) Vapor pressure.

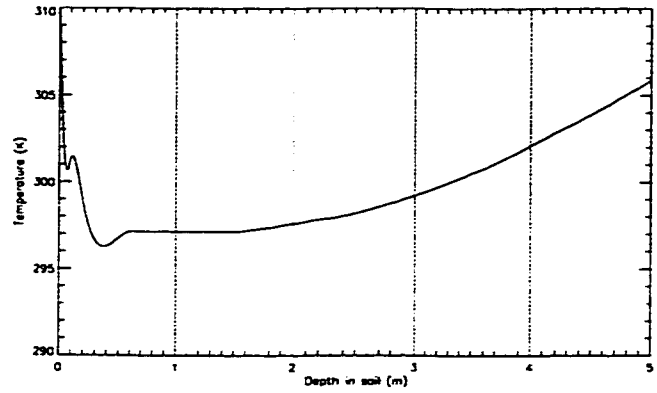

(a)

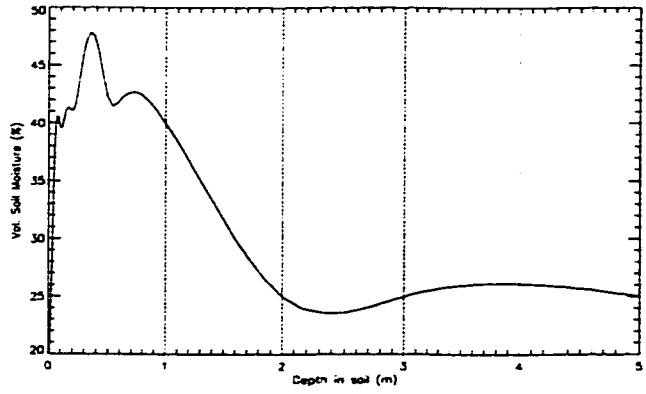

(b)

Figure 4.23: Initial conditions for the wheat stubble simulation (a) Temperature and (b) Moisture profile.

4.3.1.3 Canopy and Soil Properties

The canopy consisted of a layer of wheat-stubble, grass, and weeds overlying a layer of wheat-straw from the harvest. The canopy properties in the module are given in Table 4.9. The canopy albedo was obtained from the observed downwelling and upwelling solar fluxes measured during SGP'97. The Leaf Area Index (LAI) of

the canopy was an unconstrained parameter. The module was run for several LAI values, ranging from 0.4 to 1.0 [126], with 0.7 providing the best fit between the model estimates and the observations.

Properties	Values
LAI	0.7 (unconstrained parameter)
TIR emissivity	0.98 [195]
Root depth	10 cm [107]
Wet biomass	0.5 kg/m^2 [107]
Initial moisture	0.22 kg/m^2 [107]

Table 4.9: Canopy properties at the REBEX-5 site.

The soil properties are given in Table 4.10. The physical properties were obtained from [135]. The hydraulic and thermal properties were estimated in the same manner as in the bare soil module. The albedo of the soil was constant at 0.5.

Properties	Values
Silt fraction (%)	60
Clay fraction (%)	20
Sand fraction (%)	20
Porosity (%)	46
Field capacity (% by vol.)	0.20
Therm. cond. ($J/m.K.sec$)	1.6-2.75
Sat. hydr. cond. (m/sec)	$2x10^{-6}$-$6x10^{-8}$ (unconstrained parameter)

Table 4.10: Soil properties in the upper 10 cm at the REBEX-5 site.

4.3.1.4 Comparison with Field Observations: Results and Discussion

Figures 4.24 and 4.25 show the estimated and the observed canopy and soil temperatures. The module estimates diurnal variations and amplitudes for temperatures that match the observations well. The mean differences and their standard deviation between the estimated and the observed temperatures are given in Table 4.11. The

module also captures the moisture profiles in the deeper layers fairly well throughout the simulation period [Figure 4.27], but significantly under-estimates moisture in the upper layers (0-5 cm depth) until day 190 [Figure 4.26]. This is probably because of an unrealistic water retention curve used in the module. The measured retention curve could not be obtained from SGP'97 at the time of this dissertation. After day 190, the moisture estimates differ from the measurements by as much as 3% by volume. This difference is within the accepted range of experimental error during SGP'97 moisture measurements [37]. The mean differences and their standard deviations between the estimated and observed moisture values are given in Table 4.12.

Depths	Mean (K)	Standard Deviation (K)
Canopy	-0.27	1.81
3 cm	0.27	1.55
10 cm	0.03	0.86
20 cm	-0.02	0.64
40 cm	1.02	0.34
60 cm	-0.18	0.46

Table 4.11: Mean differences and their standard deviations between the estimated and the observed temperatures. (Difference = Estimated-Observed).

Depths	Mean % by vol.	Standard Deviation % by vol.
3 cm	-0.61	2.71
5 cm	-2.30	3.22
10 cm	-0.04	2.17
15 cm	0.61	1.8
20 cm	1.67	1.09
30 cm	-1.15	0.91

Table 4.12: Means and standard deviations of the differences between the estimated and the observed soil moisture. (Difference = Estimated -Observed).

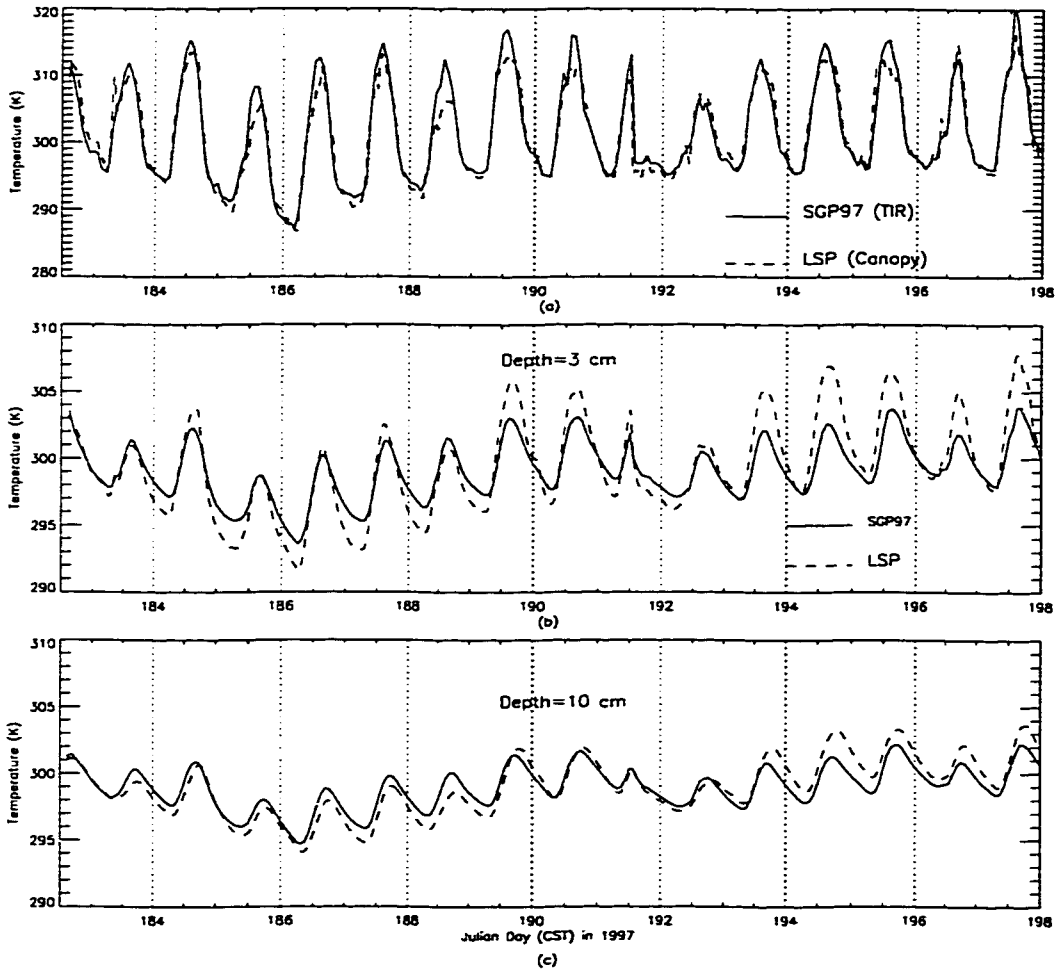

Figure 4.24: A comparison of the estimated and the observed temperatures for the wheat stubble. (a) Canopy (b) Soil at 3 cm, and (c) Soil at 10 cm.

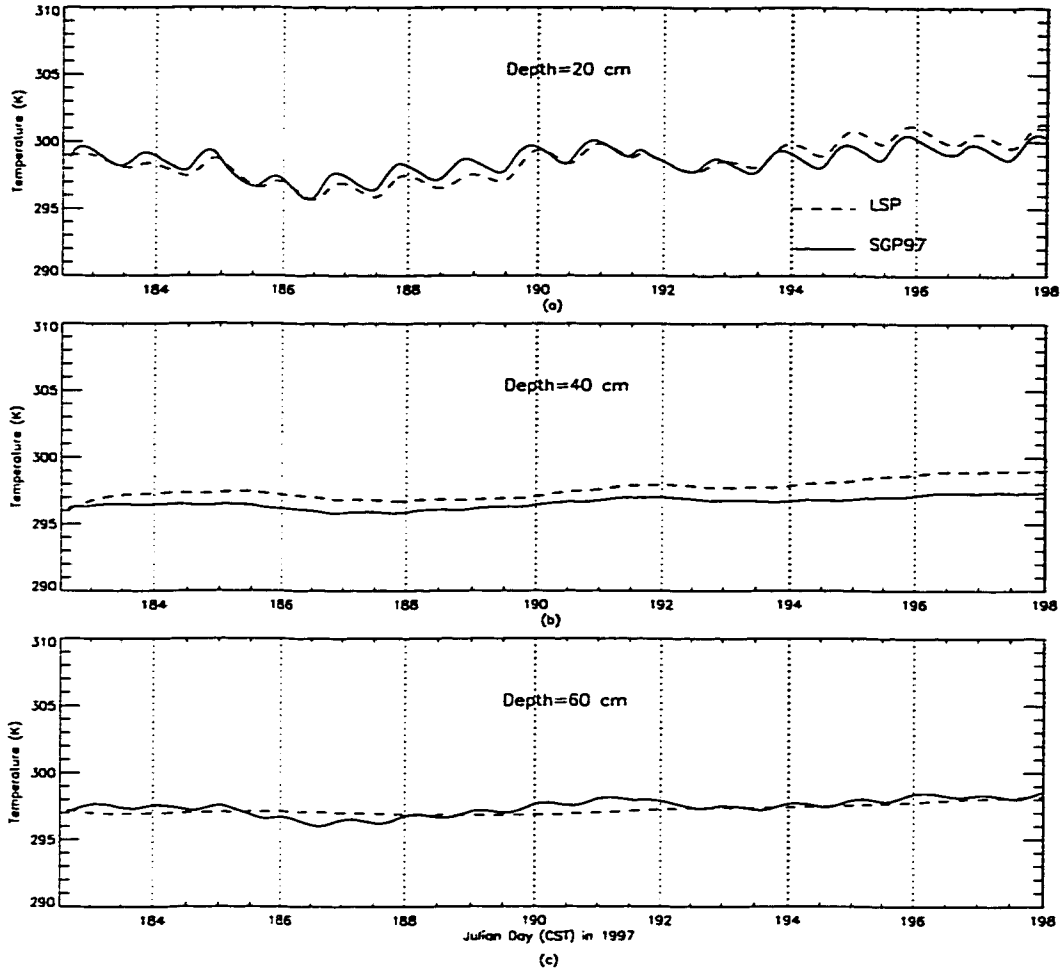

Figure 4.25: A comparison of the estimated and the observed soil temperatures for the wheat stubble. (a) 20 cm (b) 40 cm, and (c) 60 cm.

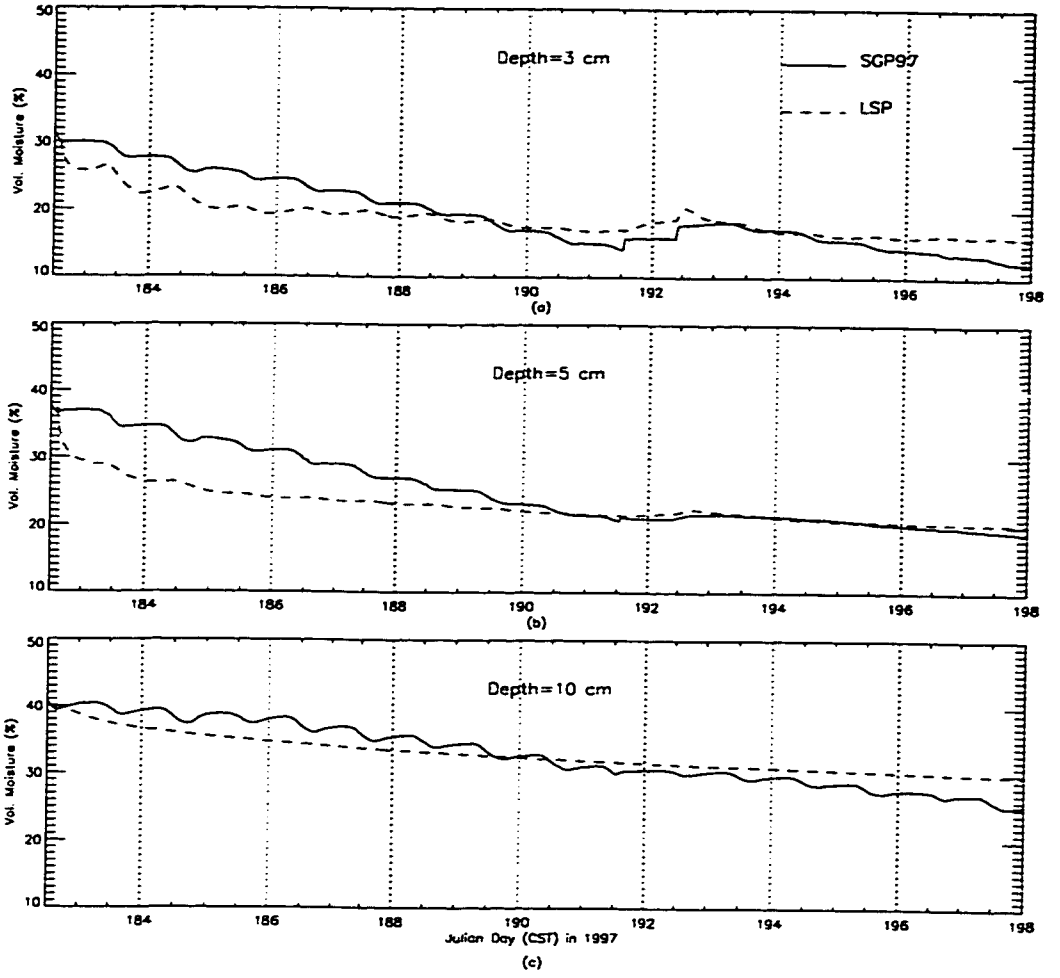

Figure 4.26: A comparison of the estimated and the observed soil moisture for the wheat stubble. (a) 3 cm (b) 5 cm, and (c) 10 cm.

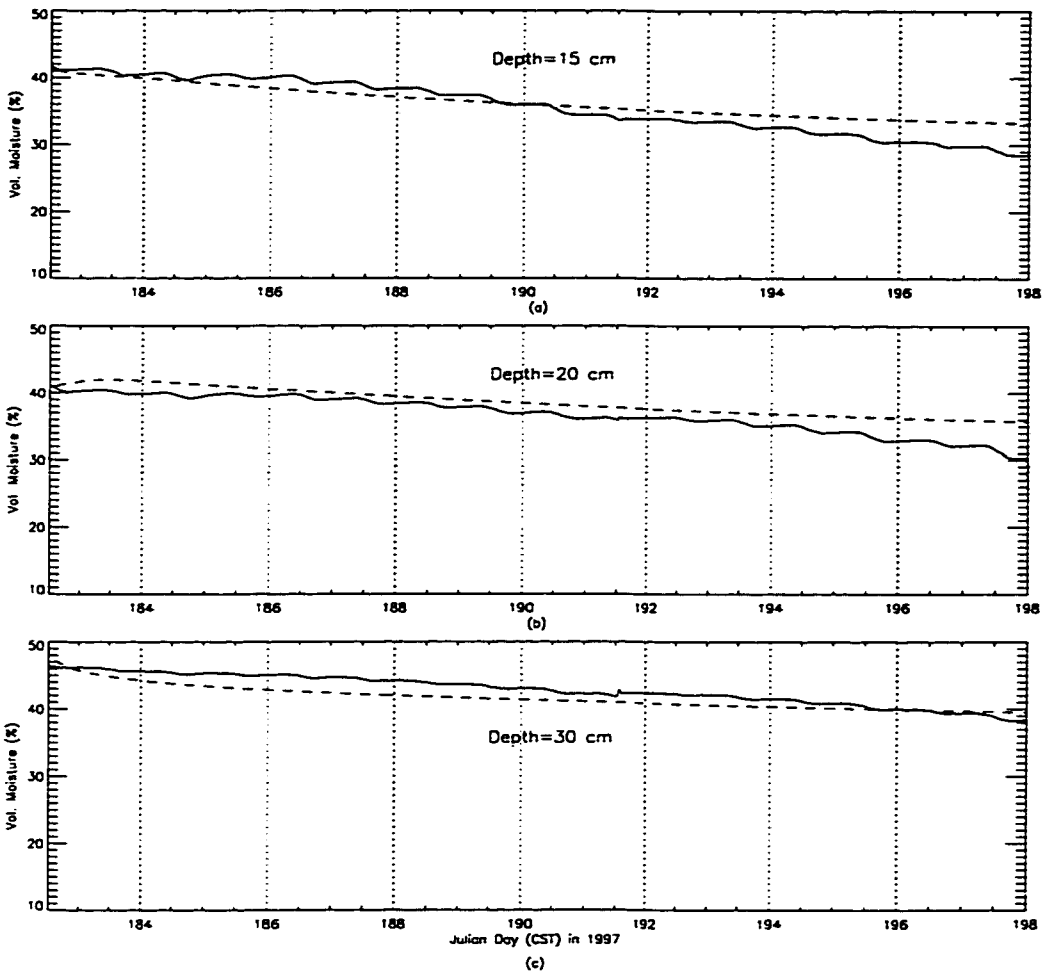

Figure 4.27: A comparison of the estimated and the observed soil moisture for the wheat stubble. (a) 15 cm (b) 20 cm, and (c) 30 cm.

4.3.2 The R-Module

This section describes the calibration of the R-module for wheat-stubble and compares its results with the observations.

4.3.2.1 Input Variables and Terrain Properties

The R-module was run from JD 182 through 191, constrained by periods of missing brightness data after day 191. The module obtained the temperature gradients, canopy and soil surface temperature and moisture estimates from the 1-dTH module. The dielectric properties of the canopy were from modified dual-dispersion model by Ulaby and El-Rayes [198]. In the dispersion model, the water is partitioned into bound-water (estimated by a sugar solution) and free water. It is unclear whether this is appropriate for inactive wheat-stubble. For simplicity, I assumed that all the water in the canopy was free water. The soil was a smooth-surfaced, incoherent, multi-layer emitter as in the grass model.

4.3.2.2 Comparison with Field Observations: Results and Discussion

Figure 4.28 show the estimated and the observed V and H-pol terrain brightnesses at 19 GHz. The module gives realistic estimates for the brightnesses at both polarizations as given by the low mean differences and their standard deviations in Table 4.13. The sensitivity of the H-pol brightnesses to soil moisture for the given canopy biomass is approximately 2 K/% by volume, so that a mean difference of 3.1 K in the brightnesses translates to a 1.6% by volume error in the soil moisture. Differences between the estimated and observed H-pol brightnesses are largely due to errors in the near-surface soil moisture estimates. The V-pol brightnesses are less sensitive to soil moisture because their incidence angles are close to the Brewster angle. Some of the differences may be a result of the smooth surface approximation in the R-module.

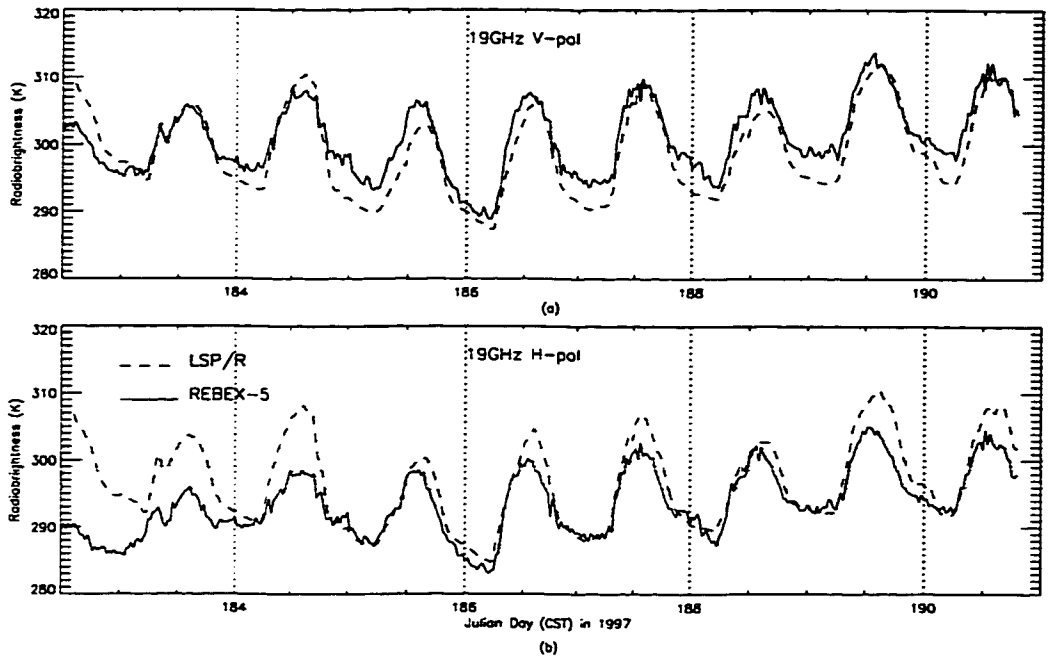

Figure 4.28: A comparison of the estimated and the observed terrain brightnesses at 19 GHz for the wheat stubble.

Polarization	Mean difference K	Standard Deviation K
V	-1.8	2.32
H	3.1	3.58

Table 4.13: Means differences and their standard deviations between the estimated and the observed terrain brightnesses at 19 GHz for the wheat stubble. (Difference = Estimated-Observed).

4.4 Terrain Brightness vs. Soil Moisture

The 19-GHz brightnesses observed at the three experimental sites were compared with the model estimates of soil moisture to understand how the sensitivity of brightnesses to soil moisture varies for different terrains. Figures 4.29(a) and (b) show the

respective V and H-pol brightnesses as functions of the water column in the upper 1 cm of the soil. As expected, V-pol brightnesses are less sensitive to soil moisture than H-pol brightnesses for bare soil because of the nearness of the incident angle to the Brewster angle, where V-pol emissivity is independent of moisture content. Moisture sensitivity in brome grass is almost polarization-independent because the $\sim$ 3 kg/m^3 canopy was nearly optically thick. Moisture sensitivity for wheat stubble is also polarization independent probably because dry, inactive stubble acts as a rough surface emitter.

Because the optical thickness of the grass canopy was greater than that of wheat-stubble, I had anticipated that the brightness moisture sensitivity to be the highest for bare soil, intermediate for wheat-stubble, and the lowest for grass. Figure 4.29(b) shows similar sensitivities for grass and wheat-stubble, with increased sensitivity under low soil moisture conditions for grass. It is possible that we are observing the dynamics of the canopy's response to low soil moisture. Under these conditions, the canopy ceases to take water from the soil and minimizes its transpiration to the atmosphere.

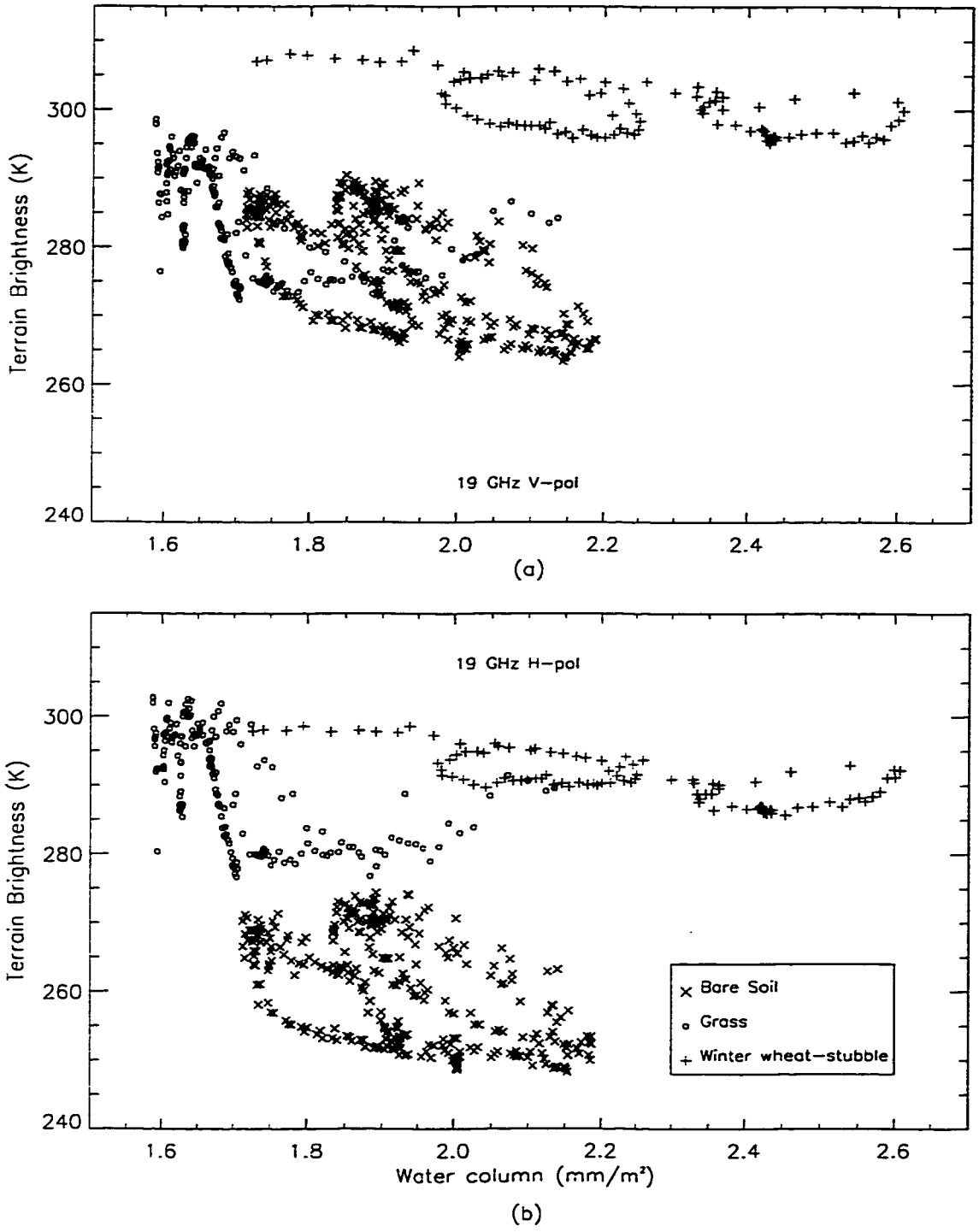

Figure 4.29: 19 GHz brightnesses observed at the bare soil and the grass sites during REBEX-4, and at the winter wheat-stubble site during REBEX-5, as functions of the water column in the upper 1 cm of soil. (a) V-pol (b) H-pol.

4.5 Summary

- The LSP/R model achieved convergence with respect to the time steps and number of nodes after 5 days. For all of the model simulations, the time step was 3 seconds and the total number of nodes was 61, and 8 of these nodes were located in the upper 5 cm of the soil.
- The LSP/R model was calibrated for bare soil, brome grass, and winter wheat-stubble using the data from the REBEX-4 and REBEX-5 experiments.
- For the bare-soil case, the model estimates of soil temperature and moisture profiles compared well with the observations. The model surface temperature was under-estimated by as much as ~10 K because the thermal conductivity estimates did not account for inter-particulate radiative transfer within the soil surface. The 19 GHz V-pol brightnesses were less sensitive to the soil conditions than the H-pol brightnesses. The specular surface approximation in the R-module under-predicted the H-pol brightnesses by ~70 K. Surface roughness was demonstrated as one of the major causes for this underprediction. The brightnesses appeared more realistic when two semi-empirical surface roughness models were incorporated in the R-module.
- For the brome-grass case, model estimates of canopy and thatch matched the observations well, with mean differences and standard deviations of less than 1 K and 3 K, respectively. Soil temperature estimates in the

upper 16 cm of the soil exhibited less diurnal amplitudes than those observed due to high thermal conductivity and/or intrinsic density of the modeled soil. Soil moisture profiles could not be evaluated with the limited available moisture data. R-module predictions of the 19 GHz H-pol brightnesses matched the observations well, with mean differences of less than 1 K. I conclude that 19 GHz brightnesses are insensitive to the grass canopy structure for biomasses $\sim 3\ kg/m^2$, and that a "cloud" model of the canopy is adequate to estimate 19 GHz brightness. V-pol brightnesses were over-estimated by as much as 6 K, most likely due to the specular surface approximation in the R-module.

- For the wheat-stubble case, the model temperature profiles matched the observed profiles well. Soil moisture profiles for the upper 5 cm were under-estimated by as much as ~ 3 % due to unrepresentative soil water retention curves estimated by the two-parameter junction model. The brightness predictions by the R-module were higher than those observed due to the soil moisture under-estimation.

- The 19 GHz H-pol brightness was found to be most sensitive to the surface moisture in bare soil. The grass exhibited larger sensitivity at lower surface moisture. The wheat-stubble showed very low sensitivity to surface moisture.

CHAPTER 5

Ground-based vs. Satellite Terrain Brightnesses

In this chapter, I compare the terrain brightnesses observed during REBEX-4 and REBEX-5 with those observed from the Special Sensor Microwave/Imager (SSM/I), and discuss implications of the results.

5.1 Observations from the SSM/I

The SSM/I is a seven-channel, four-frequency dual polarized[1] microwave radiometric system [90] launched by the Defense Meteorological Satellite Program (DMSP) aboard six platforms; F8, F10, F11, F12, F13, and F14. It measures brightness temperatures at 19.35, 22.2, 37.0, and 85.5 GHz at an incidence angle of 53.1°. The satellite operates in a sun-synchronous near-polar orbit. Each conical scan consists of 128 observations at 85 GHz and 64 observations at all other frequencies, with a separation between the scan rows of 12.5 and 25 km, respectively. Figure 5.1 shows the scan geometry of the SSM/I. It makes 14 revolutions covering a swath of 1400

[1]Only V polarized at 22 GHz.

km every 24 hours [168]. Detailed descriptions of the SSM/I instrumentation and radiometer specifications are given in [51, 91, 89, 90, 145]. Data from the SSM/I were archived in Temperature Data Record (TDR) format by the NASA Marshal Space Flight Center (MSFC) Distributed Active Archive Center (DAAC) till March 1997, and are now archived at NOAA Satellite Active Archive (SAA) by the National Climatic Data Center (NCDC).

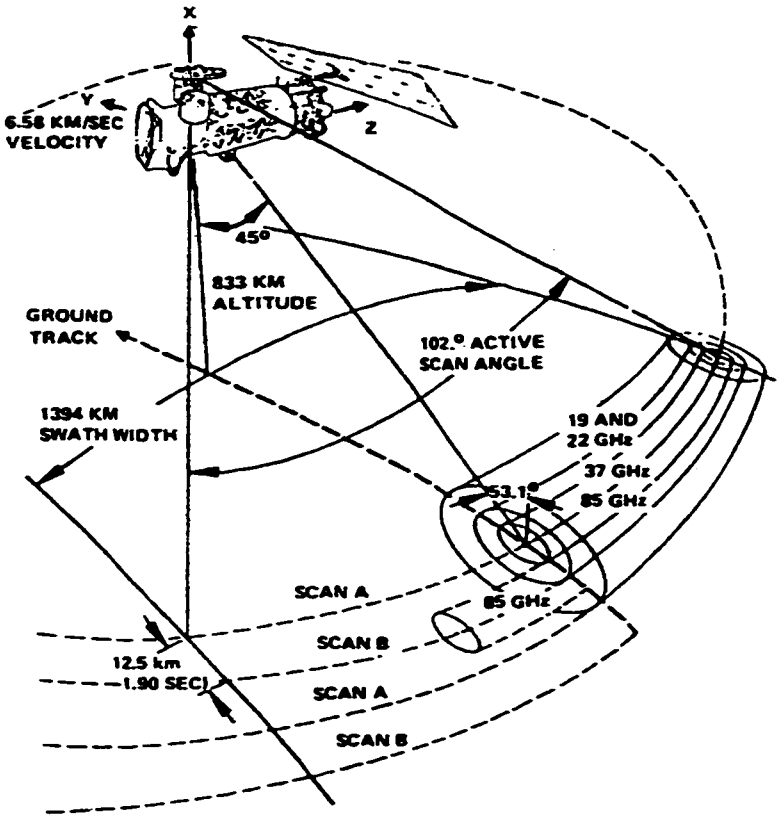

Figure 5.1: Scan geometry of the SSM/I [168].

The satellites F10, F11, and F13 were operational during REBEX-4, and F14 became operational during REBEX-5. The data from F10 were unusable because the satellite orbit had high eccentricity, and were not used in this investigation. The SSM/I data processing was conducted in two steps. The first step was to subset the

global data obtained from the TDR antenna temperature tapes to a localized region around the field-sites. This was done primarily to decrease hard-drive space requirements and computing time for further processing. The second step was to resample the subsetted antenna temperatures[2] to a fixed geolocation and spatial resolution for all frequencies. The resampling was necessary to compare data from different frequencies because the fields of view of the radiometers vary with frequency. It was also important for conducting temporal studies using the same frequency because the scans are shifted and do not observe the same pixels during their twice-daily local coverage. They repeat approximately every 16 days [168]. The resampling software used in this dissertation was a customized version [156, 111] of the Equal Area Scalable Earth-Grid (EASE-Grid) developed by National Snow and Ice Data Center (NSIDC) [145] with help from Galantowicz and England [71, 70]. The EASE-Grid is an application of Backus and Gilbert inversion technique [8] described by Stogryn [193] and Poe et al. [168]. Figure 5.2 shows an example of a daily EASE-Grid image.

Because the field sites were located in the mid-latitude region, I used a cylindrical projection [see Figure 5.2] [145, 23] to calculate the row and column for EASE-Grid pixels that would include the sites [see equations 5.1 and 5.2].

$$row = -\frac{R}{C}\frac{sin\theta}{cos30^\circ} + row0 \tag{5.1}$$

$$column = \left[\frac{R}{C}\,\phi\, cos30^\circ\right] + col0 \tag{5.2}$$

[2]In this chapter, the terms "antenna temperature" and "brightness temperature" are used synonymously. One can correct the observed antenna temperatures to account for the energy from the side-lobes, from cross-polarization coupling, and from spillover loss, to estimate effective brightness temperatures as described by Wentz [215]. This correction has not been tested extensively and was not used in this thesis.

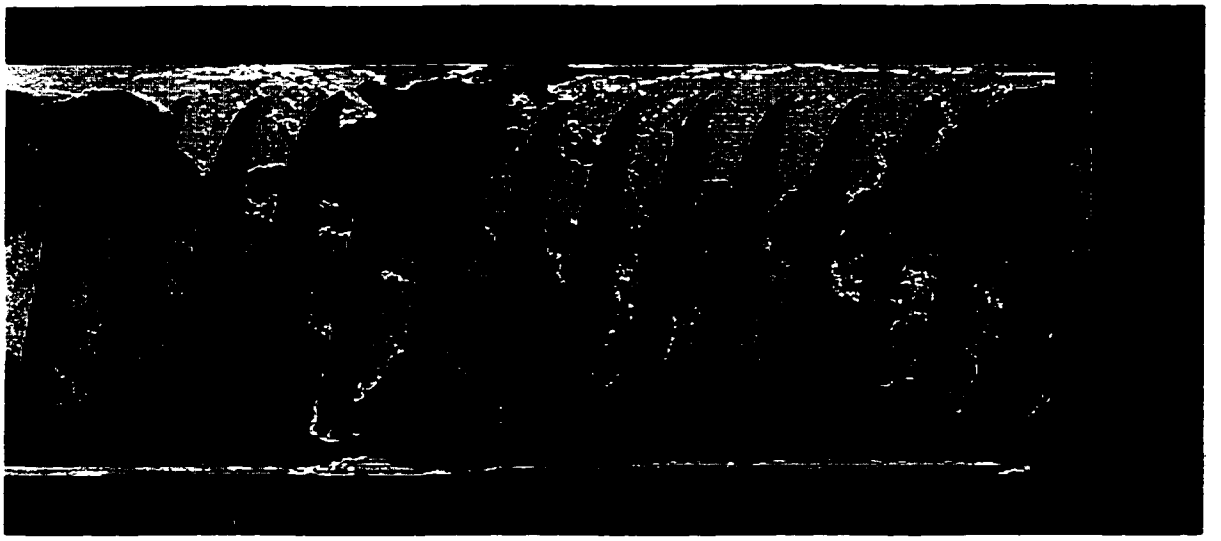

Figure 5.2: An example of 19 GHz H-pol EASE-Grid brightness temperatures during a descending pass using the cylindrical projection from the NSIDC. [145]

where,

- R is the radius of earth = 6371.228 km,
- C is the nominal cell size = 25.067525 km,
- θ and ϕ are the latitude and longitude, respectively (radians),
- $row0 = 292.5$ and $col0 = 691$.

5.2 Ground-based vs. EASE-Grid Brightnesses: Results

In this section, I compare the ground-based brightnesses observed during REBEX-4 and REBEX-5 with the satellite observations to demonstrate how well the field sites represented their corresponding SSM/I pixels. The satellite brightnesses are spatially averaged over pixel sizes of hundreds of kilometers. Future assimilation of

these brightnesses to improve soil moisture retreival require investigating the effects of significantly varying land-cover within the pixel, even in relatively homogeneous regions.

5.2.1 REBEX-4

The REBEX-4 site (43.7 N, 96.6 W) was included in the EASE-Grid pixel corresponding to row 89 and column 319. Figure 5.3 shows the exact location of the site within the pixel. Bare soil brightnesses at 19 GHz were compared with the EASE-Grid SSM/I brightnesses from JD 193 to 226 in 1996. Data at 37 GHz were not available for the comparison due to hardware problems [see section 3.1.3.1]. Brightnesses at 19 and 37 GHz from the grass site were compared with the EASE-Grid brightnesses from JD 153 to 268 in 1996. Figures 5.4(a-b), 5.5(a-b), and 5.6(a-b) show the results of the comparison. Figures 5.5(a) and (b) present the comparison during the period when the bare-soil brightnesses were available. As expected, brightnesses of the grass site are consistently higher than those of the bare-soil due to emission from the vegetation.

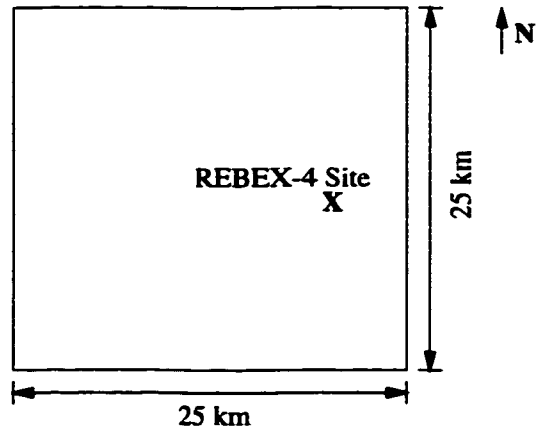

Figure 5.3: Location of the REBEX-4 site within the EASE-Grid pixel.

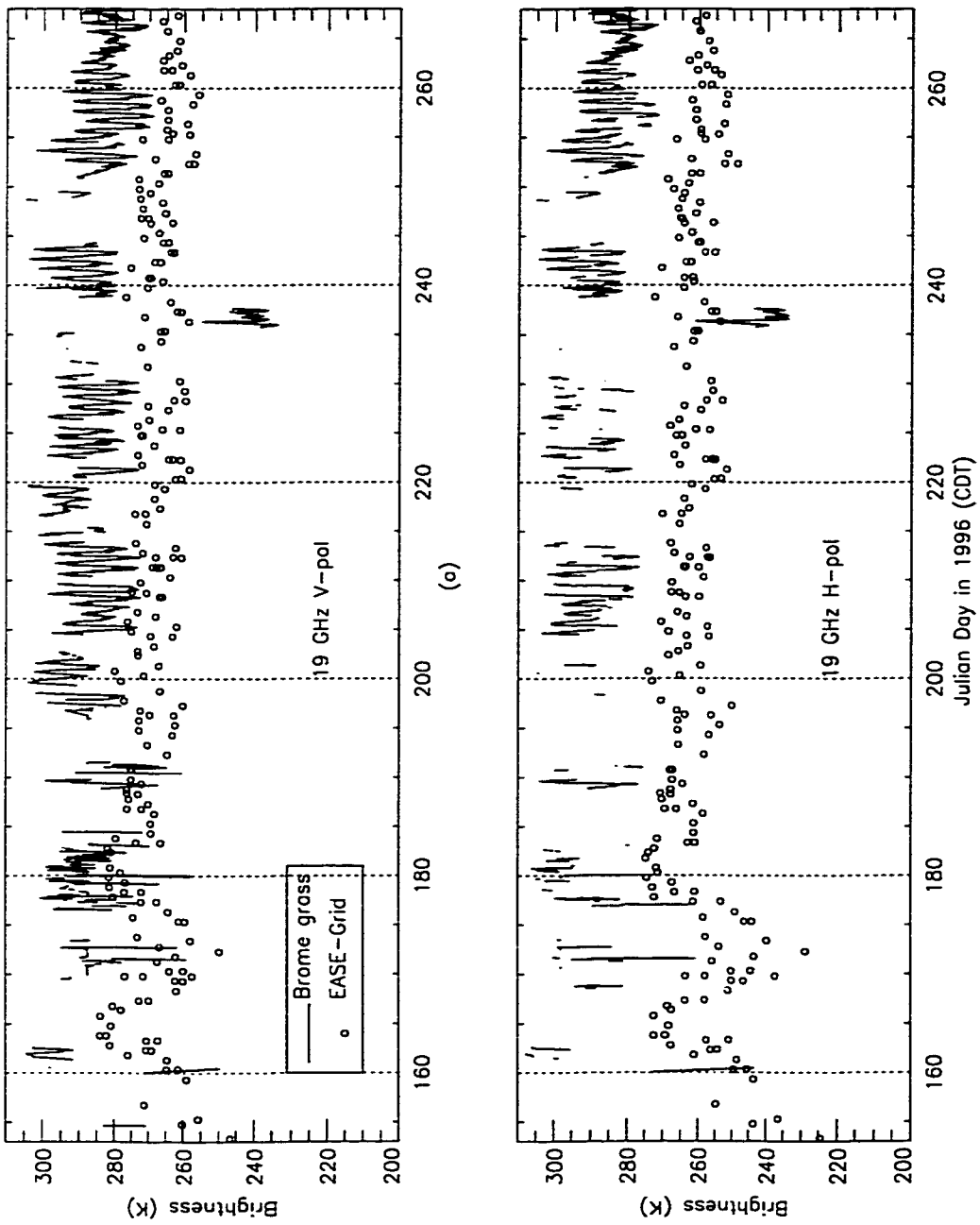

Figure 5.4: A comparison of the REBEX-4 brightnesses of brome grass with the EASE-Grid brightnesses. (a) 19 GHz V-pol (b) 19 GHz H-pol

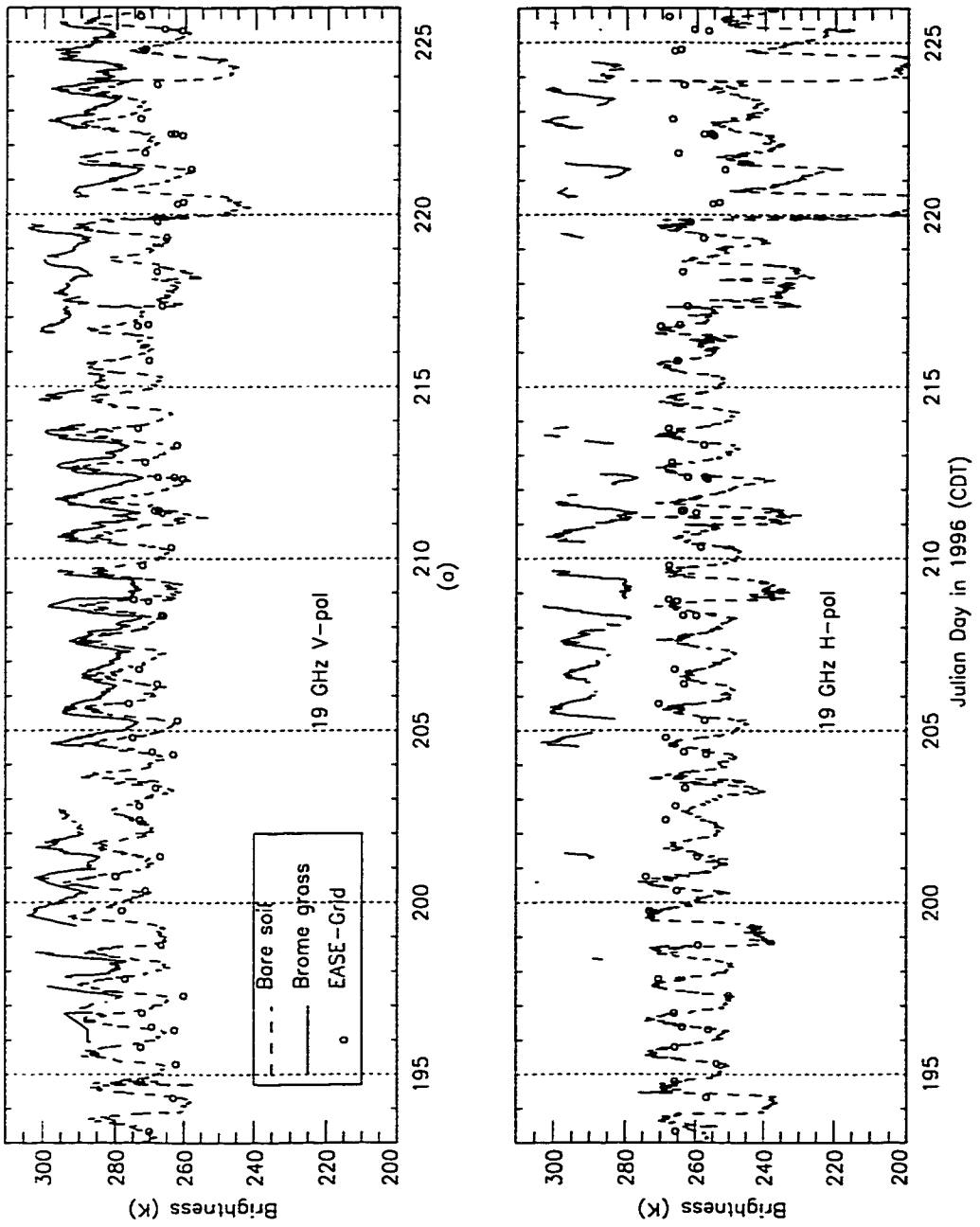

Figure 5.5: A comparison of the REBEX-4 brightnesses of bare soil and brome grass with the EASE-Grid brightnesses. (a) 19 GHz V-pol (b) 19 GHz H-pol

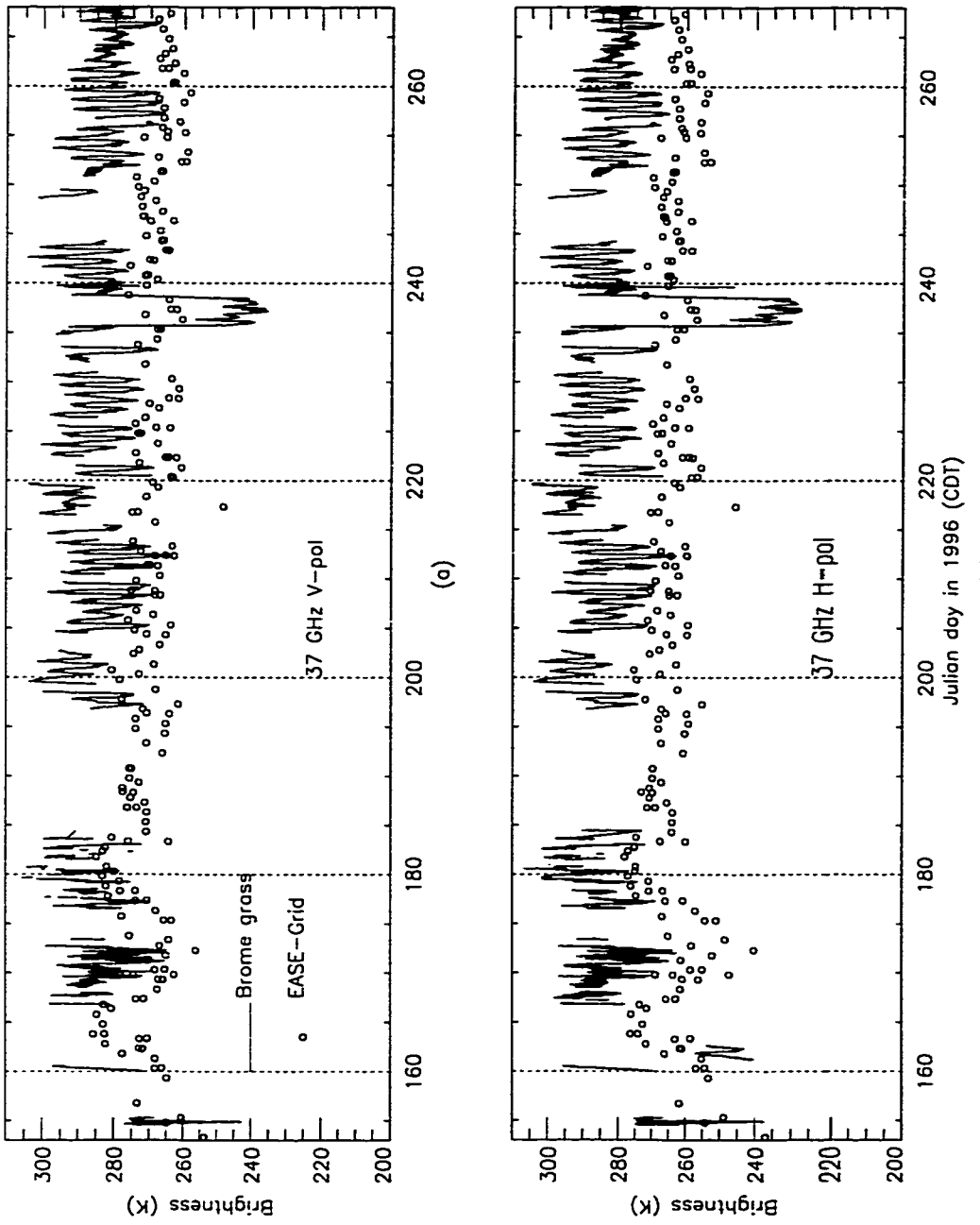

Figure 5.6: A comparison of REBEX-4 brightnesses observed at the brome grass site with the corresponding EASE-Grid brightnesses. (a) 37 GHz V-pol (b) 37 GHz H-pol.

Figures 5.7 and 5.8 show the comparisons at 19 and 37 GHz with the EASE-Grid brightnesses that were within 5 minutes for bare soil and within 15 minutes for the grass site, respectively.

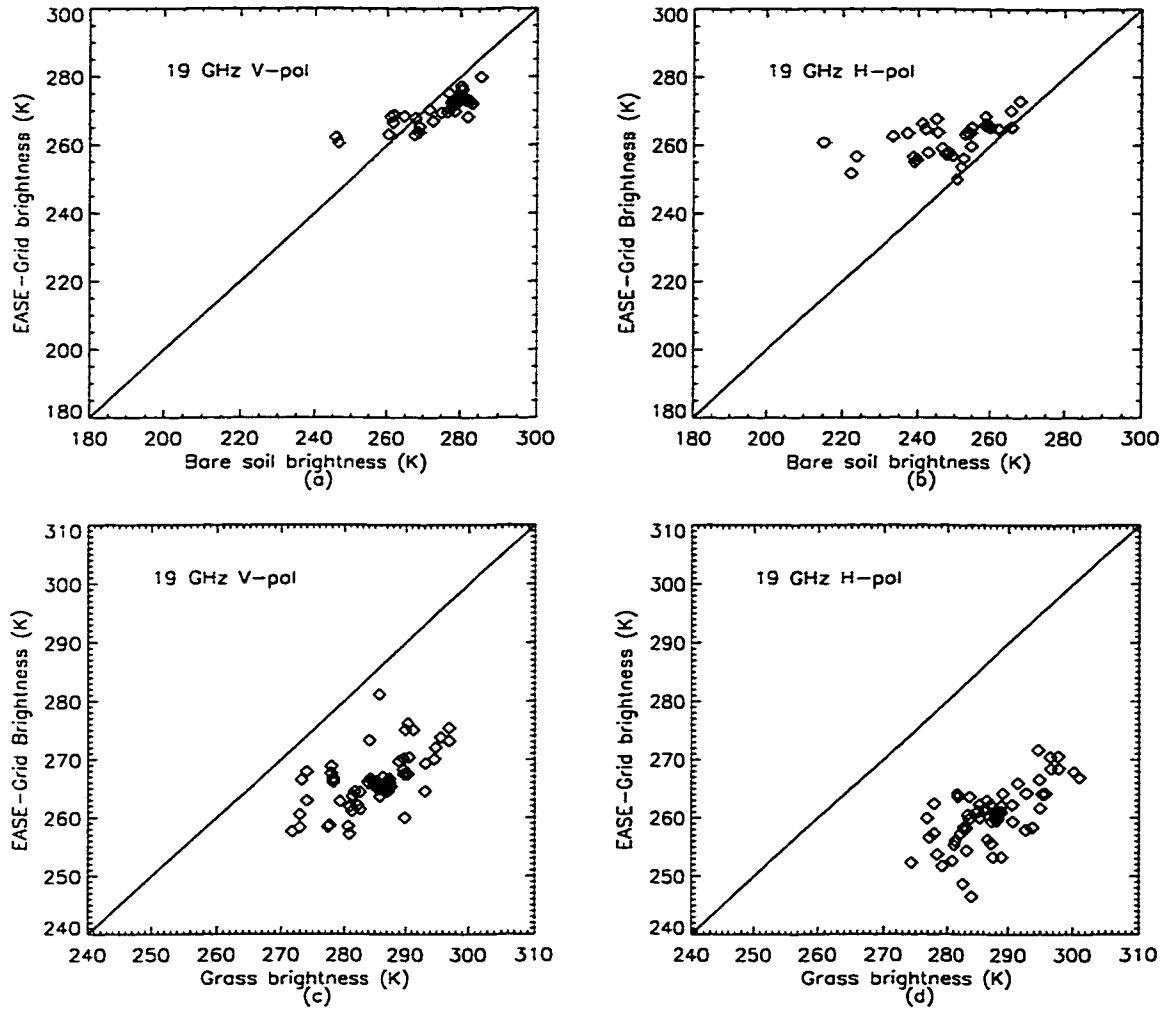

Figure 5.7: A comparison of the 19 GHz terrain brightnesses measured at the bare soil and the grass sites during REBEX-4 with the EASE-Grid SSM/I brightnesses observed within 15 minutes.

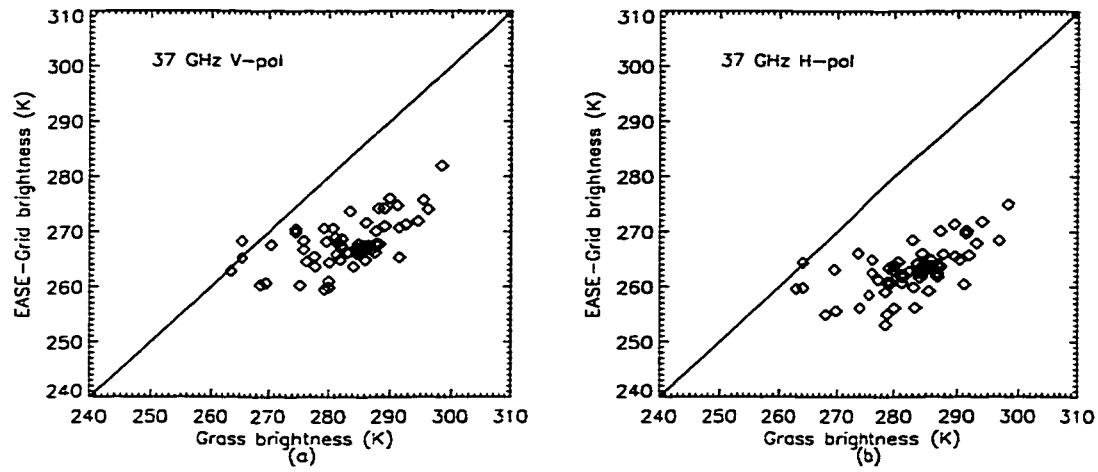

Figure 5.8: A comparison of the 37 GHz terrain brightnesses measured at the grass site during REBEX-4 with the corresponding EASE-Grid SSM/I brightnesses.

5.2.2 REBEX-5

The REBEX-5 site (36.6 N, 97.5 W) was included in the EASE-Grid pixel corresponding to row 117 and column 316. Figure 5.9 shows the exact location of the site within the pixel. Brightnesses at 19 and 37 GHz were compared with the EASE-Grid brightnesses from JD 170-196 for the 19 GHz and from JD 170-199 in 1997 for the 37 GHz, as shown in Figure 5.10(a-d). Figures 5.11(a-d) compare the REBEX-5 observations to the EASE-Grid brightnesses that were within 15 minutes.

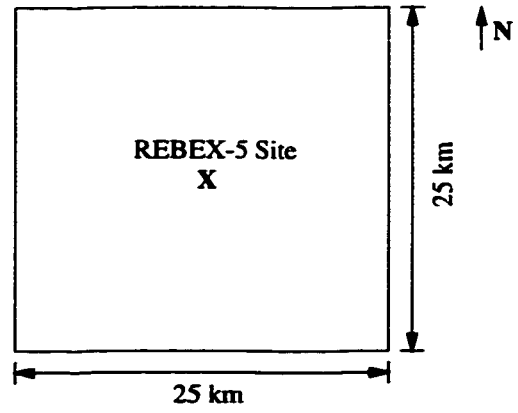

Figure 5.9: Location of the REBEX-5 site within the EASE-Grid pixel.

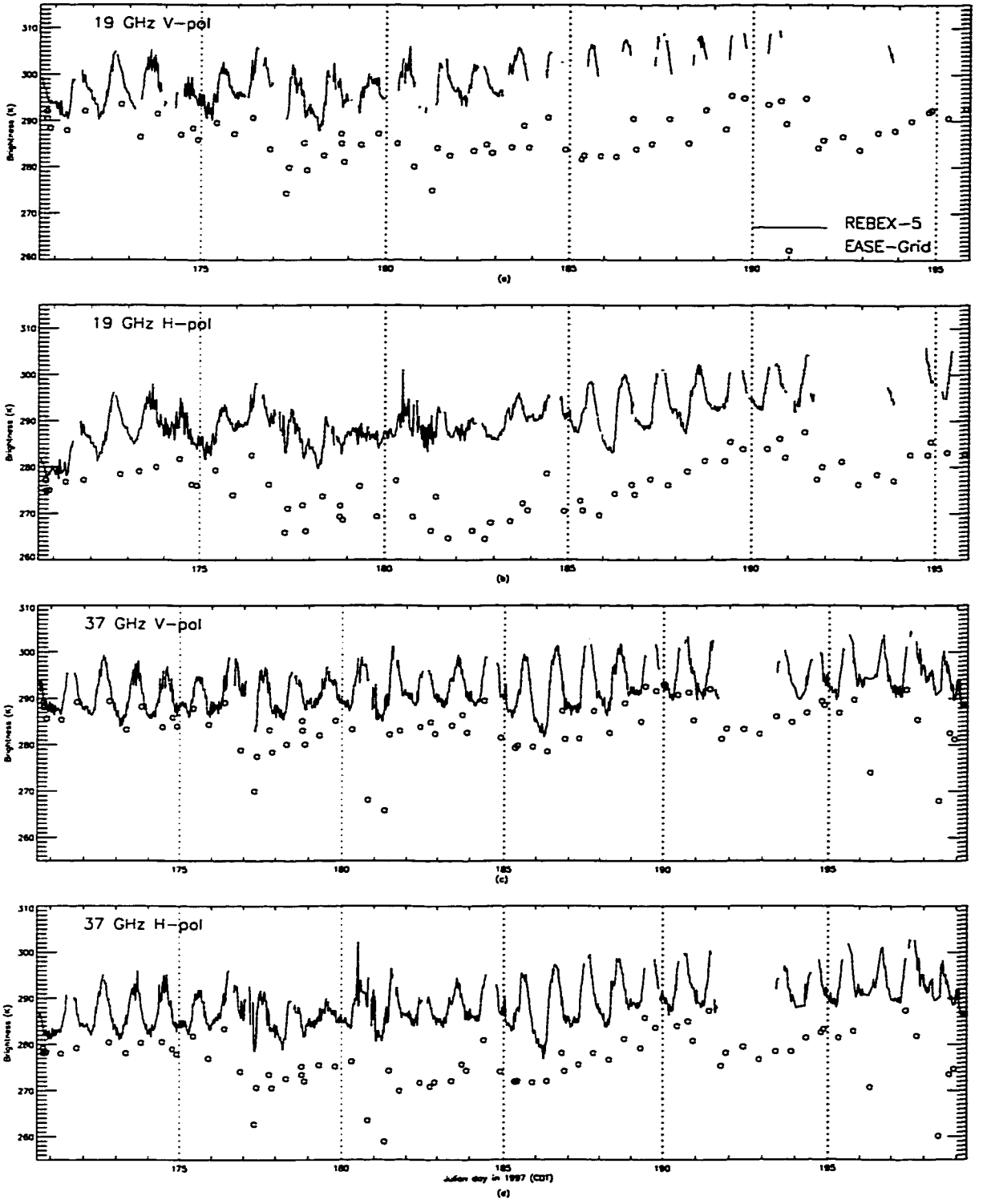

Figure 5.10: A comparison of the 19 and 37 GHz terrain brightnesses measured at the winter wheat site during REBEX-5 with the corresponding EASE-Grid SSM/I brightnesses.

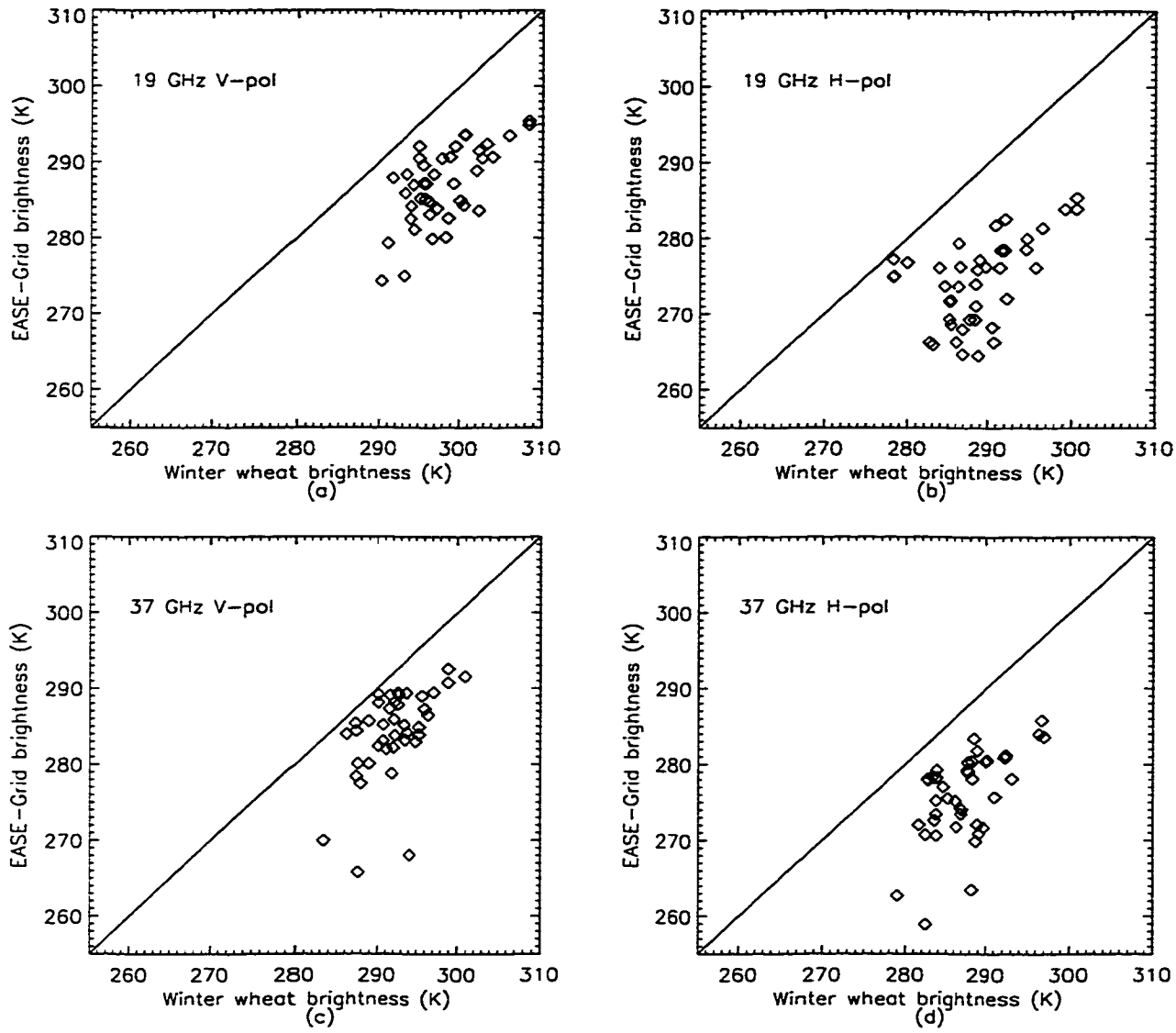

Figure 5.11: A comparison of the 19 and 37 GHz terrain brightnesses measured at the winter wheat site during REBEX-5 with the EASE-Grid SSM/I brightnesses observed within 15 minutes.

5.3 Ground-based vs. EASE-Grid Brightnesses: Discussion and Implications

The SSM/I brightnesses are sensitive to terrain moisture at both 19 and 37 GHz, with a larger sensitivity at 19 GHz. The REBEX-4 and REBEX-5 brightness-clusters lie roughly parallel to the 1:1 line [see Figures 5.7, 5.8, and 5.11], implying a strong correlation between the ground-based and the satellite brightnesses in spite of the large difference in the observation area between the ground-based ($12.6m^2$) and the EASE-Grid (625 km^2) measurements.

In regions with significant vegetation biomass, as in REBEX-4 ($\sim$3 kg/m^2), the 37 GHz brightnesses exhibit more variability than the 19 GHz brightnesses because they are more sensitive to the vegetation column density and structure, as observed in Figures 5.7(c-d) and 5.8(a-b). The scattering and emission from the vegetation accounts for most of the 37 GHz brightness, and the contribution from soil is minimal. Both the SSM/I and the ground-based radiometers are largely sensitive to the moisture in the vegetation at 37 GHz, as evidenced by the similar variabilities of V and H-pol brightnesses and the closeness to the 1:1 line at 37 GHz. In the regions with low vegetation biomass, as in REBEX-5 ($\sim$0.5-1.5 kg/m^2), both 19 and 37 GHz show comparable variabilities [Figures 5.11(a-d)].

In general, the 19 GHz H-pol brightnesses show more variability than the corresponding V-pol brightnesses [Figures 5.7 and 5.11] because of their greater sensitivity to terrain moisture. The V-pol channels are less sensitive due to their high emissivities at the SSM/I incidence angle of 53° which is close to the Brewster angle.

For the REBEX-4 sites, the 19 GHz brightness clusters are closer to the 1:1 line for the bare soil, than for the brome grass (Tables 5.1 and 5.2), and the EASE-Grid H-pol brightnesses are radiometrically warmer than the bare soil brightnesses but colder than the grass brightnesses [see Figures 5.5(a) and (b)]. The SSM/I observed an average pixel brightness that is a weighted sum of contributions from a bare soil and a homogeneous vegetation, with the bare soil contribution being larger than the vegetated surface. About 80% of the 25 km x 25 km pixel consisted of row crops, primarily corn, with pasture, bare soil, and urban dwellings occupying the rest of the pixel area. The row crops have tiled vegetation distributions, in contrast with the homogeneous distribution found in pasture and grasslands. In a scaling effect study conducted by Liou et al. [127], brightnesses at 19 GHz were found to be sensitive to the distribution pattern and increased by as much as 50 K from tiled to homogeneous. Because the grass-site during REBEX-4 observations was homogeneous, its brightnesses were higher than the SSM/I brightnesses. The comparison between the brightnesses of the bare soil, grass, and the SSM/I pixel suggests an additional field experiment over row crops at a site closer to the REBEX-4 site to better interpret averaged SSM/I brightnesses over mixed pixels. It also demonstrates the importance of accounting for mixed-pixel in assimilation algorithms to estimate soil moisture.

Table 5.3 gives averages, maxima, minima, and standard deviations of the differences between the REBEX-5 and SSM/I observations. The smaller differences than those observed for the REBEX-4 site suggest that the REBEX-5 site was a better representative of the SSM/I pixel. The pixel mainly consisted of winter wheat fields (up to ~95%), with pasture and other vegetation occupying the rest of the pixel. A

Frequency (GHz)	19.35	
	V	H
Average (K)	6.5	13.7
Std. Dev. (K)	3.8	10.9
Minimum (K)	0.0	0.6
Maximum (K)	16.0	45.8

Table 5.1: Statistics of the absolute differences between the EASE-Grid and the REBEX-4 brightnesses for bare-soil.

Frequency (GHz)	19.35		37.0	
	V	H	V	H
Average (K)	18.4	26.9	14.9	19.0
Std. Dev. (K)	5.2	4.8	6.0	6.35
Minimum (K)	4.6	15.5	0.2	0.3
Maximum (K)	29.8	37.5	26.2	30.7

Table 5.2: Statistics of the absolute differences between the EASE-Grid and the REBEX-4 brightnesses for brome-grass.

similar correlation between the averaged L-band (1.4 GHz, H-pol) brightnesses observed by the aircraft-borne Electronically Scanned and Thinned Array Radiometer (ESTAR) during SGP'97 [98, 144] over the SSM/I pixel[3] and those observed for the REBEX-5 pixel further demonstrates that the land conditions within the SSM/I pixel were well represented by the experimental site [see Figure 5.12(a)]. Figure 5.12(b) shows a comparison between the surface soil moisture derived from the ESTAR brightnesses [98] for the REBEX-5 pixel and those averaged over the EASE-Grid SSM/I pixel. Table 5.4 shows the minimum and the maximum differences between the averaged and REBEX-5 pixel brightnesses and the derived soil moisture.

[3]The ESTAR pixel size is 800 m x 800 m, and the EASE-Grid pixel is 25 km x 25 km. The brightnesses of 1020 ESTAR pixels were averaged.

Frequency (GHz)	19.35		37.0	
	V	H	V	H
Average (K)	11.1	14.4	7.9	11.5
Std. Dev. (K)	4.0	5.53	4.9	4.7
Minimum (K)	3.0	1.09	0.9	4.6
Maximum (K)	18.8	24.5	26.0	24.7

Table 5.3: Statistics of the absolute differences between the EASE-Grid and the REBEX-5 brightnesses.

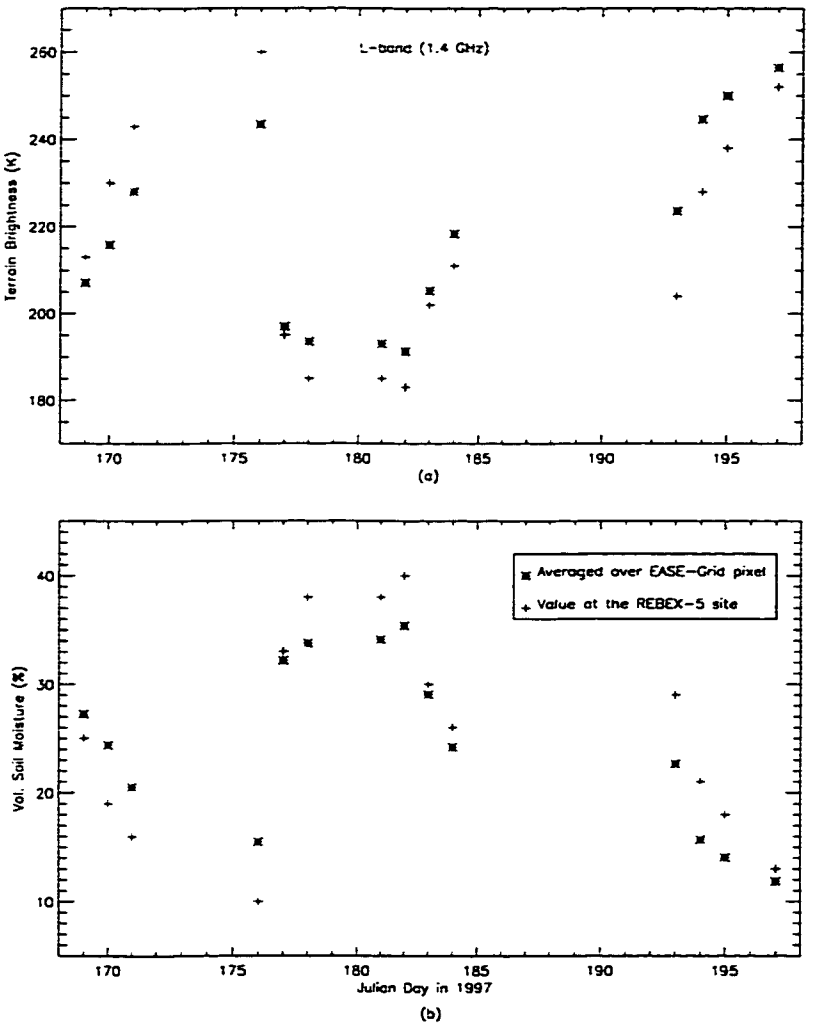

Figure 5.12: (a) Comparison between the L-band H-pol ESTAR brightnesses of the REBEX-5 pixel and those averaged over the SSM/I pixel. (b) Comparison between the surface soil moisture derived from the ESTAR brightnesses for the REBEX-5 pixel and those averaged over the SSM/I pixel.

	Brightness 1.4 GHz (K)	Soil Moisture Surface (%)
Minimum Difference	1.9	0.8
Maximum Difference	19.4	6.8

Table 5.4: Statistics of the absolute differences between the ESTAR brightnesses and the derived surface soil moisture of the REBEX-5 pixel and those averaged over the SSM/I pixel.

The differences of up to 30 K that were observed between the SSM/I and the ground observations [see Tables 5.1, 5.2 and 5.3] cannot be explained by atmospheric absorption. In an earlier research with freeze/thaw classification using SSM/I observations [105], I found that brightness differences due to atmospheric emission accounted for only 3-5 K at 19 GHz and 5-9 K at 37 GHz. Galantowicz [71] and Kim [111] also used atmospheric corrections to compare the EASE-Grid brightnesses with the REBEX-1 and REBEX-3 observations, respectively, and found similar results.

5.4 Summary

- The satellite brightnesses exhibit strong correlations with the ground based observations at both 19 and 37 GHz.
- The SSM/I pixel brightnesses lay between the ground-based REBEX-4 brightnesses of the bare soil and those of the brome grass. With brightnesses closer to those of bare soil than those of homogeneous grass, the comparison suggests a need for additional experiments with row crops to better interpret the satellite brightnesses. It also demonstrates the

importance of including mixed-pixels in assimilation algorithms that use satellite data.

- For the REBEX-5 pixel, the strong correlation of the SSM/I and the ground-based observations indicate that the satellite pixel was well represented by the experimental site. This was further demonstrated by similar correlations between the L-band ESTAR brightnesses and derived surface soil moisture averaged over the SSM/I pixel and those observed for the REBEX-5 pixel.

CHAPTER 6

Conclusions

In this chapter, I summarize some of the important results and contributions from this dissertation, and discuss their implications on current efforts in soil moisture retrieval using microwave radiometry. I also recommend possible directions for future research.

6.1 Summary

This dissertation represents an important step toward assimilating remotely sensed microwave radiometric observations to improve soil moisture estimates. It focussed on the "forward" problem of modeling terrain brightnesses through a biophysically-based LSP/R model, and correlating the ground-based brightnesses with those from the SSM/I. The LSP/R model was modified and calibrated for representative terrain in the Great Plains, viz., bare soil and brome grass in the northern plains, and winter wheat-stubble in the southern plains. It was calibrated during summertime, when surface processes are dominant, using data from two field investigations, REBEX-4

and REBEX-5 (SGP'97).

The implementation of the numerical methods in the modified LSP/R model was rigorously tested for computational accuracy. The model conserved mass and energy, with their maximum errors being $\sim 5\text{x}10^{-7}\ kg/m^2$ and $\sim 2\ J/m^2$, respectively for a 12-day simulation period. Its numerical solution was compared with an analytical solution for moisture and energy transport in a vapor-dominated homogeneous soil. The solutions compared well, with maximum differences of $\sim 2.2\ mK$ for temperature and $\sim 6\text{x}10^{-4}$ % for volumetric moisture.

The two field experiments conducted, REBEX-4 and REBEX-5, were collaborative efforts resulting in unique datasets that are publicly available for a variety of inter-disciplinary applications. In this dissertation, the datasets were used to calibrate the LSP/R model and to correlate the satellite brightnesses with the ground-based observations. The concurrent bare soil and grass data can also be used to develop and calibrate mixed pixel assimilation models. Together with the data from REBEX-1, the REBEX-4 data can also be used to study seasonal (annual) variations in thermal and moisture transport in soil and vegetation, and their estimation using microwave radiometry. The data from SGP'97 and REBEX-5 are being used for studies on spatial variability in soil moisture and other properties [64], data assimilation for soil moisture retrieval at different spatial scales [98], land-cover classification, and biomass estimation.

In general, the calibrated LSP model captured the surface processes, and the model's estimates of temperatures, moisture, and fluxes compared well with the field observations. Estimates were more sensitive to certain terrain properties than to

others. For example, model temperature and energy fluxes were largely dependent on the albedo and thermal properties of the terrain and surface. The estimates of soil moisture were primarily sensitive to the retention curves used to estimate matric head and hydraulic conductivity. Surface soil moisture was "harder" to model realistically than moisture at deeper layers because of complex interactions with the vegetation (canopy and thatch) and the atmosphere. More realistic soil thermal conductivities and soil water retention curves in the model, either through measurements or models, should improve the temperature and moisture estimates significantly.

Overall, the R-module predicted realistic mean diurnal variations in terrain brightnesses. Predictions of the brightnesses at 19 GHz were sensitive to surface temperatures, temperature gradients, surface moisture, and surface characteristics. H-pol brightnesses were more sensitive to near-surface moisture and roughness than were the V-pol brightnesses in wheat stubble and bare soil. For the bare soil case, the H-pol brightnesses were strongly affected by surface roughness. The semi-empirical rough surface emission model, developed by Wegmüller and Mätzler, improved the mean brightness estimates. For brome grass, emission from the canopy constituted approximately 98% of the total H-pol emission. The low mean differences of 0.89 K between the estimated and the observed H-pol brightnesses demonstrate that the brightnesses at 19 GHz are not sensitive to the structure of the vegetation, and that the "cloud" model for the canopy is adequate for estimating realistic brightnesses.

The comparison between the EASE-Grid SSM/I and the ground-observed brightnesses demonstrated that the brightnesses at 19 GHz exhibited virtually no scattering within the vegetation, and can potentially be assimilated to improve soil moisture es-

timates, particularly for regions with low vegetation biomasses (<3 kg/m^2). The comparison with the REBEX-4 bare soil and grass brightnesses indicated the importance of including mixed-pixels in assimilation algorithms that use satellite data. Strong correlations between the SSM/I and the REBEX-5 brightnesses, and between the L-band ESTAR brightnesses of the REBEX-5 pixel and those averaged over the SSM/I pixel, suggested that the satellite pixel was represented by the experimental site well.

6.2 Contributions

The most significant contribution of this dissertation is the LSP/R model calibrated for representative sites in the Great Plains during summertime. The model can be easily extended to similar relatively homogeneous regions, for example, the Steppes grasslands. Because it is biophysically-based with minimal parameterization, it can be also used to conduct sensitivity studies, as discussed in section 6.3.

Another major contribution is the co-located, concurrent REBEX-4 dataset of continuous dual polarized microwave brightnesses at the SSM/I frequencies and micrometeorological parameters for: A bare soil site over approximately 70 days, and a brome grass site over approximately 100 days. This was the first time that we collected diurnal ground truth data for canopy biomass and soil moisture. Together with the REBEX-1 observations during fall and winter, we have a year-long dataset for the same site that can be used for seasonal (annual) modeling of surface processes.

REBEX-5 (UM-MGG's contribution to SGP'97) produced a 30-day continuous

dataset for microwave brightnesses of the senescent winter wheat and wheat-stubble for an extensively studied site in the Southern Great Plains. The REBEX-5 dataset, including the diurnal canopy biomasses along with other datasets collected by investigators during SGP'97, are being used for a variety of inter-disciplinary projects.

This dissertation also resulted in the resampled (EASE-Grid) SSM/I brightnesses for regions including the experimental sites. Strong correlations of the resampled brightnesses with the ground-based observations suggest that the dataset can be assimilated in LSP models for improved soil moisture estimates. It can also be used for mixed-pixel studies when used in conjunction with the ground-based observations.

6.3 Recommendations for Future Research

Several recommendations included in this section are methodological in nature, concerning both modeling and field work issues. This section also suggests some interesting new lines of research that could potentially help improve soil moisture retrieval for hydrological and climatological applications.

6.3.1 Improvements: Model

First, the 1-dTH module could be significantly improved through the use of an implicit numerical method. Although the explicit forward finite difference method used in this dissertation is accurate and gives realistic outputs, an implicit implementation will make it possible to incorporate lower boundary conditions on temperature and moisture (or their fluxes) for self-consistent estimates. The lower boundary conditions

were not essential for the 20-25 day diurnal simulations used in this study, but they are crucial for annual simulations. Such a numerical implementation will also provide rapid convergence with larger time-steps, even when the weather forcings are strong, e.g., heavy precipitation.

Second, a more sophisticated infiltration model is needed to handle heavy rainfall and ponding at the surface. The current model does not account for ponding with the excess rainfall treated as runoff. It does not produce realistic estimates of soil moisture under such conditions.

Third, the estimates of thermal and hydraulic constitutive properties of soils could be improved through more physically-based models. The two parameter junction model by Rossi and Nimmo, used in this dissertation to estimate the soil water retention curve, was the best empirical model available. However, it has been studied with only seven different soil types. It may estimate unrealistic curves when the model is extended for other soil types. Sensitivity studies should also be conducted to see the effect of drainage and imbibition retention curves on soil moisture estimates. The model in this dissertation only uses the drainage curve and does not account for the hysteresis that occurs during imbibition. The thermal conductivity estimates need to account for inter-particulate radiative transfer within the soil for more realistic thermal transport at the soil surface.

Fourth, the R-module requires the addition of a physically-realistic rough surface emission model. Although the need was demonstrated for emission at 19 GHz in this dissertation, it is still a significant problem even at the L-band frequencies [185], and should be researched more physically.

Finally, the dual dispersion model, used to estimate canopy dielectric properties in this dissertation, was developed for corn and may not extend to other vegetation types. It had to be modified to be used for inactive wheat-stubble. The dispersion model should be modified and validated for other dominant vegetation types.

6.3.2 Improvements: Field Experiments

Two problems were encountered during the field experiments that need to be addressed in the future REBEXs. The first was overheating of the radiometer electronics, largely due to the use of heaters to achieve temperature control. During earlier REBEXs, this was not a problem because the ambient temperatures were usually low. Our Microwave Geophysics Group (UM-MGG) is currently testing thermo-electric coolers to maintain temperature control in the radiometer.

The second was the need for better calibration for the TDR probes used to measure soil moisture. Calibrating the probes is not easy and is a well recognized problem [97, 37]. The probes need to be calibrated for each soil use and also for thermal variations in soil. Research efforts are underway to accurately measure soil moisture using the probes [37].

Other minor, yet important, lessons were learned during the two field experiments. First, only one sample per data point was collected during the diurnal experiment for measuring grass and soil moisture. Because of large spatial variabilities, the diurnal signal was lost in the noisy data. More samples per data point, at least 5, are suggested for future experiments. Second, during REBEX-4, the downwelling longwave flux, one

of the crucial input parameters to the LSP/R model, could not be measured and is recommended for future experiments. Finally, measuring soil constitutive properties, such as thermal and saturated hydraulic conductivity, during future field experiments will considerably improve the model soil moisture and temperature estimates.

6.3.3 Projects

As mentioned earlier, this dissertation concentrated on the forward problem. An inversion model that would assimilate remotely-sensed microwave radiometry data is recommended. The model could be developed from the LSP/R model calibrated in this dissertation. Because the LSP/R model is complex, inverting it in its present state would be impossible. It can be simplified through sensitivity studies that would identify the most important physical properties and parameters influencing the predictions of land surface conditions. The other less effective properties could then be parameterized. As the current research in microwave radiometry suggests, the sensitivity studies and inversion calibration/validation are recommended at L-band frequencies for soil moisture retrieval applications. A simplified and inverted model can also be used in conjunction with Atmospheric Models for improved near-term climate and weather predictions.

An extensive field campaign, similar to the SGP'97, is also recommended, in which spatial variability issues are researched at different scales for sites with denser vegetation cover, and with mixed vegetation types. Concurrent and continuous ground-based radiometric measurements at the same frequency and polarization (L-band,

H-pol) are recommended for different terrains within an experimental region. Such experiments will help calibrate/validate our surface process and assimilation models, and improve our understanding of spatial averaging observed at satellite scales. Forests and dense-vegetation constitute almost half of earth's land-cover, and if the global satellite data are to be useful, our models need to be calibrated for such terrain.

APPENDICES

APPENDIX A

LSP/R Model Parameterizations and Modifications

A.1 Derivation of M, N, E, and F in Equation 2.10

The conservation of mass and energy equations are simplified following deVries [41] prior to applying the finite difference method to solve for temperature and moisture changes with time and depth.

Conservation of Mass

$$\frac{\partial X_m}{\partial t} = -\nabla \cdot \vec{q}_m \tag{A.1}$$

$$X_m = \rho_l(\theta_l + \theta_v) \tag{A.2}$$

$$\vec{q}_m = \vec{q}_l + \vec{q}_v \qquad \frac{\vec{q}_m}{\rho_l} = -D_\theta \nabla\theta_l - D_T \nabla T - K\hat{k} \tag{A.3}$$

$$\frac{\partial \theta_l}{\partial t} = -\nabla \cdot \frac{\vec{q}_l}{\rho_l} - \mathbb{E} \qquad \frac{\partial \theta_v}{\partial t} = -\nabla \cdot \frac{\vec{q}_v}{\rho_l} + \mathbb{E} \tag{A.4}$$

where,

- X_m is the total moisture content per unit volume (kg/m^3),
- $\vec{q}_m$ is the moisture flux ($kg/m^2.sec$),

- $\vec{q}_l$ is the liquid flux ($kg/m^2.sec$),
- $\vec{q}_v$ is the vapor flux ($kg/m^2.sec$),
- ρ_l is the density of liquid water (kg/m^3),
- θ_l is the volumetric liquid content (m^3/m^3),
- θ_v is the volumetric vapor content (m^3 precipitable water/m^3), and
- $\mathbb{E}$ is the rate of evaporation (sec^{-1})

From equation (3) in deVries [41], θ_v is defined as

$$\theta_v = (S - \theta_l)\frac{\rho_0 h}{\rho_l}$$

Taking the derivative of θ_v with respect to time t,

$$\frac{\partial \theta_v}{\partial t} = -\frac{\rho_v}{\rho_l}\left[\frac{\partial \theta_l}{\partial t}\right] + \frac{S - \theta_l}{\rho_l}\left[h\frac{\partial \rho_0}{\partial t} + \rho_0\frac{\partial h}{\partial t}\right] \tag{A.5}$$

$\rho_0 = f(T)$, and $h = f(T, \theta_l)$,

$$\frac{\partial \theta_v}{\partial t} = \left[\frac{\rho_0(S - \theta_l)}{\rho_l}\frac{\partial h}{\partial \theta_l} - \frac{\rho_v}{\rho_l}\right]\frac{\partial \theta_l}{\partial t} + \frac{S - \theta_l}{\rho_l}\left[h\frac{\partial \rho_0}{\partial T} + \rho_0\frac{\partial h}{\partial T}\right]\frac{\partial T}{\partial t} \tag{A.6}$$

Combining equations A.1, A.2, A.3, and A.6,

$$\left\{1 + \frac{\rho_0(S - \theta_l)}{\rho_l}\frac{\partial h}{\partial \theta_l} - \frac{\rho_v}{\rho_l}\right\}\frac{\partial \theta_l}{\partial t} + \frac{S - \theta_l}{\rho_l}\left\{h\frac{\partial \rho_0}{\partial T} + \rho_0\frac{\partial h}{\partial T}\right\}\frac{\partial T}{\partial t} = \nabla \cdot \left[D_\theta \nabla \theta_l + D_T \nabla T + K\hat{k}\right] \tag{A.7}$$

Conservation of Energy

$$\frac{\partial X_h}{\partial t} = -\nabla \cdot \vec{q}_h \tag{A.8}$$

From equation (11) in deVries [41],

$$X_h = C_d(T-T_0) + L_0\rho_l\theta_v + c_p\rho_l\theta_v(T-T_0) + c_l\rho_l\theta_l(T-T_0) - \rho_l\int_0^{\theta_l} W\, d\theta_l \quad \text{(A.9)}$$

$$\vec{q}_h = -\lambda\nabla T + L_0\vec{q}_v + c_p(T-T_0)\vec{q}_v + c_l(T-T_0)\vec{q}_l \quad \text{(A.10)}$$

Taking the time derivative of A.9 and divergence of A.10,

$$\frac{X_h}{dt} = C_d\frac{\partial T}{\partial t} + \rho_l\left[L_0 + c_p(T-T_0)\right]\frac{\partial\theta_v}{\partial t} + c_l\rho_l(T-T_0)\frac{\partial\theta_l}{\partial t} - \rho_l W\frac{\partial\theta_l}{\partial t} \quad \text{(A.11)}$$

$$-\nabla\cdot\vec{q}_h = \lambda\nabla\cdot(\nabla T) - c_p\vec{q}_v\cdot\nabla T - c_l\vec{q}_l\cdot\nabla T + L_0\rho_l\frac{\partial\theta_v}{\partial t} + c_p\rho_l(T-T_0)\frac{\partial\theta_v}{\partial t} + c_l\rho_l(T-T_0)\frac{\partial\theta_l}{\partial t} - L_0\rho_l\mathbb{E} - c_p\rho_l(T-T_0)\mathbb{E} + c_l\rho_l(T-T_0)\mathbb{E} \quad \text{(A.12)}$$

Combining A.11 and A.12

$$C_d\frac{\partial T}{\partial t} - \rho_l W\frac{\partial\theta_l}{\partial t} = \lambda\nabla\cdot(\nabla T) - c_p\vec{q}_v\cdot\nabla T - c_l\vec{q}_l\cdot\nabla T - L\rho_l\mathbb{E} \quad \text{(A.13)}$$

Solving for $\mathbb{E}$ from A.4 and A.6 above,

$$\mathbb{E} = \frac{\partial\theta_v}{\partial t} + \frac{1}{\rho_l}\nabla\cdot\vec{q}_v$$

$$\mathbb{E} = \left[\frac{\rho_0(S-\theta_l)}{\rho_l}\frac{\partial h}{\partial\theta_l} - \frac{\rho_v}{\rho_l}\right]\frac{\partial\theta_l}{\partial t} + \frac{S-\theta_l}{\rho_l}\left[h\frac{\partial\rho_0}{\partial T} + \rho_0\frac{\partial h}{\partial T}\right]\frac{\partial T}{\partial t} - \nabla\cdot\left[D_{\theta_v}\nabla\theta_l + D_{T_v}\nabla T - K\hat{k}\right] \quad \text{(A.14)}$$

Combining A.13, A.14, A.3, and A.4,

$$\left\{L\rho_0(S-\theta_l)\frac{\partial h}{\partial\theta_l} - L\rho_v - \rho_l W\right\}\frac{\partial\theta_l}{\partial t} + \left\{C_d - L(S-\theta_l)\left[h\frac{\partial\rho_0}{\partial T} + \rho_0\frac{\partial h}{\partial T}\right]\right\}\frac{\partial T}{\partial t} = \nabla\cdot\left[(\lambda - L\rho_l D_{T_v})\nabla T\right] + L\rho_l\nabla\cdot(D_{\theta_v}\nabla\theta_l) + \rho_l\Big[(c_p\ D_{\theta_v} + c_l\ D_{\theta_l})\nabla\theta_l + (c_p D_{T_v} + c_l D_{T_l})\nabla T + c_l K\hat{k}\Big]\cdot\nabla T \quad \text{(A.15)}$$

From A.7 and A.15, define M, E, N, and F in equation 2.10 in Chapter 2 as follows:

$$\mathrm{M} = 1 + \frac{\rho_0(S-\theta_l)}{\rho_l}\frac{\partial h}{\partial \theta_l} - \frac{\rho_v}{\rho_l} \tag{A.16}$$

$$\mathrm{E} = \frac{S-\theta_l}{\rho_l}\left[h\frac{\partial \rho_0}{\partial T} + \rho_0\frac{\partial h}{\partial T}\right] \tag{A.17}$$

$$\mathrm{N} = L\rho_0(S-\theta_l)\frac{\partial h}{\partial \theta_l} - L\rho_v - \rho_l W \tag{A.18}$$

$$\mathrm{F} = C_d - L(S-\theta_l)\left[h\frac{\partial \rho_0}{\partial T} + \rho_0\frac{\partial h}{\partial T}\right] \tag{A.19}$$

A.2 Derivation of Canopy Optical Depth (τ)

The derivation of τ follows England and Galantowicz [59], and Ulaby et al [200]:

$$\tau = \int_0^{h_c} \kappa_a dz$$

$$\kappa_a = -2k_0 \mathrm{Im}\{n_t\}$$

$$n_t = 1 + v_{wc} n_{wc}$$

where,

- h_c is the canopy height (m),
- κ_a is the absorption coefficient,
- k_0 is the vacuum wavenumber (m^{-1}),
- v_{wc} is the volume fraction of the wet canopy,
- n_{wc} is the complex refractive index of the wet canopy,

Simplifying the above equations,

$$\tau = -2k_0 \mathrm{Im}\{n_{wg}\} \int_0^{h_c} \frac{B}{\rho_{wg} V} dz$$

$$\tau = -2k_0 \mathrm{Im}\{n_{wg}\} \frac{B}{\rho_{wg}} \tag{A.20}$$

where,

- B is the wet canopy biomass (kg/m^2),
- V is the total volume of the canopy (air+wet canopy) (m^3), and
- ρ_{wg} is the density of the wet canopy (kg/m^3).

A.3 Modifications to the 1-dTH Module

- The precipitation reaching the soil was zero in the community model when there was no vegetation (veg=0) and the precipitation rate was linearly interpolated with time-step. In the modified model, all the precipitation reaches the soil when veg=0, and the total precipitation observed for a 10-minute interval is equally divided into the 3-sec time-steps.
- The equation of time (EQT), i.e., the difference in time between local apparent (LAT) and local mean time (LMT), was included in the calculation of zenith angle as follows:

$$\begin{aligned} \text{LAT} &= \text{LMT} + \text{EQT} \\ \text{LMT} &= \text{Local time} + \text{Longitudinal correction} \\ \text{EQT} &= .000075 + .001868\text{COS}\gamma - .032077\text{SIN}\gamma \\ &\quad -.014615\text{COS}2\gamma - .040849\text{SIN}2\gamma \\ \gamma &= \frac{2\pi(\text{JD}-1)}{\text{DY}} \end{aligned} \tag{A.21}$$

where, JD is the Julian Day and DY is the total number of days in the

year.

- In the community model, the latent heat of vaporization (Lv) was calculated incorrectly using specific heat of dry air (=1004.64 J/kgK). In the modified model, the specific heat of water vapor at constant pressure was used (= 1952 J/kgK) instead.
- To calculate the derivative with respect to z, half of the total thickness of the surface node was used in the community model. It was corrected to the total thickness in the modified model. [In the code; T60_d = timesteps/node thickness].
- For the time interval between the weather forcings, the community model used the difference between the past and the present forcing. Because the model propagates forward in time, the difference was calculated using the present and the future forcings in the modified module. [In the code; RHR_i(I) = (RDAY(I+1)-RDAY(I))*86400].
- An incorrect coefficient was used for the matric head calculation in the community module. It was corrected for the modified model. [In the code; In =I2_i(J)+coef_I1(J)*(Vf_H2O_i_s(J)....].
- Calculation of the zenith angle for a given time was corrected by Kim [111], and I used the corrected expression for the modified model.

APPENDIX B

REBEX-4 and REBEX-5 Observations

This appendix includes the data collected during the REBEX-4 and REBEX-5 experiments. A more detailed report of the observations recorded, is given in [78], [77], [106], and [107].

B.1 Data Summary from the Bare Soil site

Figures B.1 - B.5 show the observations made at the bare soil site during REBEX-4.

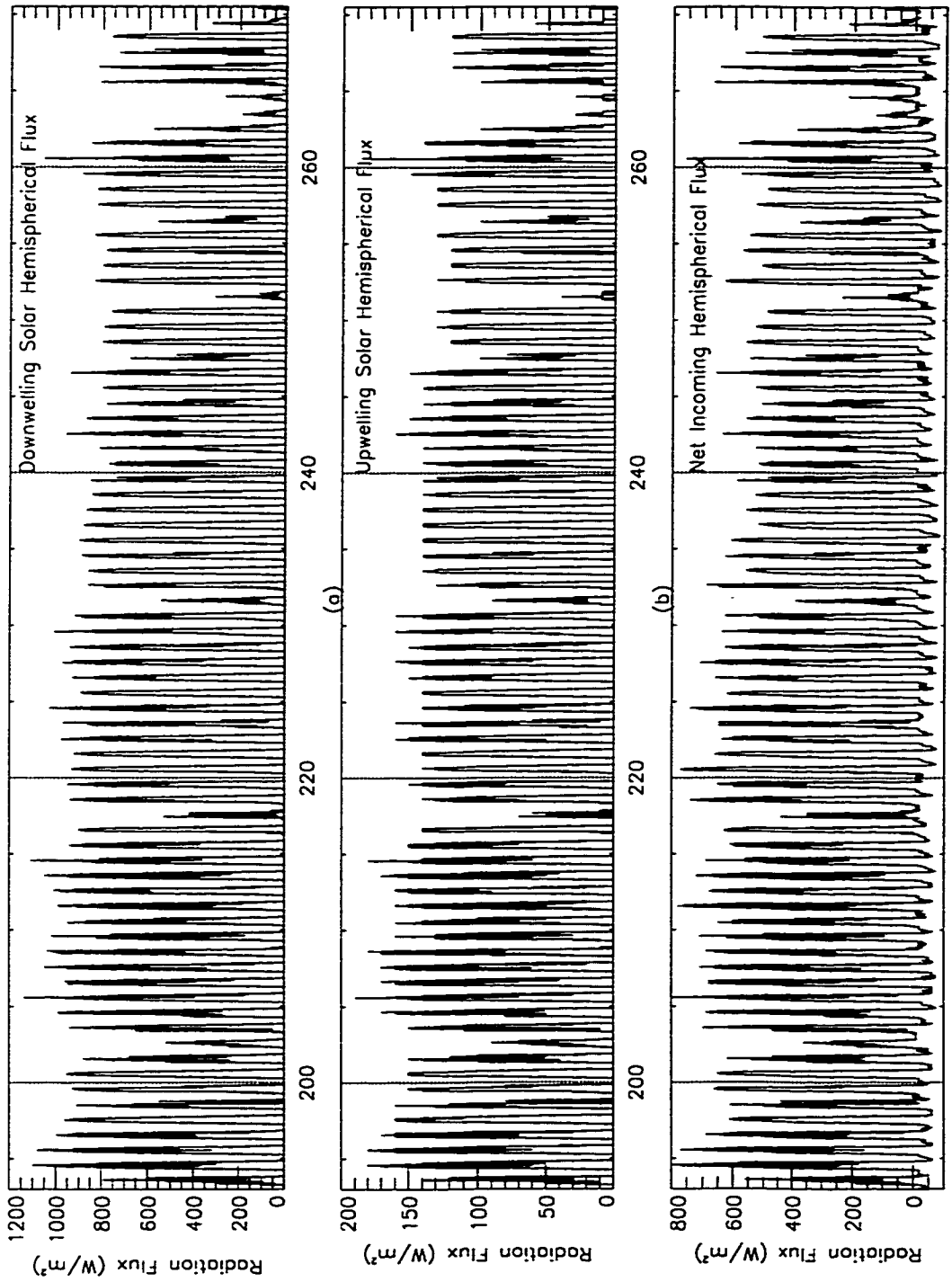

Figure B.1: Radiance observations: (a) Downwelling and (b) Upwelling solar radiation (c) Net radiation.

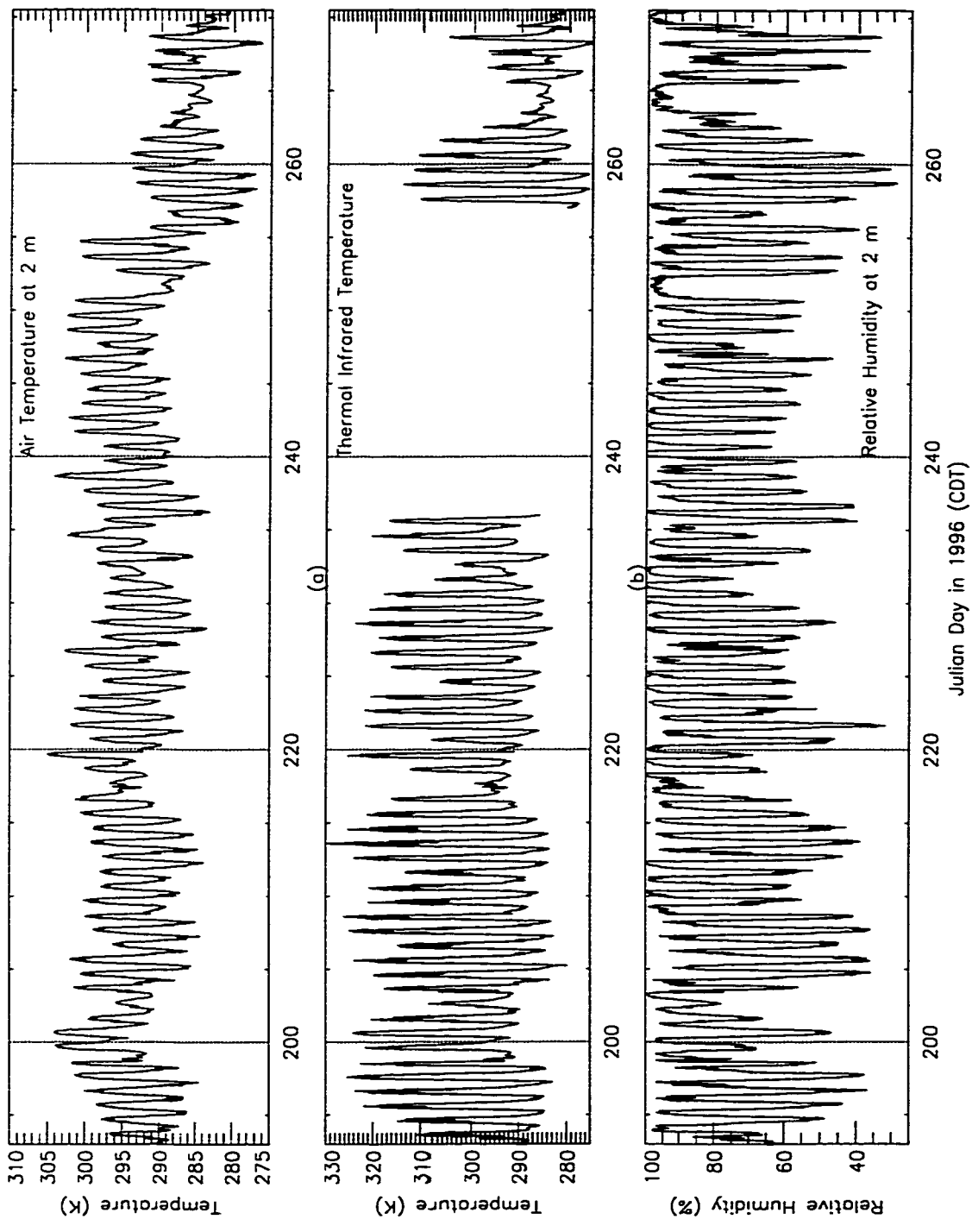

Figure B.2: Weather: (a) Air temperature at 2 m (b) Thermal infrared temperature of the surface and (c) Relative humidity at 2 m.

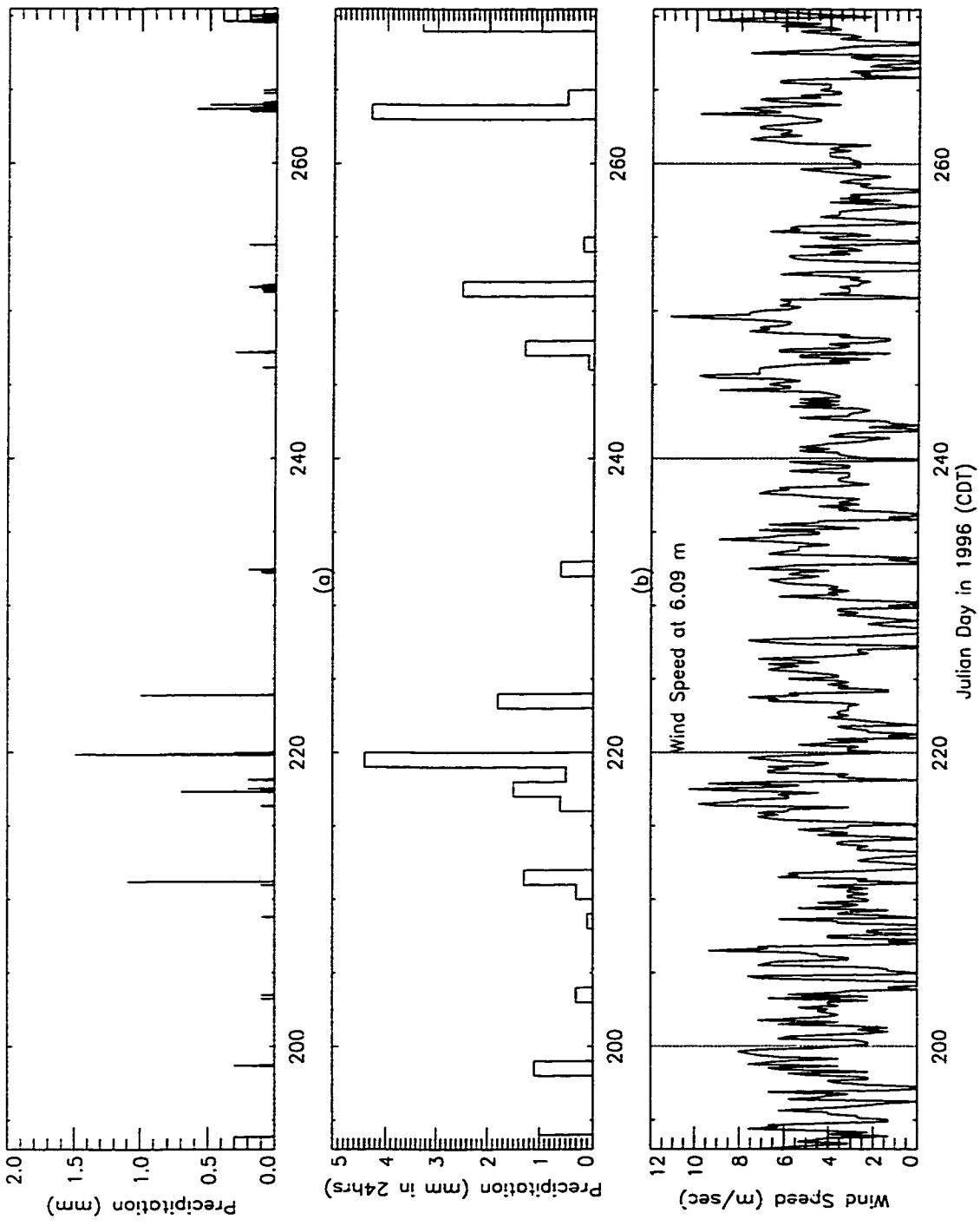

Figure B.3: Weather from Local Climatological Data (LCD): (a) Precipitation (b) Cumulative precipitation in 24 hours and (c) Wind speed at 6.9 m.

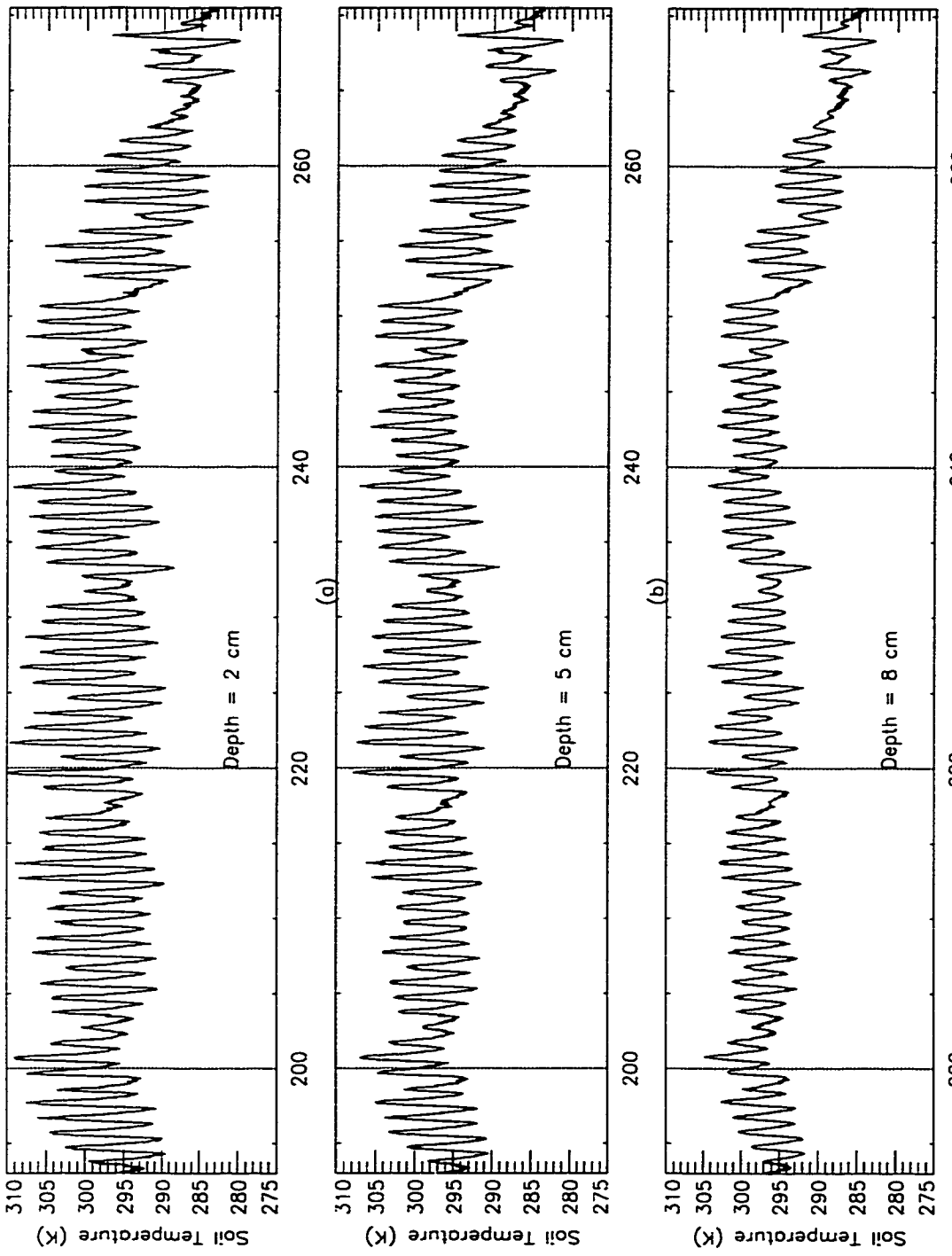

Figure B.4: Soil temperature at: (a) 2 (b) 5 and (c) 8 cm.

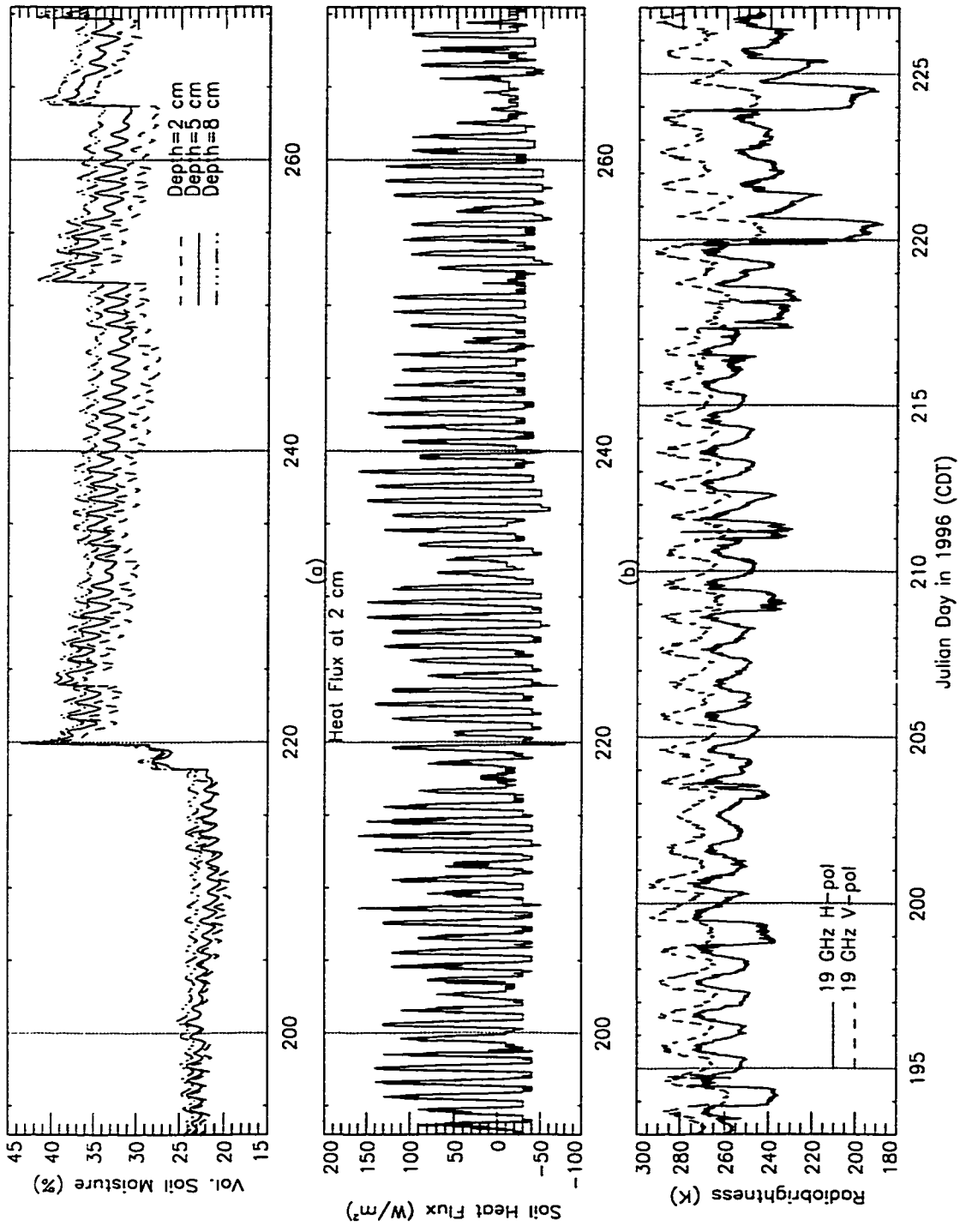

Figure B.5: (a) Volumetric soil moisture at 2, 5, and 8 cm. (b) Heat flux into the ground at the depth of 2 cm, and (c) Radiobrightness at 19 GHz.

B.2 Data Summary for the Brome Grass site

Figures B.6 - B.14 show the observed parameters at the grass site during REBEX-4.

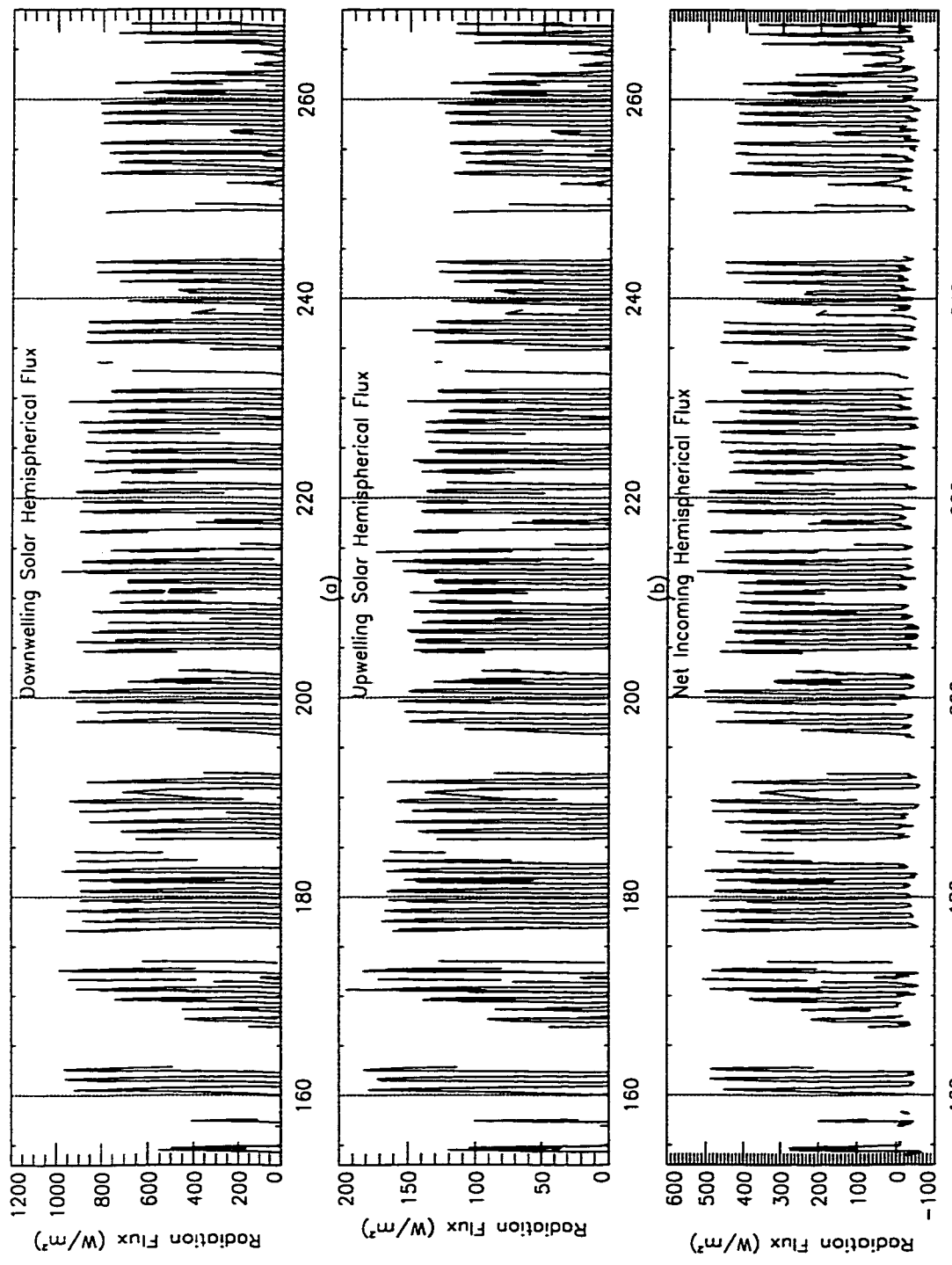

Figure B.6: Radiance observations: (a) Downwelling and (b) Upwelling solar radiation (c) Net radiation.

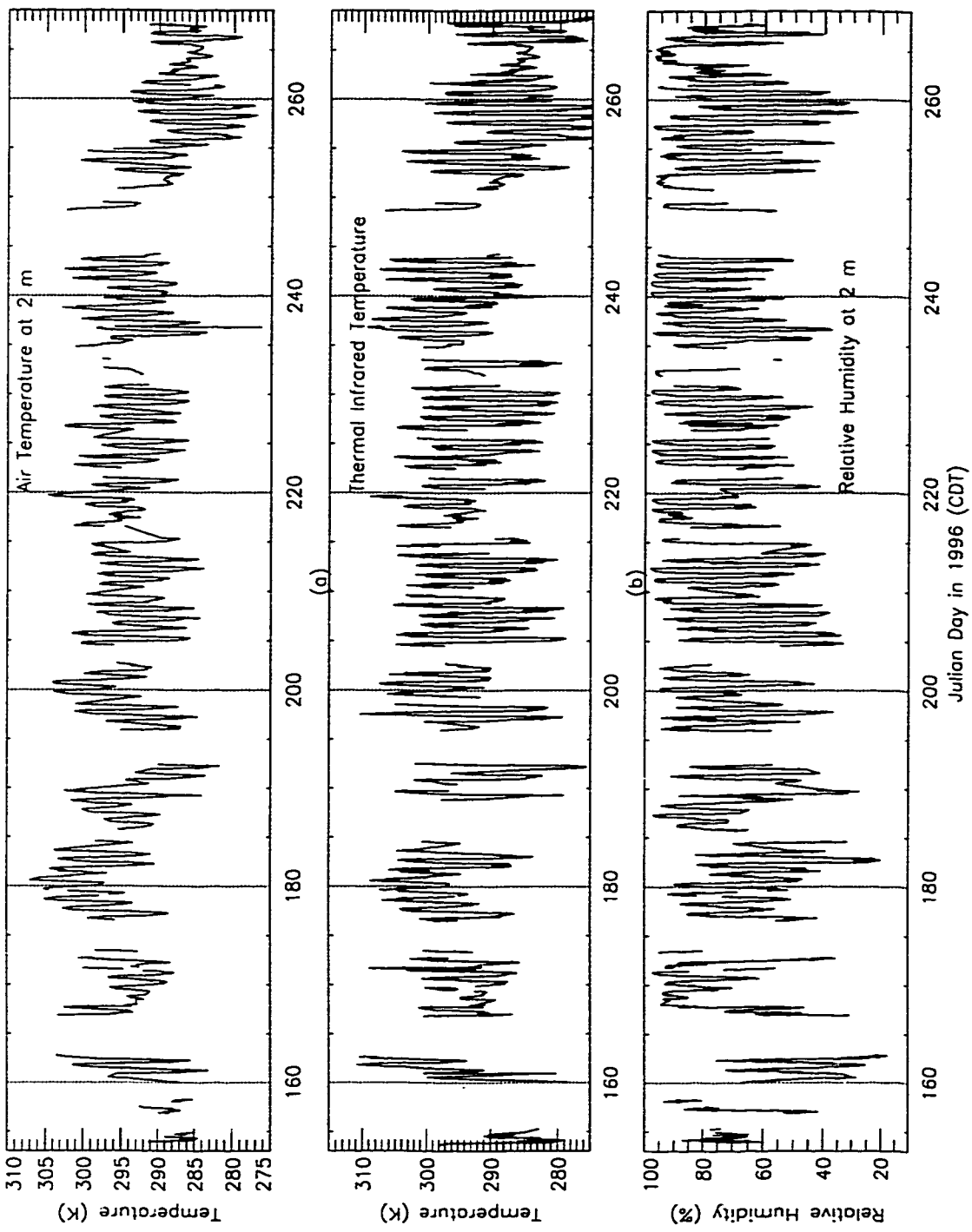

Figure B.7: Weather: (a) Air temperature at 2 m (b) Thermal infrared temperature of the surface and (c) Relative humidity at 2 m.

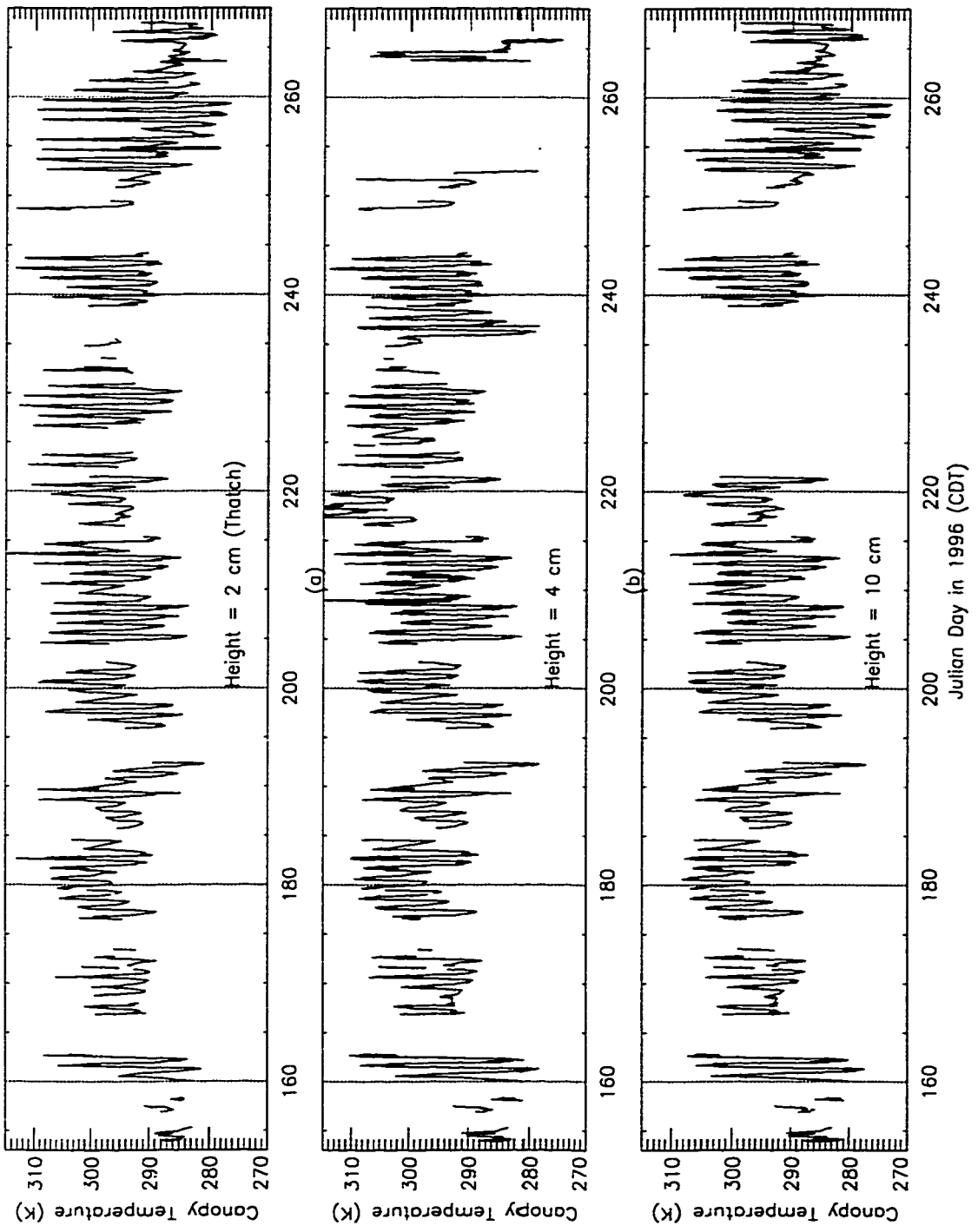

Figure B.8: Canopy temperatures at the heights of: (a) 2 (b) 4 and (c) 10 cm.

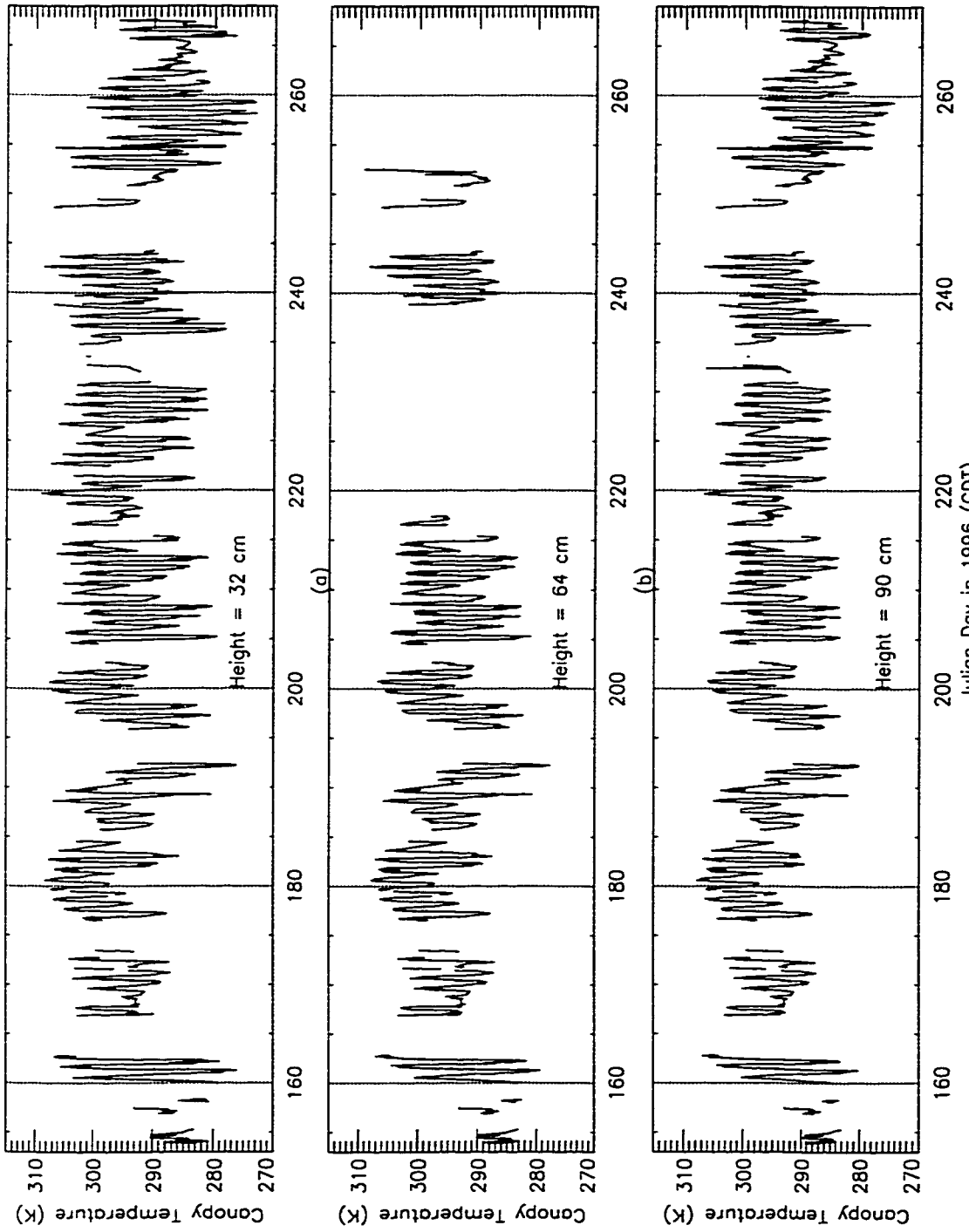

Figure B.9: Canopy temperatures at the heights of: (a) 32 (b) 64 and (c) 90 cm.

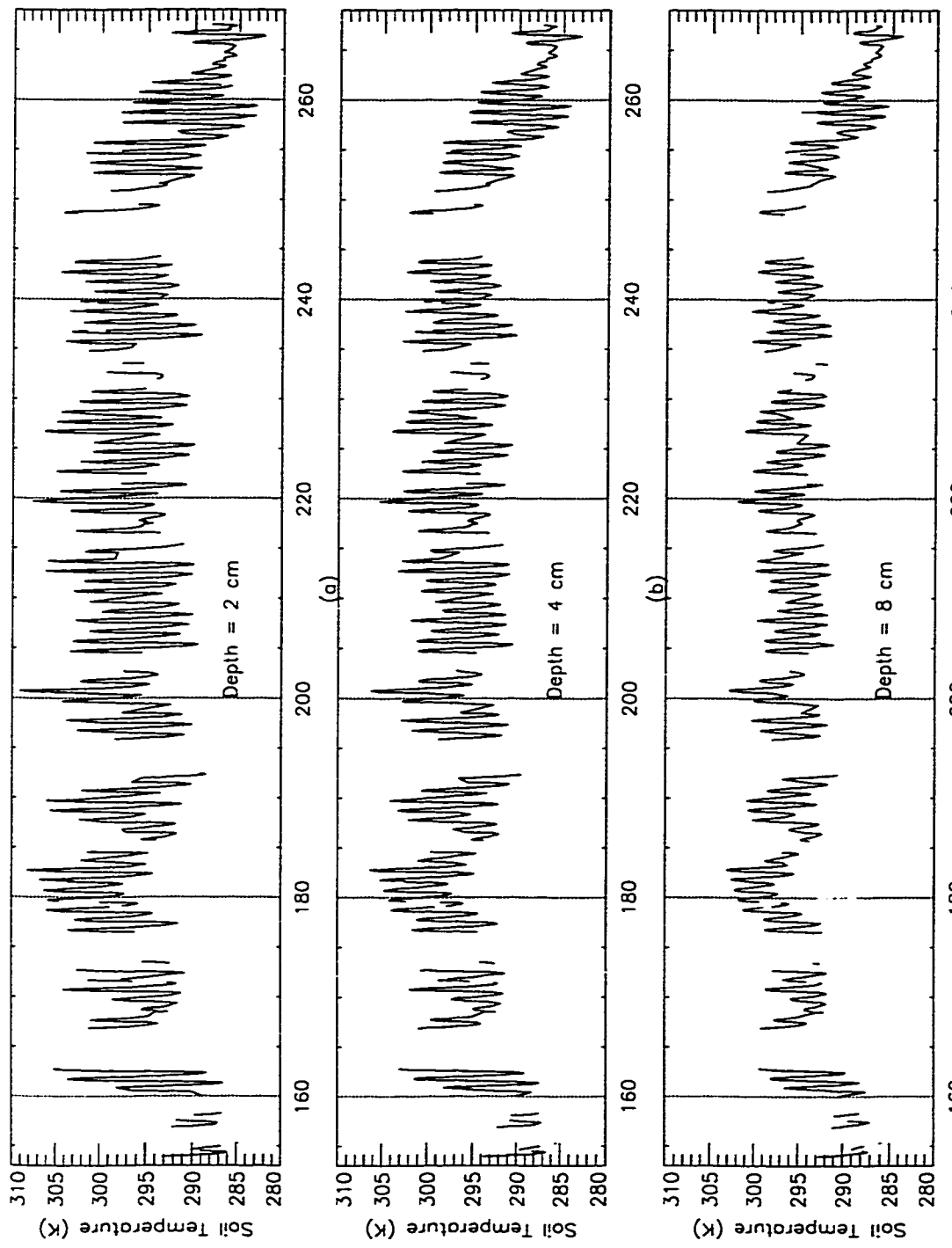

Figure B.10: Soil temperatures at the depths of: (a) 2 (b) 4 and (c) 8 cm.

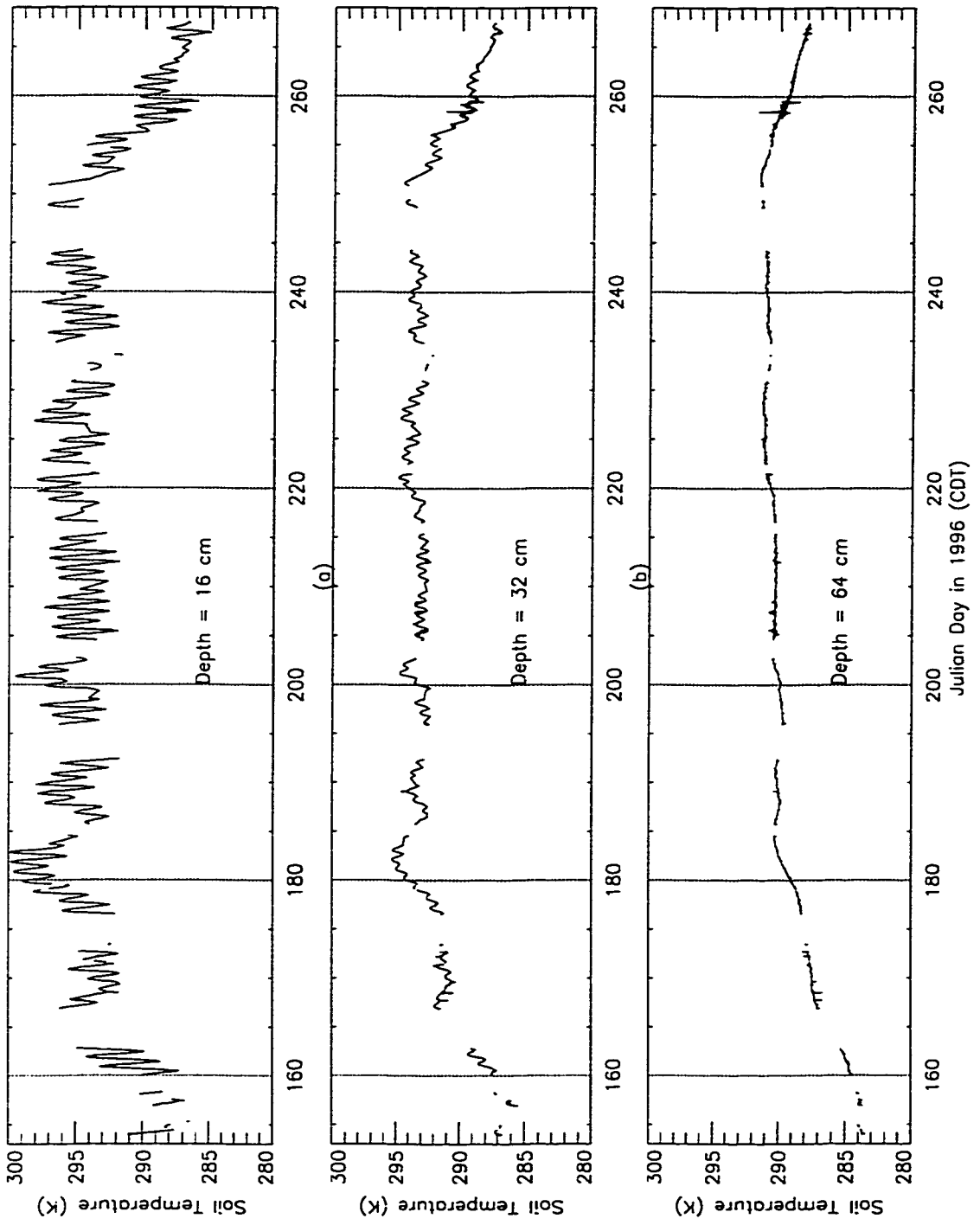

Figure B.11: Soil temperatures at the depths of: (a) 16 (b) 32 and (c) 64 cm.

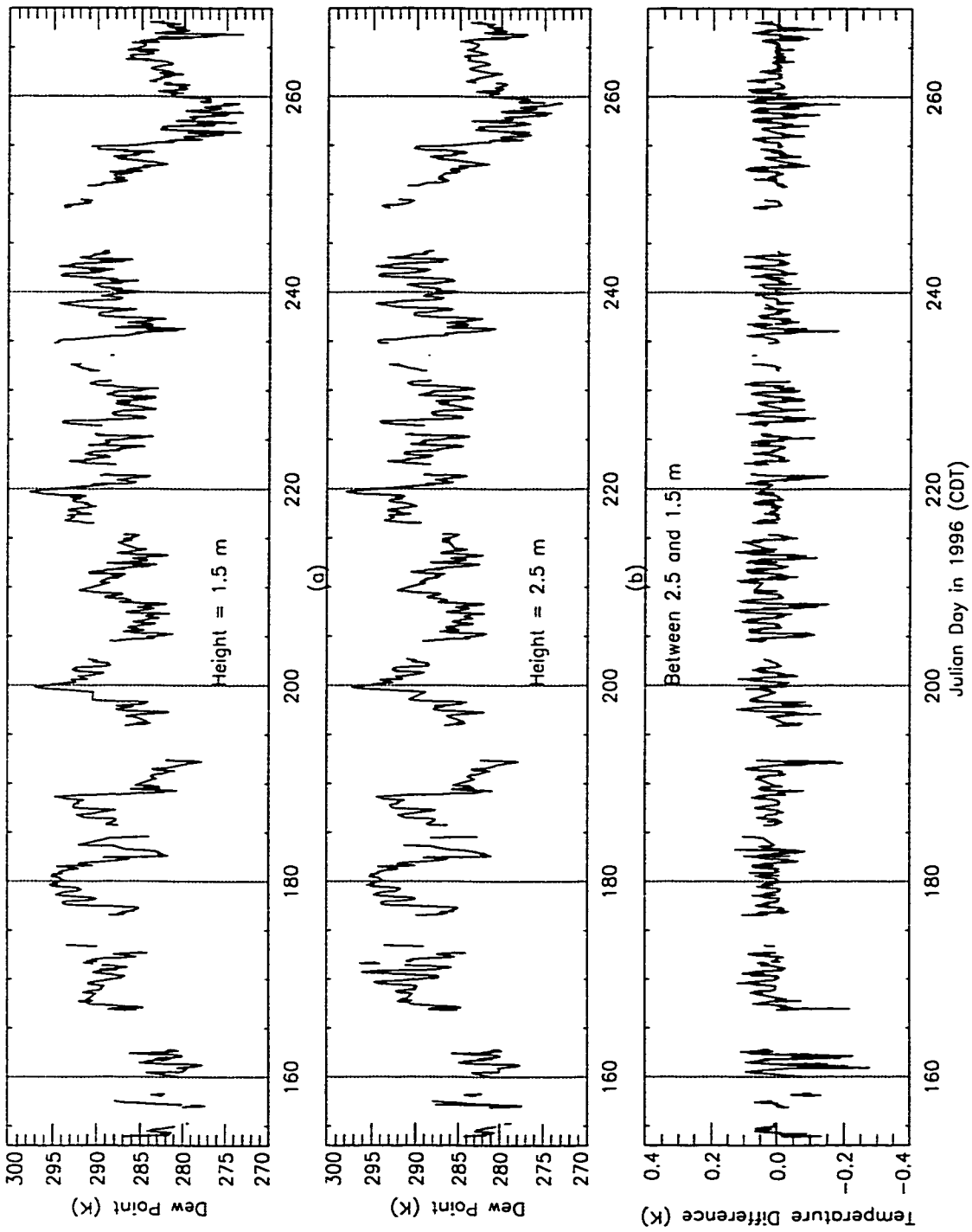

Figure B.12: Bowen Ratio measurements: (a) Dew point at 1.5 m (b) Dew point at 2.5 m and (c) Difference between the temperatures at the two heights.

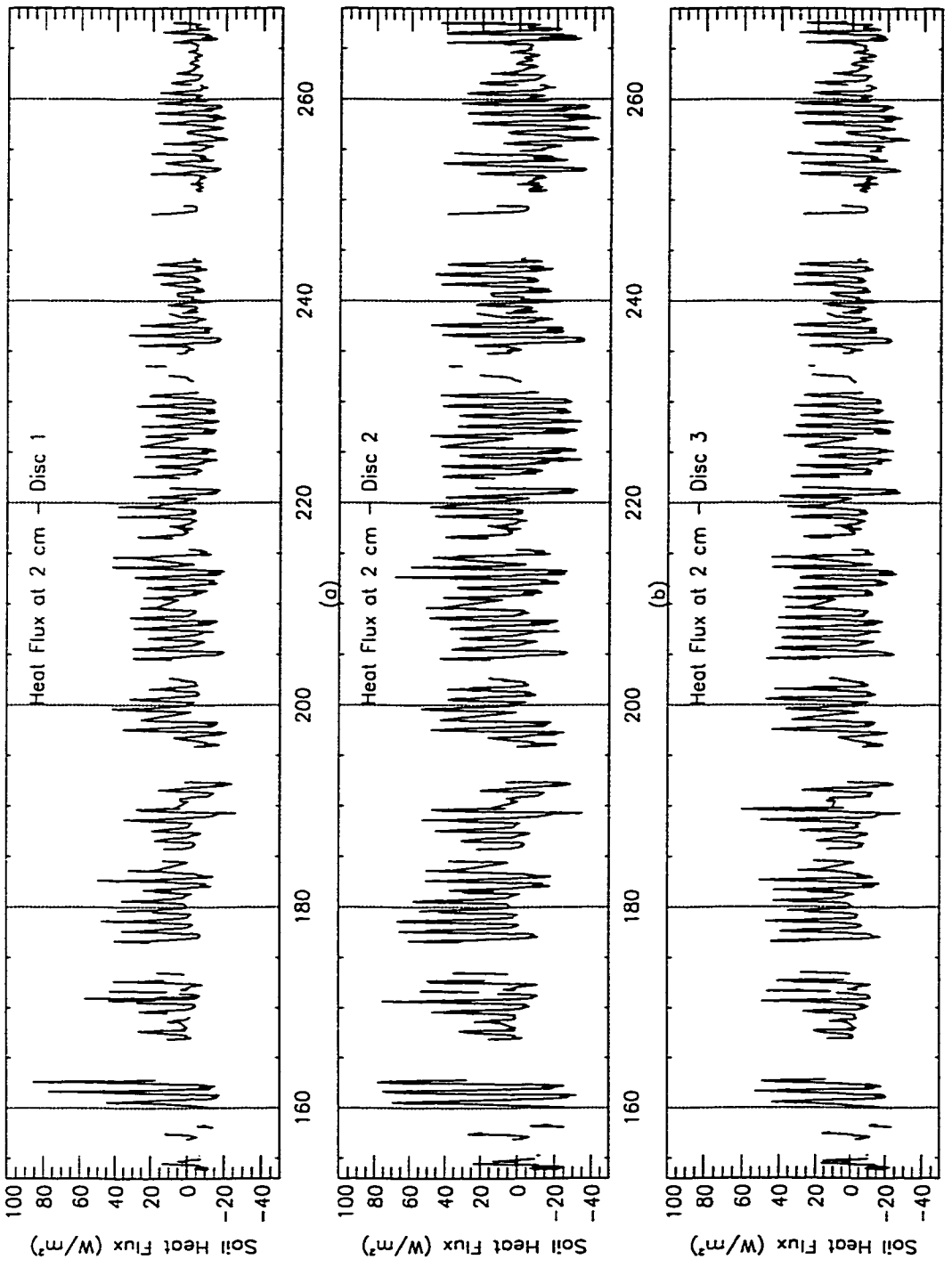

Figure B.13: Heat fluxes into the ground at 2 cm from the three heat flux discs.

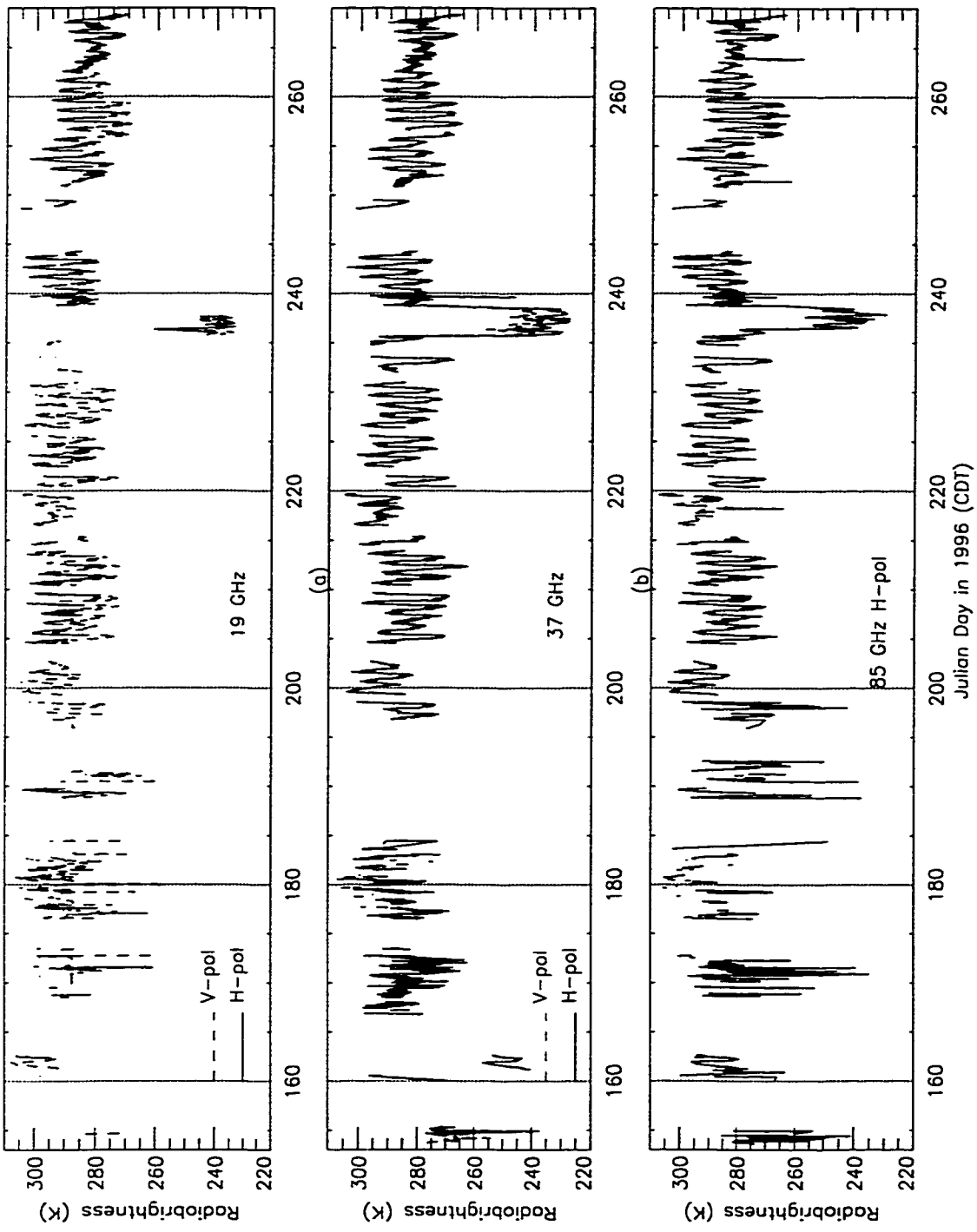

Figure B.14: Terrain brightnesses at (a) 19 (b) 37 and (c) 85 GHz.

B.3 Data Summary for the Winter Wheat site

Figures B.15 and B.16 show the parameters observed at the wheat site during REBEX-5.

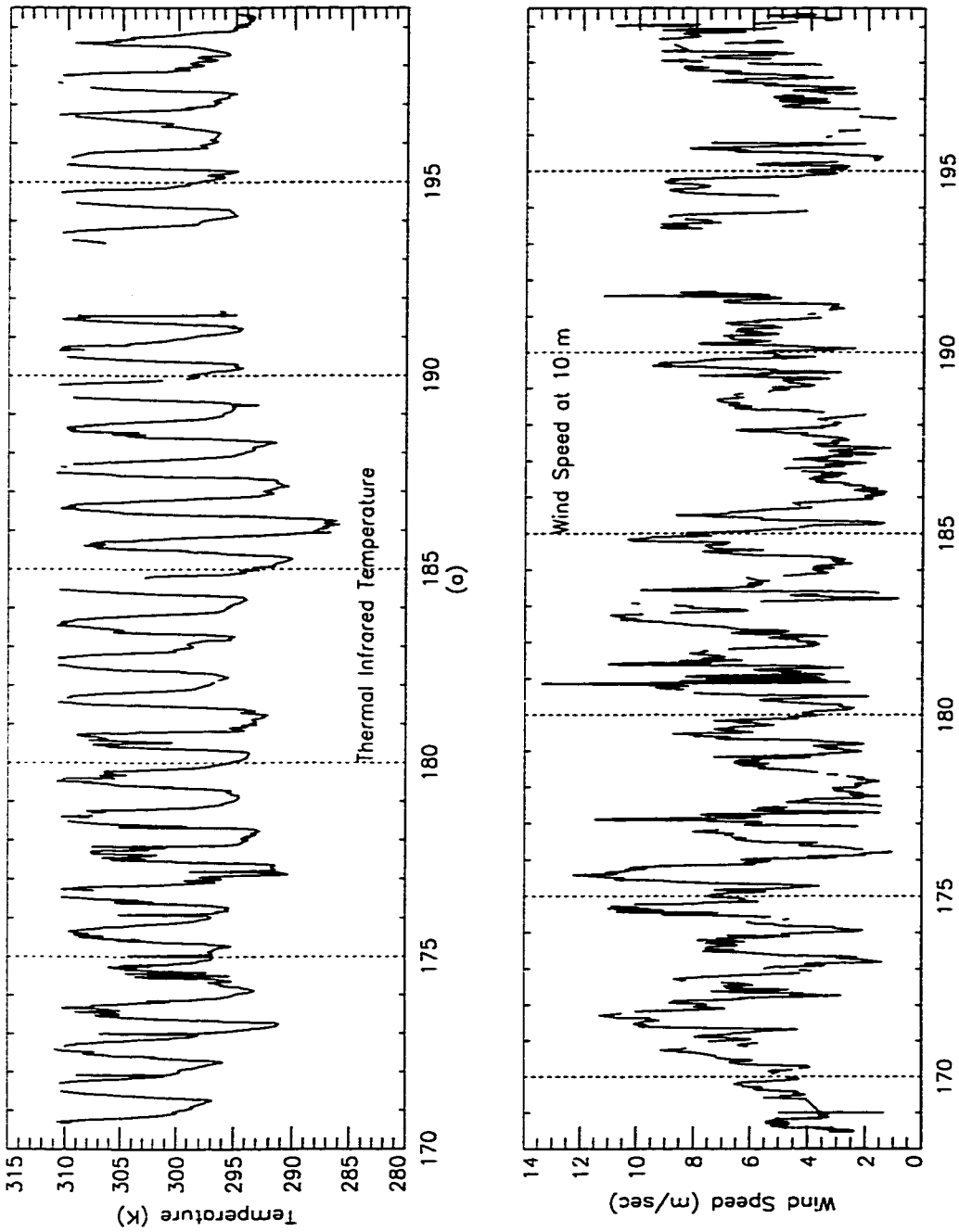

Figure B.15: (a) Thermal Infrared temperature and (b) Wind speed at 10 m.

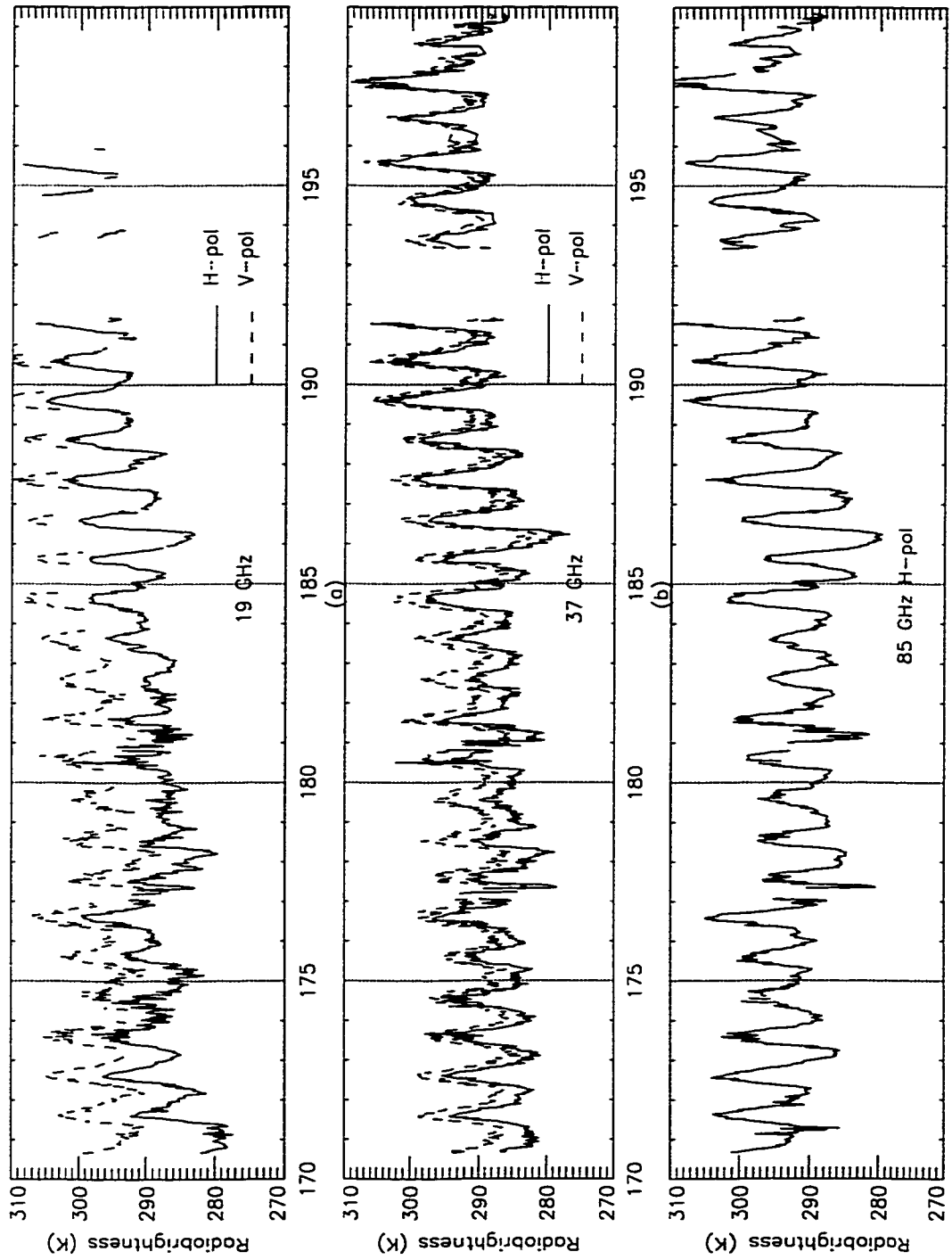

Figure B.16: Terrain brightnesses at (a) 19 (b) 37 and (c) 85 GHz.

APPENDIX C

Parameters in the LSP/R Model

This appendix lists the soil parameters and other physical constants used in the LSP/R Model.

Properties	Values
Specific heat capacity of clay (J/kgK)	758.51
Specific heat capacity of quartz (J/kgK)	755.37
Specific heat capacity of organic matter (J/kgK)	1932.0
Specific heat capacity of water (J/kgK)	4187.0
Specific heat capacity of dry air (J/kgK)	1004.64
Specific heat capacity of water vapor (J/kgK)	1952.0
Thermal conductivity of clay (W/mK)	2.93
Thermal conductivity of organic matter (W/mK)	.25
Thermal conductivity of dry air (W/mK)	0.0241
Intrinsic density of clay (kg/m^3)	2650.0
Intrinsic density of quartz (kg/m^3)	2660.0
Intrinsic density of organic matter (kg/m^3)	1300.0
Density of water (kg/m^3)	1000.0
Latent heat of vaporization at 273 K (J/kg)	2.501e6
Dry air gas constant (J/kgK)	287.05
Water vapor gas constant (J/kgK)	461.51
Volumetric content of bound water (m^3/m^3)	0.035

Table C.1: Soil parameters and other physical constants used in the LSP/R model from [122, 71, 111, 195].

BIBLIOGRAPHY

BIBLIOGRAPHY

[1] Abramopoulos, F., C. Rosenweig, and B. Choudhury, "Improved ground hydrology calculations for global climate models GCMs: Soil water movement and evapotranspiration," *J. Clim.*, vol. 1, pp. 921–941, 1988.

[2] Arya, S.P., *Introduction to Meteorology*, Academic Press Inc.: New York, 1988.

[3] Atlas, R., N. Wolfson, and J. Terry, "The effect of SST and soil moisture anomalies on GLA model simulations of the 1988 U.S. summer drought," *J. Clim.*, vol. 6, no. 11, pp. 2034–2048, 1993.

[4] Austin, R.T., *Electromagnetic Wave Scattering by Power-Law Surfaces*, PhD thesis, University of Michigan, 1994.

[5] Austin, R.T., A. England, and G. Wakefield, "Special problems in the estimation of power-law spectra as applied to topographical modeling," *IEEE Trans. Geosci. Remote Sensing*, vol. 32, pp. 928–939, 1994.

[6] Avissar, R. and R. Pielke, "A parametrization of heterogeneous land surfaces for atmospheric numerical models and its impact on regional meteorology," *Month. Weat. Rev.*, vol. 117, pp. 2113–2136, 1989.

[7] Bach, L.B., "Soil water movement in response to temperature gradients: Experimental measurements and model evaluation," *Soil Sci. Soc. Am. Proc.*, vol. 56, pp. 37–46, 1992.

[8] Backus, G. and F. Gilbert, "Uniqueness in the inversion of inaccurate gross earth data," *Phil. Trans. Roy. Soc. London*, vol. A266, pp. 123–192, 1970.

[9] Beljaars, A., P. Viterbo, M. Miller, and A. Betts, "The anomalous rainfall over the us during July 1993 - Sensitivity to land-surface parametrization and soil moisture," *Month. Weat. Rev.*, vol. 124, no. 3, pp. 362–383, 1996.

[10] Betts, A., J. Ball, and A. Beljaars, "Comparison between the land surface response of the ECMWF model and the FIFE-1987 data," *Q. J. Royal Meteo. Soc.*, vol. 119, pp. 975–1001, 1993.

[11] Betts, A., F. Chen, K. Mitchell, and Z. Janjic, "Assessment of land-surface and boundary-layer models two operational versions of the Eta model using FIFE data," *Month. Weat. Rev.*, vol. 124, , 1996.

[12] Betts, A., S. Hong, and H. Pan, "Comparison of NCEP/NCAR reanalysis with 1987 FIFE data," *Month. Weat. Rev.*, vol. 124, pp. 1480–1498, 1996.

[13] Bhumralkar, C.M., "Numerical experiments on the computatuion of ground surface temperature in an atmospheric general circulation model," *J. Appl. Meteo.*, vol. 14, pp. 1246–1258, 1975.

[14] Blackadar, A.K., "Modeling the nocturnal boundary layer," in *Third Symp. on Atmospheric Turbulence, Diffusion, and Air Quality*, Rayleigh, Amer. Meteor. Soc., 1976.

[15] Blanchard, B.J. and A. Chang, "Estimation of soil moisture from SEASAT SAR data," *Water Res. Research*, vol. 19, pp. 803–10, 1983.

[16] Bliss, N., "Personal communication,", 1997.

[17] Blondin, V., "Parameterization of land-surface processes in numerical weather prediction," in *Land Surface Evaporation Measurement and Parametrization*, T. Schmugge and J. André, editors, pp. 31–54, Springer-Verlag, 1991.

[18] Bonan, G. B., "Land-atmosphere CO_2 exchange simulated by a land surface process model coupled to an atmospheric general circulation model," *J. Geophys. Res.*, vol. 100, no. D2, pp. 2817–2831, February 1995.

[19] Bonan, G.B., "Comparison of two land surface process models using prescribed forcings," *J. Geophys. Res.*, vol. 99, no. D12, pp. 25803–19, December 1994.

[20] Bonan, G.B., "Land-atmosphere interactions for climate system models: Coupling biophysical,biogeochemical, and ecosystem dynamical processes," *Remote Sens. Env.*, vol. 51, pp. 57–73, 1995.

[21] Bonan, G.B., "A Land Surface Model (LSM Version 1.0) for ecological, hydrological, and atmospheric studies: Technical description and user's guide," Technical Report NCAR/TN-417+STR, Climate and Global Dynamics Division, NCAR, January 1996.

[22] Bonan, G.B., "The NCAR Land Surface Model (LSM Version 1.0) coupled to the NCAR Community Climate Model," Technical Report NCAR/TN-429+STR, Climate and Global Dynamics Division, NCAR, September 1996.

[23] Brodzik, M., "Personal communication,", 1994-99.

[24] Budyko, W.F., *Climate and Life*, Academic Press: New York, 1974.

[25] Burke, E.J., R.J. Gurney, L. Simmonds, and T. Jackson, "Calibrating a soil water and energy budget model with remotely sensed data to obtain quantitative information about the soil," *Water Res. Research*, vol. 33, no. 7, pp. 1689–1697, July 1997.

[26] Burke, E.J., R.J. Gurney, L. Simmonds, and P. O'Neill, "Using a modeling approach to predict soil hydraulic properties from passive microwave measurements," *IEEE Trans. Geosci. Remote Sensing*, vol. 36, no. 2, pp. 454–462, March 1998.

[27] Burke, W.J., T. Schmugge, and J. Paris, "Comparison of 2.8- and 21-cm microwave radiometer observations over soils with emission model calculations," *J. Geophys. Res.*, vol. 84, no. C1, pp. 287–294, January 1979.

[28] Camillo, P.J., R.J. Gurney, and T.J. Schmugge, "A soil and atmosphere boundary layer model for evapotranspiration and soil moisture studiess," *Water Res. Research*, vol. 19, no. 2, pp. 371–380, April 1983.

[29] Camillo, P.J. and T. Schmugge, "Correlating rainfall with remotely sensed microwave radiation using physically based models," *IEEE Trans. Geosci. Remote Sensing*, vol. GE-22, no. 4, pp. 415–23, July 1984.

[30] Charney, J.G., "Dynamics of deserts and drought in the sahel," *Q. J. Royal Meteo. Soc.*, vol. 101, no. 428, pp. 193–202, April 1975.

[31] Charney, J.G., W. Quirk, S. Chow, and J. Kornfield, "A comparitive study of the effects of albedo change on drought in semi-arid regions," *J. Atmos. Sc.*, vol. 34, pp. 1366–85, September 1977.

[32] Chen, F., Z. Janjic, and K. Mitchell, "Impact of atmospheric surface layer parametrization in the new land-surface scheme of the NCEP mesoscale Eta numerical model," *Boundary-Layer Meteor.*, 1996.

[33] Chen, F., K. Mitchell, J. Schaake, Y. Xue, H. Pan, V. Koren, Q. Duan, K. Ek, and A. Betts, "Modeling of land-surface evaporation by four schemes and comparison with FIFE observations," *J. Geophys. Res.*, vol. 101, pp. 7251–7268, 1996.

[34] Choudhury, B.J., T. Schmugge, R. Newton, and A.Chang, "Effect of surface roughness on the microwave emission from soils," *J. Geophys. Res.*, vol. 84, pp. 5699–5706, 1979.

[35] Cloetingh S., C. Covey, A. Henderson-Sellers, L. Sloan, B. Moore, and P. Pirazzoli, "Special issue on coupling land and atmosphere," *Global and Planetary Change*, vol. 19, no. 1-4, pp. 1–276, 1998.

[36] Crank, J., *The Mathematics of Diffusion*, Clarendon Press: Oxford, 1975.

[37] Crosson, W.L., "Personal communication,", 1997.

[38] Crosson, W.L., C. Laymon, R. Inguva, and M. Schamshula, "Assimilation of remotely-sensed soil moisture estimates in a distributed surface flux-hydrology model using a kalman filter," in *14th Conf. on Hydrology*, pp. 269–272, Jan 10-15, Dallas,Texas, 1999, Amer. Meteor. Soc.

[39] Dahl, P., J. Judge, J. Gallo, and A. England, "Vertical distribution of biomass and moisture in a prairie grass canopy," Technical Report Rad. Lab. Tech. Note RL-902, University of Michigan, 1993.

[40] Dcoudré, N.I., K. Laval, and A. Perrier, "SECHIBA, a new set of parameterizations of the hydrological exchanges at the land-atmosphere interface for within the LMD atmospheric general circulation model," *J. Clim.*, vol. 6, pp. 248–273, 1993.

[41] de Vries, D.A., "Simultaneous transfer of heat and moisture in porous media," *Trans. Am. Geophys. Union*, vol. 39, no. 5, pp. 909–16, 1958.

[42] de Vries, D.A., "Thermal properties of soils," in *Physics of Plant Environment*, pp. 210–235. Interscience Publishers: New York, 1963.

[43] Deardorff, J.W., "A parametrization of ground-surface moisture content for use in atmospheric prediction models," *J. Appl. Meteo.*, vol. 16, pp. 1182–85, November 1977.

[44] Deardorff, J.W., "Efficient prediction of ground surface temperature and moisture, with inclusion of a layer of vegetation," *J. Geophys. Res.*, vol. 83, no. C4, pp. 1889–1903, April 1978.

[45] Dickinson, R.E., "Global change and terrestrial hydrology-a review," *Tellus*, vol. 43AB, pp. 176–181, 1991.

[46] Dickinson, R.E. and A. Henderson-Sellers, "Modelling tropical deforestation: A study of GCM land-surface parametrizations," *Q. J. Royal Meteo. Soc.*, vol. 114, pp. 439–462, 1988.

[47] Dickinson, R.E., A. Henderson-Sellers, and P. Kennedy, "Biosphere-atmosphere transfer scheme (BATS) version 1e as coupled the NCAR Community Climate Model," Technical Report NCAR/TN-387+STR, Climate and Global Dynamics Division, NCAR, August 1993.

[48] Dickinson, R.E., A. Henderson-Sellers, P. Kennedy, and M. Wilson, "Biosphere-atmosphere transfer scheme (BATS) for the NCAR Community Climate Model," Technical Report NCAR/TN-275+STP, Atmospheric Analysis and Prediction Division, NCAR, December 1986.

[49] Dickinson, R.E. and P. Kennedy, "Impacts of regional climate of Amazon deforestation," *Geophys. Res. Letters*, vol. 19, pp. 1947–1950, 1992.

[50] Divers, Jeff, "Personal communication,", 1996.

[51] DMSP, "Platform document," *NASA/MSFC*, 1995.

[52] Dobson, M.C., F. Ulaby, M. Hallikainen, and M. El-Rayes, "Microwave dielectric behavior of wet soil-part II: Dielectric mixing models," *IEEE Trans. Geosci. Remote Sensing*, vol. GE-23, pp. 35–46, 1985.

[53] Eagleman, J. and W. Lin, "Remote sensing of soil moiture by a 21 cm passive radiometer," *J. Geophys. Res.*, vol. 81, pp. 3660–3666, 1976.

[54] El-Rayes, M.A. and F. Ulaby, "Microwave dielectric spectrum of vegetation-PartI: Experimental observations," *IEEE Trans. Geosci. Remote Sensing*, vol. GE-25, no. 5, pp. 541–549, September 1987.

[55] England, A.W., "Thermal microwave emission from a scattering halfspace," *Radio Sc.*, vol. 9, pp. 447–454, 1974.

[56] England, A.W., "Thermal microwave emission from a scattering layer," *J. Geophys. Res.*, vol. 80, pp. 4484–4496, 1975.

[57] England, A.W., "Relative influence upon microwave emissivity of fine-scale stratigraphy internal scattering and dielectric properties," *Pure and Applied Geophysics*, vol. 114, pp. 287–299, 1976.

[58] England, A.W., "Radiobrightness of diurnally heated, freezing soil," *IEEE Trans. Geosci. Remote Sensing*, vol. 28, no. 4, pp. 464–76, July 1990.

[59] England, A.W. and J. Galantowicz, "Moisture in a grass canopy from ssm/i radiobrightness," in *Proc. 2nd Tropical Symposium on Combined Optical-Microwave Earth and Atmos. Sensing*, volume Atlanta, GA, pp. 12–14, April 1995.

[60] England, A.W., J. Galantowicz, and M. Schretter, "The radiobrightness thermal inertia measure of soil moisture," *IEEE Trans. Geosci. Remote Sensing*, vol. 30, no. 1, pp. 132–139, January 1992.

[61] England, A.W. and G. Johnson, "Microwave brightness spectra of layered media," *Geophysics*, vol. 42, no. 3, pp. 514–521, April 1977.

[62] Entekhabi, D. and P. Eagleson, "Land surface hydrology parameterization for atmospheric general circulation models including subgrid scale spatial variability," *J. Clim.*, vol. 2, pp. 816–831, 1989.

[63] Entekhabi, D., H. Nakamura, and E. Njoku, "Solving the inverse problem for soil moisture and temperature profiles by sequential assimilation of multifrequency remotely sensed observations," *IEEE Trans. Geosci. Remote Sensing*, vol. 32, no. 2, , March 1994.

[64] Famiglietti, J., J. Devereaux, C. Laymon, T.Tsegaye, P. Houser, T. Jackson, S. Graham, M. Rodell, and P. Oevelen, "Effects of spatial variability and scale on areally averaged evapotranspiration," *Water Res. Research*, vol. 31, no. 3, pp. 699–712, March 1992.

[65] Famiglietti, J. and E. Wood, "Effects of spatial variability and scale on areally averaged evapotranspiration," *Water Res. Research*, vol. 31, no. 3, pp. 699–712, March 1992.

[66] Ferrazzoli, P. and L. Guerriero, "Modeling microwave emission from vegetation-covered surfaces: a parametric analysis," in *Passive microwave remote sensing of land-atmosphere interacations*, pp. 389–402. VSP: Netherlands, 1994.

[67] Fischman, M.F., "Personal communication,", 1996.

[68] Fischman, M.F., "Investigation of the Tower Mounted Radiometer System and proposed improvements," Technical Report Rad. Lab. Tech. Note RL-949, University of Michigan, 1997.

[69] *http://app.fao.org*, Food and Agr. Org.

[70] Galantowicz, J.F., "The michigan earth grid: Description, registration method for SSM/I data and derivative map projections," Technical Report Rad. Lab. Tech. Note 027396-2-T, University of Michigan, Ann Arbor, MI, 1991.

[71] Galantowicz, J.F., *Microwave radiometry of snow-covered grasslands for the estimation of land-atmosphere energy and moisture fluxes*, PhD thesis, University of Michigan, 1995.

[72] Galantowicz, J.F. and A. England, "Field data report for the first Radiobrightness Energy Balance Experiment (REBEX-1): October 1992-april 1993," Technical Report Rad. Lab. Tech. Note RL-904, University of Michigan, Ann Arbor, MI, 1993.

[73] Galantowicz, J.F. and A. England, "Seasonal snowpack radiobrightness interpretation using a svat-linked emission model," *J. Geophys. Res.*, vol. 102, no. D18, pp. 21933–46, September 1997.

[74] Galantowicz J.F., D. Entekhabi, and E. Njoku, "Tests of sequential data assimilation for retrieving profile soil moisture and temperature from observed l band radiobrightness," *IEEE Trans. Geosci. Remote Sensing*, vol. 37, no. 4, pp. 1860–1870, 1999.

[75] Georgakakos, K., J. Sperfslage, and A. Guetter, "Operational GIS-based models for NEXRAD radar data in the U.S.," in *Proc. of the Int. Conf. on Water Resources and Environ. Res.*, volume 1, pp. 603–609, Kyoto, Japan, Oct. 29-31, 1996.

[76] Ghildyal, B.P. and R. Tripathi, *Soil physics*, John Wiley:New York, 1987.

[77] Goodison, B.E., J. Metcalfe, D. McNichol, M. Davey, and H. Le, "Participation in REBEX-4: Data collection and completion phase report," Technical report, Atmospheric Environment Service, Canada, 1996.

[78] Goodison, B.E., J. Metcalfe, D. McNichol, M. Davey, and H. Le, "Participation in REBEX-4: Installation phase report," Technical report, Atmospheric Environment Service, Canada, 1996.

[79] Green, W.H. and G. Ampt, "Studies on soil physics," *J. Agri. Sc.*, vol. 4, no. 5, pp. 1, 1911.

[80] Hallikainen, M.T., F. Ulaby, M. Dobson, and M. El-Rayes, "Microwave dielectric behavior of wet soil-Part I: Empirical models and experimental observation," *IEEE Trans. Geosci. Remote Sensing*, vol. GE-23, pp. 25–34, 1985.

[81] Hartke, Gregory J. and David Rind, "Improved surface and boundary layer models for the Goddard Institute for Space Studies general circulation model," *J. Geophys. Res.*, vol. 102, no. D14, pp. 16407–16422, July 1997.

[82] Haverkamp, R., M. Vauclin, J. Tauma, P.J. Wierenga, G. Vachaud, "A comparison of numerical simulation models for one- dimensional infiltration," *Soil Sci. Soc. Am. J.*, vol. 41, no. 2, pp. 285–294, 1977.

[83] Heilman, J.L. and D.G. Moore, "HCMM detection of high soil moisture areas," *Remote Sens. Env.*, vol. 11, pp. 73–76, 1981.

[84] Heilman, J.L. and D.G. Moore, "Evaluating near-surface soil moisture using heat capacity mapping mission data," *Remote Sens. Env.*, vol. 12, pp. 117–21, 1982.

[85] Henderson-Sellers A., A.J. Pitman, P.K. Love, P. Irannejad, and T.H. Chen, "The Project for Intercomparison of Land Surface Parametrization Schemes (PILPS): Phases 2 and 3," *Bulletin of Amer. Meteor. Soc.*, vol. 76, no. 4, pp. 489–503, April 1995.

[86] Henderson-Sellers, A., Z.L. Yang, and R.E. Dickinson, "The Project for Intercomparison of Land Surface Parametrization Schemes," *Bulletin of Amer. Meteor. Soc.*, vol. 74, no. 7, pp. 1335–49, July 1993.

[87] Hillel, D., *Fundamentals of soil physics*, Academic Press, 1980.

[88] Hoekstra, P. and A. Delaney, "Dielectric properties of soils at uhf and microwave frequencies," *J. Geophys. Res.*, vol. 79, pp. 1699–1708, 1974.

[89] Hollinger, J.P., "SSM/I calibration/validation final report," Technical report, NRL Rep. Branch Rep., 1989.

[90] Hollinger, J.P., J. Pierce, and G. Poe, "SSM/I instrument evaluation," *IEEE Trans. Geosci. Remote Sensing*, vol. 28, no. 5, pp. 781–790, 1990.

[91] Hollinger, J.P., G. Poe, R. Savage, and J. Pierce, "Special Sensor Microwave/Imager user's guide," Technical report, NRL Rep. Branch Rep., 1987.

[92] Houser, P.R., W. Shuttleworth, J. Famiglietti, H. Gupta, K. Syed, and D. Goodrich, "Integration of soil moisture remote sensing and hydrologic modeling using data assimilation," *Water Res. Research*, vol. 34, no. 12, , December 1998.

[93] Hunt, B.G., "A model study of some aspects of soil hydrology relevant to climatic modelling," *Q. J. Royal Meteo. Soc.*, vol. 111, pp. 1071–85, 1985.

[94] Idso, S.B., R.J. Jackson, R.J. Reginato, B.A. Kimball, and F.S. Nakayama, "The dependence of bare soil albedo on soil water content," *J. Appl. Meteo.*, vol. 14, pp. 109–113, February 1975.

[95] Idso, S.B., T.J. Schmugge, R.D. Jackson, and R.J. Reginato, "The utility of surface temperature measurements for the remote sensing of surface soil water status," *J. Geophys. Res.*, vol. 80, no. 21, pp. 3044–3049, July 1975.

[96] Jackson, R.D., R.J. Reginato, B.A. Kimball, and F.S. Nakayama, "Diurnal soil-water evaporation: Comparison of measured and calculated soil-water fluxes," *Soil Sci. Soc. Am. Proc.*, vol. 38, pp. 861–866, 1974.

[97] Jackson, T.J., "Personal communication,", 1998.

[98] Jackson, T.J., D. LeVine, A. Hsu, A. Oldak, P. Starks, C. Swift, J. Ishman, and M. Haken, "Soil moisture mapping at regional scales using microwave radiometry: the southern great plains hydrology experiment," *Accepted by IEEE Trans. Geosci. Rem. Sensing*, 1999.

[99] Jackson, T.J. and P. O'Neill, "Temporal observations of surface soil moisture using a passive microwave sensor," *Remote Sens. Env.*, vol. 21, pp. 281–296, 1987.

[100] Jackson, T.J. and R. O'Neill, "Attenuation of soil microwave emission by corn and soybeans at 1.4 and 5 GHz," *IEEE Trans. Geosci. Remote Sensing*, vol. 28, no. 5, pp. 978–980, September 1990.

[101] Jackson, T.J. and T. Schmugge, "Passive microwave remote sensing of soil moisture," *Advances in Hydroscience*, vol. 14, pp. 123–58, 1978.

[102] Jackson, T.J., T. Schmugge, and P. O'Neill, "Passive microwave remote sensing of soil moisture from an aircraft platform," *Remote Sens. Env.*, vol. 14, pp. 135–142, 1984.

[103] Jackson, T.J., T. Schmugge, and J. Wang, "Passive microwave sensing of soil moisture under vegetation canopies," *Water Res. Research*, vol. 18, no. 4, pp. 1137–1142, 1982.

[104] Johnson, G.R. and A. England, "Microwave radiometric survey of the San Joaquin Nuclean Project site, Kern County, CA," *J. Research, USGS*, vol. 5, pp. 431–435, 1977.

[105] Judge, J. and A. England, "Freeze/thaw classification using SSM/I," *IEEE Trans. Geosci. Remote Sensing*, vol. 36, , 1997.

[106] Judge, J. and A. England, "Field data report for the fourth radiobrightness energy balance experiment (REBEX-4): June - september 1996," Technical Report Rad. Lab. Tech. Note RL-974, University of Michigan, 1999.

[107] Judge, J., A. England, B. Hornbuckle, C. D.L. Boprie, and E. Kim, "Field data report for the fifth radiobrightness energy balance experiment (REBEX-5)," Technical Report Rad. Lab. Tech. Note RL-964, University of Michigan, 1998.

[108] Judge, J., A. England, C. L. W. Crosson, B. Hornbuckle, D. Boprie, E. Kim, and Y. Liou, "A growing season land surface process/radiobrightness model for wheat-stubble in the southern great plains," *IEEE Trans. Geosci. Remote Sensing*, vol. 37, no. 5, , 1999.

[109] Kim, E. and A. England, "Field data report for Radiobrightness Energy Balance Experiment 0 (REBEX-0), 8/92-9/92," Technical Report Rad. Lab. Tech. Note RL-916, University of Michigan, Ann Arbor, MI, 1996.

[110] Kim, E. and A. England, "Field data report for radiobrightness energy balance experiment 3 (REBEX-3), 9/94-9/95, alaskan north slope," Technical Report Rad. Lab. Tech. Note RL-918, University of Michigan, 1998.

[111] Kim, E.J., *Remote sensing of land surface conditions in arctic tundra regions for climatological applications using microwave radiometry*, PhD thesis, University of Michigan, 1999.

[112] Kimball, B.A., R. Jackson, R. Reginato, F. Nakayama, and S. Idso, "Comparison of field-measured and calculated soil-heat fluxes," *Soil Sci. Soc. Am. J.*, vol. 40, pp. 18–25, 1976.

[113] R. Koster and M. Suarez, "The influence of land surface moisture retention on precipiation statistics," *J. Clim.*, vol. 9, no. 10, pp. 2551–2567, 1996.

[114] Koster, R. and M. Suarez, "Modelling the land surface boundary in climate models as a compostie of independent vegetation stands," *J. Geophys. Res.*, vol. 97, no. D3, pp. 2697–2715, 1992.

[115] Kowalczyk, E.A, J. Garratt, and P. Krummell, "A soil-canopy scheme for use in a numerical model of the atmosphere-1D stand-alone model," Technical Report Research Tech. Paper 23, CSIRO Division of Atmospheric Research, 1991.

[116] Krazewski, A., "A model of the dielectric properties of wheat at 9.4 GHz," *J. Microwave Power*, vol. 13, pp. 293–296, 1978.

[117] Lai, S., J. Tiedje, and A. Erickson, "In situ measurement of gas diffusion coefficients in soils," *Soil Sci. Soc. Am. Proc.*, vol. 40, pp. 3–6, 1976.

[118] Lakshmi, Venkataraman, Eric F. Wood, and Bhaskar J. Choudhury, "A soil-canopy-atmosphere model for use in satellite microwave remote sensing," *J. Geophys. Res.*, vol. 102, no. D6, pp. 6911–6927, March 1997.

[119] Laymon, C.A., "Personal communication,", 1997.

[120] Lee, T.J., R. Pielke, T. kittel, and J. Weaver, "Atmospheric modelling and its spatial representation of land surface characteristics," in *Itegrated Geographic Information Systems and Environmental Modelling*, M. Goodchild, L. Parks, and L. Steyaert, editors, Oxford University Press, 1992.

[121] Liang, X., D. Lettenmaier, E. Wood, and S. Burges, "One-dimensional stastical dynamical representation subgrid spatial variability of precipitation in the 2-layer variable infiltration capacity model," *J. Geophys. Res.*, vol. 101, no. D16, pp. 21403–21422, September 1996.

[122] Liou, Y.A., *Land surface process/radiobrightness models for northern prairie*, PhD thesis, University of Michigan, 1996.

[123] Liou, Y.A. and A. England, "Annual temperature and radiobrightness signatures for bare soils," *IEEE Trans. Geosci. Remote Sensing*, vol. 34, no. 4, pp. 981–990, 1996.

[124] Liou, Y.A. and A. England, "A land surface process / radiobrightness model with coupled heat and moisture transport in soil," *IEEE Trans. Geosci. Remote Sensing*, vol. 36, no. 1, pp. 273–286, January 1998.

[125] Liou, Y.A. and A. England, "A land surface process/radiobrightness model with coupled heat and moisture transport for freezing soils," *IEEE Trans. Geosci. Remote Sensing*, vol. 36, no. 2, pp. 669–677, March 1998.

[126] Liou, Y.A., J. Galantowicz, and A. England, "A land surface process/radiobrightness model with coupled heat and moisture transport for prairie grassland," *IEEE Trans. Geosci. Remote Sensing*, vol. 37, no. 4, pp. 1848–1859, 1999.

[127] Liou, Y.A., E. Kim, and A. England, "Radiobrightness of prairie soil and grassland during dry-down simulations," *Radio Sc.*, vol. 33, no. 2, pp. 259–265, 1998.

[128] Local climatological data, Sioux Falls, SD, National Climatic Data Center, June-Sept 1996.

[129] Mahrt, L. and H. Pan, "A two layer model of soil hydrology," *Boundary-Layer Meteor.*, vol. 29, pp. 1–20, 1984.

[130] Manabe, S., "Climate and the ocean circulation. 1. The atmosphere circulation and the hydrology of the earth's surface," *Month. Weat. Rev.*, vol. 97, no. 11, pp. 739–774, November 1969.

[131] Matzler, C., "Seasonal evolution of microwave radiation from an oat field," *Remote Sens. Env.*, vol. 31, pp. 161–173, 1990.

[132] McDonald K.C., M. Dobson, and F. Ulaby, "Determination of soil moisture beneath a stalk or trunk-dominated canopy," in *Proc. IGARSS'88 Symp.*, volume Edinburgh, Scotland, 1988.

[133] Meehl, G.A., G. Boer, C. Covey, M. Latif, and R. Stouffer, "Intercomparison makes for a better climate model," *EOS Trans. Am. Geophys. Union*, vol. 78, no. 41, pp. 445–6, October 1997.

[134] Metcalfe, J., "Personal communication,", 1997.

[135] Miller, D.A. and R. White, "A conterminous united states multi-layer soil characteristics data set for regional climate and hydrology modeling," *Earth Interactions [online]: Available http://EarthInteractions.org*, vol. 2, , 1998.

[136] Milly, P.C.D., "Moisture and heat transport in hysteretic, inhomogeneous porus media: A matric head-based formulation and a numerical method," *Water Res. Research*, vol. 18, no. 3, pp. 489–498, June 1982.

[137] Milly, P.C.D., "Potential evaporation and soil moisture in general ciculation models," *J. Clim.*, vol. 5, pp. 209–226, 1992.

[138] Milly, P.C.D. and P. Eagleson, "Parametrization of moisture and heat fluxes across the land surface for use in atmospheric general circulation models," Technical Report Technical Report 279, Mass. Inst. of Tech., 1982.

[139] Mo, T., B. Choudhury, T. Schmugge, J. Wang, and T. Jackson, "A model for microwave emission from vegetation-covered fields," *J. Geophys. Res.*, vol. 87, pp. 11229–11237, 1982.

[140] Mo, T. and T. Schmugge, "Monte carlo simulation of the effect of soil moisture variation on the microwave emission from soils," *IEEE Trans. Geosci. Remote Sensing*, vol. GE-21, no. 4, pp. 473–479, October 1983.

[141] Mo, T. and T. Schmugge, "A parameterization of the effect of surface roughness on microwave emission," *IEEE Trans. Geosci. Remote Sensing*, vol. 25, no. 4, pp. 481–486, 1987.

[142] Moore, B.A., S. Bertone, K. Mitchell, P. Rice, and R. Neill, "A worldwide near-real time diagnostic agrometeorological model," in *20th Conf. on Agricultural and Forest Meteorology*, pp. 7–11, Salt Lake City, 1991, Amer. Meteor. Soc.

[143] Mualem, Y., "A new model for predicting the hydraulic conductivity of unsaturated porous media," *Water Res. Research*, vol. 12, no. 3, pp. 513–22, June 1976.

[144] NASA Goddard DAAC Archive, "The Southern Great Plains '97 (SGP '97) data archive," *http://daac.gsfc.nasa.gov/CAMPAIGN_DOCS/SGP97/sgp97.html*, 1998.

[145] National Snow and Ice Data Center (NSIDC), "NOAA/NASA Pathfinder program EASE-Grid DMSP SSM/I brightness temperatures," Technical report, CD-ROM, 1988-present.

[146] Nelson, S.O., "Microwave dielectric properties of grain and seed," *Trans. Am. Soc. Ag. Engineers*, vol. 16, pp. 902–905, 1973.

[147] Nelson, S.O., "Microwave dielectric properties of insects and grain kernels," *J. Microwave Power*, vol. 11, pp. 299–303, 1976.

[148] Nelson, S.O., "Electrical properties of grain and other food materials," *J. Food Proc. and Preserv.*, vol. 2, pp. 137–154, 1978.

[149] Nelson, S.O., "RF and microwave dielectric properties of shelled, yellow-dent field corn," *Trans. Am. Soc. Ag. Engineers*, vol. 23, pp. 1314–1317, 1979.

[150] Nelson, S.O. and L. Stetson, "Frequency and moisture dependence of the dielectric properties of hard red winter wheat," *J. Agric. Eng. Res.*, vol. 21, pp. 181–192, 1976.

[151] Nestrud, L.M., W. Bourne, J. Wennblom, and W. Wiesner, *Soil Survey of Minnehaha County, South Dakota*, United States Department of Agriculture, Soil Conservation Service, 1964.

[152] Newton, R.W., *Microwave remote sensing and its applications to soil moisture detection*, PhD thesis, Texas A&M University, 1977.

[153] Newton, R.W. and W. McClellan, "Permittivity measurements of soils at l-band," Technical Report Rep. RSC-58, Remote Sensing Center, Tex. A & M Univ., 1975.

[154] Njoku, E.G. and J. Kong, "Theory for passive microwave remote sensing of near-surface soil moisture," *J. Geophys. Res.*, vol. 82, no. 20, pp. 3108–18, July 1977.

[155] Noilhan, J and S. Planton, "A simple parametrization of land surface processes for meterological models," *Month. Weat. Rev.*, vol. 117, pp. 536–549, March 1989.

[156] O'Kray, C., "TDR to EASE-Grid conversion process documentation," Technical Report Rad. Lab. Tech. Note RL-960, University of Michigan, Ann Arbor, MI, 1998.

[157] O'Leary, D., G. Johnson, and A. England, "Fracture detection by airborne microwave radiometry in parts of the Mississippi embayment, Missouri and Tennessee," *Remote Sens. Env.*, vol. 13, pp. 509–523, 1983.

[158] Paegle, J., K. Mo, and J. Nogues-Paegle, "Dependence of simulated precipitation on surface evaporation during the 1993 US summer floods," *Month. Weat. Rev.*, vol. 124, no. 3, pp. 345–361, 1996.

[159] Pampaloni, P. and S. Paloscia, "Microwave emissions and plant water content: A comparison between field measurements and theory," *IEEE Trans. Geosci. Remote Sensing*, vol. GE-24, no. 6, pp. 900–905, November 1986.

[160] Pan, H.L., "A simple parametrization scheme of evapotranspiration over land for the NMC Medium-Range Forecast Model," *Month. Weat. Rev.*, vol. 118, pp. 2500–2512, 1990.

[161] Peake, William, "Interaction of electromagnetic waves with some natural surfaces," *IEEE Trans. Ant. Prop.*, vol. S-324, pp. 138–143, April 1978.

[162] Peixoto, J.P. and A. Oort, *Physics of Climate*, American Institute of Physics: New York, 1992.

[163] Philip, J.R., "Theory of infiltration, 1. The infiltration equation and its solution," *Soil Sc.*, vol. 83, no. 5, pp. 345–357, 1957.

[164] Philip, J.R., "Inverse solution for one-dimensional infiltration and ratio A/K1," *Water Res. Research*, vol. 26, no. 9, pp. 2023–2027, 1987.

[165] Philip, J.R., "The infiltration joining problem," *Water Res. Research*, vol. 23, no. 12, pp. 2239–2245, 1987.

[166] Philip, J.R. and D. de Vries, "Moisture movement in porous materials under temperature gradients," *Trans. Am. Geophys. Union*, vol. 38, no. 2, pp. 222–232, 1957.

[167] Pitman, A.J., Z. Yang, J. Cogley, and A. Henderson-Sellers, "Description of bare essentials of surface transfer for the Bureau of Metorology Research Center AGCM," Technical Report Research Report 32, BMRC, 1991.

[168] Poe, G.A., "Optimum interpolation of imaging microwave radiometer data," *IEEE Trans. Geosci. Remote Sensing*, vol. 28, no. 5, pp. 800–810, 1990.

[169] Poe, G.A., A. Stogryn, and A. Edgerton, "Determination of soil moisture content using microwave radiometry," Technical Report Final Tech. Rep. 1684 FR-1, Aerojet General Corp, El Monte, CA, 1971.

[170] Rawls, W.J., T.J. Gish, and D.L. Brakensiek, "Estimating soil water retention from soil physical properties and characteristics," *Adv. in Soil Sc.*, vol. 16, pp. 213–234, 1991.

[171] Reginato, R.J., S. Idso, J. Vedder, R. Jackson, M. Blanchard, and R. Goettelman, "Soil water content and evaporation determined by thermal parameters obtained from ground-based and remote measurements," *J. Geophys. Res.*, vol. 81, no. 9, pp. 1617–20, March 1976.

[172] Reible, D.D., T. Illangasekare, D. Doshi, and M. Malhiet, "Infiltration of immiscible contaminants in unsaturated zone," *Ground Water*, vol. 28, no. 5, pp. 685–692, 1990.

[173] Reutov, E.A. and A. Shutko, "Microwave spectroradiometry of water content of nonuniformly moistened soil with a surface transition layer," *Sov. J. Remote Sensing*, vol. 6, pp. 72–79, 1990.

[174] Ridder, K.D. and G. Schayes, "The IAGL land surface model," *J. Appl. Meteo.*, vol. 36, pp. 167–182, February 1997.

[175] Rossi, C. and J. Nimmo, "Modeling of soil water retention from saturation to oven dryness," *Water Res. Research*, vol. 30, no. 3, pp. 701–8, March 1994.

[176] Sato, N., P. Sellers, D. Randall, E. Schneider, J. Shukla, J. Kinter, Y. Hou, and E. Albertazzi, "Effects of implementing the simple biosphere model in a general circulation model," *J. Atmos. Sc.*, vol. 46, pp. 2757–2782, 1989.

[177] Schmugge, T.J., "Effect of texture on microwave emission from soils," *IEEE Trans. Geosci. Remote Sensing*, vol. GE-18, no. 4, pp. 353–61, October 1980.

[178] Schmugge, T.J., "Soil moisture sensing with microwave radiometers," in *Proc. of Remotely sensed Data Symposium*, pp. 346–54, 1980.

[179] Schmugge, T.J. and B. Blanchard, "Soil moisture sensing with aircraft observations of soil moisture variations," *J. Geophys. Res.*, vol. 79, pp. 317–323, 1978.

[180] Schmugge, T.J., P. Gloersen, T. Wilheit, and F. Geiger, "Remote sensing of soil moisture with microwave radiometers," *J. Geophys. Res.*, vol. 79, no. 2, pp. 317–23, 1974.

[181] Schmugge, T.J. and T. Jackson, "A dielectric model of the vegetation effects on the microwave emission from soils," *IEEE Trans. Geosci. Remote Sensing*, vol. 30, no. 4, pp. 757–760, July 1992.

[182] Schmugge, T.J., T. Jackson, and H. McKim, "Survey of methods for soil moisture determination," *Water Res. Research*, vol. 16, no. 6, pp. 961–79, December 1980.

[183] Schmugge, T.J., M. Meneely, A. Rango, and R. Neff, "Satellite microwave observations of soil moisture variations," *Water Resour. Bull.*, vol. 13, pp. 265, 1977.

[184] Schmugge, T.J. and P. O'Neill, "Passive microwave soil moisture research," *IEEE Trans. Geosci. Remote Sensing*, vol. GE-24, no. 1, pp. 12–22, January 1986.

[185] Schmugge, T.J., T. Wilheit, W. Webster, and P. Gloersen, "Remote sensing of soil moisture with microwave radiometers II," Technical Report TN D-8321, NASA, 1976.

[186] Sellers, P.J., Y. Mintz, Y. Sud, and A. Dalcher, "A Simple Biosphere model SiB for use within general circulation models," *J. Atmos. Sc.*, vol. 43, no. 6, pp. 505–531, March 1986.

[187] Sellers, William D., *Physical Climatology*, The University of Chicago Press: Chicago, 1965.

[188] Shmakin, A.B., "Parametrization of the orography-induced hydrology for GCMs: Semi-distributed landscape approach," *J. Hydrology*, vol. In press, , 1994.

[189] Shukla, J. and Y. Mintz, "Influence of land-surface evapotranspiration on the earth's climate," *Science*, vol. 215, pp. 1498–1501, 1982.

[190] Solheim F., *Use of pointed water vapor radiometer observations to improve vertical GPS surveying accuracy*, PhD thesis, University of Colorado, 1993.

[191] Southern Great Plains ARM-CART, U.S. DOE, "Data Archive Center,", 1998.

[192] Stogryn, A., "The brightness temperature of a vertically structured medium," *Radio Sc.*, vol. 5, pp. 1397, 1970.

[193] Stogryn, A., "Estimates of brightness temperatures from scanning radiometer data," *IEEE Trans. Ant. Prop.*, vol. AP-26, no. 5, pp. 720–726, 1978.

[194] Sud, Y.C. and W. Smith, "Influence of local land-surface processes on the indian monsoon: A numerical study," *J. Clim. Appl. Meteo.*, vol. 24, pp. 1015–36, 1985.

[195] Trenberth, Kevin E., *Climate System Modeling*, Cambridge University Press: New York, 1995.

[196] Tsang, L. and R. Newton, "Microwave emissions from soils with rough surfaces," *J. Geophys. Res.*, vol. 87, pp. 9017–24, 1982.

[197] Ulaby, F.T. and P. Batlivala, "Optimum radar parameters for mapping soil moisture," *IEEE Trans. Geosci. Remote Sensing*, vol. GE-14, pp. 81–93, 1976.

[198] Ulaby, F.T. and M. El-Rayes, "Microwave dielectric spectrum of vegetation-PartII: Dual- dispersion model," *IEEE Trans. Geosci. Remote Sensing*, vol. GE-25, pp. 550–557, September 1987.

[199] Ulaby, F.T. and R. Jedlicka, "Microwave dielectric properties of plant materials," *IEEE Trans. Geosci. Remote Sensing*, vol. GE-22, pp. 406–415, July 1984.

[200] Ulaby, F.T., R. Moore, and A. Fung, *Microwave Remote Sensing Active and Passive, Vol I*, Artech House:Massachussetts, 1981.

[201] Ulaby, F.T., R. Moore, and A. Fung, *Microwave Remote Sensing Active and Passive, Vol III*, Artech House:Massachussetts, 1986.

[202] Ulaby, F.T., M. Razani, and M. Dobson, "Effects of vegetation cover on the microwave radiometeric sensitivity to soil moisture," *IEEE Trans. Geosci. Remote Sensing*, vol. GE-21, pp. 51–61, 1983.

[203] Ulaby, F.T., A. Tavakoli, and T. Senior, "Microwave propogation constant for a vegetation canopy with vertical stalks," *IEEE Trans. Geosci. Remote Sensing*, vol. GE-25, pp. 714–725, 1987.

[204] Ulaby, F.T. and E. Wilson, "Microwave attenuation properties of vegetation canopies," *IEEE Trans. Geosci. Remote Sensing*, vol. GE-23, pp. 746–753, 1985.

[205] Verseghy, S.B., "CLASS-A Canadian land suface scheme for GCMs. I. Soil model," *Int. J. Climatology*, vol. 11, pp. 111–133, 1991.

[206] Verseghy, S.B., N. McFarlane, and M. Lazare, "CLASS-A Canadian land suface scheme for GCMs.ii. vegetation model and coupled runs," *Int. J. Climatology*, vol. 13, pp. 347–370, 1993.

[207] Viterbo, P. and A. Beljaars, "An improved land surface parametrization scheme in the ECMWF model and its validation," *J. Clim.*, vol. 8, , 1996.

[208] Walker, J. and P. Rowentree, "The effect of soil moisture on circulation and rainfall in a tropical model," *Q. J. Royal Meteo. Soc.*, vol. 103, pp. 29–46, 1977.

[209] Wang, J.R., "Effect of vegetation on soil moisture sensing observed from orbiting microwave radiometers," *Remote Sens. Env.*, vol. 17, pp. 141–51, 1985.

[210] Wang, J.R. and B. Choudhury, "Remote sensing of soil moisture content over bare field at 1.4 GHz frequency," *J. Geophys. Res.*, vol. 86, no. C6, pp. 5277–5282, June 1981.

[211] Wang, J.R., J. McMurtrey, E. Engman, T. Jackson, T. Schmugge, W. Gould, J. Fuchs, and W. Glazar, "Radiometric measurements over bare and vegetated fields at 1.4-GHz and 5-GHz frequencies," *Remote Sens. Env.*, vol. 12, pp. 295–311, 1982.

[212] Wang, J.R., P. O'Neill, T. Jackson, and E. Engman, "Multifrequency measurements of the effects of soil moisture , soil texture, and surface roughness," *IEEE Trans. Geosci. Remote Sensing*, vol. GE-21, no. 1, pp. 44–50, January 1983.

[213] Wang, J.R., T. Schmugge, W. Gould, W. Glazar, J. Fuchs, and J. McMurtrey, "A multi-frequency radiometric measurement of soil moisture content over bare and vegetated fields," *Geophys. Res. Letters*, vol. 9, no. 4, pp. 416–419, 1982.

[214] Wegmüller, U. and C. Mätzler, "Rough bare soil reflectivity model," *IEEE Trans. Geosci. Remote Sensing*, vol. 37, no. 3, pp. 1391–1396, 1999.

[215] Wentz, F.J., "User's manual of SSM/I antenna temperature tapes," Technical Report RSS Tech. Rep. 120191, Remote Sensing Systems, 1991.

[216] Wetzel, P.J. and J. Chang, "Evapotranspiration from nonuniform surfaces: A first approach for short-term numerical weather prediction," *Month. Weat. Rev.*, vol. 116, pp. 600–621, 1988.

[217] Wiesnet, D., "Remote sensing and its applications to hydrology," in *Facets of Hydrology*. Wiley: Chichester, 1976.

[218] Wood, E.F., D. Lettenmaier, and V. Zartarian, "A surface hydrology parametrization with subgrid variability in general circulation models," *J. Geophys. Res.*, vol. 97, no. D3, pp. 2720–2728, 1992.

[219] Xue, Y., P. Sellers, J. Kinter, and J. Shukla, "A simplified biosphere model for global climate studies," *J. Clim.*, vol. 4, pp. 345–364, March 1991.